Study of Magnetic Interlayer Coupling in Synthetic Antiferromagnets for use in MRAM Devices

by

Tommy McKinnon

B.Sc., Simon Fraser University, 2014

Thesis Submitted in Partial Fulfillment of the
Requirements for the Degree of
Doctor of Philosophy

in the
Department of Physics
Faculty of Science

SIMON FRASER UNIVERSITY
Fall 2020

Declaration of Committee

Name: **Tommy McKinnon**

Degree: **Doctor of Philosophy**

Thesis title: **Study of Magnetic Interlayer Coupling in Synthetic Antiferromagnets for use in MRAM Devices**

Committee: **Chair:** Malcolm Kennett
Associate Professor, Physics

Erol Girt
Supervisor
Professor, Physics

Brett Heinrich
Committee Member
Professor Emeritus, Physics

Karen Kavanagh
Committee Member
Professor, Physics

David Broun
Examiner
Associate Professor, Physics

Tim Mewes
External Examiner
Professor, Physics and Astronomy
University of Alabama

Abstract

In recent years, there has been an ever-increasing level of effort focused on creating novel technologies based on spintronics. One of the most exciting of these technologies is spin transfer torque random access memory (STT-MRAM), which is a solid-state non-volatile memory technology that is orders of magnitude better than flash memory in terms of speed and write endurance. One critical component of an STT-MRAM memory cell is the so-called fixed magnetic layer. The direction of magnetization of this layer must remain fixed so that it can act as a reference for the reading and writing of information to the cell. This layer is ideally composed of a synthetic antiferromagnet (SAF) with zero net magnetization because it can offer thermal stability, have its magnetization be less effected by external magnetic fields, and have reduced stray fields. One challenge with integrating a SAF into an STT-MRAM memory cell is that they are typically not thermally robust. Creating an STT-MRAM device generally requires at least one annealing step at temperatures between 200 and 300C. During this annealing process, the antiferromagnetic coupling (AFC) within the SAF changes dramatically and usually becomes ferromagnetic, thereby eliminating the SAF and all of its advantages. The work in this thesis centers around understanding exactly how and why this magnetic coupling changes during the annealing process, and how to prevent it so that a SAF fixed magnetic layer can be used in STT-MRAM devices. We start by depositing thin films containing two FeCoB layers coupled across several different non-magnetic spacer layers of varying thicknesses. We determine the magnitude and direction of the magnetic coupling between the two FeCoB layers both before and after annealing my analyzing ferromagnetic resonance (FMR) and magnetostatics measurements. Next, we study the role that boron has on the magnetic coupling by co-depositing it into the Ru spacer layer of samples with the structure NiFe/Ru/FeCo. From this, we conclude that the presence of boron within the FeCoB layer leads to increased diffusion of magnetic atoms into the non-magnetic spacer layer during the annealing process, which is responsible for the change in coupling seen in SAF structures. In order to prevent this, we insert diffusion barriers next to the FeCoB layers within a SAF. We find that with the diffusion barriers, we are able to create a thermally robust SAF structure that maintains AFC coupling even after annealing at temperatures of up to 350 °C.

Keywords: Magnetism; MRAM; Synthetic antiferromagnets; Interlayer magnetic coupling

Table of Contents

List of Tables

List of Figures

Chapter 1

Introduction

In recent years, there has been an ever increasing amount of effort focused on creating novel technologies based on spintronics. This research and development has made it apparent that there are many physical properties of magnetism on the nano scale that have yet to be fully exploited for technological purposes, making it very conducive for the creation of such novel technologies. Some examples of such technologies include high density hard disk drive storage [107, 110, 34], spin transfer torque magnetic random access memory (STT-MRAM) for solid state storage [50, 96, 115], neuromorphic computing [109], and magnetic field sensors. [51, 53]

Several of these technologies make use of a phenomenon known as giant magnetoresistance (GMR) or tunneling magnetoresistance (TMR). These two phenomena cause the electrical resistance through a trilayer structure, composed of two magnetic layers separated by a non magnetic spacer layer, to be dependent on the direction of magnetization of the two magnetic layers relative to one another, as shown in Fig 1.1. This kind of structure is known as a pseudospin valve. [58] The main difference between GMR and TMR is that the non magnetic layer is metallic in GMR, and insulating in TMR. When the magnetic layers are parallel with one another the electrical resistance is low, and when they are antiparallel with one another the electrical resistance is high. These pseudospin valve structures are very common in novel spintronics devices because, while their functionality exploits the spin property of the electron, they provide an interface that traditional electronic devices are able to use.

STT-MRAM is a non-volatile information storage technology that stores binary information in the direction of magnetization of a magnetic layer. For example, if the magnetization is pointing up, it corresponds to a 1, if it is pointing down, it corresponds to a 0. These devices make use of a pseudospin valve for the purpose of measuring this layer's direction of magnetization, and also for setting its direction of magnetization using spin transfer torque (STT). They do this by including a second magnetic layer that has its direction of magnetization fixed, acting as a reference. This second magnetic layer is separated from the first by a non-magnetic spacer so that the structure exhibits GMR or TMR. These two magnetic

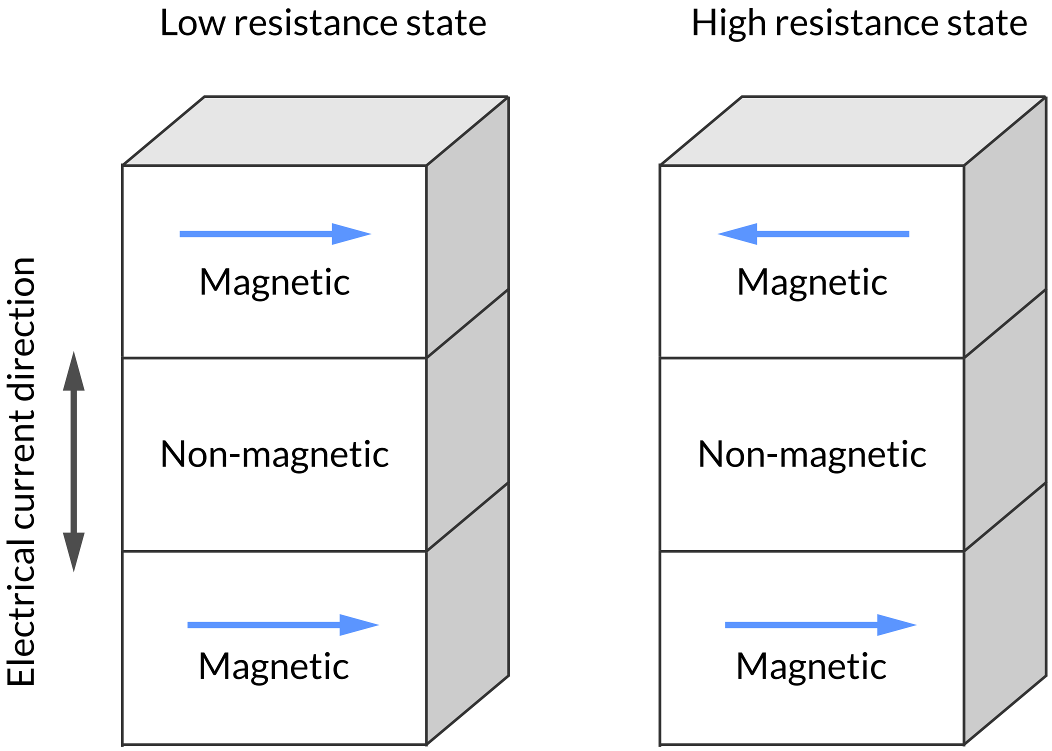

Figure 1.1: Schematic of a pseudospin valve structure with two magnetic layers separated by a non-magnetic spacer layer that exhibits GMR (with a metallic non-magnetic layer) or TMR (with an insulating non-magnetic layer). The resistance to electrical current running vertically through the structure is dependent on the direction of magnetization of the two magnetic layers, shown here as blue arrows.

layers are known as the free and fixed layers, for the former and latter, respectively. With this configuration, a standard electrical computer is able to measure the information stored on the device by simply measuring its electrical resistance.

STT-MRAM is one of the most exciting new technologies because it will have an immediate impact on a very large fraction of humanity. Memory and storage technology is now seamlessly integrated into our lives inside applications such as cloud storage, personal computers, smart devices, and everything in between. STT-MRAM improves on existing non-volatile memory and storage in many ways. Specifically, it is expected to be faster, 2-30 ns write time latency [60] compared to 200 μs for flash [95], have close to infinite endurance, exceeding 10^{15} write cycles [93] compared with 10^5 for flash, [95] and have high memory density. [19] All of this while being relatively easily integrated into the CMOS process. [22, 15]

For this kind of device, the magnetization of the fixed layer needs to be more stable than that of the free layer. This is typically achieved by either making the fixed layer thicker, or antiferromagnetically coupling (AFC) it to another magnetic layer to form a

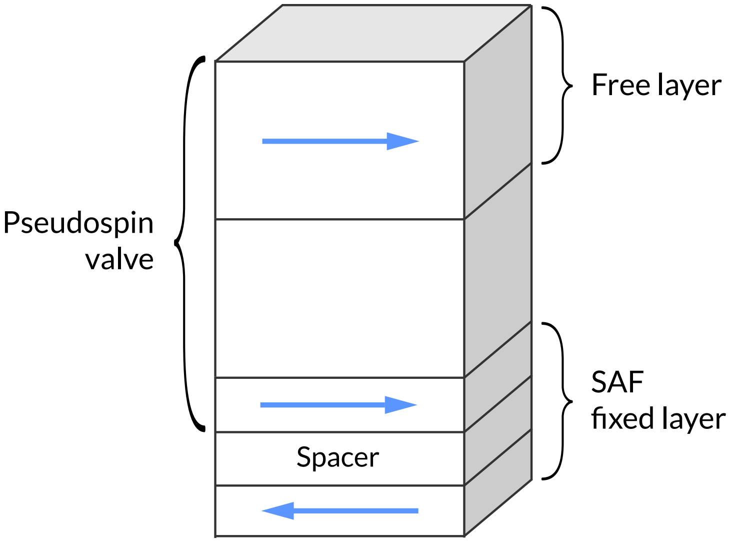

Figure 1.2: Schematic of a typical STT-MRAM pseudospin valve containing a free and fixed layer, where the fixed layer is composed an AFC coupled SAF. The layers with blue arrows are magnetic layers, and the direction of magnetization is identified by the direction of the arrow. The SAF is composed of two magnetic layers separated by a non-magnetic spacer layer. The pseudospin valve section is shown in greater detail in Fig. 1.1

synthetic antiferromagnet (SAF). The latter case is superior because a SAF can have zero net magnetization. This results in the magnetization of the fixed layer being less effected by weak external magnetic fields, allowing it to be more stable. It also results in dramatically reduced stray fields, improving free layer reversal characteristics. [56, 112, 39, 40] A schematic of a trilayer structure that includes the SAF fixed layer is shown in Fig. 1.2.

The FeCoB/MgO/FeCoB tunnel junction structure, which forms a pseudospin valve, is one of the most commonly studied structures for use as part of an STT-MRAM device. This is because, after being annealed at a temperature between 200 °C and 300 °C, it has a very large difference in resistance between the parallel and anti-parallel state, which is called TMR in this case. This large TMR is ideal because it allows the device to be read more quickly using modern electronics devices. After annealing, this tunnel junction structure also contains large perpendicular magnetic anisotropy (PMA) at the FeCoB/MgO interface. [49, 104] This large PMA allows the memory density to be increased because the shape anisotropy and interface anisotropy are in the same direction for very small nanopillars, which will be explained in detail in a later section.

One serious problem with the usage of FeCoB/MgO/FeCoB tunnel junctions in devices requiring a fixed layer, is that the annealing step tends to reduce or eliminate the AFC coupling within the SAF fixed layer, causing the two magnetic layers within the SAF to instead become ferromagnetically coupled (FC). If this occurs, the fixed layer will no longer function properly because it can have its magnetization easily rotated by external magnetic fields, making it unstable. It will also have increased stray magnetic fields that can effect the other FeCoB layer on the other side of the MgO layer.

This unwanted change in interlayer exchange coupling, seen at these annealing temperatures, is specific to FeCoB magnetic layers, and doesn't occur for other magnetic layers such as Co or FeCo, for example. But the FeCoB material is a vital component of the FeCoB/MgO/FeCoB tunnel junction, and cannot be changed without degrading the performance and density of the device.

Previous work has examined the effect that annealing has on samples with the structure Ta/FeCoB/MgO/FeCoB/Ta, and Ta/FeCoB/MgO structure. [58, 37] One key result that both works found is that after the samples were annealed at temperatures of 300 °C and above, boron was rejected from the FeCoB layers and was found to be dissolved in the adjacent MgO and Ta layers. This indicates that boron diffusion may play a part in changing the coupling within an FeCoB containing SAF structure. However, to the best of our knowledge, there have been no studies looking at the effect that annealing has on the diffusion of elements or interlayer exchange coupling in FeCoB containing SAF structures.

The ability to create a SAF fixed layer structure containing FeCoB that can withstand annealing is of great technological importance because it will allow for the creation of novel spintronics devices containing FeCoB/MgO/FeCoB tunnel junctions that are high performance and reliable.

The goal of the work done throughout this thesis is to understand why FeCoB containing SAF fixed layers have magnetic coupling that is very sensitive to annealing, when similar structures containing other magnetic layers are not. After that, we will develop a solution to the problem that allows the creation of FeCoB containing SAF fixed layers that can withstand the annealing process and remain strongly AFC coupled.

This thesis is organized as follows: in Chapter 2, the experimental tools and methods for the characterization of various properties of our samples is described. In Chapter 3, the sample preparation methods are described. This includes substrate cleaning, the sputtering process for thin film growth, and the sample annealing process. In Chapter 4, the theoretical considerations needed to understand the work that follows. This includes the understanding of ferromagnetic resonance, our micromagnetics model, and interlayer exchange coupling. Chapter 5 details the ferromagnetic resonance spectrometer that is used to study the magnetic properties of the samples in this thesis. This spectrometer, in combination with the theory from Chapter 4, will allow us to measure the coupling strength between two magnetic layers separated by a non magnetic spacer. Chapter 6 details the magneto-optic Kerr effect magnetometer capable of quickly and easily measuring the static magnetic properties of some samples in this thesis. In Chapter 7, we will fully characterize the interlayer exchange coupling of two FeCoB layers coupled across some of the most relevant non-magnetic spacer layers, both before and after being annealed. This will allow us to understand exactly how coupling changes during the annealing process. In Chapter 8, we will study the role that boron has on interlayer exchange coupling, and learn why the coupling within SAF structures changes so dramatically when the boron containing FeCoB is used, but not when boron free layers like FeCo or Co are used. In Chapter 9, we will use our results to develop several novel SAF fixed layers containing FeCoB that remain strongly AFC coupled even after being annealed at up to 350 °C. In Chapter 10, we will analyze the interlayer exchange coupling oscillations of several series of samples containing two magnetic layers separated by Ru spacer layers. We will do this by using the interface-reflection RKKY-like interlayer exchange model. This will allow us to gain useful insight into the fundamental physics giving rise to oscillatory interlayer exchange coupling.

Throughout this thesis, all units will in the SI system. It is common for work in magnetism to use the old CGS system of units. When comparing that work using the old CGS system to the work in this thesis, there will be many small differences involving many 4π's and μ_0's. Additionally, we will refer to all elements by their abbreviated form, like Ru and Co, except for boron to avoid confusion with the magnetic B field.

Chapter 2

Experimental Methods for Characterization

2.1 Magnetostatics Magnetometry

The exchange stiffness, saturation magnetization, and interlayer exchange coupling constants of our samples can be determined by measuring the magnetization as a function of applied external magnetic field, $M(H)$. Throughout the work in this thesis, this is done using one of three experimental techniques: A superconducting quantum interference device (SQUID), a vibrating sample magnetometry (VSM), or magneto-optic Kerr effect (MOKE) magnetometry. In the last case, the measurements are not on an absolute scale and can be used to extract magnetic properties only if the saturation magnetization of the magnetic layers within the sample is known.

This section will explain the experimental methods, and the details of how results are determined from the measurements will be explained in Chapter 4.3.

These tools are first calibrated by measuring the magnetization of a sample with known magnetic properties. For VSM and SQUID, this allows us to set the measurement scale so that it corresponds to the correct absolute magnetization of the sample.

2.2 SQUID

A SQUID is one of the most sensitive methods for measuring magnetization, able to measure tiny fractions of a single flux quanta. A DC SQUID, which is the type used here, consists of a superconducting ring bisected by two Josephson junctions as shown in Fig 2.1. A Josephson junction is where two superconducting electrodes are separated by a very thin insulating or non-superconducting section. In 1961, Josephson showed that the current I flowing through a junction is given by [16]

$$I = I_0 \sin \delta, \tag{2.1}$$

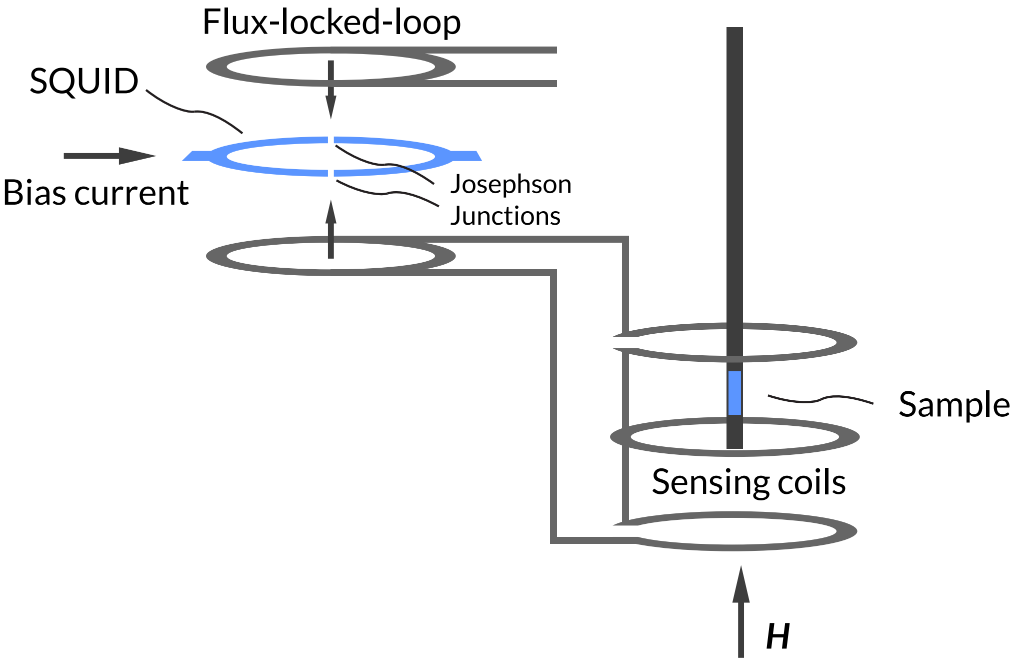

Figure 2.1: SQUID schematic. The sample moves through the sensing coils and induces a current. This current travels through the conductors and creates a magnetic field through the SQUID. Feedback from the SQUID voltage measurement is used to create an equal and opposite magnetic field in the flux-locked-loop.

where $\delta = \phi_1 - \phi_2$ is the difference between the phases ϕ_1 and ϕ_2 of the condensates in the two superconducting electrodes, and I_0 is the critical current. He also showed that when the critical current is surpassed, and a voltage U forms between the electrodes, δ evolves in time t according to

$$\frac{\mathrm{d}\delta}{\mathrm{d}t} = \frac{2eU}{\hbar} = \frac{2\pi U}{\Phi_0}, \tag{2.2}$$

where $\Phi_0 = \hbar\pi/e$ is the magnetic flux quantum.

Unlike in the case of an entirely superconducting ring, the condensate wavefunction phase in the SQUID ring can be discontinuous at the location of the two junctions, as shown in Eq. 2.1. This allows the magnetic flux within the ring to no longer be quantized, and can be increased continuously. As this occurs, it causes a change in the phase difference across the two junctions δ_1 and δ_2, which results in the modulation of I through the junctions as described by Eq. 2.1. This modulation is periodic with respect to magnetic flux, with a period of one flux quanta Φ_0. Thus, one is able to determine magnetic flux through the ring by measuring the critical current.

In practice, measuring the critical current through the SQUID is cumbersome. Instead, the SQUID is biased with a current I_B, that is slightly greater than the sum of the critical currents through both junctions. This causes a voltage to form across the junctions that behaves according to Eq. 2.2. In this configuration, it can be shown that the voltage across the junctions is also periodic with respect to the flux through the ring, just like the current.[16] This configuration is used in most real devices because it is relatively easy to measure the voltage across the junctions.

Finally, when measuring magnetic flux through the ring, a flux-locked-loop is used to create an equal and opposite flux. This is done for 2 reasons, to keep the voltage within a single period of the $V(\Phi)$ curve, and at the most sensitive point where $\mathrm{d}V/\mathrm{d}\Phi$ is maximized.

2.3 VSM

A schematic for a VSM is shown in Fig. 2.2. VSM works by vibrating a magnetized sample through conducting pickup coils, which are situated within a large magnet that generates a magnetic field, $\boldsymbol{H}$. The magnitude of the magnetic field can be varied, and if the sample is magnetic, it will become magnetized in response.

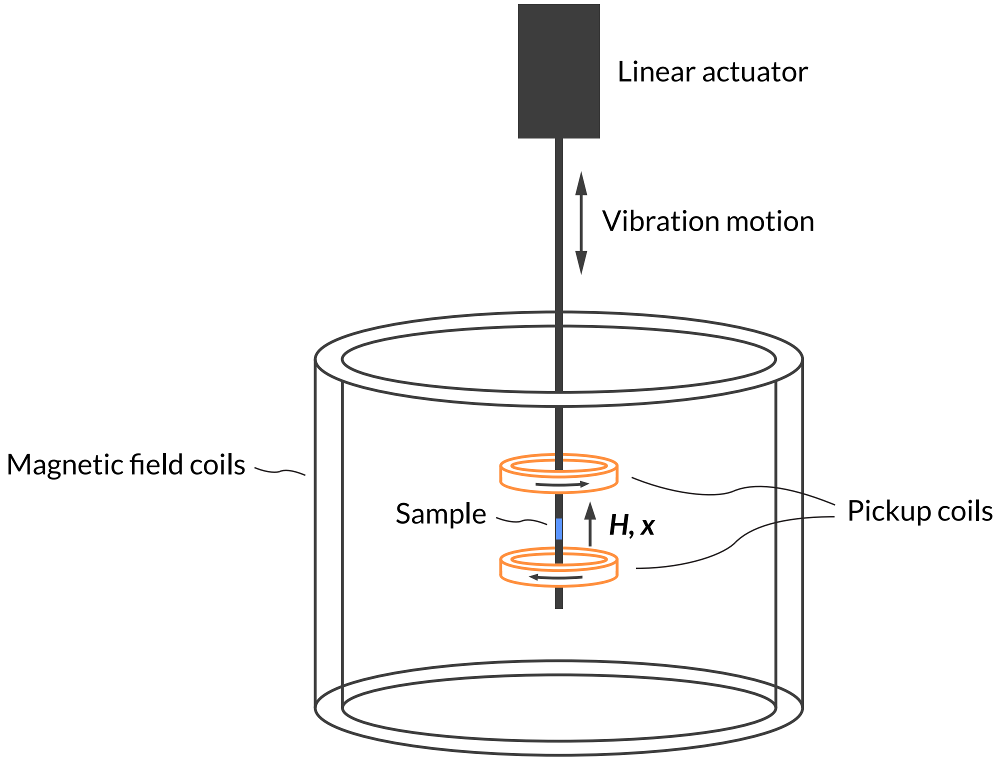

Figure 2.2: Schematic of a VSM tool. The sample size has been enlarged to show it more clearly. The pickup coils have also been separated to show the sample in between. The windings of the two pickup coils are in opposite directions. $\boldsymbol{H}$ is parallel with the $\boldsymbol{x}$ axis, as shown.

The magnetization of the sample is determined by measuring the voltage across the pickup coils, which obeys Faraday's law according to

$$\varepsilon = -\frac{\mathrm{d}\mathbf{\Phi}_B}{\mathrm{d}t}, \tag{2.3}$$

where Φ_B is the magnetic flux through the coils. For a pickup coil with N turns, an area A this becomes

$$\varepsilon = -NA\cos(\theta)\frac{\mathrm{d}B_x}{\mathrm{d}t}, \tag{2.4}$$

where $B_x = \mu_0(H + M_x)$ is the magnitude of the magnetic flux density, H is the magnitude of the magnetic field, and M_x is the magnitude of the magnetization, all through a single turn of the pickup coil. The x subscript denotes that it is only the component of the vector in the x direction as shown in Fig. 2.2. If the sample is vibrated sinusoidal, then $B_x = \mu_0(H + M_x \sin(\omega t))$, where H is stepped through a range of fields for the measurement, but held constant for the measurement at each step. Taking the time derivative of this and plugging it into Eq. 2.4 results in

$$\varepsilon = CM_x \sin\omega t, \tag{2.5}$$

where the contribution from H is gone because it is constant in time, $C = NA\mu_0$ is a constant that is determined experimentally by calibrating using a sample of known magnetization. The tool uses two oppositely wound pickup coils so that any time varying external field will be equal and opposite and can be subtracted out, leaving only the contribution from the magnetization of the sample. Thus, by measuring the induced voltage in the pickup coils, we are able to determine M_x as a function of H, which is the magnetization measurement that we desire.

In order to measure the $M_x(H)$ of our samples, we first calibrate the tool using a pure Fe sample of known volume and saturation magnetization. Every time we measure a sample we make sure to center the sample within the two pickup coils both vertically and horizontally.

2.4 MOKE

MOKE magnetometry exploits the interaction between light and magnetic materials in order to measure the magnetization of thin films. A typical MOKE setup uses a laser beam to probe the magnetization of the sample, which is only sensitive to the surface as it can only penetrate to depths on the order of the penetration depth, which is on the order of tens of nanometers. [91] For films thinner than this, MOKE is the ideal tool to quickly measure magnetization because of its sensitivity, local probing nature, and experimental simplicity.

MOKE, as a magnetization measurement technique, is based on the fact that when linearly polarized light is reflected off of the surface of a magnetic material, its polarization can be changed (and become elliptically polarized) proportionally to the direction and magnitude of the magnetization of the material.

Linearly polarized light is composed of the superposition of right and left circularly polarized light. In the context of the classical picture of the electrons within a material, a left-circularly polarized electric field will drive the electrons into left circular motion, and a right-circularly polarized electric field will drive the electrons into right circular motion. In the presense of a magnetic field, this electron motion will be modified according to the Lorentz force, of which the magnetic component is given by

$$\boldsymbol{F} = -e\boldsymbol{v} \times \boldsymbol{B} \tag{2.6}$$

where e is the elementary charge of an electron, $\boldsymbol{v}$ is the velocity of the electron, and $\boldsymbol{B}$ is the magnetic field within the material. This force points toward or away from the circle's center for left or right circular motion, which will cause the radius to be smaller for the former and larger for the latter. This difference in radii of the left and right circularly polarized modes will give rise to different reflection coefficients for each, causing a Kerr rotation in the reflected light. [91, 31] The MOKE experimental setup and example measurements will be shown in chapter 6.

2.5 X-Ray Diffraction (XRD)

In this work, we use XRD to study the details of the crystal structure of our samples. Specifically, we determine the lattice constants, crystal orientation, and texture of our polycrystalline films. We are able to determine these properties by analyzing the reflections of X-rays from planes of atoms within our samples. When many reflections from individual planes of atoms interfere constructively, they produce a detectable signal. This occurs when the incoming parallel X-rays reflecting from the individual planes have a path length differences equal an integer number of wavelengths $\Delta L = n\lambda$ as shown in Fig. 2.4. For a crystal where all of the atoms are in a regular periodic array with interplanar spacing d, this will occur when Bragg's Law is satisfied by [113]

$$\Delta L = 2d \sin\theta = n\lambda, \tag{2.7}$$

where θ is the angle of the incident X-ray relative to the plane as shown in Fig. 2.4, λ is the wavelength of X-rays used, which is 0.15418 nm Cu-Kα in our case, and n is a positive integer.

In an unknown crystal, the atomic planes could be oriented in any direction with any spacing. In order to fully characterize its lattice, the X-ray source, detector, and sample would have to be systematically varied through all possible angles that satisfy the Bragg condition. This is obviously very tedious to do, and generally not attempted. Luckily for us,

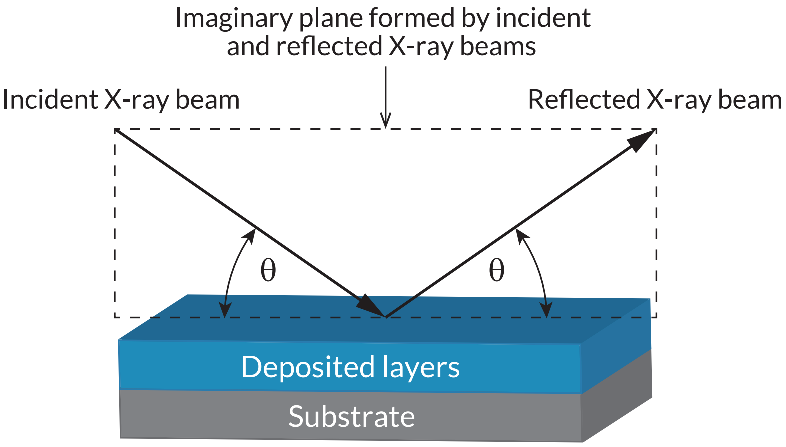

Figure 2.3: Schematic diagram showing the geometry used in XRD and XRR measurements where the imaginary plane formed by the incident and reflected X-rays is also normal to the surface of the sample. The subsequent 2d schematics will be a slice through this imaginary plane so that the plane normal, incident and reflected x-rays are all in the plane of the page of this thesis.

for the samples that we grow throughout this thesis, we know the elemental composition, expected crystal structure and orientation, and that they are polycrystalline. This allows us to look for reflections from a small subset of atomic planes, and compare with literature in order to determine the properties of the crystal structure.

The first kind of XRD measurement we perform in this work is where we measure the lattice spacing of planes with normal vectors perpendicular to the surface of the sample. We will refer to this as a perpendicular measurement configuration. This is done using a scan configuration called a θ-2θ scan, where the angle between the X-ray source and the plane of the sample, which is called ω, is half of the angle between the X-ray source and the detector, which is called 2θ. The imaginary plane formed by the incident and reflected X-rays is also normal to the surface of the sample, as shown in Fig. 2.3. After determining the spacing between the planes parallel to the surface, we compare with the expected crystal structure from literature. From this, we can determine how the crystal structure is oriented perpendicular to the plane of the sample. This measurement will not allow us to determine how the crystal structure is oriented in the plane of the sample, but since our samples are polycrystalline, in most cases it will be random.

In some instances, we also use XRD to measure the lattice spacing of planes with normal vectors that lay in the plane of the sample. We will refer to this as an in-plane measurement configuration. This shares the same confuration as the perpendicular measurement, except the imaginary plane created by the incident and reflected X-rays would now ideally lay in the plane of the sample. In practice, the sample is rotated slightly so that the incident X-rays are at a very small angle to the plane of the sample so that fewer X-rays are blocked

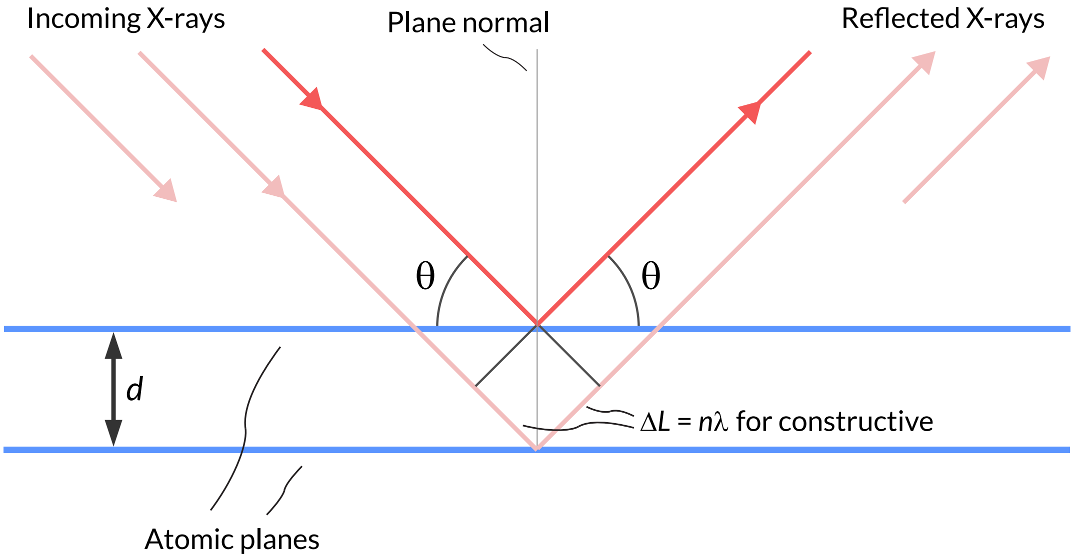

Figure 2.4: Schematic diagram of diffraction of X-rays by the atomic planes within a crystal.

by the sample, and a larger signal is detected. In our measurements, the sample is rotated so that the incident beam comes in at a grazing angle of 0.65° relative to the plane of the sample. Since our samples are polycrystalline with approximately random orientation of the crystalites in the plane of the sample, this kind of measurement will usually result in more peaks than a perpendicular measurement, allowing more precise characterization of the lattice spacing of the crystal structure. A typical example of raw in-plane and perpendicular XRD measurements is shown in Fig. 2.5. These measurements are of a hexagonal close packed Ru thin film textured in the [0001] direction.

We measure the texture of our films using a scan configuration known as an ω scan, also known as a rocking curve. A schematic diagram of this kind of scan is shown in Fig. 2.6. This scan starts in the same configuration as the θ-2θ scan, at an angle where a reflection is detected. At this angle, $\omega = \theta$, and the detector is at an angle of 2θ. The sample is rotated from the angle $\omega = \theta - \varphi$ to $\omega = \theta + \varphi$, where φ is typically 15°. The full-width-half-maximum (FWHM) of the peak obtained through this measurement quantifies the degree to which the polycrystals are aligned with respect to one another. A small FWHM indicates that the polycrystals are very well aligned, or highly textured, while a large FWHM indicates that they are not well aligned. The width of the rocking curve has also been shown to be proportional to the density of defects in thin films. [64, 76, 45, 108, 8] An example of a rocking curve measurement of the (0001) peak of a Ru thin film is shown in Fig. 2.7

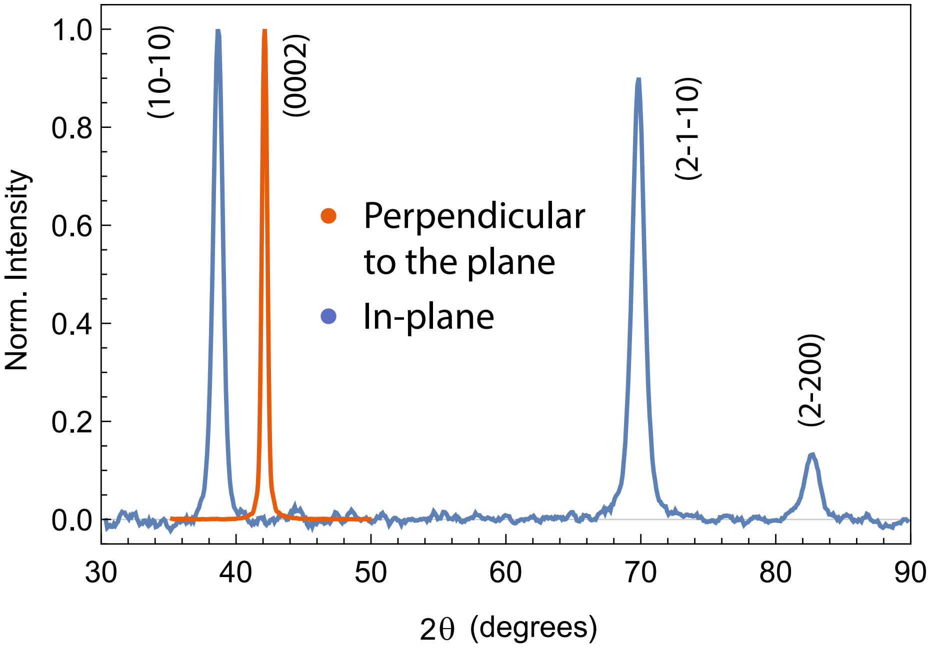

Figure 2.5: Example of a typical in-plane and perpendicular XRD measurement for a 23 nm hexagonal close packed Ru thin film textured in the [0001] direction. The orange data are reflections from planes with normals perpendicular to the plane of the sample, and the blue data are reflections from planes with normals that lay in the plane of the sample. The planes that caused each reflection are labeled in the figure. The in-plane data has more noise because the measurements were done with incoming X-rays hitting the sample at a small grazing angle. For this particular sample, we were only interested in the (0002) perpendicular reflection, which is why we only scanned a limited range of angles.

2.6 X-Ray Reflectivity (XRR)

Low angle perpendicular θ-2θ XRD measurements are known as X-ray reflectivity XRR. XRR is used to determine the thickness of the deposited films in our samples. Instead of analyzing reflections from individual atomic planes within the film, XRR looks at reflections from the boundaries of the film layers where the index of refraction is discontinuous. A low-angle θ-2θ scan, typically from approximately $2\theta = 0.2^\circ$ to 8°, will result in intensity oscillations with an exponentially decreasing envelope, known as Kiessig fringes, as shown in Fig. 2.8. The oscillation peaks are where reflections, occurring at the discontinuities of the index of refraction throughout the thickness of the sample, interfere constructively, and the valleys are where they interfere destructively.

In order to determine the film thickness from the Kiessig fringes, we start by looking at the paths X-rays take through the sample. Using the labels in Fig. 2.9, the difference in path length of the two X-rays δL is given by

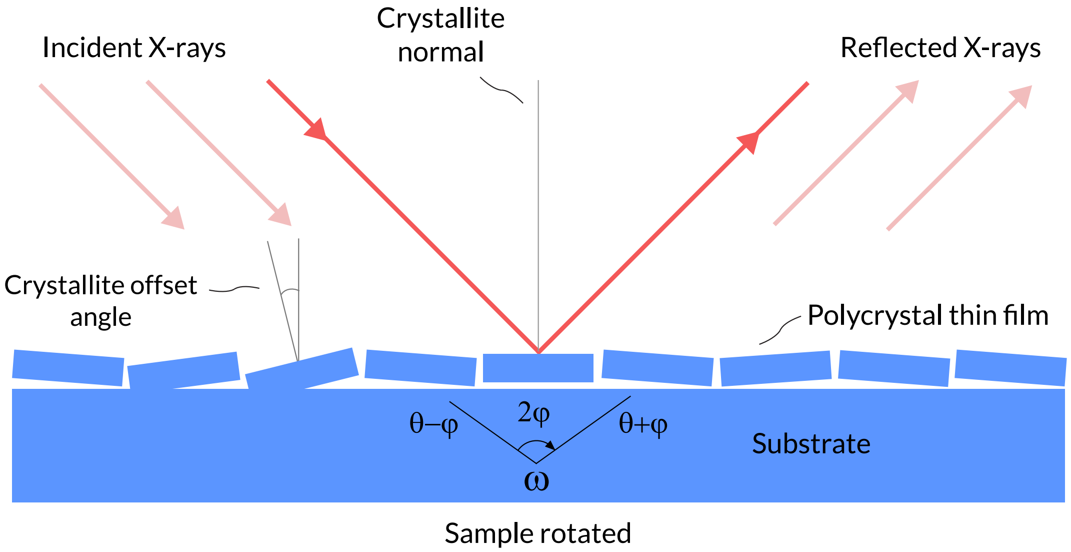

Figure 2.6: A schematic diagram showing the geometry of a rocking curve measurement of a polycrystalline sample composed of many crystallites that can have their crystal lattice offset at slightly different angles, as shown in the figure. Individual crystallites will create X-Ray reflections at different substrate angles relative to one another. The sample is rotated from the angle $\omega = \theta - \varphi$ to $\omega = \theta + \varphi$, while X-Ray reflection intensity is recorded in order to determine the distribution of orientations of the crystallites.

$$\delta L = n_1(AB + BC) - AD, \tag{2.8}$$

where n_1 is the refractive index of the film, and AB, BC, AD are path lengths between the points.

Path lengths AB and BC are identical and equal to

$$AB = BC = \frac{d}{\sin\theta_1}, \tag{2.9}$$

and the path length AD can be written as

$$AD = AC\cos\theta = 2AB\cos\theta_1\cos\theta = 2\frac{d}{\sin\theta_1}\cos\theta_1\cos\theta. \tag{2.10}$$

Using Snell's Law, the refracted angle, θ_1, is given by

$$\cos\theta_1 = \frac{n\cos\theta}{n_1} = \frac{\cos\theta}{n_1}. \tag{2.11}$$

Additionally, it can be shown that n is related to the critical angle θ_c, which the incident angle below which total internal reflection occurs, according to [44]

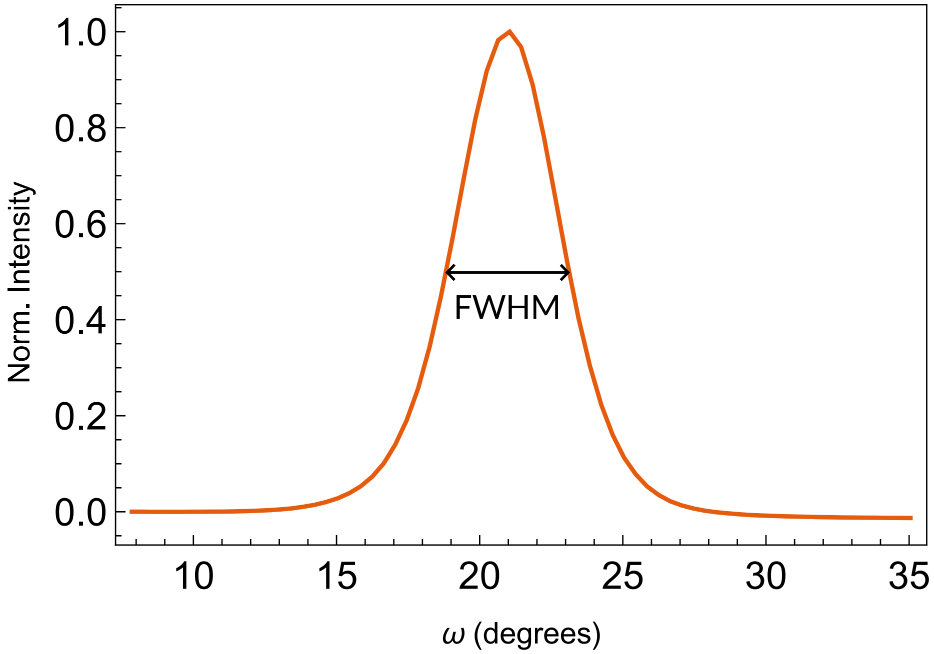

Figure 2.7: Example of a typical rocking curve measurement with a FWHM of 4.04 ± 0.05 degrees. This measurement is for the (0001) reflection of a Ru thin film.

$$n_1 = \frac{n\cos\theta_c}{\cos 0} = \cos\theta_c. \tag{2.12}$$

Combining Eq. 2.8, 2.10, 2.11, 2.12, we can write δL as

$$\begin{aligned}\delta L &= 2\cos\theta_c \frac{d}{\sin\theta_1} - 2\frac{d}{\sin\theta_1}\cos\theta_1\cos\theta \\ &= \frac{2dn_1}{\sin\theta_1}(1-\cos^2\theta_1). \end{aligned}\tag{2.13}$$

As we saw earlier, Braggs' law tells us constructive interference occurs when $\delta L = m\lambda$, which gives us

$$\frac{2dn_1}{\sin\theta_1}(1-\cos^2\theta_1) = m\lambda. \tag{2.14}$$

Finally, we replace θ_1 with θ_m to account for m interference maxima, and simplify Eq. 2.14, to obtain [44]

$$\frac{m\lambda}{2} = d\sqrt{\sin^2(\theta_m) - \sin^2(\theta_c)}. \tag{2.15}$$

In order to obtain a value for the film thickness d, we estimate θ_c as the angle at which the intensity is half of the maximum value, then we plot $\frac{m\lambda}{2}$ vs $\sqrt{\sin^2(\theta_m) - \sin^2(\theta_c)}$, and d is the slope. A typical example of this data for a Co thin film, along with linear fit to determine d, is shown in Fig. 2.10.

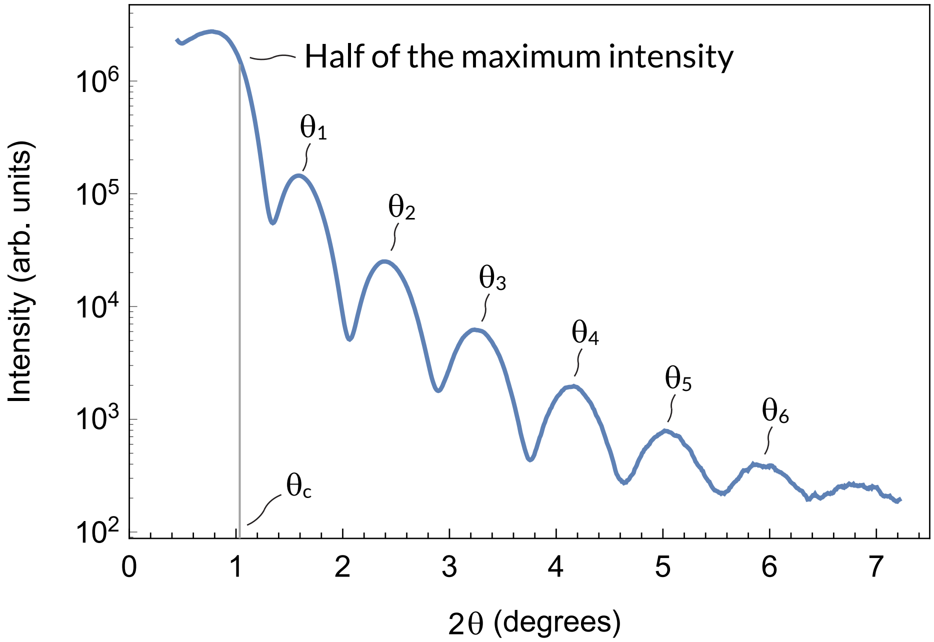

Figure 2.8: Example of a typical XRR measurement showing Kiessig fringes and the critical angle. This corresponds to a single layer Ru thin film with a thickness of 9.65 nm.

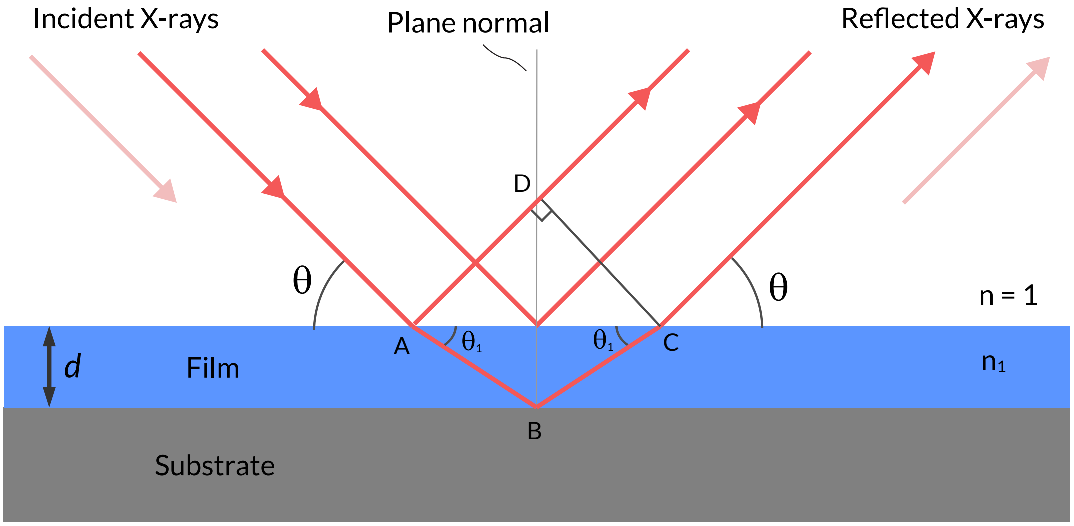

Figure 2.9: A diagram showing the paths that two X-rays take through a single layer film on a substrate. This figure contains the geometry used in the calculations to determine film thickness from Kiessig fringes. The index of refraction of the film is n_1.

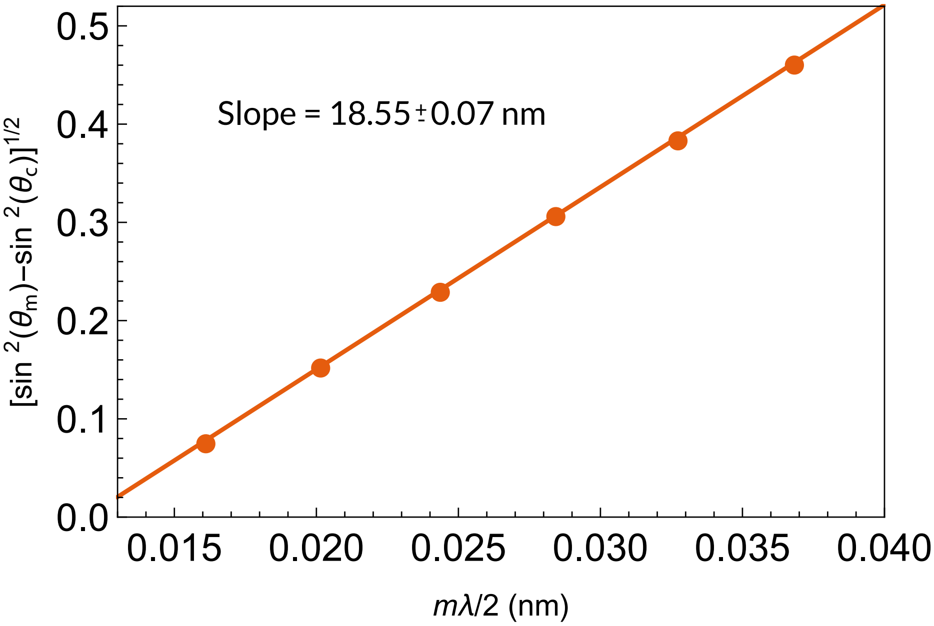

Figure 2.10: Example of fitting typical XRR data $\frac{m\lambda}{2}$ vs $\sqrt{\sin^2(\theta_m) - \sin^2(\theta_c)}$ where the slope is the film thickness. The orange circles are data and the line is the linear fit. In this case the data is for sputtered Co film with a thickness determined from the fit of $d = 18.55 \pm 0.07$ nm.

2.7 Scanning Transmission Electron Microscopy Energy-dispersive X-ray Spectroscopy (STEM-EDXS)

STEM-EDXS is used to measure the elemental composition throughout some of our samples. Specifically, we use it to measure relative differences in composition of individual elements across our samples.

The tool creates a focused electron beam that scans across the sample in a raster motion. As the electron beam interacts with the sample, the electrons stimulate the atoms to emit characteristic X-rays with sharply defined energies that are specific to each atomic species. [36]

The process of generating characteristic X-rays is shown for a carbon atom in Fig. 2.11. In this example, a K-shell electron from the ground state carbon atom is scattered by an energetic beam electron. This leaves a K-shell vacancy, which is then filled by an electron from an outer L-shell. As this occurs, an X-ray photon is emitted with energy equal to the energy difference between the two shells $E_K - E_L$.

Every element has a unique set of energy differences between electron orbitals, which has been previously tabulated. By measuring the energy of emitted X-rays and comparing with this data, one is able to determine which element must have emitted the X-ray, and hence, the composition of the sample.

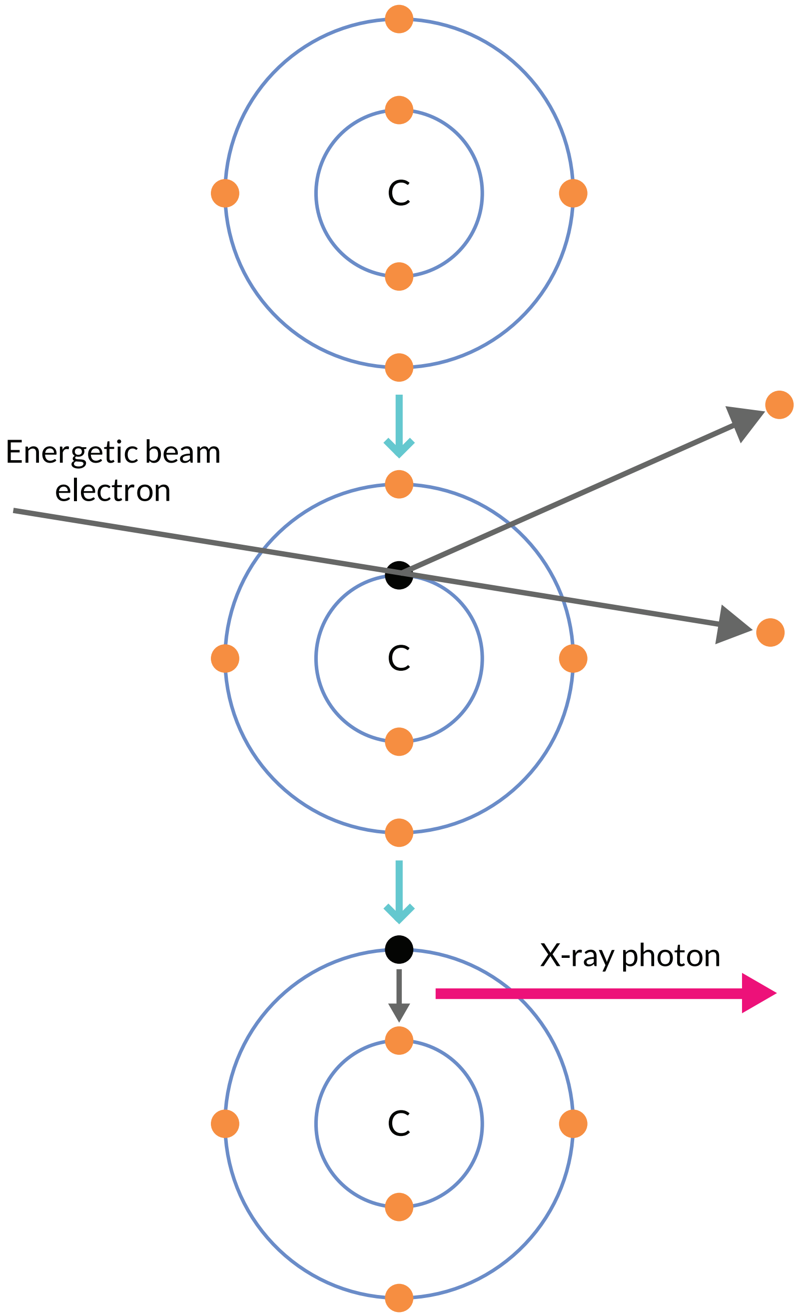

Figure 2.11: A schematic diagram showing one process of X-ray generation. A K-shell electron from the ground state carbon atom is scattered by an energetic beam electron. This leaves a K-shell vacancy, which is then filled by an electron from an outer L-shell. As this occurs, an X-ray photon is emitted with energy equal to the energy difference between the two shells $E_K - E_L$.

Furthermore, the integrated intensity of the individual characteristic X-rays is proportional to the concentration of the element within the sample interaction volume. While it is generally difficult to calculate accurate absolute concentrations of each element, this technique is very effective at measuring relative concentration differences of each element across a sample. [36]

All STEM-EDXS measurements were performed at the Institute of Ion Beam Physics and Materials research, HZDR, Germany, by Dr. Rene Hübner. Analysis of the EDXS results were performed at SFU, with the assistance of Dr. Rene Hübner. Spectrum imaging was performed using a Talos F200X (FEI) high-angle annular dark-field scanning transmission electron microscope equipped with an X-FEG electron source and a Super-X EDXS detector system at an accelerating voltage of 200 kV.

The sample was prepared for EDXS analysis by first being placed into a Model 1020 Plasma Cleaner (Fischione) for 8 seconds to remove possible contamination.

TEM lamella preparation was done by in situ lift-out using a Zeiss Crossbeam NVision 40 system. To protect the sample surface from damage, a carbon cap layer was first deposited. Afterwards, the TEM lamella was prepared using a 30 keV focused Ga ion beam. Its transfer to a 3-post copper lift-out grid (Omniprobe) was done with a Kleindiek micromanipulator. To minimize sidewall damage, Ga ions with only 5 keV energy were used for final thinning of the TEM lamella to electron transparency.

2.8 Atomic Force Microscopy (AFM)

AFM, in contact mode, was used to measure the surface roughness of some samples studied in this work. AFM is an ideal tool for this purpose because it has atomic scale resolution and works on a large variety of samples including conductive, non-conductive and soft-matter. [111]

Contact mode AFM is a technique that scans the surface of a sample with a very fine tip located on the end of a cantilever, as shown in Fig. 2.12. Any changes in elevation of the surface of the sample will exert a force on the tip. The cantilever acts as a spring, and Hooke's law can be used to determine the force:

$$F_{spring} = -k z_{spring}, \tag{2.16}$$

where z_{spring} is the distance the cantilever spring is bent relative to its equilibrium position without the sample present, and k is the cantilever spring constant. z_{spring} is typically measured using a laser beam reflected from the back of the cantilever into a photodiode detector, as shown in Fig. 2.13. The x,y,z positioner, as shown in Fig. 2.13 is moved in the x,y plane so that the tip can scan an area of the sample, and the z component is varied in order to achieve a constant force on the tip. Note, this z component of the positioner is

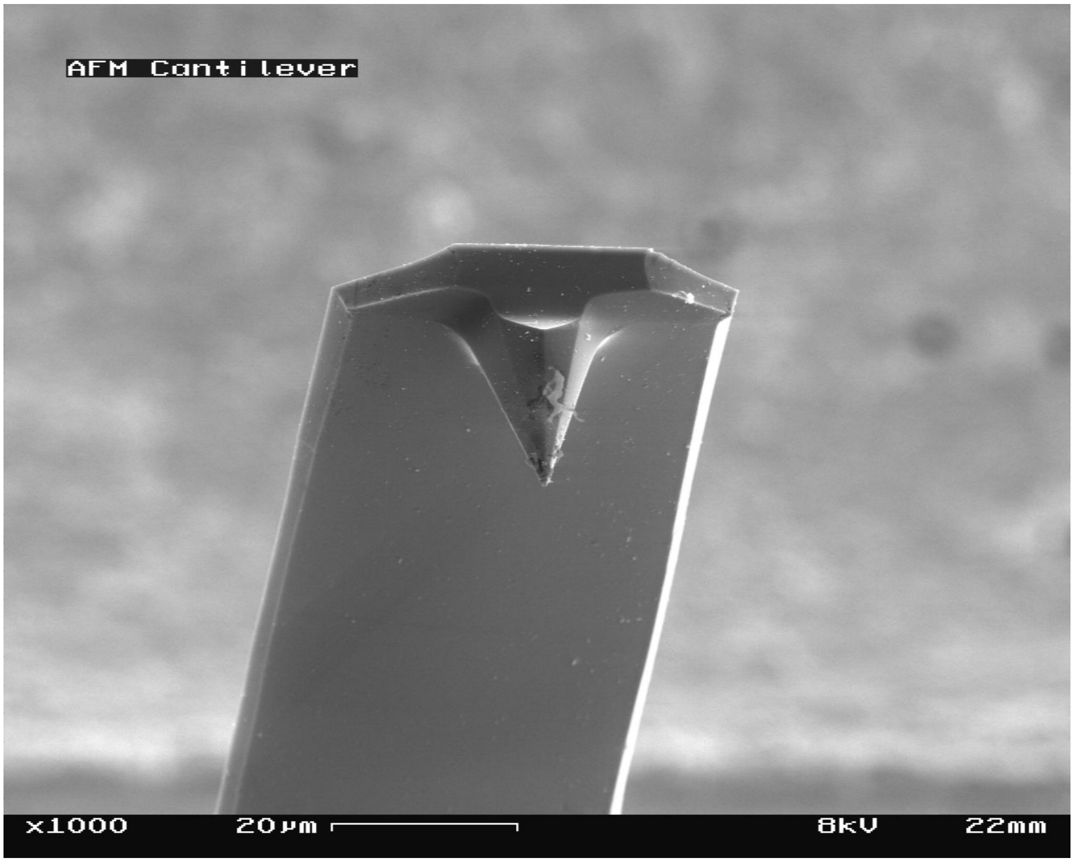

Figure 2.12: An electron micrograph of a used AFM cantilever. Taken from https://en.wikipedia.org/wiki/Atomic_force_microscopy. Usage of this image is governed by the CC BY-SA 3.0 licence.

different than z_{spring}. A computer is used to put all of the scan data together to create an image of the topology of the sample.

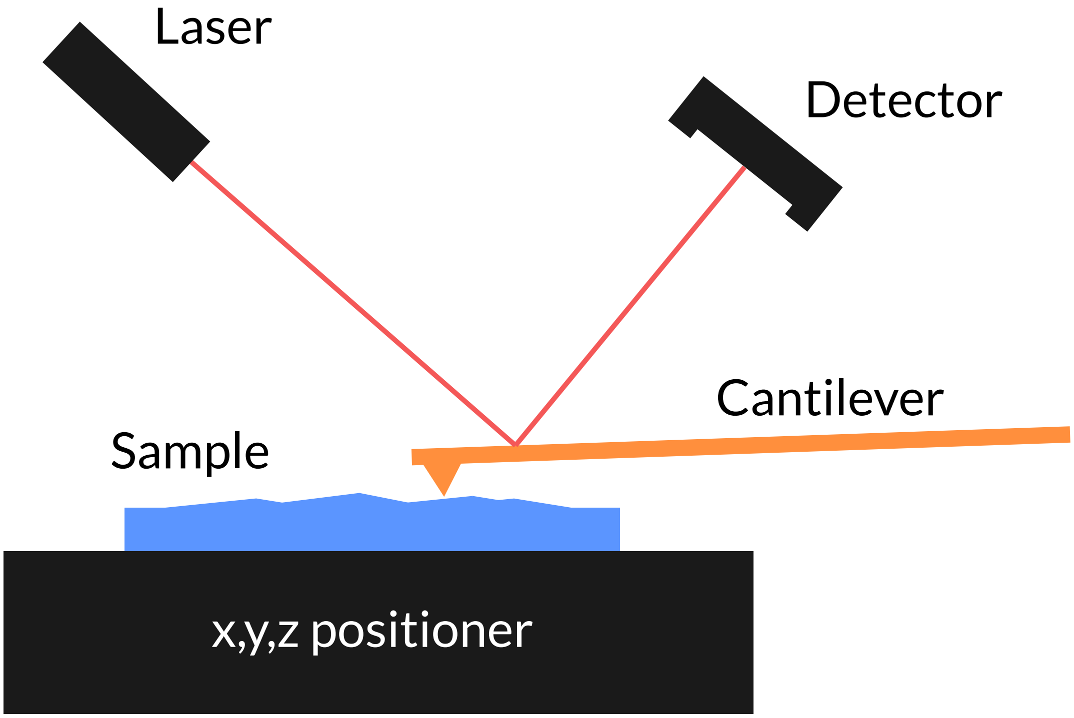

Figure 2.13: A schematic diagram showing a typical AFM tool. The cantilever is held fixed while the sample scans in x and y. Any force exerted on the tip is detected as a deflection in the cantilever, which is measured by a laser beam reflected from it.

Chapter 3

Sample Preparation

3.1 RF Magnetron Sputter Deposition

RF magnetron sputter deposition is the method used to deposit the multilayer thin films studied in this work.

The sputter deposition process is shown schematically in Fig. 3.1, where material is being removed from a source that has a desired composition, known as the target, and deposited onto a sample substrate.

To describe the sputtering process, we will begin chronologically. This process occurs inside a vacuum chamber with a typical base pressure less than 1×10^{-7} Torr. A sputter gas is first injected into the vacuum chamber that brings the pressure up to the 1 to 30 mTorr range. In our case, we have used Ar gas because it is noble and won't react with the target material. An alternating rf voltage is then applied between the sample and the target, while holding the substrate at ground, as shown in Fig. 3.1. After a short time, a stray electron will travel into the potential difference and be accelerated and collide with a neutral Ar atom, leading to the reaction:

$$\mathrm{Ar} + e^{-} \longrightarrow \mathrm{Ar}^{+} + 2e^{-} \tag{3.1}$$

Depending on the phase of the rf voltage, the Ar^{+} ion will be attracted, or repelled from the target, and the electrons will travel in the opposite direction. The magnetic field created by the magnets behind the target, as shown in Fig. 3.2, will confine the electrons to the region just above the target, with the highest density of electrons being just above the region known as the sputter track. These confined electrons then have a probability to collide and ionize more Ar atoms and repeat the process over and over again, which leads to a constant supply of electrons and Ar^{+} ions. This confinement of electrons just above the target increases ionization efficiency, meaning there is a large probability of Ar ionization if the atoms enter the region just above the target. This allows for higher deposition rates and sputtering at lower pressures. Unlike the electrons, the trajectory of the Ar^{+} ions are relatively unaffected by the magnetic field due to their much larger mass.

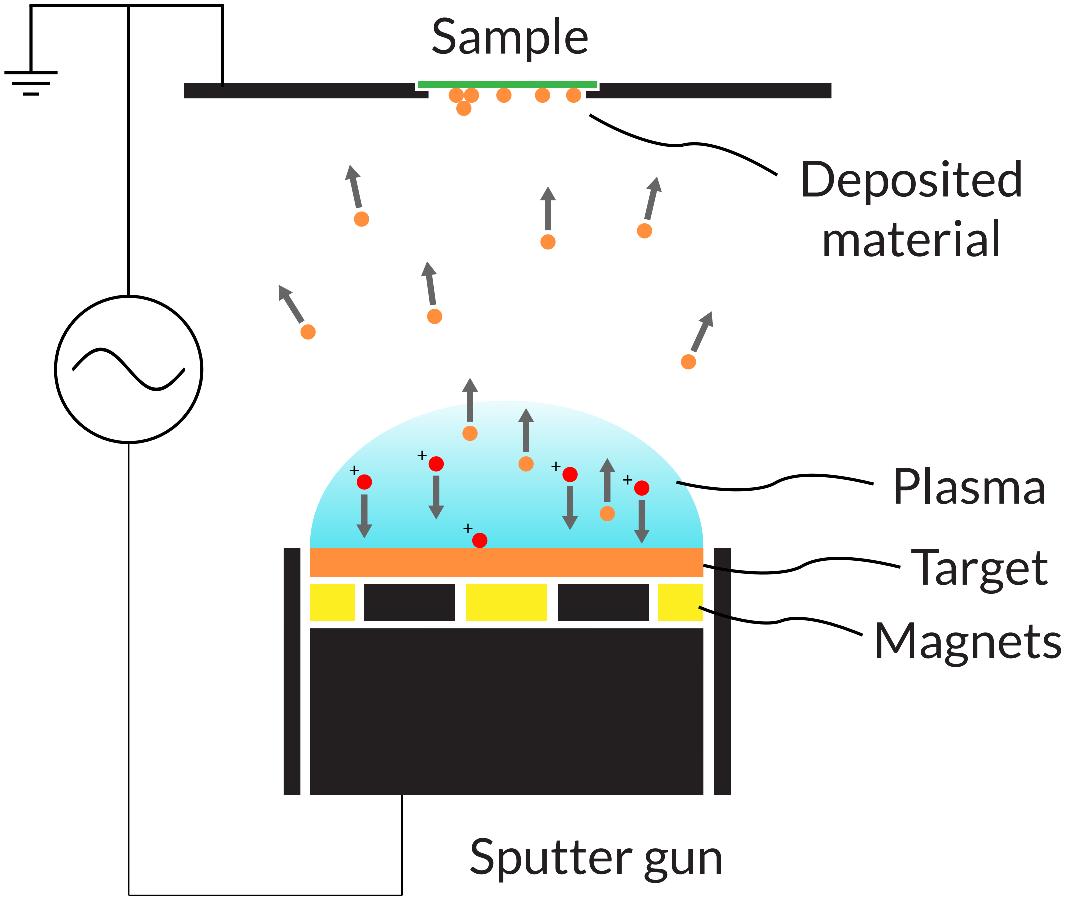

Figure 3.1: A schematic diagram illustrating the magnetron sputter deposition process. The sample is grounded, and the target is connected to an rf power supply. The plasma is composed of ionized Ar atoms shown in red. For part of the rf cycle, the Ar^+ ions are attracted to the target and bombard it, which ejects particles of the target material, shown in orange. Some of these particles end up landing on the sample, which forms films of target material. For a more detailed view of the magnetic field electron confinement, see Fig. 3.2.

During the part of the rf cycle when the target is at a negative potential, the Ar^+ ions will be accelerated towards the target, shown as red circles in Fig. 3.1. If the acceleration has given the Ar^+ ions sufficient energy, they will collide with the target and cause microscopic particles of the target material to be thrown off in all directions, shown as orange circles in Fig. 3.1. Some of these particles will travel ballistically in the direction of the sample and land on it. Given enough time, the particles will pile up on the sample in a way very similar to snow piling up on the ground, leading to films of the desired material.

If a reactive sputter gas such as oxygen or nitrogen is used instead, some of the target particles will react with the sputter gas before landing on the sample. This can be useful for sputtering oxides or nitrides from a metallic target.

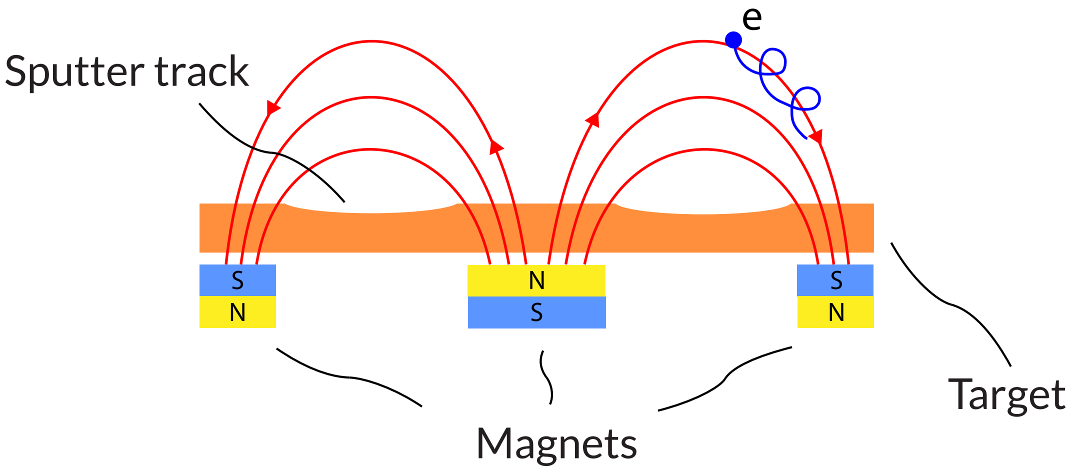

Figure 3.2: A close-up schematic cross-section of the sputter target. The magnets behind the target form a magnetic field above it that confines electrons. This confinement creates areas of increased ionization density, which lead to increased bombardment and erosion of the target, shown here as sputter tracks.

The reason for the rf voltage, as opposed to a DC voltage, is to allow for the sputtering of insulating targets as well as conductive targets. As positive Ar^+ ions bombard an insulating target, they will leave a net positive charge on the surface. As this charge builds up, it will begin to repel other Ar^+ ions, which will stop the sputtering process. In order to continue sputtering, this charge must be neutralized, which is exactly what occurs during the positive phase of the rf voltage cycle. During this phase, electrons from the plasma will be attracted towards the target and neutralize the positive charge buildup.

When a high frequency rf power supply is used, which is typically 13.56 MHz, the field is alternating too quickly to provide substantial acceleration to the Ar^+ ions. Under these conditions they would normally not gain enough energy to sputter the target. However, the lighter electrons are accelerated much more easily, causing an abundance of them to bombard the target during the positive part of the rf cycle. This mass disparity between the ions and electrons leads to a build up of negative charge on the target, known as a self bias. This negative self bias is strong enough to provide the additional acceleration needed to give the Ar^+ ions enough energy to sputter the target. Thus, the self bias is required for rf sputtering. If a conductive target is used, a capacitor must be placed in series with it to allow for this self bias. [84, 92]

3.1.1 Sample Resputtering

The oscillating potential difference between the target and sample in rf sputtering is symmetric between the two electrodes. With all else equal, this would obviously lead to sputtering from both the target and the sample, which would be undesired. Sputtering of the sample is known as resputtering. This problem is normally mitigated by two main factors. The first is to ensure that the sample and sample holder is conductive and grounded. This will avoid the development of a self bias at the sample, and any Ar^+ ions near the sample to not gain enough energy for sputtering. The second factor is that unlike the target, at the sample there is no strong magnetic field to confine the electrons, so there are fewer electrons to ionize Ar atoms.

However, under certain conditions, some of these mitigating factors can be lost, which will lead to sample resputtering. For example, if the substrate is insulating, or if the materials being deposited onto it are insulating. This allows for a negative self bias to develop at the sample, which results in acceleration of Ar^+ ions to high enough energy to sputter the sample. [62] Another condition that can help lead to sample resputtering is if the sample and target are too closely spaced. In this case, the magnetic field electron confinement will be adjacent to both the target and the sample, leading to relatively large numbers of Ar^+ ions available for sputtering at each electrode. If resputtering occurs, it can cause a lower deposition rate, or it can stop the process entirely and etch the substrate material away. [41]

3.1.2 Experimental Setup

A sputter deposition system was used to deposit all of the samples studied in this work. The system has 2 high-vacuum process chambers ($< 10^{-7}$ Torr) connected by a loadlock. The loadlock can hold up to 6 substrates each up to 6" diameter, and can be moved into either of the two processing chambers using an automatic computer-controlled linearly extendable arm. The first of the two process chambers (PC1) is used for thin film deposition, while the second chamber (PC2) was used for rapid thermal annealing.

A cross-sectional schematic of the sputtering configuration of PC1 is shown in Fig. 3.3, along with a top-down picture of the chamber shown in Fig. 3.4. This chamber has six 2" sputter guns arranged in a hexagonal shape below the sample, angled inwards to point directly at the sample. It also has two 4" sputter guns attached to an extendable arm that can be moved in and out of the chamber. The target in the two 4" guns is only approximately 5 cm away from the sample, while the six 2" guns are much further away at approximately 30 cm.

All six 2" sputter guns have pneumatic shutters used to quickly start and stop sputtering and minimize target contamination. There is an additional shutter just below the substrate that is useful when sputtering from multiple targets at once.

The sputter guns are powered by two rf power supplies running at 13.56 MHz. They are connected to an impedance-matching network to minimize reflected power and ensure it is transferred efficiently to the plasma discharge.

All components of the sputtering machine are computer controlled. This includes the shutters, the turbo pumps, gate valves, and power supplies. All multilayer thin films are deposited using custom-made programs that control all of the components during the de-

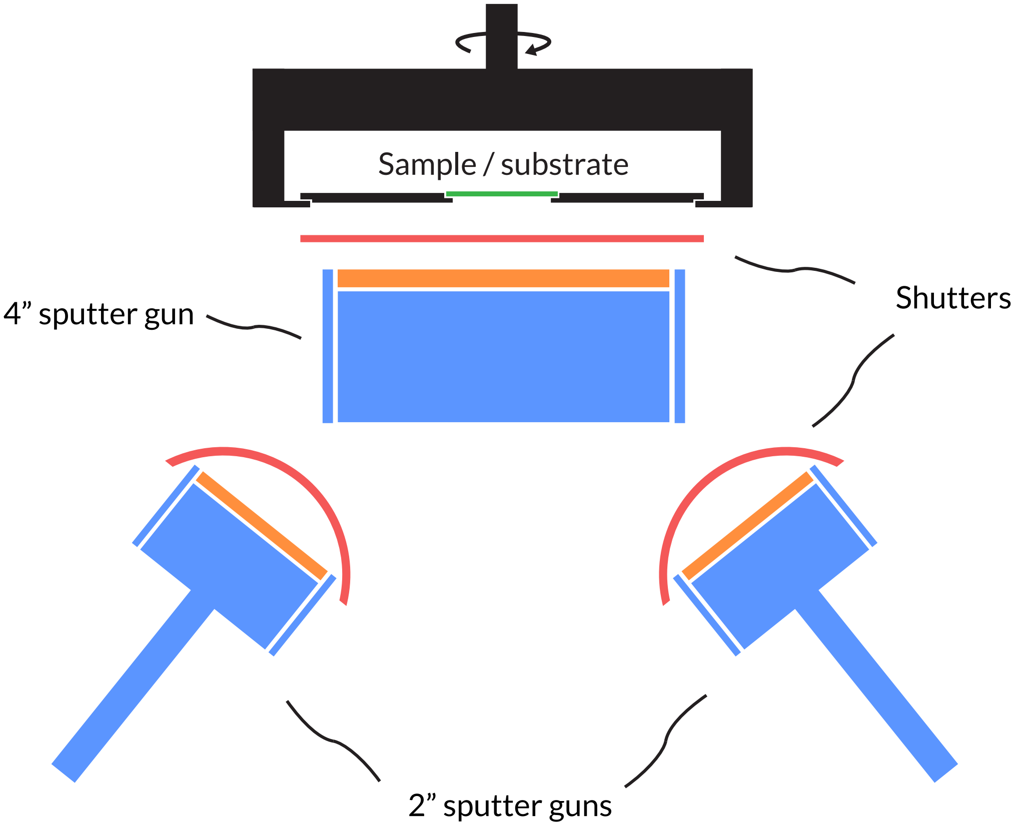

Figure 3.3: A cross-sectional schematic diagram of the sputter configuration used to deposit samples in this work. The sample assembly rotates during deposition for a more uniform thin film. One of the two 4" sputter guns, attached to an extendable arm, is shown here, and is retracted when not in use to allow for deposition using the lower guns. Two of the six 2" sputter guns are shown. These six guns are positioned rotationally symmetrically under the sample in the shape of a hexagon. All 2" guns have their own shutter, and there is an additional shutter in front of the sample.

position process. Multilayer thin films are achieved by opening and closing shutters to start and stop deposition of different materials in the desired order.

When co-depositing from multiple targets at once, the relative rf power going to each gun is adjusted to vary the ratio of elements in the deposited layers.

3.1.3 Substrate Preparation

Si (001) wafers are used as a substrate for all samples in this work. Before deposition, the wafers are cleaned using a process that is based on the RCA-1 clean developed by Werner Kern at RCA laboratories in the late 1960's. [61, 5]

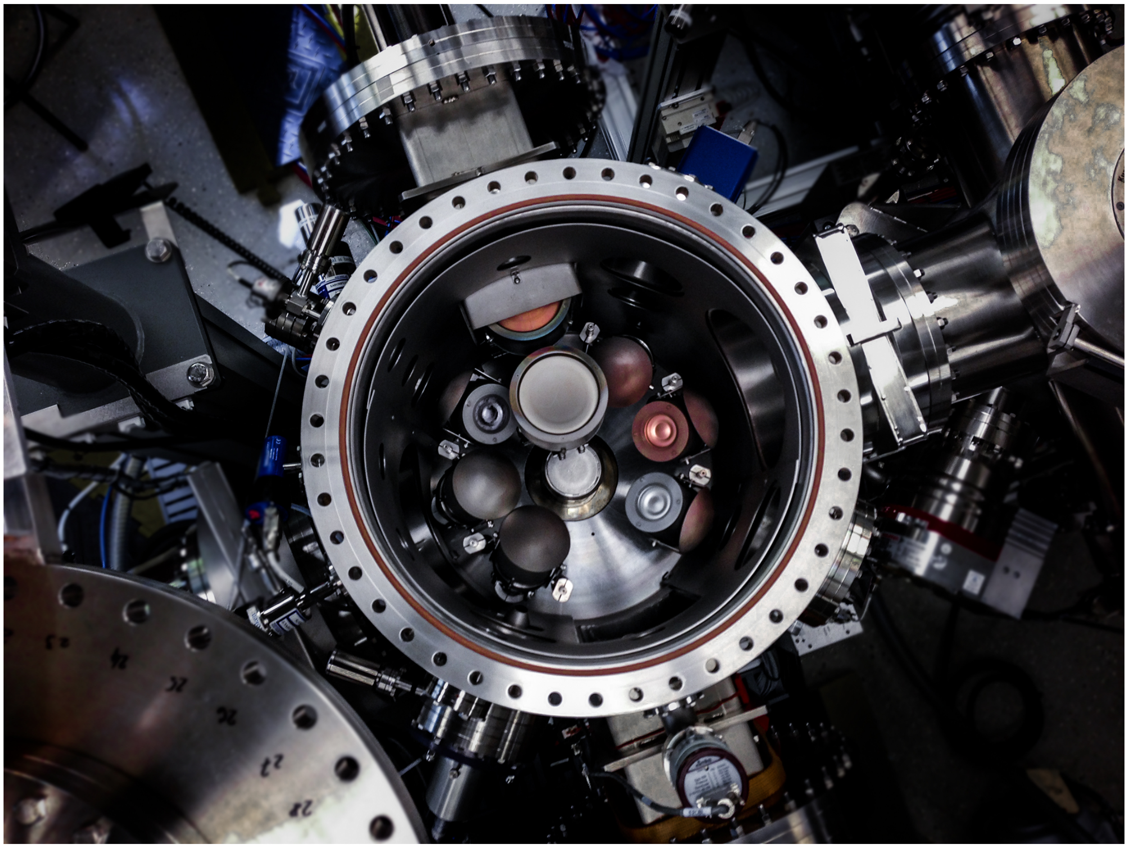

Figure 3.4: A top-down picture of the sputter chamber used showing the six 2" sputter guns, and one of two retractable 4" guns.

Before cleaning, the Si wafers are cut into smaller 25 × 25 mm pieces using a diamond scribe, and cleaving by hand along the scribe lines.

The cleaning process is performed in 2 separate clean rooms and transferred between them in sealed containers. The cleaning process starts by submerging the Si substrates into an acetone bath which is heated to 50°C inside an ultrasonic cleaner for 10 minutes. This first step will clean any oils and organic residues that may be on the silicon surfaces during handling or cutting. Next, the substrates are moved into an ethanol bath heated to 50°C inside an ultrasonic cleaner for 10 minutes. This step will remove any residues left by the acetone itself. After this, the substrates are removed one at a time and quickly blow dried using filtered nitrogen, as shown in Fig. 3.5

Next, the substrates are cleaned in a solution composed of 5 parts water (H_2O), 1 part 27% ammonium hydroxide (NH_4OH), and 1 part 30% hydrogen peroxide (H_2O_2). This solution was first heated to 70°C, and then the substrates are submerged into it for 15 minutes. After this, the substrates are transfered to a container with overflowing DI water. A tap is used to provide a constant stream of DI water into the container while allowing it to overflow into a sink. This is continued for a few minutes until the water has been

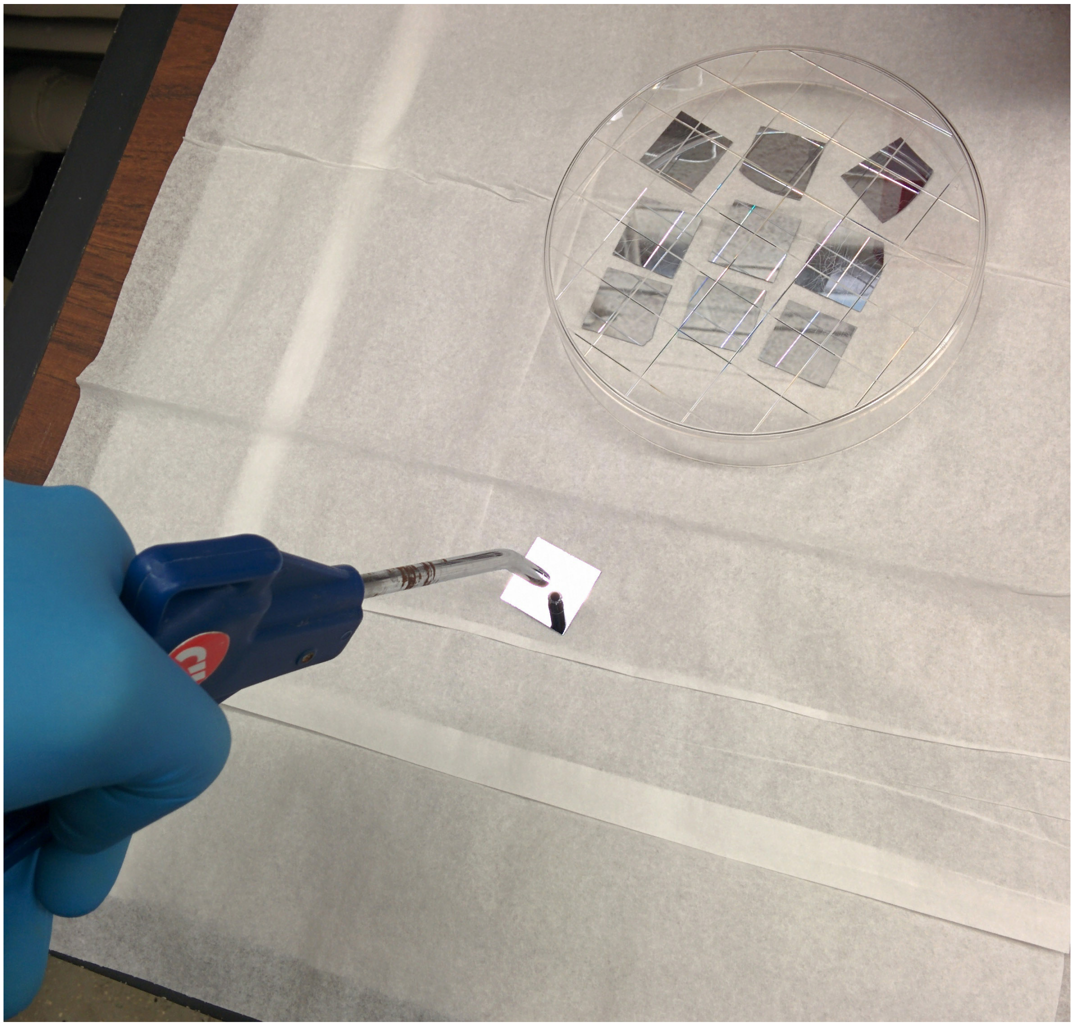

Figure 3.5: A picture showing how to blow dry Si wafers with a nitrogen gun. Care should be taken to point the gun directly at the center of the Si wafer or else it will fly away. Immediately after drying they are placed under a cover to minimize dust falling on the surface.

replaced approximately 4 times. Next, the substrates are removed one at a time while being engulfed in a stream of flowing DI water. This is because still water will contain residue on the surface which would cover the substrates if they are removed through it. After removing each wafer, they are blow dried one at a time using nitrogen. Immediately after drying, they are placed inside a container to stop particles from landing on the surface.

The chemical reaction in the second part of this cleaning process leaves a thin oxide layer on the surface of the wafer. For epitaxial growth on Si, an additional hydrofluoric acid cleaning step would normally be required. [4, 5] However, since our films are not epitaxially grown on top of the Si substrate, the last step is not required. All of our multilayer films are also grown on top of an amorphous Ta seed layer, which provides a predictable growth

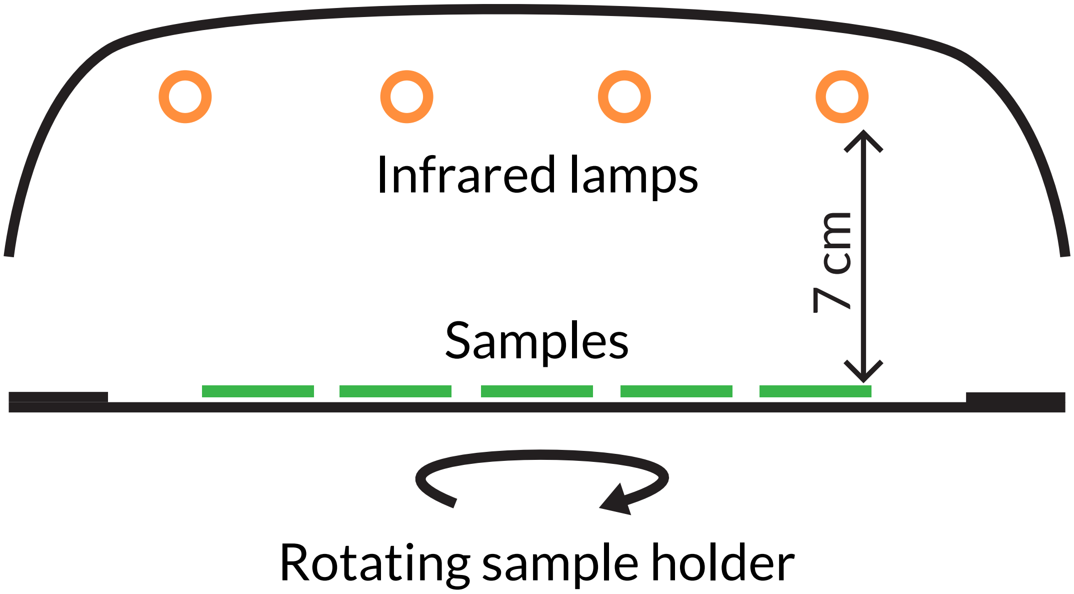

Figure 3.6: Schematic cross-section of the rapid thermal annealing setup in PC2. The entire apparatus is inside a high-vacuum chamber. There are 4 infrared quartz halogen lamps approximately 7 cm away from the samples. The samples are rotated for more uniform heating.

surface independent of the crystal structure below it. Hydrofluoric acid is also extremely dangerous and should be avoided unless necessary. Thus, we stop the cleaning process here and deposit our thin films on cleaned Si wafers that contain a thin oxide layer on top.

The surface roughness of a Si (100) wafer, after being cleaned with this procedure, was measured using AFM. The surface had an RMS roughness of approximately 0.1 nm, as expected from prime grade silicon wafers. [81]

3.1.4 Sample Annealing Procedure

For most of the samples prepared in this work, sample annealing was carried out using rapid thermal annealing (RTA). This takes place in vacuum with a pressure of 5×10^{-8} Torr. The annealing procedure consists of heating the samples with a rate of 5 °C/s (300 °C/min), and immediately after reaching the desired temperature, cooling of the sample with an initial cooling rate of approximately 1 °C/s (60 °C/min). A schematic cross-section of the RTA setup is shown in Fig. 3.6. RTA is used because it reduces the amount of time spent at elevated temperatures, which in turn reduces elemental diffusion within the samples. [99]

For the last part of the work in this thesis, samples are annealed with a slower heating rate of 20 °C/min, then held at the temperature for 30 minutes, and then cooled at the same rate as the RTA procedure. The reason why two different annealing procedures are used in different parts of this thesis is because at some times, one of the systems was broken and waiting to be repaired, requiring us to use another one. This second annealing procedure also took place in vacuum with a pressure of 5×10^{-8} Torr.

For both procedures, the annealing system was calibrated using thermocouples, along with an ice water bath held at 0 °C as a reliable reference. The temperature was calibrated once before any samples were annealed. The calibration thermocouple was placed exactly where the sample would be to ensure we know the temperature of the sample even if the system is not in thermal equilibrium.

In some parts of this thesis, we compare results from samples that have been annealed with the two different procedures. To ensure that the results are comparable, and that the annealing procedures produce the same results, we annealed the same sample with both procedures and measured the relevant property to confirm that they are in agreement. We have also repeated the same annealing process on different pieces of the same sample, and measured the relevant property, and found it to yield the same results each time. This demonstrates a high level of reproducibility in our annealing procedure. Additionally, as an extra precaution, we have chosen to anneal large groups of samples together at once to ensure that they are all exposed to identical temperatures and conditions.

Chapter 4

Theory

4.1 Magnetic Free Energy

The total magnetic free energy is the sum of many free energies originating from different aspects of the magnetization environment as shown in the following equation

$$U_{tot} = U_{ex} + U_{coupling} + U_{zee} + U_{an} + U_{d}, \tag{4.1}$$

where U_{ex} is the energy due to the exchange interaction between magnetic atoms, $U_{coupling}$ is the energy from the interlayer exchange coupling between magnetic films separated by a non-magnetic spacer layer, U_{zee} is the Zeeman energy arising from the interaction of the magnetization of the sample with an external magnetic field, U_{an} is the crystallographic and interface magnetic anisotropy energy, and U_{d} is the energy due to the demagnetizing field caused by dipole-dipole interactions. Unless stated otherwise, all of these energy contributions will be represented as an energy density, or energy per unit volume.

4.1.1 Exchange Interaction

Exchange interaction is a purely quantum mechanical effect without a classical analogue. It defines how electron spins prefer to be oriented when near each other, parallel or antiparallel. It arises from the fact that particles in a quantum mechanical system must be indistinguishable. In addition, the Pauli exclusion principle requires that a system of fermions must be antisymmetric under exchange. For electrons, this means that if the spatial and spin coordinates of the two are exchanged, then the total wave function changes its sign (shown here for a two electron system):

$$\Psi(r_1, \sigma_1, r_2, \sigma_2) = -\Psi(r_2, \sigma_2, r_1, \sigma_1). \tag{4.2}$$

The wave function can be written as the product of a spatial component and a spin component:

$$\Psi(r_1, \sigma_1, r_2, \sigma_2) = \psi(r_1, r_2)\chi(\sigma_1, \sigma_2) \tag{4.3}$$

If the spatial component is symmetric, then the spin component must be antisymmetric and vice versa. Which of the two is the case depends on the details of the state of the electrons. For example, a singlet state has a symmetric spatial component, and an antisymmetric spin component. [38] This leads to the electons being attracted together spatially (called a bond in chemistry), but preferring to have spins point in opposite directions. A triplet state is the opposite, with an antisymmetric spatial component and a symmetric spin component. [38] This leads to electrons being repelled, but with spins pointing in the same direction. Thus, depending on the state of the electrons within a magnetic material, the Pauli exclusion principle can favor unpaired spins being parallel with one another, which results in ferromagnetism, or antiparallel, which results in antiferromagnetism.

Expressing U_{ex} in the Micromagnetics Model

In our micromagnetics model, which will be described in detail later in this thesis, we simulate each plane of magnetic dipoles individually. This model assumes our samples have planar symmetry. Because of this, in this section we will derive the energy per unit area, rather than the energy per unit volume that we use for the FMR model. To distinguish the energy per unit area from the energies per unit volume, we will use the symbol E instead of U.

In 1928, Heisenberg formalized this interaction between spins $\boldsymbol{S}_1$ and $\boldsymbol{S}_2$ with the interaction energy [18]

$$w_{1,2} = -2J\boldsymbol{S}_1 \cdot \boldsymbol{S}_2, \tag{4.4}$$

where J is the exchange integral between the spins. In ferromagnetic materials, J is positive, in antiferromagnetic materials, J is negative.

We will consider a lattice of spins, where all spins are situated at the location of an atom, which we will call a spin lattice. This will give the spin lattice the same geometry as the crystal, such as face-centered-cubic (FCC), body-centered-cubic (BCC) or hexagonal-close-packed (HCP), for example. The total exchange energy for any single spin S_i would equal the sum of Eq. 4.4 between all other spins S_j in the lattice. However, the exchange interaction is very short range, so we can approximate it for spin S_i by summing over only z nearest neighbor spins S_j, see Fig. 4.1:

$$w_i = -2\sum_{j=1}^{z} J_{ij}\boldsymbol{S_i} \cdot \boldsymbol{S_j} \tag{4.5}$$

For a spin lattice, the magnitudes of all of the spins are equal and given by $\boldsymbol{S} = S\hat{\text{u}}$, where $\hat{\text{u}}$ is the unit vector pointing in the direction of the spin. Additionally, for FCC, BCC,

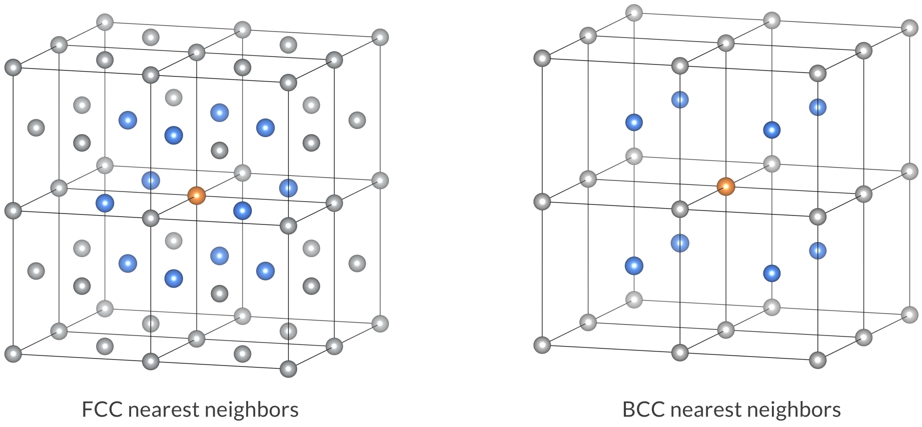

Figure 4.1: Nearest neighbors of for FCC geometry on the left, and BCC geometry on the right. The orange sphere is the reference point, and the blue spheres are the nearest neighbors. FCC and HCP have 12 nearest neighbors, and BCC has 8 nearest neighbors.

and HCP geometries, the distances between a spin and all of its nearest neighbors are equal, and given by $a/\sqrt{2}$ for FCC, HCP, and $a\sqrt{3}/2$ for BCC. This allows us to assume J_{ij} is equal for all nearest neighbors, which we will now call J. This, along with the definition of the dot product $\boldsymbol{a} \cdot \boldsymbol{b} = ab\cos\theta$, allows us to re-write Eq. 4.5 as

$$w_i = -2JS^2 \sum_{j=1}^{z} \cos(\theta_i - \theta_j), \tag{4.6}$$

where $\theta_i - \theta_j$ is the difference in angle between $\boldsymbol{S}_i$ and $\boldsymbol{S}_j$.

The thin films studied in this thesis are symmetric in the plane of the sample, so we can model the spin lattice as planes of spins where all the spins in each plane are aligned parallel to one another, while the directions of spins can vary from one plane to another, as shown in Fig. 4.2. This results in $\cos 0 = 1$ is constant for all the terms in Eq. 4.6 between nearest neighbors within the same plane. For our purposes, we are only looking at differences in energy between spin configurations, and so we can ignore these constant terms. This simplifies Eq. 4.6 further to be

$$w_i = -2JS^2 \Bigg(\sum_{j \in z_{\text{below}}} \cos(\theta_i - \theta_j) + \sum_{j \in z_{\text{above}}} \cos(\theta_i - \theta_j) \Bigg), \tag{4.7}$$

where we have explicitly split it up into summing over only the nearest neighbors in the plane below with z_{below} and the plane above with z_{above}, and ignoring the nearest neighbors within the same plane.

To calculate the energy per unit area, we first determine the spin density per area per atomic plane. For FCC, and BCC, this is given by

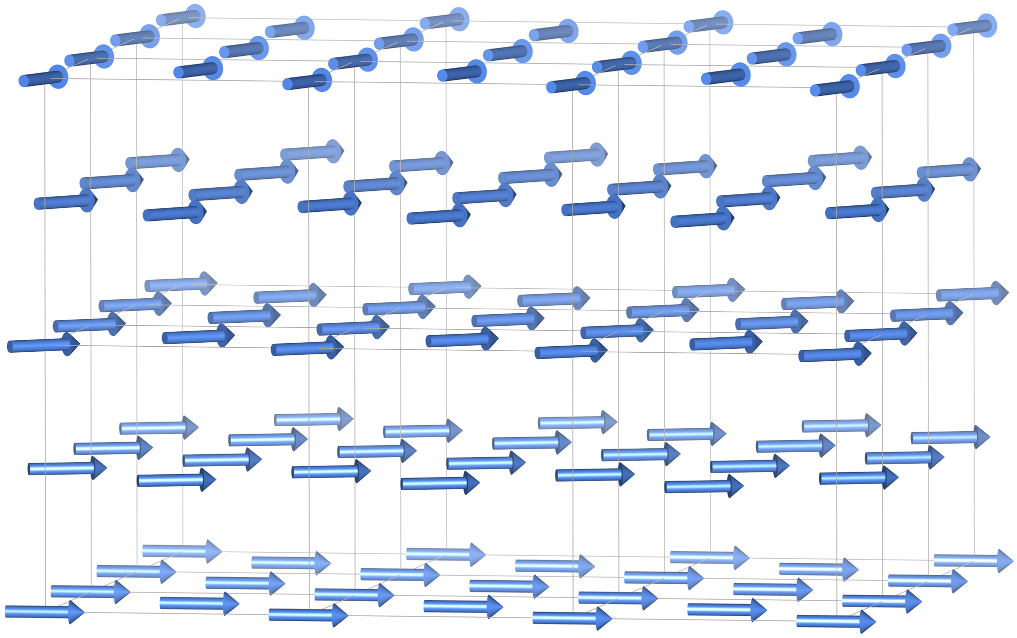

Figure 4.2: A schematic of several planes of spins within an FCC (100) oriented spin lattice. All of the spins within a single plane are oriented in the same direction, while the directions of spins can vary from one plane to another. The FCC unit cells are shown in gray for convenience.

$$\rho_{\text{plane}} = \frac{n}{a^3} d, \tag{4.8}$$

where n is the number of atoms per unit cell, a is the length of an edge in the cubic unit cell, and d is the spacing between atomic planes. $n = 4$ for FCC, and $n = 2$ for BCC. Next, we multiply the exchange energy per spin by this spin density per area per atomic plane, and sum over all planes in the thin film, which leads to the exchange energy per unit area

$$\begin{aligned} E_{ex} &= \frac{1}{2} \frac{n}{a^3} d \sum_{i=1}^{N} w_i & (4.9) \\ &= \frac{-d}{a^2} \left(\frac{nJS^2}{a} \right) \sum_{i=1}^{N} \left(\sum_{j \in z_{\text{below}}} \cos(\theta_i - \theta_j) + \sum_{j \in z_{\text{above}}} \cos(\theta_i - \theta_j) \right), & (4.10) \end{aligned}$$

where i is summing over N planes. Note, θ_i is the angle of the spin in atomic plane i, while θ_j is the angle of the nearest neighbor spin j in the layers above. i is the plane index, while j is the nearest neighbor index. We have also multiplied everything by $1/2$ because each interaction energy between every pair of spins is counted twice when we include interactions

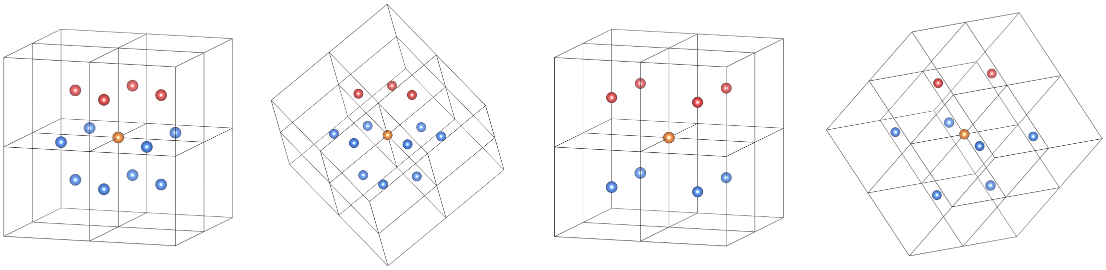

FCC 100 orientation FCC 111 orientation BCC 100 orientation BCC 110 orientation

Figure 4.3: Locations of nearest neighbor spins in the atomic plane above the reference spin for FCC (100), FCC (111), BCC (100), and BCC (110) geometries and orientations. The orange sphere is the reference point, the red spheres are the nearest neighbors in the layer above, and the blue spheres are the other nearest neighbors. The unit cells are shown for convenience.

with the plane above and below. We can remove this factor and simplify the equation further if we only include the contribution to w_i from nearest neighbors in the layer above. All of the interaction energies will still be counted, just in different parts of the sum. This simplification leads to

$$E_{ex} = \frac{-2d}{a^2}\left(\frac{nJS^2}{a}\right)\sum_{i=1}^{N}\sum_{j\in z_{\text{above}}}\cos(\theta_i - \theta_j). \tag{4.11}$$

In order to compare our results with known quantities, we want to relate our result to the well known exchange stiffness constant A_{ex} which is given by [18] $A_{ex} = \frac{nJS^2}{a}$. Substituting this into our result leads to

$$E_{ex} = \frac{-2dA_{ex}}{a^2}\sum_{i=1}^{N}\sum_{j\in z_{\text{above}}}\cos(\theta_i - \theta_j). \tag{4.12}$$

This is the most general equation for exchange energy in our model, however, for specific crystal structure geometries and orientations, the second sum over z_{above} can be further simplified. As long as all the nearest neighbors that we are counting are in the same atomic plane directly above, each term will be identical. In these cases, we can remove the sum and multiply everything by the number of nearest neighbors in the plane above. Additionally, for all of the geometries and orientations shown in Table 4.1.1 and Fig. 4.3, they share the same relationship of $d = a/\sqrt{z_{\text{above}}}$, which allows for the simplification of Eq. 4.12 to

$$E_{ex} = \frac{-2dA_{ex}z_{\text{above}}}{(d\sqrt{z_{\text{above}}})^2} \sum_{i=1}^{N} \cos(\theta_i - \theta_j) \tag{4.13}$$

$$= \frac{-2A_{ex}}{d} \sum_{i=1}^{N} \cos(\theta_i - \theta_j). \tag{4.14}$$

Lattice Geometry	Plane Normal Direction	z_{above}	d
FCC	(100)	4	$a/\sqrt{4}$
FCC	(111)	3	$a/\sqrt{3}$
BCC	(100)	4	$a/\sqrt{4}$
BCC	(110)	2	$a/\sqrt{2}$

This simplification made in Eq. 4.14 won't be correct for all possible spin lattice geometries and orientations, BCC (111), for example, but it is correct for all listed in Table 4.1.1. For general geometries and orientations, use Eq. 4.12

Expressing U_{ex} for the FMR Model

To simplify matters for our dynamic FMR model, which will be explained in detail later, we will assume that the exchange stiffness is infinite and that all the spins in each layer are locked together and point in the same direction at all times. This has been shown to be an accurate assumption for layers thinner than the exchange length [46]

$$\delta_{ex} = \sqrt{\frac{A_{ex}}{\mu_0 M_s^2}}, \tag{4.15}$$

where M_s is the saturation magnetization of the layer. For $Fe_{60}Co_{20}B_{20}$, with $M_s = 1270$ kA/m, and $A_{ex} = 2 \times 10^{-11}$ J/m, this results in an exchange length of $\delta_{ex} = 3.2$ nm. All of the thin films studied with FMR in this thesis fall within or are on the same order as this exchange length. This allows us to consider these thin films as a single macrospin.

4.1.2 Interlayer Exchange Coupling Energy

Interlayer exchange coupling energy, $U_{coupling}$ describes the exchange interaction that occurs between two magnetic thin films separated by a non-magnetic spacer layer. Unlike the previously discussed exchange energy, this kind of exchange interaction is indirect, and mediated by conduction electrons through the spacer layer.

We will introduce the subscripts 1 and 2 to keep track of the two coupled magnetic layers. Variables with a subscript 1 are for the bottom layer, and variables with the subscript 2 are for the top layer. We will derive everything from the perspective of layer 1, and reversing the indices will describe layer 2.

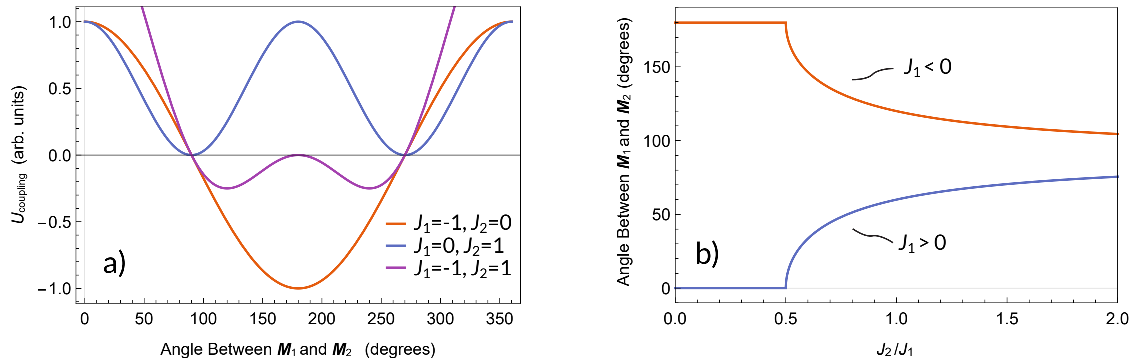

Figure 4.4: a), $U_{coupling}$ for three different configurations of J_1 and J_2 showing the differing energy minima, and b), the location of the energy minima in terms of the angle between $\boldsymbol{M}_1$ and $\boldsymbol{M}_2$, for a range of J_1 and J_2 values.

The coupling energy per unit volume between atomic planes of magnetic material separated by a non magnetic spacer layer is given by: [46, 63]

$$U_{coupling,1} = -\frac{J_1}{d_1}\frac{\boldsymbol{M}_1 \cdot \boldsymbol{M}_2}{M_{s,1}M_{s,2}} + \frac{J_2}{d_1}\left(\frac{\boldsymbol{M}_1 \cdot \boldsymbol{M}_2}{M_{s,1}M_{s,2}}\right)^2, \tag{4.16}$$

where J_1 and J_2 are the bilinear and biquadratic coupling terms, respectively, the 1 and 2 subscripts correspond to each of the two coupled layers, $M_{s,i} = |\boldsymbol{M}_i|$, as is the case for ferromagnetic materials, which is what is studied in this work. The term d_1 is the thickness of layer 1, which is added to obtain the expression for energy density, as desired. The bilinear term favors parallel (positive J_1) or antiparallel (negative J_1) alignment of the separated magnetic layers. The biquadratic term can only be positive, and favors 90° alignment of the separated magnetic layers.

Fig. 4.4 shows how the energy minima for $U_{coupling}$ depends on the magnitude of J_1 relative to J_2, and the relative angle between the magnetization of layer 1 and layer 2, $\boldsymbol{M}_1$ and $\boldsymbol{M}_2$. If J_2 is less than half of the absolute value of J_1, then the angle is determined by J_1. In this case, if J_1 is positive or (negative), then the angle between $\boldsymbol{M}_1$ and $\boldsymbol{M}_2$ is 0° (180°) resulting in purely ferromagnetic coupling (FC) (antiferromagnetic coupling (AFC)). If J_2 is larger than half of J_1, then the angle between $\boldsymbol{M}_1$ and $\boldsymbol{M}_2$ asymptotically approaches 90°, as J_2 increases relative to J_1, as shown in Fig. 4.4 b).

Bilinear Interlayer Exchange Coupling Constant J_1

Interlayer exchange coupling is not fully understood, and are several models including RKKY [12], quantum-confinement [28], free-electron [23, 43, 29], and interface-reflection (also called quantum interference) [105, 10]. However, for thick spacer layers, all of the models predict the same periodicity of J_1 oscillations, and the theories only differ in the

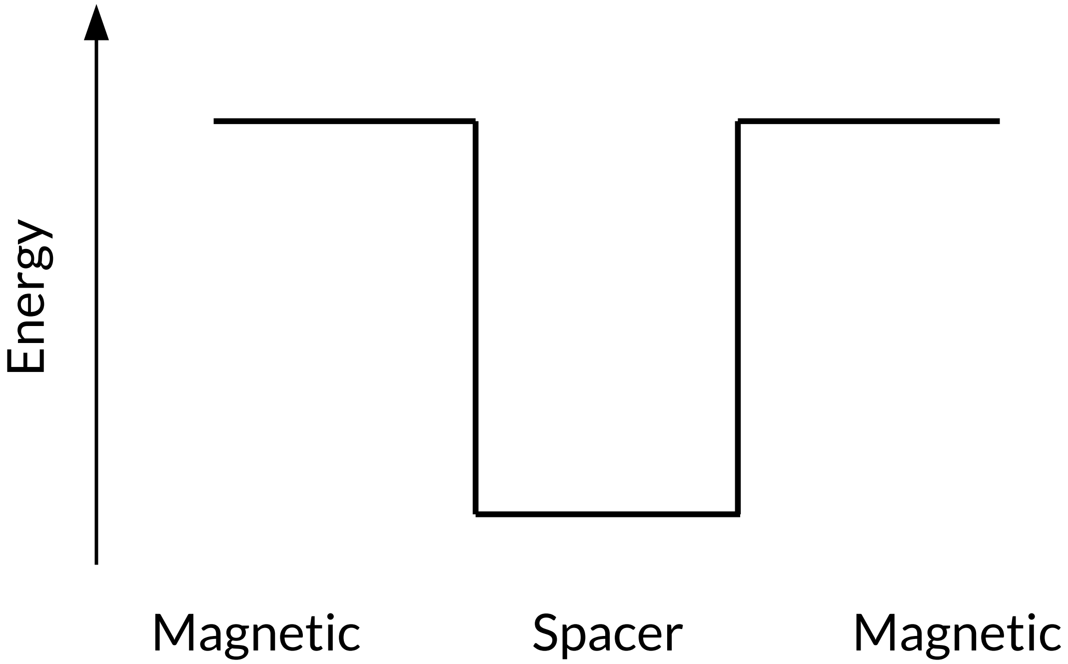

Figure 4.5: Potential energy of the quantum well created from a M/S/M (magnetic/ spacer/ magnetic) trilayer structure, as seen by electrons.

prediction of the amplitude of the oscillations. Bruno *et al.* was able to show that the interface-reflection model can treat metal and insulator spacers in a unified manner, which required separate theories previous to this. This theory also correctly predicts experimental findings such as the dependence on the magnetic layer composition and thickness and the temperature dependence of conductive and insulating spacer layers. [105, 10] Because of this, we will be using the interface-reflection model to simulate J_1 and fit our data.

The interface-reflection model considers the M/S/M (magnetic/ spacer/ magnetic) trilayer structure as a quantum well, where the magnetic layers are the walls of the well, and the spacer layer is the middle of the well, as shown in Fig. 4.5.

For a qualitative understanding of this model, lets start by considering an electron traveling through the spacer layer in the direction perpendicular to the M/S interfaces. This electron will encounter the wall of the well and have a probability to be reflected that depends on the height of the wall. The reflected wave will travel in the opposite direction and encounter the other wall and, again, have a probability to be reflected. If the phase shift throughout this round trip is equal to an integer multiple of the wavelength of the election wavefunction, then it will have fully constructive interference, if it is equal to half of a wavelength, then it will have fully destructive interference.

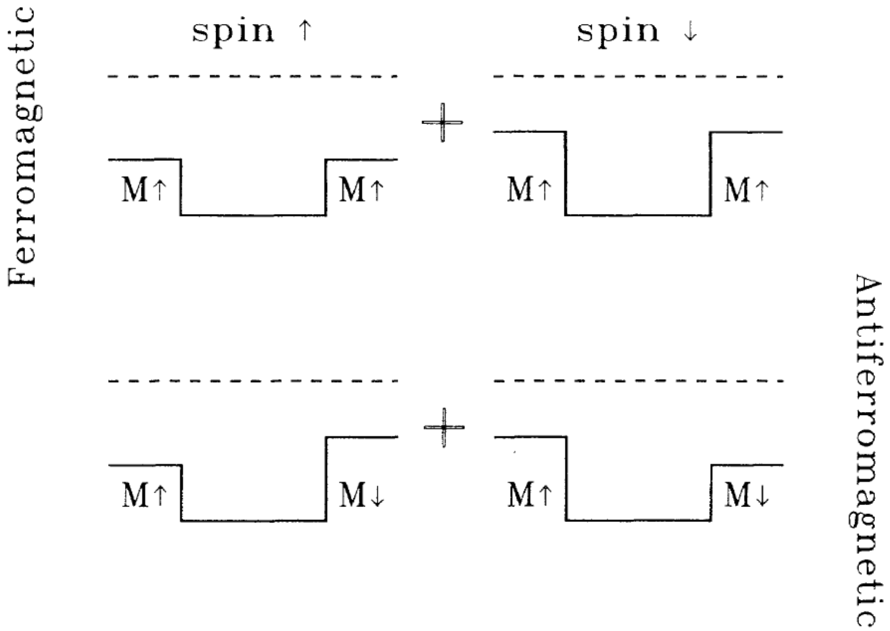

Figure 4.6: Quantum well potential barriers seen by electrons traveling through a structure consisting of two magnetic layers coupled across a non-magnetic spacer layer. The top left (right) quantum well shows the potential seen by spin-up (-down) electrons when both magnetic layers have magnetization aligned parallel with one another, and in the up direction. The bottom left (right) quantum well shows the potential seen by spin-up (-down) electrons when the magnetic layers have magnetization pointing in opposite directions relative to one another. The dotted line is the Fermi energy level. Figure reproduced from Ref. [105] with kind permission from APS (https://aps.org/).

The conduction electrons traveling through the spacer layer are only allowed to have specific wavevectors, as determined by the periodicity of the crystal lattice. For each individual wavevector, whether it interferes constructively or destructively depends on the width of the spacer layer, and will have sinusoidal dependence.

Electron states that constructively interfere will increase the density of states in the system, while the opposite will occur for destructive interference. The energy required to fill up all of the states to the Fermi level will also depend sinusoidally on the thickness of the spacer layer.

The height of the quantum well energy walls that spin up and spin down electrons see depends on the direction of magnetization of the magnetic layers, as shown in Fig. 4.6. This will cause the reflection probabilities, and consequently the density of states, to depend on the relative orientation of magnetization of the magnetic layers. Therefore, the energy required to fill all of the electron states to the Fermi level will also depend on the relative direction of magnetization of the magnetic layers, and whether electrons are spin up or spin

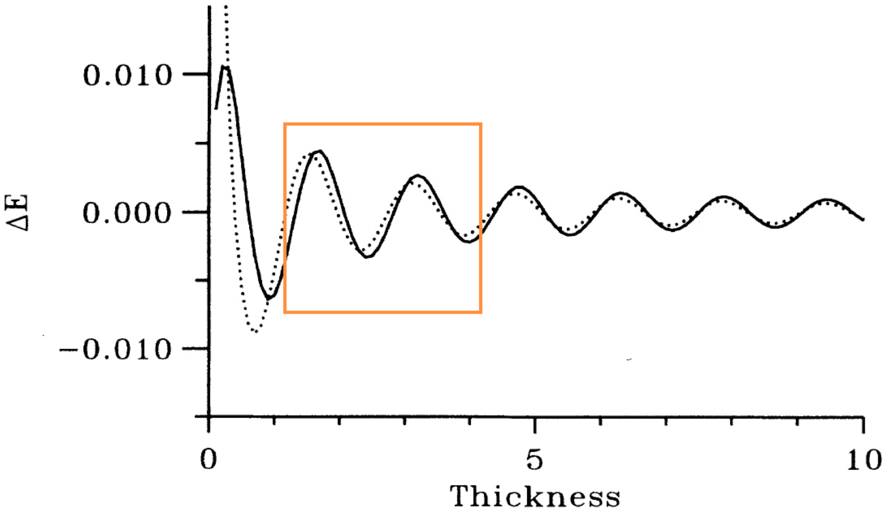

Figure 4.7: The total energy of a quantum well filled to the Fermi level (solid line) as a function of the spacer layer thickness. The dotted line is the approximate form used in the derivation of Eq. 4.17. The orange highlighted section is the region of thicknesses that we study for most of the work in this thesis. The bottom axis is in units of $2/q_\perp^\alpha$. Part of this figure is reproduced from Ref. [105] with kind permission from APS (https://aps.org/).

down. The difference in total energy when the magnetic layers have their magnetization parallel and antiparallel, $\Delta E = E_{\text{parallel}} - E_{\text{antiparallel}}$ is the coupling energy, and is shown in Fig. 4.7.

All of the interlayer exchange coupling models predict that for large spacer layer thicknesses, the coupling constant J_1 has the form [105, 10]

$$J_1(d) = \operatorname{Im} \sum_\alpha \frac{J^\alpha}{d^2} e^{i(q_\perp^\alpha d + \phi^\alpha)}, \tag{4.17}$$

where we are summing over contributions from several different electron states within the spacer layer labeled by α, d is the thickness of the spacer layer, J^α is the coupling strength of the electron state, $q_\perp^\alpha$ is the critical spanning vector of the electron state, and ϕ^α is the phase of the electron wavefunction after scattering from the magnetic layer adjacent to the spacer layer.

The only electron states that contribute to this coupling, are the ones corresponding to critical spanning vectors of the Fermi surface of the spacer layer material. Critical spanning vectors, which are shown in Fig. 4.8, are k vectors in the direction of the M/S interface normal, that connect two sheets of the Fermi surface that are parallel to each other at the endpoints of the vector.

The phase ϕ^α of each state α is defined by the topology of the Fermi surface of the spacer layer at the endpoints of its critical spanning vector $q_\perp^\alpha$. For thick spacer layers, ϕ^α

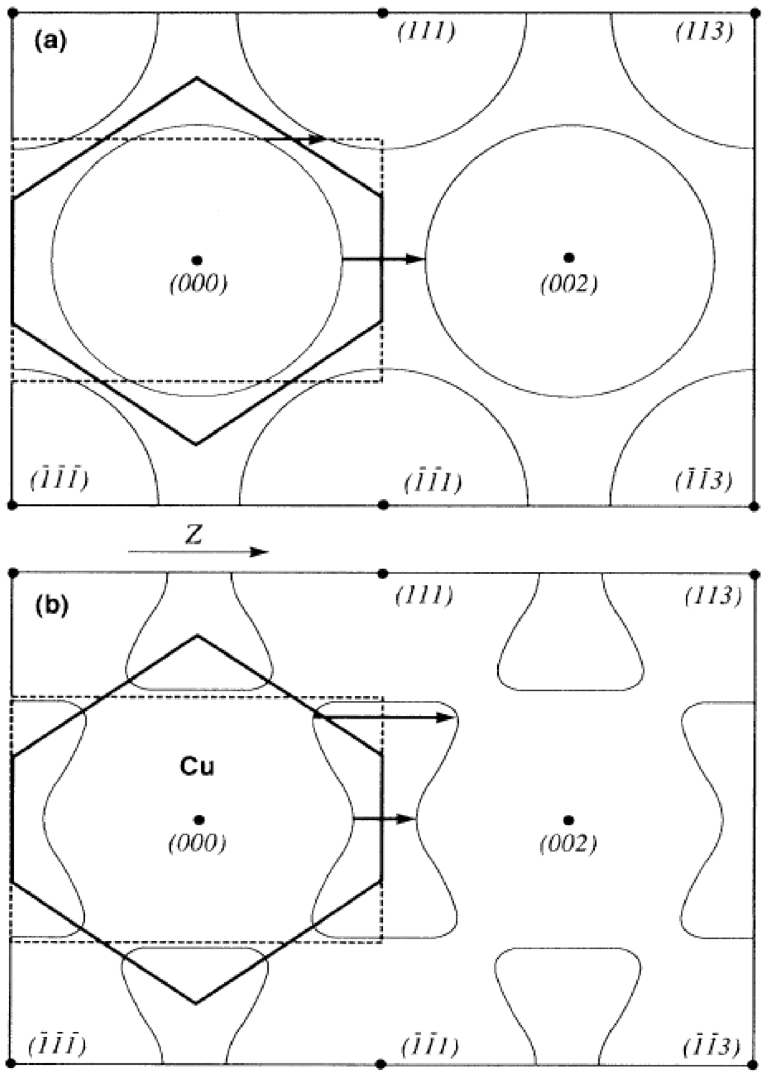

Figure 4.8: Cross section of the Fermi surface for FCC (001) Cu. a) is the free-electron approximation, and b) is the Cu Fermi surface. The critical spanning vectors for the (001) direction are shown as bold arrows. Figure reproduced from Ref. [11] with kind permission from APS (https://aps.org/).

is equal to 0, $\pi/2$, and π when the Fermi surface at this location is a minimum, a saddle point, and a maximum, respectively. [12]

The period of oscillation of interlayer exchange coupling from each critical spanning vector, which is equal to $2\pi/q_{\perp}^{\alpha}$, is determined entirely by the Fermi surface of the spacer layer. Therefore, the period of oscillation of interlayer exchange coupling is independent of the composition of the magnetic layers adjacent to the spacer layer, unless they cause a change in the Fermi surface of the spacer layer. One should note, however, that the apparent period of oscillation for thin spacer layer thicknesses, when calculating by the position of

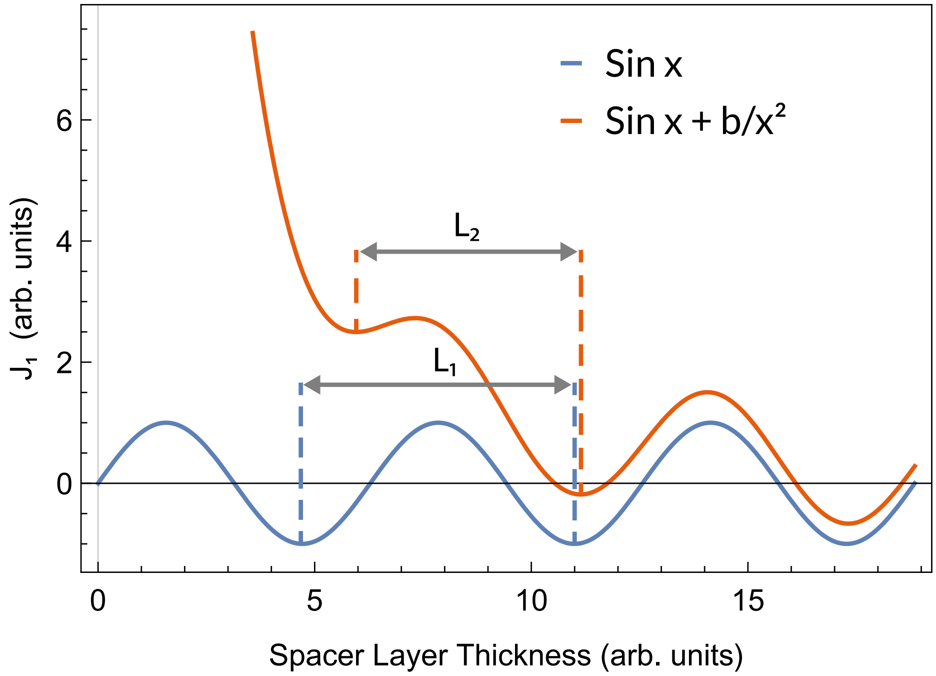

Figure 4.9: A diagram showing that the apparent period of oscillation, when determined from the maxima and minima positions, can change slightly when non-linear terms are added together. The two periods of oscillations determined from the minima location are labelled L_1 and L_2, and are different from one another even though the underlaying periodic function has the same period of 2π.

the minima or maxima in oscillations, can appear to change slightly when the amplitude of oscillation of the individual terms are changed significantly in the sum in Eq. 4.17. This is because the coupling oscillations is the sum of many non-linear terms, and when a non-linear function is added to a sin wave, in most cases it will shift the position of the maxima or minima slightly. This is illustrated in Fig. 4.9.

An example showing the individual contributions from several real critical spanning vectors, and the resulting J_1 which is the sum of them can be seen in Fig. 4.10. a), b), and c) are individual contributions (terms of the sum) in Eq. 4.17 corresponding to critical spanning vectors with different periods of oscillations. d) is the sum of all three contributions, which is the measured J_1.

The interface-reflection model predicts that J^α is equal to [105, 10]

$$J^\alpha = -\left[\frac{\hbar}{2\pi^2}\kappa^\alpha v_\perp^\alpha\right]\left[|R_\uparrow^\uparrow|^2 + |R_\downarrow^\uparrow|^2 - 2|R_\uparrow^\uparrow R_\downarrow^\uparrow|\right]F^\alpha(d,T), \tag{4.18}$$

where κ^α is the radius of curvature of the Fermi surface of the spacer layer material, and $v_\perp^\alpha$ is the electron state velocity, within the spacer layer material, in the direction perpendicular to the M/S (magnetic/ spacer) interface, both calculated at the location of the endpoints of the

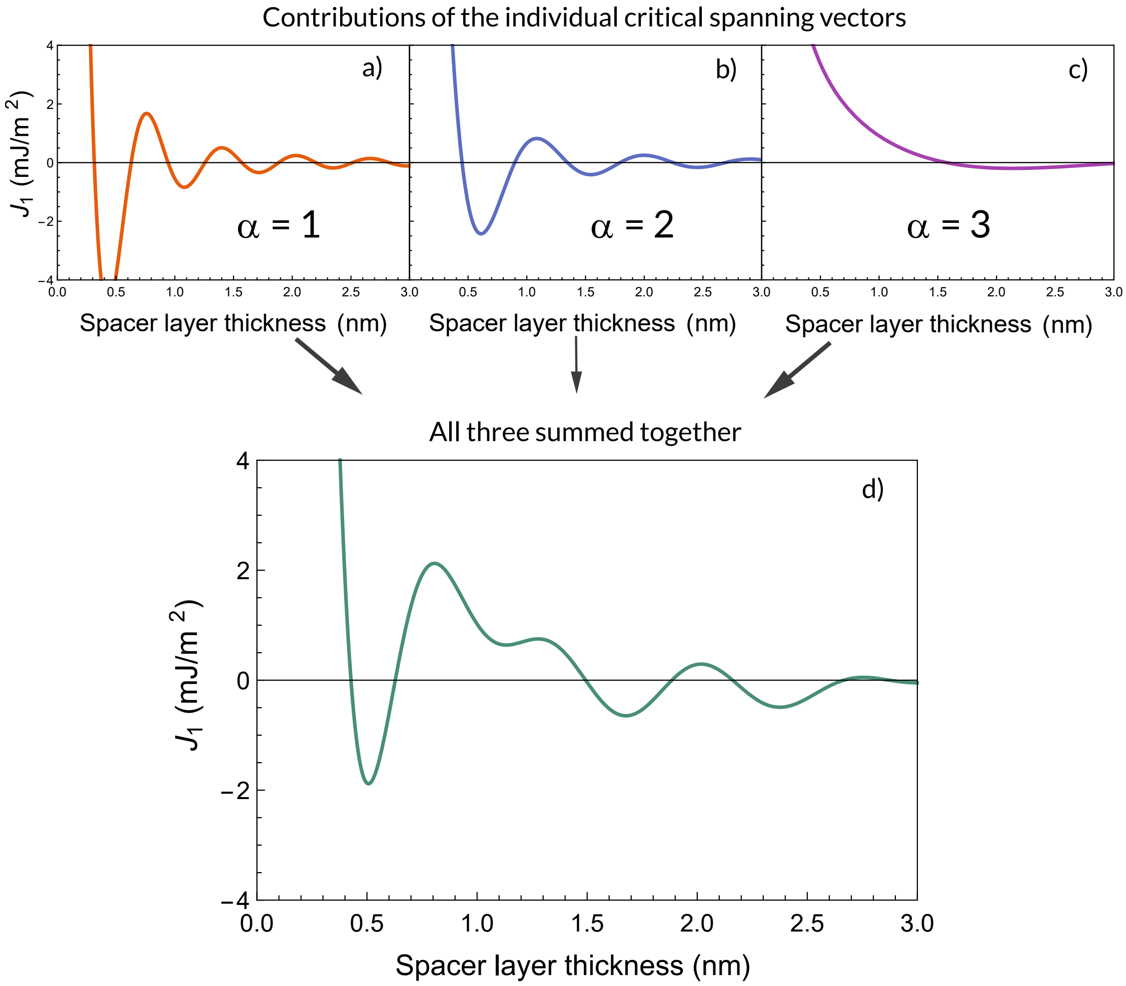

Figure 4.10: An example showing the individual contributions from real number critical spanning vectors, and the resulting J_1 which is the sum of them. a), b), and c) are individual terms in Eq. 4.17 corresponding to critical spanning vectors with indices $\alpha = 1, 2, 3$, all with different periods of oscillations. d) is the sum of all three contributions, which is the measured J_1.

critical spanning vectors. $R^{\uparrow}_{\uparrow}$ ($R^{\uparrow}_{\downarrow}$) is the reflection amplitude for a spin-up (-down) electron reflecting from the energy barrier formed when both magnetic layers have magnetization parallel with one another in the up direction.

A schematic representation of the potential wells for each part of the second term in Eq. 4.18, $|R^{\uparrow}_{\uparrow}|^2$, $|R^{\uparrow}_{\downarrow}|^2$, $|R^{\uparrow}_{\uparrow}R^{\downarrow}_{\uparrow}|$, and $|R^{\uparrow}_{\downarrow}R^{\downarrow}_{\downarrow}|$, is shown in Fig. 4.6. It is assumed that the barriers are symmetric for spin up and spin down so that $R^{\uparrow}_{\uparrow} = R^{\downarrow}_{\downarrow}$ and $R^{\uparrow}_{\downarrow} = R^{\downarrow}_{\uparrow}$. This term is the difference in reflection amplitudes seen by electrons (both spin-up and spin-down) traveling through the spacer layer where both magnetic layers have parallel, and anti-parallel magnetizations. It depends on the height of the potential barrier of the two magnetic layers as seen by an electron traveling through the structure. Therefore, this term is dependent on the composition of the magnetic layers.

$F^\alpha(d,T)$, in Eq. 4.18, is the temperature dependence, which is given by [27, 67, 98, 73]

$$F^\alpha(d,T) = \frac{x^\alpha}{\sinh x^\alpha}, \tag{4.19}$$

where

$$x^\alpha = 2\pi k_B T\left[\frac{d}{\hbar v_\perp^\alpha} + D_\phi^\alpha\right], \tag{4.20}$$

where k_B is Boltzmann's constant and $\hbar$ is the reduced Planck's constant. The first term in the square brackets is the temperature dependence contribution from the spacer layer, and D_ϕ^α is the temperature dependence contribution from the interface reflections on either side of the spacer layer. When Bruno *et al.* first derived the temperature dependence of J_1, they only considered the dependence of the spacer layer, and not the magnetic layers. As such, their derived temperature dependence only included the first term in Eq. 4.20. This first term arises due to the fact that at finite temperatures, the Fermi surface, and critical spanning vectors, are broadened. This results in a distribution of critical spanning vectors with slightly different lengths, which smooths out the J_1 oscillations, leading to a reduction in their magnitude.

Later, Castro *et al.* [27] and Lee *et al.* [67] independently derived a temperature dependence that includes the contribution from the magnetic interfaces, which is the second term in Eq. 4.20. This second term, to first order, is equal to the derivative of the phase shift caused by the reflection of electrons at the interfaces with respect to energy, $D_\phi^\alpha = \frac{\mathrm{d}\phi^\alpha}{\mathrm{d}E}$. [67, 98, 27] Like before, finite temperature broadens the Fermi surface, resulting coupling electron states with a distribution of energies. If $\frac{\mathrm{d}\phi^\alpha}{\mathrm{d}E}$ is large, this distribution of coupling electron states will have relatively large distributions in their phase. When added together, this results in a smearing of the J_1 oscillations, leading to a reduction in their magnitude.

For thicker spacer layers, the first term in Eq. 4.20, which depends on d, becomes larger, making the second interface term insignificant. Thus, for thicker spacer layers, one can approximate the temperature dependence with only the first spacer layer term. However, in our case, the spacer layers are thin enough that the two terms are of comparable magnitude, and must both be included.

At zero temperature, $F^\alpha(d,T) = 1$. So the temperature dependence can also be expressed as $J_1^\alpha(T=0)F^\alpha(d,T)$, which is the temperature dependence weighted by the zero temperature J_1 for each critical spanning vector, which we have called $J_1^\alpha(T=0)$.

The first term in Eq. 4.20 depends on the spacer layer thickness d, while the second term doesn't. So, the temperature dependence of J_1 for several samples with different spacer layer thicknesses can be measured and fit in order to determine both terms independently.

The first term in Eq. 4.18 depends entirely on the properties of the Fermi surface of the non magnetic spacer layer. Therefore, as long as the spacer layer remains the same, the composition of the magnetic layers will have no effect on this term.

In deriving Eq. 4.17, using the interface-reflection model, approximations were made that are only exact in the limit of infinitely thick spacer layers. However, as is seen in Fig. 4.7, it is quite accurate for thicknesses greater than one period of J_1 oscillations. The typical range of spacer layer thicknesses studied in this work is shown as an orange box. In this range, the model is less accurate than it would be for thicker spacer layers, but accurate enough for us to gain some useful insight into the fundamental physics of the interlayer exchange coupling.

As mentioned earlier, the interface-reflection model is able to describe coupling across metallic and insulating spacer layers. The only difference is that the electron states contributing to coupling have oscillatory wavefunctions for the metallic case, and exponentially decaying tunneling wavefunctions for the insulating case. In the latter case, the critical spanning vector, $q_\perp^\alpha$ in Eq. 4.17, will be imaginary instead of real. This will result in J_1 that decreases exponentially with spacer layer thickness rather than being oscillatory.

In a crystal, the allowed states are Bloch waves,

$$\psi(\boldsymbol{r}) = u(r)e^{i\boldsymbol{k}\cdot\boldsymbol{r}}, \tag{4.21}$$

where $u(r)$ is a periodic function with the periodicity of the crystal lattice. This holds true for any complex wave vector. [3] For bulk crystals, states with imaginary wave vectors cannot exist because they increase exponentially to infinity, and cannot be normalized. However, for finite systems, like the spacer layer we study, the wave function is limited in space and doesn't go to infinity. This allows states with imaginary wave vectors to exist. Therefore, just like insulating layers, metallic spacer layers can also have evanescent electron states that contribute to coupling. Since these decay exponentially, their contribution will be significantly smaller than that of the real wavevectors, and are usually ignored. However, we will be measuring coupling across spacer layers as thin as 0.4 nm, so there is a possibility for these to contribute.

If the wavevector is real, Eq. 4.17 becomes [105, 10]

$$J_1(d) = \sum_\alpha \frac{J^\alpha}{d^2}\sin(q_\perp^\alpha d + \phi^\alpha), \tag{4.22}$$

and if the wavevector is imaginary, Eq. 4.17 becomes [105, 10, 9]

$$J_1(d) = \sum_\alpha \frac{J^\alpha}{d^2} e^{i\phi^\alpha} e^{-d/\delta_\perp^\alpha}, \tag{4.23}$$

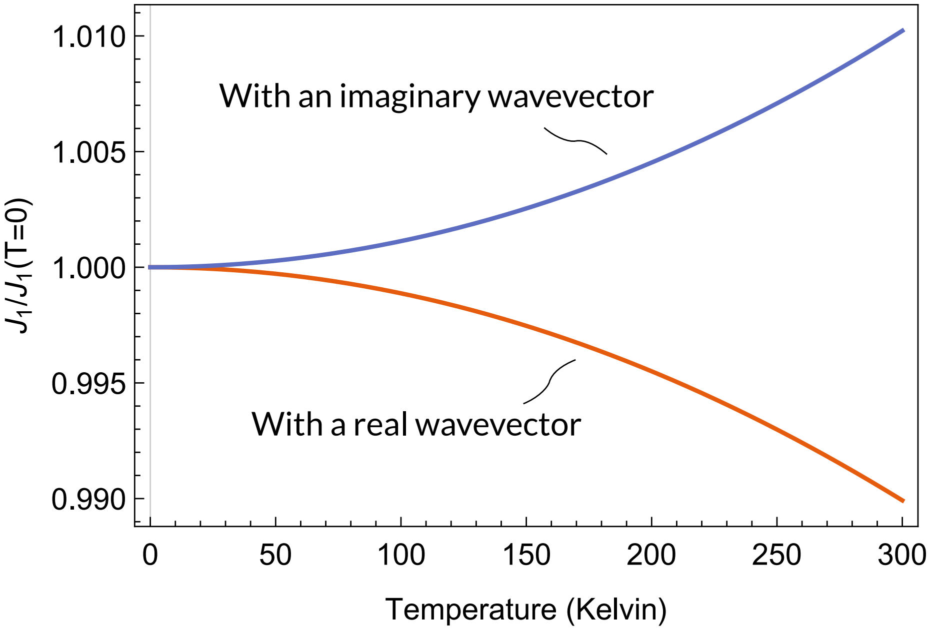

Figure 4.11: The temperature dependence of J_1 when the critical spanning vector is real, using Eq. 4.19 with $d = 0.4$ nm, $v_\perp^\alpha = 4 \times 10^5$ m/s, $D_\phi^\alpha = 0$ J^{-1} (orange), or imaginary, with $d = 0.4$ nm, $v_\perp^\alpha = i4 \times 10^5$ m/s, $D_\phi^\alpha = 0$ J^{-1} (blue).

where $\delta_\perp^\alpha = 1/\mathrm{Im}(q_\perp^\alpha)$ is the decay length, and the term $e^{i\phi^\alpha}$ determines whether the exponential favors ferromagnetic or antiferromagnetic coupling. ϕ^α is no longer constrained to the range of 0 to π in the case of evanescent states and the complex Fermi surface, so this term can be positive or negative. [10, 9]

One useful difference between coupling caused by electron states with real and imaginary wave vectors is that they have opposite temperature dependence. This can be seen easily using the following relation

$$\frac{ix}{\sinh ix} = \frac{x}{\sin x}, \tag{4.24}$$

along with the fact that if the wavevector is imaginary, its velocity will be as well. The different dependence of J_1 for oscillating and evanescent wavefunctions is shown in Fig. 4.11. The opposite dependence, allows for the determination of which case is contributing to coupling by measuring the temperature dependence of J_1 in a sample. It should be noted that each term in the sum in Eq. 4.17 has its own temperature dependence, and depending on the spacer layer thickness and critical spanning vector, the zero temperature $J_1^\alpha(T = 0)$ could be positive for some terms and negative for others. Since the measured temperature dependence is the sum of all terms, this can also lead to opposite temperature dependence than expected. Therefore, in order to compare the model to experiment one has to consider the sum of the individual temperature dependence of each critical spanning vector.

Néel "Orange-peel" Contribution to J_1

Surface roughness can result in an additional contribution to J_1. If we make an approximation that the interface between the magnetic materials and the spacer layer can be described by a sinusoidally varying function, $Z_L = \delta\cos(2\pi x/L)$ for the lower interface and $Z_U = d + \delta\cos(2\pi x/L)$ for the upper interface, it can be shown that the strength of this type of coupling can be calculated as [6]

$$J_{1,op} \approx \mu_0 M_{s,1} M_{s,2} \frac{\delta^2}{L} e^{-2\pi d/L}, \tag{4.25}$$

where δ is the amplitude of the roughness oscillations, L is the in-plane period of roughness oscillations, $M_{s,1}$ and $M_{s,2}$ are the saturation magnetizations of the two magnetic layers, and d is the spacer layer thickness.

Néel "Orange-peel" coupling of this form only occurs as long as the amplitude of the surface roughness is small compared to the thickness of the spacer layer. Thus, as the thickness of the spacer layer is reduced to 0, this kind of coupling will no longer be applicable.

Biquadratic Coupling Term

J_2 can originate from intrinsic and extrinsic sources. [30] In the samples studied throughout this thesis, the measured J_2 always favors a perpendicular alignment, suggesting an extrinsic source [6] Extrinsic sources of biquadratic coupling could be due to uncorrelated film roughness [6], pin-holes [7], loose spins, [101] and spatial fluctuations. [100]

While we will measure J_2 in many of the samples studied in this thesis, our work will be focusing on analyzing J_1.

4.1.3 Zeeman Energy

The Zeeman energy density is written as

$$U_{zee} = -\mu_0 \boldsymbol{M} \cdot \boldsymbol{H}_{ext}, \tag{4.26}$$

where $\boldsymbol{M}$ is the saturation magnetization vector, and $\boldsymbol{H}_{ext}$ is the external magnetic field vector. This energy is minimized when the magnetic moments line up with the external magnetic field. In general, the magnetic moments do not always align with the external magnetic field due to the fact that the material has high anisotropy energy or interlayer exchange coupling. For FMR, $\boldsymbol{H}_{ext} = \boldsymbol{H}_{dc} + \boldsymbol{h}_{rf}$, where $\boldsymbol{H}_{dc}$ is a large constant magnetic field that the moments precess around, and $\boldsymbol{h}_{rf}$ is the oscillating that drives precession. In order make an FMR measurement, $\boldsymbol{H}_{dc}$ must be strong enough that all of the magnetic moments are aligned parallel with it.

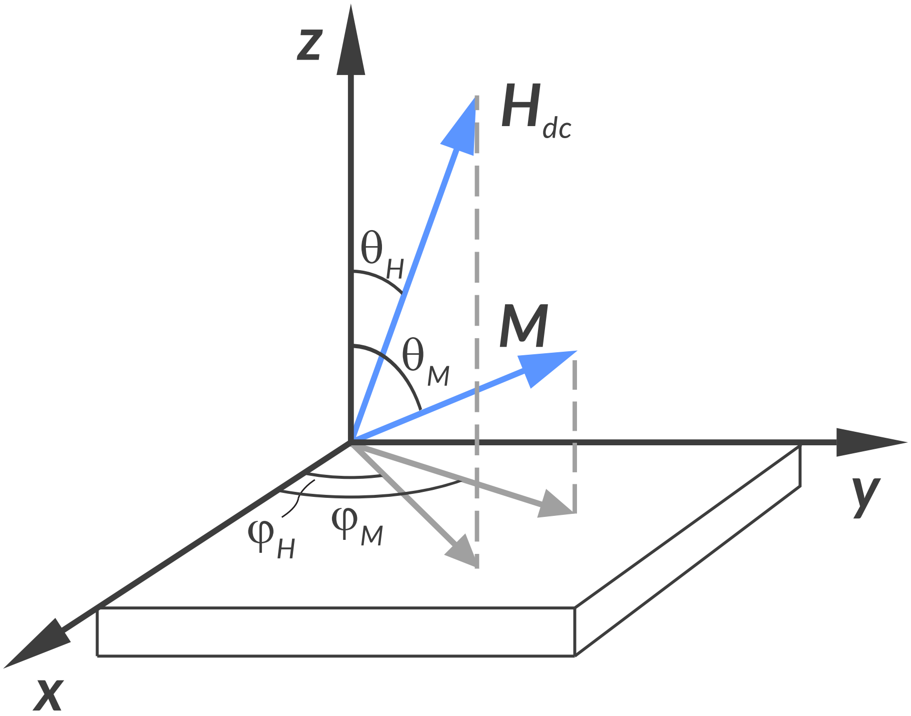

Figure 4.12: The coordinate systems used in this section. $\boldsymbol{M}$ is the magnetization vector, and $\boldsymbol{H}_{dc}$ is the external magnetic field vector. The sample lies in the plane of $\boldsymbol{x}$ and $\boldsymbol{y}$ as shown.

4.1.4 Magnetic Anisotropy Energy

The potential energy of a magnetic thin film depends on the direction of magnetization relative to the sample. Thus, it is anisotropic with regards to the direction of magnetization. Energies that depend on the direction of magnetization relative to the sample are known as magnetic anisotropy energies (MAE). The directions which correspond to a MAE minima, are called the easy axis. The directions which correspond to a MAE maxima, are called the hard axis. The next three energies that we will describe, namely crystalline anisotropy energy, surface anisotropy energy, and demagnetization energy, are types of magnetic anisotropy energies.

Fig. 4.12 describes the coordinate system used for describing MAE in this section.

4.1.5 Crystalline and Interface Anisotropy Energy

The crystalline anisotropy energy describes the dependence of energy on the direction of magnetization relative to the crystal lattice. For the samples studied in this thesis, this energy is uniaxial because it is tied to the crystal structure, which is polycrystalline with uniaxial symmetry.

The interface anistropy energy describes the dependence of energy on the direction of magnetization relative to the top and bottom interfaces of the magnetic thin films. For polycrystalline materials, this energy is also uniaxial, and therefore we have grouped it together with crystalline anisotropy energy. The fundamental source of these energies is spin-orbit interaction.

All of the samples created in this thesis are polycrystalline. Hence, there is no macroscopic ordering of the lattice in the plane of the sample, and so the MAE is averaged out in the plane and can have no $\boldsymbol{x}$ or $\boldsymbol{y}$ (Figure 4.12) dependence. The phenomenological anisotropy energy density to first order is given by:

$$U_{an} = -\frac{K_u}{M_s^2} M_\perp^2, \tag{4.27}$$

where $K_u = K_c + \frac{K_i}{d}$ is the uniaxial anisotropy constant perpendicular to the plane of the sample, and d is the thickness of the magnetic layer, $M_\perp = M_Z$ is the component of magnetization perpendicular to the plane of the sample. K_c is the uniaxial anisotropy coefficient that describes the magnitude of the crystalline anisotropy, which is energy per volume. K_i is the uniaxial anisotropy coefficient that describes the magnitude of the interface anisotropy, which is energy per area, and depends on the thickness of the magnetic layer. When these coefficients are positive, the energy is minimized when the magnetization is perpendicular to the plane of the sample.

For the micromagnetics model we will treat the volume and surface anisotropy separately, which are given by

$$U_{an,volume} = -\frac{K_c}{M_s^2} M_\perp^2, \tag{4.28}$$

$$U_{an,surface} = -\frac{K_i}{dM_s^2} M_\perp^2, \tag{4.29}$$

where $U_{an,volume}$ is the contribution from the volume, and $U_{an,surface}$ is the contribution from the surface.

4.1.6 Demagnetizing Energy

The demagnetizing energy occurs due to the macroscopic shape of the sample. Our samples can be considered approximately infinite planes. A magnetic material is made up of a large number of small dipoles which can be oriented in any direction. If the dipoles are oriented perpendicular with a surface of the film then magnetic charge will be present on that surface which costs energy. These charges will create an internal field inside the magnetic material

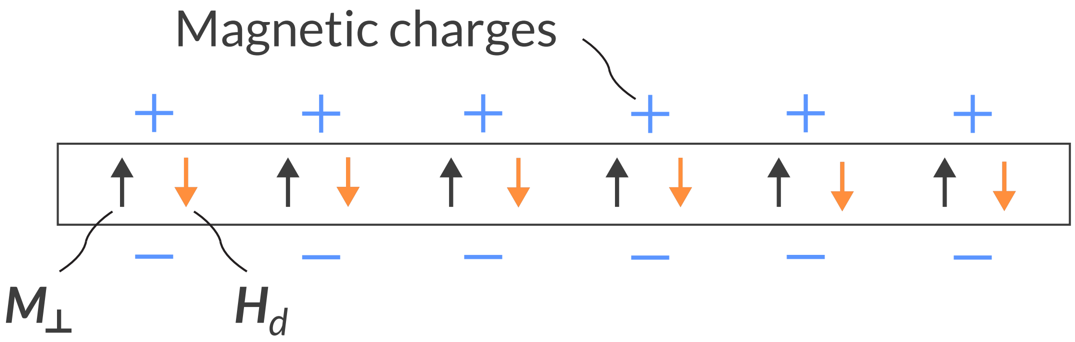

Figure 4.13: The demagnetization field created by magnetic charge on the surface of a perpendicularly magnetized infinite plane.

known as the demagnetization field, as shown in Fig. 4.13. This field costs energy and, as a result, the sample will prefer to be magnetized in-plane to avoid this.

The demagnetization energy can be calculated from the demagnetization field, which is created by the presence of the surface charge. Using Gauss's law for an infinite plane, it can be shown that the demagnetization field is equal and opposite to the perpendicular component of magnetization $\boldsymbol{H}_d = -\boldsymbol{M}_\perp$. From this we can calculate the demagnetization energy as follows:

$$\begin{aligned} U_d &= -\frac{\mu_0}{2V}\iiint \boldsymbol{M}\cdot\boldsymbol{H}_d \mathrm{d}V \\ &= \frac{\mu_0}{2V}\iiint M_\perp^2 \mathrm{d}V \\ &= \frac{\mu_0 M_\perp^2}{2V}\iiint \mathrm{d}V \\ &= \frac{\mu_0}{2}M_\perp^2. \end{aligned} \tag{4.30}$$

For thin films that are only a few atomic layers thick, this is scaled by an effective demagnetization coefficient, D,

$$U_d = \frac{\mu_0 D}{2}M_\perp^2, \tag{4.31}$$

where D is very close to 1 for films thicker than a few atomic layers. It will be assumed that the samples in this thesis are thick enough so that $D = 1$.

4.2 FMR Theory

4.2.1 Undamped Magnetization Equation of Motion

Given a rigid body containing angular momentum, like a spinning top, we can use classical mechanics to come up with an equation of motion

$$\boldsymbol{T} = \frac{d\boldsymbol{L}}{dt} = \boldsymbol{r} \times \boldsymbol{F}, \tag{4.32}$$

where $\boldsymbol{L}$ is the angular momentum, $\boldsymbol{T}$ is the torque exerted on the body, $\boldsymbol{r}$ is the position vector of the center of mass, and $\boldsymbol{F}$ is the force applied to the body. This equation shows that the torque is perpendicular to the force applied to the rigid body. This causes the center of mass to spin around an axis and precess. Inside an atom there are three main sources of angular momentum, electron spin, electron orbital, and nuclear spin. FMR studies materials with unpaired electrons allowing it to probe the electron spin and electron orbit, while NMR probes the nuclear spin. The classical picture of an electron is a spinning negative charge, which also has an associated angular momentum, and any force applied to it will cause it to precess. Another property of a spinning charge is that it creates a magnetic moment, $\boldsymbol{M}$, which, for a negative charge, is antiparallel with the angular momentum. In this situation, the magnetic moment and angular momentum are directly coupled and so any force applied to the magnetic moment will be a force on the angular momentum, causing precession. The magnetic moment of a spinning negative charge is related to its angular momentum by the following equation

$$\boldsymbol{M} = -\gamma \boldsymbol{L}, \tag{4.33}$$

where $\gamma = g\frac{e}{2m}$ is the gyromagnetic ratio, g is the g-factor, e is the electron charge, m is the electron mass. The torque exerted on a magnetic moment $\boldsymbol{M}$ by the field $\boldsymbol{B}$ is given by

$$\boldsymbol{T} = \boldsymbol{M} \times \boldsymbol{B} \tag{4.34}$$

Equations 4.32, 4.33, 4.34 can be combined to give the undamped magnetization equation of motion

$$\frac{d\boldsymbol{M}}{dt} = -\gamma \boldsymbol{M} \times \boldsymbol{B}_{eff}, \tag{4.35}$$

where $\boldsymbol{B}_{eff}$ is the total effective field. The term on the right hand side of Eq. 4.35 represents the precessional torque.

The motion of the magnetization vector that results from Equation 4.35 is illustrated as the blue line in Figure 4.14. It can be seen that the motion of the magnetization vector will continue to precess about the effective field $\boldsymbol{B}_{eff}$ in a circular path indefinitely. Considering the analogous spinning top, it is clear that a spinning top doesn't stay up forever, and so this picture is unrealistic for the real world, and that is because it ignores damping. In order to account for the damping, another term must be added to the equation of motion.

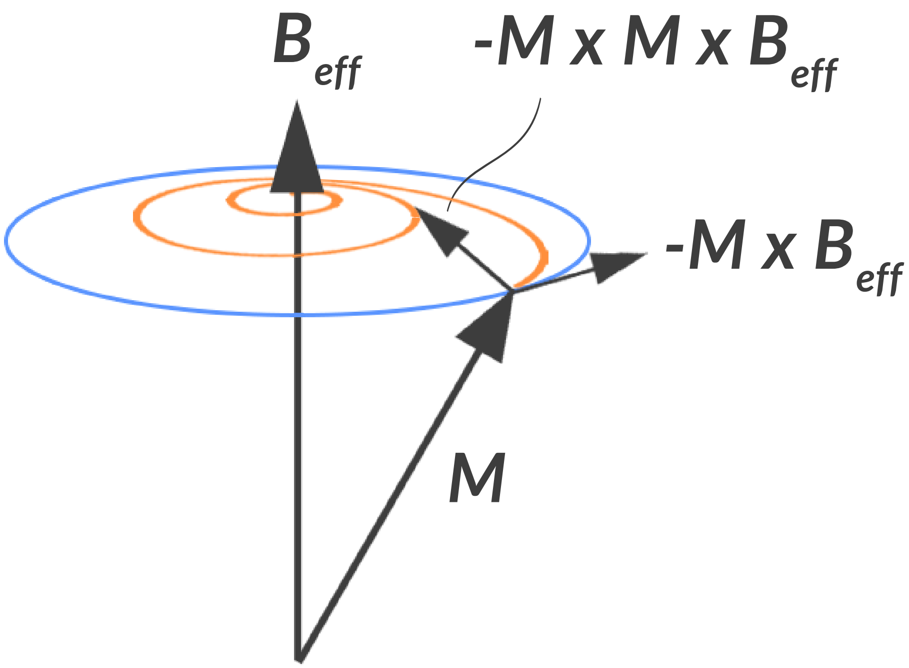

Figure 4.14: Diagram showing the directions of each term in the LL equation of motion. The first term on the right hand side is the precessional torque, the second term is the damping. The blue ellipse represents the path $\boldsymbol{M}$ will take in the absence of damping. The orange spiral represents the path $\boldsymbol{M}$ will take with damping.

4.2.2 Damped Magnetization Equation of Motion

In 1935, L. Landau and E. Lifshitz were the first to describe damped magnetization dynamics with the Landau-Lifshitz (LL) equation of motion [65, 57, 17]

$$\frac{\partial \boldsymbol{M}}{\partial t} = -\gamma \left[\boldsymbol{M} \times \boldsymbol{B}_{eff}\right] - \frac{\lambda}{M_S^2} \left[\boldsymbol{M} \times \boldsymbol{M} \times \boldsymbol{B}_{eff}\right], \tag{4.36}$$

where $\boldsymbol{B}_{eff}$ is the effective field, and $\lambda = \frac{1}{\tau}$ is the damping parameter that defines the degree of damping action, and is equal to the inverse of the relaxation time τ. The first term on the right hand side of the LL equation is the precessional torque as seen in the undamped case. The second term on the right hand side of the LL equation represents the LL damping term. The direction of the damping term can be seen in Figure 4.14. The effect of the damping term is to move $\boldsymbol{M}$ towards $\boldsymbol{B}_{eff}$ so that they eventually become parallel. It causes $\boldsymbol{M}$ to trace a spiral pattern as it approaches $\boldsymbol{B}_{eff}$. Damping involves transfer of energy from the motion of $\boldsymbol{M}$ to microscopic thermal motion. The mechanisms by which this occurs include coupling of the magnetization field to spin waves, eddy currents, lattice vibrations, spin-orbit interactions, and the effects of crystalline structure which can include strains, crystal defects such as voids, interstitial atoms, and foreign atoms [33]. In the mid

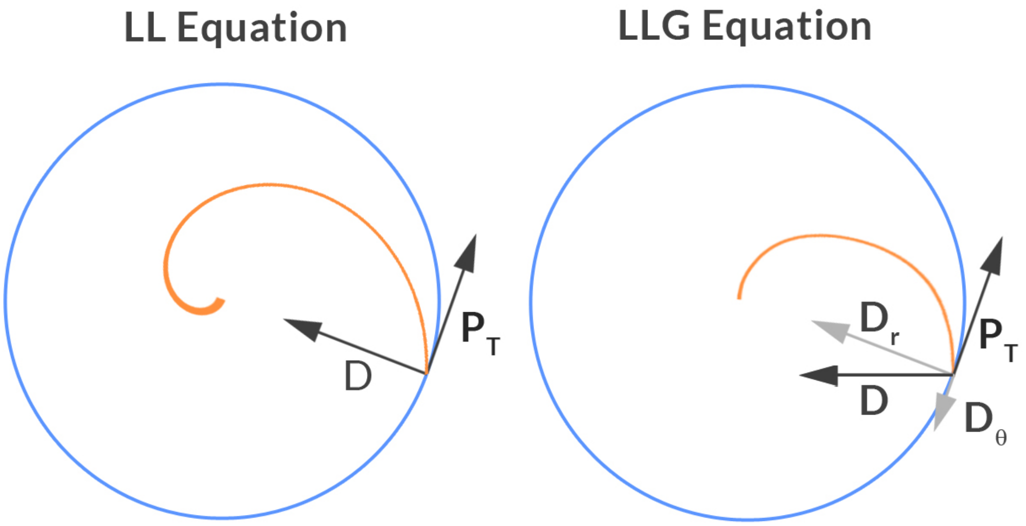

Figure 4.15: Diagram comparing the damping term in the LL equation and LLG equation. The diagram is drawn looking down on the precession with the effective field $\boldsymbol{B}_{eff}$ coming out of the page. The orange path represents the path taken by the magnetization vector during precession. The damping vector is labeled as D and the precession vector is labeled as P_T. It can be seen that the damping in the LLG equation reduces the precessional torque by the vector D_θ due to the fact that the precessional torque and damping are not orthogonal.

1900's, the LL equation of motion was well established and supported by a considerable amount of experimental data. However, as more experimental data was obtained, it was clear that the damping term in the LL equation was failing to account for all mechanisms of damping [33]. It was initially thought that the extra damping came from eddy currents within the material, but experiments on permalloy materials determined that the extra damping could not have been caused by eddy currents and must have been from another mechanism. In 1955 Thomas L. Gilbert re formulated the damped magnetization equation of motion using the lagrangian and Rayleigh dissipation function [33] to give the the Landau Lifshitz Gilbert equation (LLG) [17]

$$\frac{\partial \boldsymbol{M}}{\partial t} = -\gamma \left[\boldsymbol{M} \times \boldsymbol{B}_{eff}\right] + \frac{\lambda}{\gamma M_s^2}\left[\boldsymbol{M} \times \frac{\partial \boldsymbol{M}}{\partial t}\right]. \tag{4.37}$$

Equation 4.37 can be rewritten using the popular Gilbert damping parameter $\alpha = \frac{\lambda}{\gamma M_s}$ to give

$$\frac{\partial \boldsymbol{M}}{\partial t} = -\gamma \left[\boldsymbol{M} \times \boldsymbol{B}_{eff}\right] + \frac{\alpha}{M_s}\left[\boldsymbol{M} \times \frac{\partial \boldsymbol{M}}{\partial t}\right]. \tag{4.38}$$

The LL and LLG equation differ only in the direction and magnitude of the damping term. The change in direction of the damping term between the two can be seen graphically in Figure 4.15 where the damping term in the LLG equation has a component anti

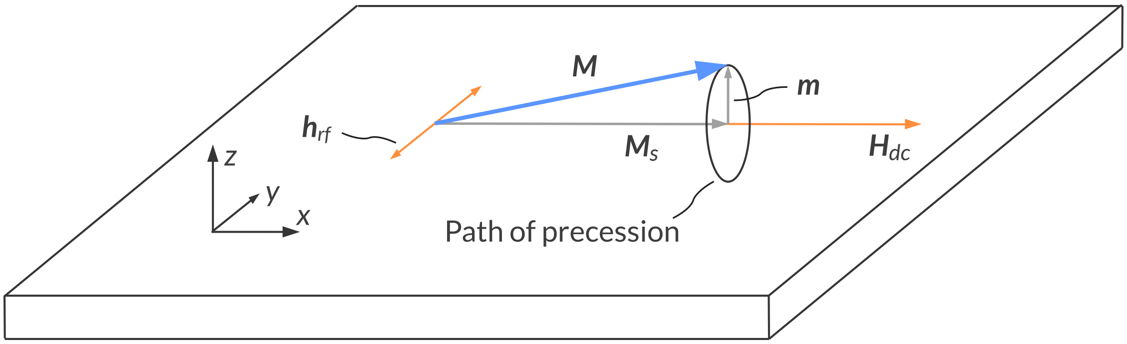

Figure 4.16: A diagram showing the directions of the magnetization and field vectors relative to the sample and coordinate system for the in-plane FMR configuration. Using the $\langle x, y, z\rangle$ coordinate system shown, $\boldsymbol{H}_{dc} = \langle H_{dc}, 0, 0\rangle$, $\boldsymbol{h}_{rf} = \langle 0, h_{rf}, 0\rangle$, $\boldsymbol{H}_{ext} = \boldsymbol{H}_{dc} + \boldsymbol{h}_{rf} = \langle H_{dc}, h_{rf}, 0\rangle$, $\boldsymbol{M} = \langle M_s, m_y, m_z\rangle$.

parallel with the precession torque and therefore reduces the precessional torque allowing the magnetization vector to align with the effective field more quickly.

4.2.3 Ferromagnetic Resonance Equations

Ferromagnetic resonance measurements can be made by putting the sample inside a large dc magnetic field and applying a small perpendicular microwave magnetic field $\boldsymbol{h}_{rf} = \boldsymbol{h}e^{i2\pi ft}$ with a fixed frequency f. Since there is a damping force acting on the precessional motion, this rf magnetic field is required to continuously input energy and maintain the motion. Changing the amplitude of the dc magnetic field will change the precessional frequency. When the frequency of the perpendicular microwave magnetic field is equal to the precessional frequency for the particular dc field strength, then resonance will occur. Ferromagnetic resonance will be accompanied by an increase in microwave losses in the perpendicular microwave magnetic field, which is what our spectrometer uses to probe it.

This section will cover the theoretical aspect of FMR measurements. The experimental technique to achieve FMR measurements will be covered in a later section of this thesis. The FMR equations are found by solving the LLG equation, Eq. 4.38, using the effective fields that are related to the total energy from Eq. 4.1 by the relation

$$\boldsymbol{B} = -\frac{\partial U}{\partial \boldsymbol{M}} = -\langle \frac{\partial U}{\partial M_x}, \frac{\partial U}{\partial M_y}, \frac{\partial U}{\partial M_z}\rangle \tag{4.39}$$

In Plane Configuration

The geometry of the in-plane configuration is shown in Fig. 4.16. The in plane configuration will have $\boldsymbol{H}_{dc}$ in the plane of the sample pointing along the $\boldsymbol{x}$ axis.

In the absence of a driving field, $\boldsymbol{M}$ will align itself with $\boldsymbol{H}_{dc}$ and also be in the plane of the sample. When the rf driving field is turned on, $\boldsymbol{M}$ will precess around $\boldsymbol{H}_{dc}$. For the work in this thesis, we will be operating in the small perturbation limit, where $\boldsymbol{M}$ will only make small perturbations away from $\boldsymbol{H}_{dc}$ as it precesses. This allows us to accurately approximate $\boldsymbol{M}$ as

$$\boldsymbol{M} = \boldsymbol{M}_s + \boldsymbol{m} = \langle M_s, m_x, m_y \rangle \tag{4.40}$$

where $\boldsymbol{M}_s$ and $\boldsymbol{m}$ are the orthogonal components of $\boldsymbol{M}$, $\boldsymbol{M}_s$ is directed along the axis of precession and is in the plane of the sample, $\boldsymbol{m}$ is perpendicular to $\boldsymbol{M}_s$.

The total effective field is given by the sum

$$\boldsymbol{B}_{eff} = -\left[\frac{\partial U_{zee}}{\partial \boldsymbol{M}} + \frac{\partial U_{an}}{\partial \boldsymbol{M}} + \frac{\partial U_{d}}{\partial \boldsymbol{M}} + \frac{\partial U_{coupling}}{\partial \boldsymbol{M}}\right] \tag{4.41}$$

$$= \boldsymbol{B}_{zee} + \boldsymbol{B}_{an} + \boldsymbol{B}_{d} + \boldsymbol{B}_{coupling}. \tag{4.42}$$

The individual effective fields for layer 1, in vector form using the $< x, y, z >$ coordinate system in Fig. 4.16, are given by

$$\boldsymbol{B}_{zee} = \mu_0 \langle H_{dc}, h_{rf}, 0 \rangle \tag{4.43}$$

$$\boldsymbol{B}_{an,1} = \langle 0, 0, \frac{2K_{u,1}M_{z,1}}{M_{s,1}^2} \rangle \tag{4.44}$$

$$\boldsymbol{B}_{d,1} = -\mu_0 \langle 0, 0, M_{z,1} \rangle \tag{4.45}$$

$$\boldsymbol{B}_{coupling,1} = \frac{(J_1 - 2J_2)}{d_i}\left[\frac{1}{M_{s,1}M_{s,2}}\right]\langle M_{s,2}, M_{y,2}, M_{z,2} \rangle, \tag{4.46}$$

where, like before, the 1 and 2 subscripts refer to the indices of the two coupled magnetic layers. We have assumed that the sample is saturated so that $\boldsymbol{M}_i \cdot \boldsymbol{M}_j = 1$.

The total effective field to enter the LLG equation is given by

$$\boldsymbol{B}_{eff,1} = \langle \mu_0 H_{dc} + \frac{(J_1 - 2J_2)}{d_1 M_{s,1}}, \mu_0 h_{rf} + \frac{(J_1 - 2J_2)M_{y,2}}{d_1 M_{s,1} M_{s,2}}, \frac{(J_1 - 2J_2)M_{z,2}}{d_1 M_{s,1} M_{s,2}} + \left(\frac{2K_{u,1}}{M_{s,1}^2} - \mu_0\right) M_{z,1} \rangle \tag{4.47}$$

for layer 1 and

$$\boldsymbol{B}_{eff,2} = \langle \mu_0 H_{dc} + \frac{(J_1 - 2J_2)}{d_2 M_{s,2}}, \mu_0 h_{rf} + \frac{(J_1 - 2J_2)M_{y,1}}{d_2 M_{s,1} M_{s,2}}, \frac{(J_1 - 2J_2)M_{z,1}}{d_2 M_{s,1} M_{s,2}} + \left(\frac{2K_{u,2}}{M_{s,1}^2} - \mu_0\right) M_{z,2} \rangle \tag{4.48}$$

for layer 2.

The response of the magnetization of the two coupled layers to the driving field is characterized by the magnetic susceptibility. When the magnetization is being driven at a frequency far from resonance, the susceptibility will be small. When it is driven at a frequency close to resonance, the susceptibility will be large. The precessing magnetization will absorb power from the rf driving field that is proportional to the sum of the magnetic susceptibility of both layers. In our FMR setup, this is the quantity that we measure. The sum of the magnetic susceptibility of both layers in the direction of the driving field $\boldsymbol{h}_{rf}$, is defined as

$$\chi_y = \mathrm{Re}(\chi_y) + i\mathrm{Im}(\chi_y) \equiv \frac{M_{y,1} + M_{y,2}}{h_{rf}}. \tag{4.49}$$

$M_{y,1}$ and $M_{y,2}$ are determined by inputting $\boldsymbol{B}_{eff,1}$ and $\boldsymbol{B}_{eff,2}$ into the Eq. 4.38, and assuming m_y, m_z, and h_{rf} take the form $e^{i2\pi ft}$. This provides two coupled LLG equations in three dimensions, for a total of 6 coupled equations describing the x, y, z coordinates of the magnetization of layers 1 and 2. The complexity of these equations means that it is only practical to solve for this susceptibility computationally, which is how we have done it.

4.2.4 FMR Measurement and Lineshape

χ_y has both a real and imaginary part. An example simulation of the real and imaginary parts of χ_y, for two uncoupled magnetic layers, can be seen in Fig. 4.17. The two FMR resonance peaks can be seen with the lower field one being for the layer with the higher M_s, and the higher field one being for the lower M_s layer. If there is a phase shift between the absorbed power and the driving field, the measured signal can be a mixture of the two. The proportionality between χ_y, and the measured power absorption is also highly variable and depends on the FMR setup. The relative contribution to absorbed power of layer 1 and layer 2 also depends on many variables such as the penetration depth of the rf signal, and the thickness of the layers. There can also be a linear and constant background in the measured signal. Considering these effects, the actual measured FMR power absorption signal is of the form

$$\begin{split} FMR_{meas} = C_1\left[\mathrm{Re}(\chi_{y,1})\cos\phi_{\chi,1} + \mathrm{Im}(\chi_{y,1})\sin\phi_{\chi,1}\right] + \\ C_2\left[\mathrm{Re}(\chi_{y,2})\cos\phi_{\chi,2} + \mathrm{Im}(\chi_{y,2})\sin\phi_{\chi,2}\right] + \mathrm{Bg}, \end{split} \tag{4.50}$$

where C_1 and C_2 scale the signal from each layer, Bg is the linear and constant background signal, $\chi_{y,i}$ is the magnetic susceptibility relative to the rf driving field for layer i, and $\phi_{\chi,i}$ is the phase shift of the magnetic susceptibility relative to the rf driving field for layer i, which is shown in Fig. 4.18. All 4 of these variables are fitting parameters.

In some FMR measurement configurations, as will be explained in a later section, the derivative of $\chi_{y,1}$ with respect to H_{dc} is measured instead. In that case, the measured signal

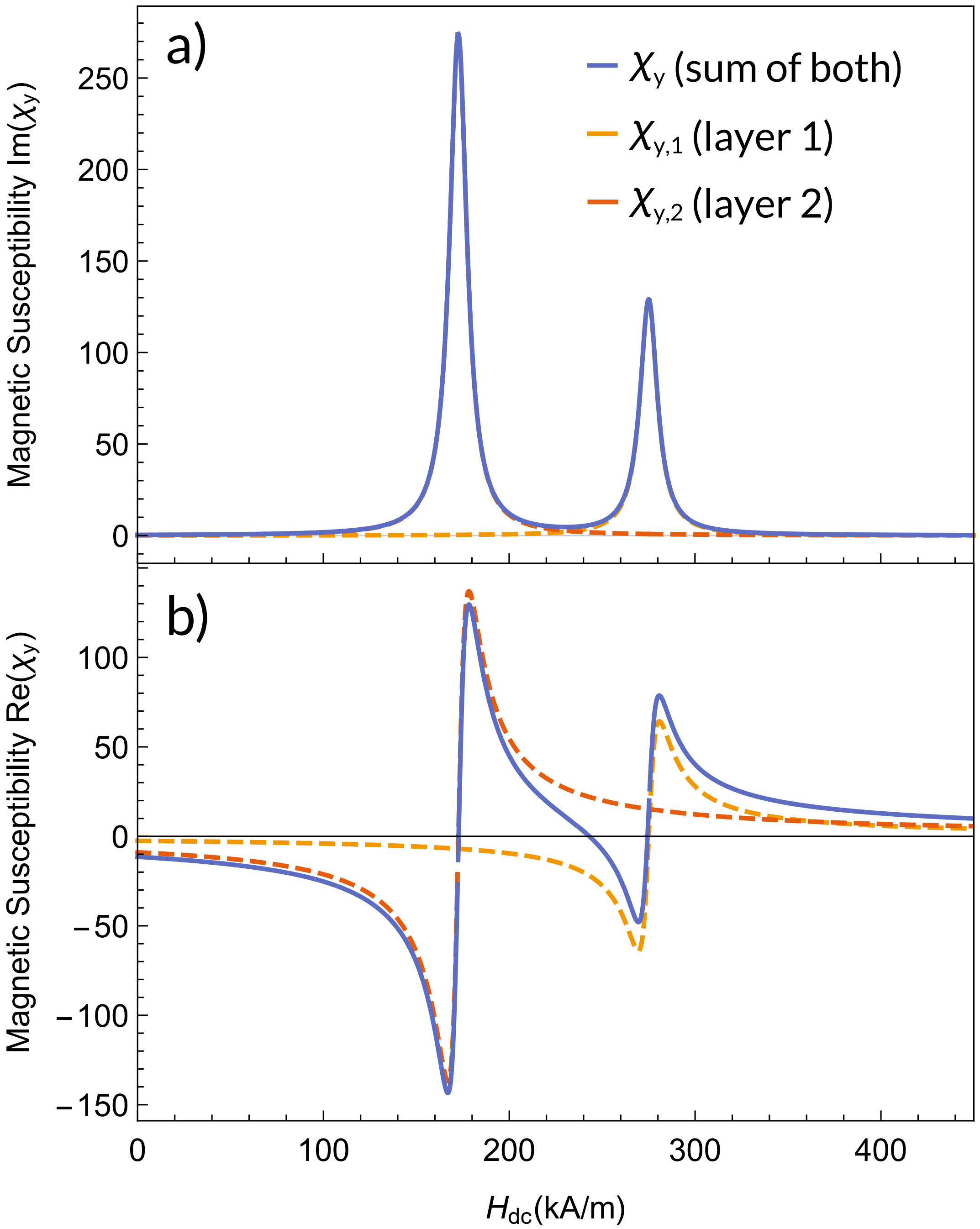

Figure 4.17: A plot of the imaginary part, a), and real part, b), of χ_y from Eq. 4.2.3 for two magnetic layers with $J_1 = 0$ mJ/m^2, $J_2 = 0$ mJ/m^2, $\alpha_1 = \alpha_2 = 0.01$, $f = 20$ GHz, $d_1 = d_2 = 2$ nm, $g_1 = g_2 = 2$, $M_{s,1} = 900$ kA/m, $M_{s,2} = 1700$ kA/m. The yellow and red dashed lines are the magnetic susceptibility of layer 1 and 2, respectively, the blue line is the sum of the two, which is the total χ_y.

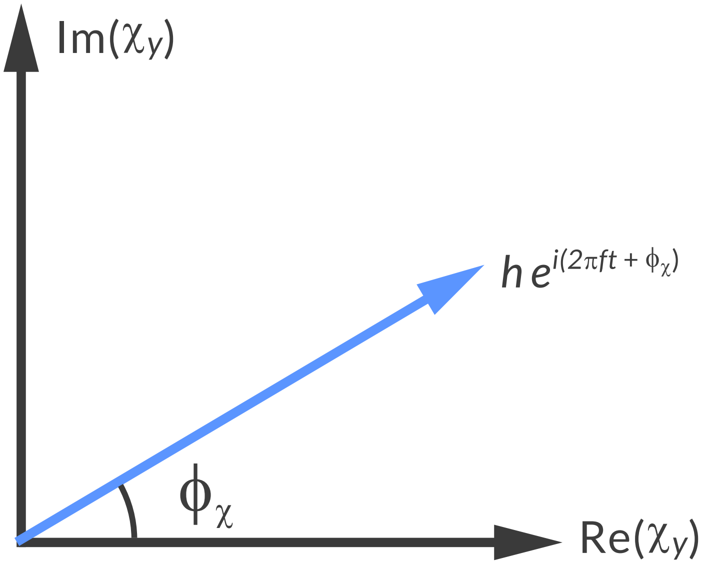

Figure 4.18: Showing the phase shift of the magnetic susceptibility χ_y relative to the rf driving field $\boldsymbol{h}e^{i2\pi ft}$ in the imaginary plane. The phase has been shifted by ϕ_χ

would correspond to

$$\begin{aligned} FMR'_{meas} = C_1\left[\mathrm{Re}(\chi'_{y,1})\cos\phi_{\chi,1} + \mathrm{Im}(\chi'_{y,1})\sin\phi_{\chi,1}\right] + \\ C_2\left[\mathrm{Re}(\chi'_{y,2})\cos\phi_{\chi,2} + \mathrm{Im}(\chi'_{y,2})\sin\phi_{\chi,2}\right] + \mathrm{Bg}, \end{aligned} \quad (4.51)$$

where $\chi'_{y,i} = \frac{\mathrm{d}\chi_{y,i}}{\mathrm{d}H_{dc}}$.

In order to extract all of the parameters from FMR measurements, we need to make several measurements at different frequencies. This is because for a single frequency, γ and k_u are not independent of one another.

After measuring FMR at several frequencies, one method to extract the parameters is to simply simultaneously fit all measurements using Eq. 4.51. However depending on the computer hardware and programming language, it can be difficult to fit the large amount of data using a very massive fitting function with many parameters. To make the computer's job easier, we first fit all of the FMR peaks with lorentzian functions to determine the resonance positions, $H_{FMR,1}$ and $H_{FMR,2}$, and then fit them with our model. That gives us all of the parameters except for damping. Then after that, we simultaneously fit all FMR measurements using the newly fitted parameters held fixed, while the computer only has to fit for damping.

It is important to note that in order to extract the anisotropy constants, the saturation magnetization of each of the magnetic layers must be known. One would typically measure this using a magnetostatic measurement technique such as SQUID or VSM, and then plug these values into the FMR fitting functions in order to extract anisotropy constants. Throughout the rest of this FMR section, we will be showing typical data, along with fits and extracted parameters that include the anisotropy constants. It should be assumed by the reader that the saturation magnetization of the magnetic layers is already known, which is what allows us to extract that information.

4.2.5 Fitting Resonance Positions

With zero damping, the real part of the susceptibility, as shown in Fig. 4.17 a), will go to infinity. Thus, we can determine FMR resonance positions H_{FMR} from our model, we set damping to zero and solving for $\frac{1}{\mathrm{Re}(\chi_y)_{\alpha=0}} = 0$. Like before, we solved this using a computer and are unable to write it down here. However, we will refer to this solution as

$$H_{FMR,1} = F\left(f, J_{total}, K_{u,1}, K_{u,2}, M_{s,1}, M_{s,2}, g_1, g_2\right), \tag{4.52}$$

for resonance position 1, and

$$H_{FMR,2} = F\left(f, J_{total}, K_{u,2}, K_{u,1}, M_{s,2}, M_{s,1}, g_2, g_1\right), \tag{4.53}$$

for resonance position 2, where $J_{total} = J_1 - 2J_2$. An example plot of these functions, fit to typical data from one of our samples, can be seen in Fig. 4.19.

In order to extract accurate resonance positions from our measurements, we have fit them with lorentzian and so-called anti-lorentzian functions of the form

$$F_{peak,i} = C_i\left[\frac{H_{dc} - H_{FMR,i}}{\Delta H_{dc,i}^2 + (H_{dc} - H_{FMR,i})^2}\sin\phi_i + \frac{\Delta H_{dc,i}}{\Delta H_{dc,i}^2 + (H_{dc} - H_{FMR,i})^2}\cos\phi_i\right], \tag{4.54}$$

where, as usual, the i is the layer index, ΔH_{dc} is the linewidth, and C_i is a scaling fitting parameter. In our previous work, we have shown that this function is a very accurate approximation of χ_y for a single magnetic layer, and the measured FMR resonance peaks, and that ΔH is proportional to damping. [78] It can be seen in Fig. 4.20 that this function is also a very good approximation for two coupled layers. However, unlike for the single magnetic layer case, for two coupled magnetic layers, the ΔH_{dc} of each resonance peak is now proportional to a combination of the damping terms of both layers in a complicated way. Because of this, we can no longer accurately extract α_1 and α_2 from ΔH_{dc}. With that said, this doesn't matter for us because we are able to extract α_1 and α_2 by fitting our data later with Eq. 4.51. The only parameter we want to extract from our fit using Eq. 4.54 is H_{FMR}.

In order to confirm that H_{FMR} from Eq. 4.54 matches H_{FMR} determined from the susceptibility for coupled magnetic layers, we can apply the same method as we had before. We need a function where, when we set damping to zero and $H_{dc} \to H_{FMR}$, it will go to

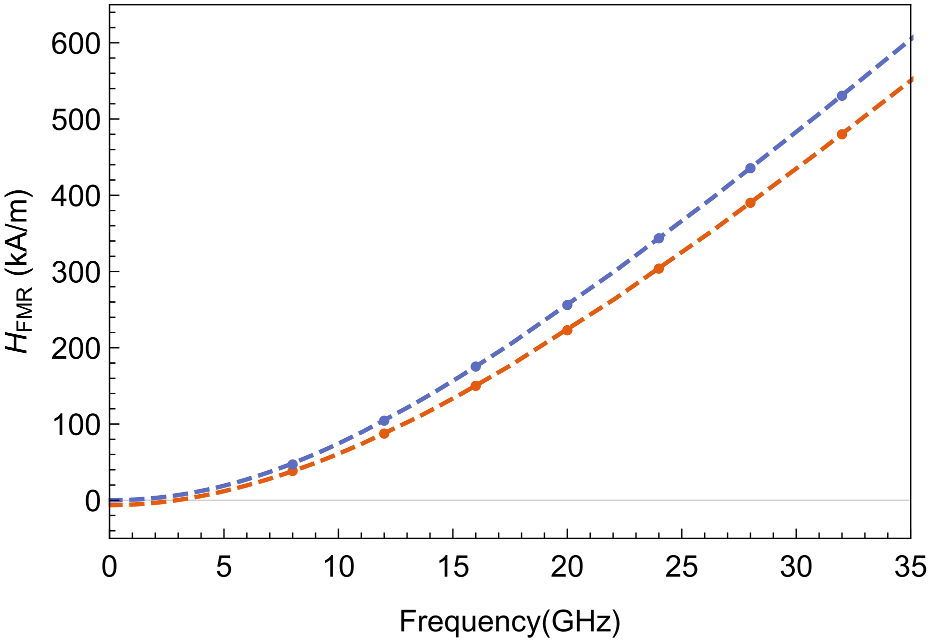

Figure 4.19: Example of typical H_{FMR} data and fit for two coupled magnetic layers with the structure MgO(2 nm)/Fe(2.3 nm)/FeCoB(1.2 nm)/Ta(4 nm)/FeCoB(1.2 nm)/ NiFe(4.5 nm)/MgO(2 nm). The blue points are for the top FeCoB/NiFe magnetic layer, and the orange points are for the bottom Fe/FeCoB magnetic layer. The dashed lines are simultaneous fits using Eqns. 4.52 and 4.53, which resulted in $J_{total} = 0.019 \pm 0.003$ mJ/m^2, $K_{u,1} = 370 \pm 20$ kJ/m^3, $K_{u,2} = -35 \pm 6$ kJ/m^3, $g_1 = 2.10 \pm 0.02$, $g_2 = 2.09 \pm 0.01$.

infinity. Since ΔH_{dc} in coupled layers is proportional to the damping in layer 1 and layer 2, if we set damping in both layers to zero, it will also to to zero. This brings the second term in Eq. 4.54 to zero. Then as $H_{dc} \rightarrow H_{FMR}$, the denominator of the first term goes to zero, making the first term go to infinity. Thus, H_{FMR} in our approximate lorentzian fit represents the same field as H_{FMR} from our model, and we can use the fit from Eq. 4.54 to accurately determine our resonance positions.

One important consideration when measuring FMR of two coupled magnetic layers, is that the M_s of each of the layers must differ from one another so that the resonance positions are at different fields. If they have the same M_s, then they would be at the same position and we would be unable to determine J_{total} from the measurements.

An example set of H_{FMR} position data for two coupled magnetic layers with the structure MgO(2 nm)/Fe(2.3 nm)/FeCoB(1.2 nm)/Ta(4 nm)/FeCoB(1.2 nm)/ NiFe(4.5 nm)/MgO(2 nm) is shown in Fig. 4.19. The peak positions were determined by fitting the raw measurement data with Eq. 4.54. The peak position vs H_{FMR} data is fit using Eqns. 4.52 and 4.53, shown as dashed lines, in order to determine $J_{total} = 0.019 \pm 0.003$ mJ/m^2, $K_{u,1} = 370 \pm 20$ kJ/m^3, $K_{u,2} = -35 \pm 6$ kJ/m^3, $g_1 = 2.10 \pm 0.02$, $g_2 = 2.09 \pm 0.01$.

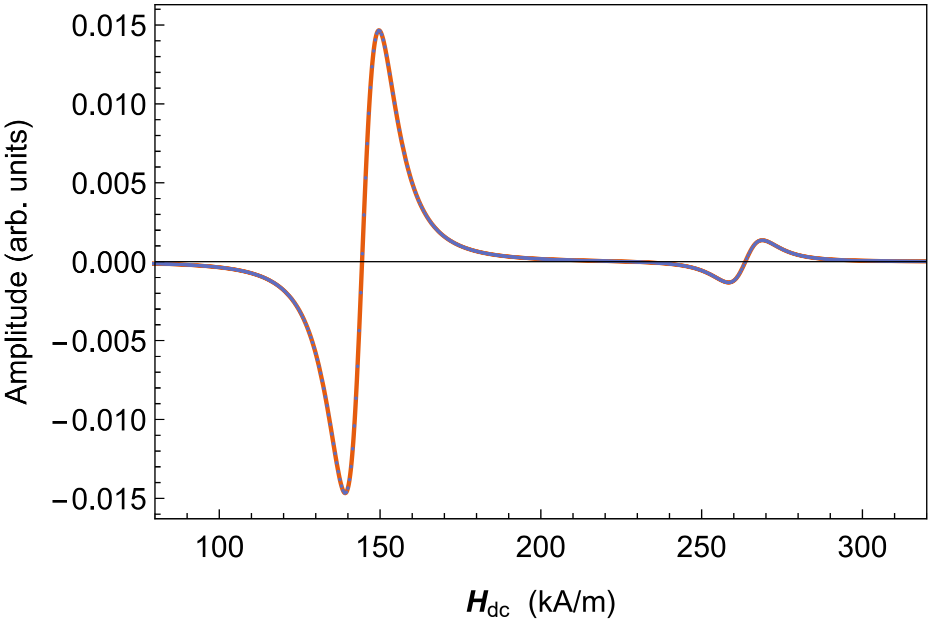

Figure 4.20: Illustration of the high accuracy of the approximate Lorentzian function fit to exact susceptibility data for two coupled magnetic layers. The blue points are Eq. 4.51 with parameters $f = 16$ GHz, $J_{total} = -0.1$ mJ/m^2, $\alpha_1 = \alpha_2 = 0.02$, $M_{s,1} = 1470$ kA/m, $M_{s,2} = 817$ kA/m, $g_1 = g_2 = 2$, $d_1 = d_2 2$ nm, $K_{u,1} = K_{u,2} = 0$, $C_1 = C_2 = 1$, $\phi_{\chi,1} = \phi_{\chi,2} = \pi/2$. The orange line is fit of $\frac{\mathrm{d}F_{peak,1}}{\mathrm{d}h_{dc}} + \frac{\mathrm{d}F_{peak,2}}{\mathrm{d}h_{dc}}$ which resulted in parameters $C_1 = 1.86$, $C_2 = 0.17$, $H_{FMR,1} = 144.39$ kA/m, $H_{FMR,2} = 263.63$ kA/m, $\Delta H_{dc,1} = 9.10$ kA/m, $\Delta H_{dc,2} = 9.1$ kA/m, $\phi_1 = \pi$, $\phi_2 = \pi$. The errors on these fitted parameters are all less than 10^{-7} indicating an extremely good fit.

4.2.6 Determination of Gilbert Damping

Gilbert damping is determined by fitting all of our raw FMR measurements, at several different frequencies, using Eq. 4.51. Since we previously fit the peak position data to obtain J_{tot}, $K_{u,1}$, $K_{u,2}$, g_1, and g_2, the only physical values left to determine are α_1 and α_2. We fit all of the measured FMR data, one at a time, to determine α_1 and α_2 for each one, then take the average. An example of all of these fits is shown in Fig. 4.21 for a sample with two coupled magnetic layers with the structure
MgO(2 nm)/Fe(2.3 nm)/FeCoB(1.2 nm)/Ta(4 nm)/FeCoB(1.2 nm)/
NiFe(4.5 nm)/MgO(2 nm). The determined Gilbert damping constants are $\alpha_1 = 0.0061 \pm 0.0003$ and $\alpha_2 = 0.0081 \pm 0.0003$ for the Fe/FeCoB layer and FeCoB/NiFe layer, respectively.

4.2.7 The Effect of Interlayer Exchange Coupling on FMR

The position of the two FMR resonance peaks, $H_{FMR,1}$ and $H_{FMR,2}$, relative to one another depends on the magnitude of the two coupling constants, $J_{total} = J_1 - 2J_2$. When the layers are completely uncoupled, these two positions correspond to the usual resonance peaks

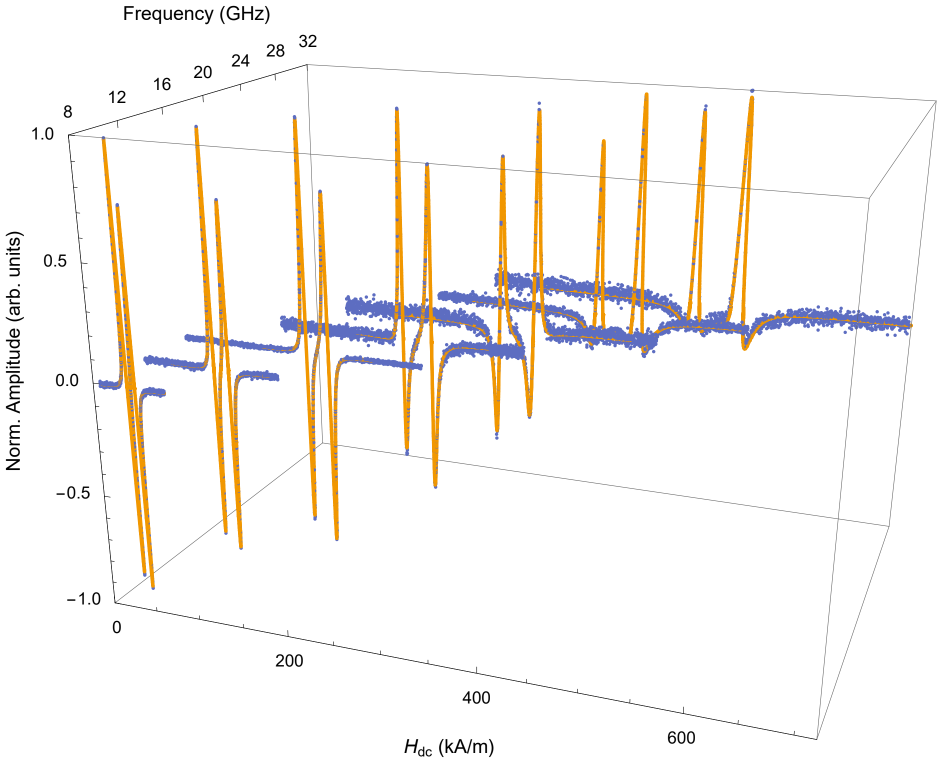

Figure 4.21: Example plot of FMR measurement data (blue points) fit with Eq. 4.51 (orange lines) in order to determine Gilbert Damping. Data is from two coupled magnetic layers with the structure MgO(2 nm)/Fe(2.3 nm)/FeCoB(1.2 nm)/Ta(4 nm)/FeCoB(1.2 nm)/NiFe(4.5 nm)/MgO(2 nm). The determined Gilbert damping constants are $\alpha_1 = 0.0061 \pm 0.0003$ and $\alpha_2 = 0.0081 \pm 0.0003$ for the Fe/FeCoB layer and FeCoB/NiFe layer, respectively.

of each of the two independent magnetic layers. However, as coupling is turned on, the precessional modes of layer 1 and and layer 2 become coupled and result in an acoustic mode in which the magnetization in the two layers precess in-phase and in an optical mode in which the magnetization precess in antiphase. [46] These two phases can also be seen in a plot of the imaginary part of the magnetic susceptibility of each of the two layers as shown in Fig. 4.22. The magnetic susceptibility of the two layers for the lower optical mode peak have opposite signs. This means that they are rotating in opposite directions relative to the driving field and relative to one another. They both have the same sign for the higher field acoustic peak and are rotating in the same direction relative to one another.

For ferromagnetic coupling, the FMR resonance peak corresponding to the acoustic mode originates from the position of the higher field peak in the uncoupled case. With increasing coupling, the acoustic peak moves to lower field, and its intensity increases. The FMR resonance peak corresponding to the optical mode originates from the position of the lower field peak in the uncoupled case. With increasing coupling, the optical peak moves

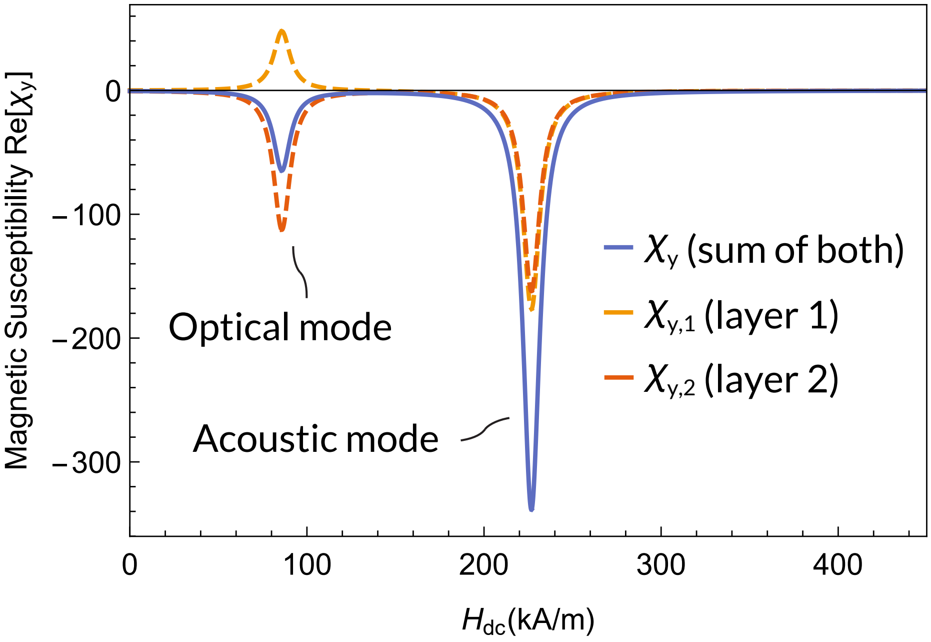

Figure 4.22: A plot of the imaginary part of χ_y from Eq. 4.2.3 for two magnetic layers with $J_1 = 0.1$ mJ/m^2, $J_2 = 0$ mJ/m^2, $\alpha_1 = \alpha_2 = 0.01$, $f = 20$ GHz, $d_1 = d_2 = 2$ nm, $g_1 = g_2 = 2$, $M_{s,1} = 900$ kA/m, $M_{s,2} = 1700$ kA/m. The yellow and red dashed lines are the magnetic susceptibility of layer 1 and 2, respectively, the blue line is the sum of the two, which is the total χ_y.

to lower field, and its intensity decreases. The reason for the change in intensity is due to the magnetic susceptibility of each layer being additive and for one of the peaks, leading to an increase in intensity, and subtracting from one another in the other peak, leading to a decrease in intensity. This is shown in Fig. 4.22

This behavior of the optical and acoustic peaks as a function of coupling strength is shown in Fig. 4.23. This figure serves as an example to demonstrate how the two peaks move with an increase in ferromagnetic coupling strength between two magnetic layers.

For ferromagnetic coupling, both the acoustic peak and optical peak move to lower fields because the coupling effective field term scales with J and has a large component in the direction of $\boldsymbol{H}_{dc}$. So the magnitude of $\boldsymbol{H}_{dc}$ required to reach H_{FMR} needed for resonance must be lower than for the uncoupled case. The acoustic peak moves towards a fixed point that lies in between the positions of the two peaks from the uncoupled case. The acoustic peak does this because it is the in-phase mode where the magnetization of the two coupled magnetic layers, become more and more parallel as J_{total} is increased.

As they become more parallel, the coupling effective field term in Eqns. 4.2.3 and 4.2.3 contributes less to the effective exchange torque in the LLG Eq. 4.38 due to the cross product in the first term which results in $\boldsymbol{M}_i \times \boldsymbol{M}_j$ approaching zero. This fixed point corresponds to the appropriate average of the magnetic properties of FM1 and FM2. [46] On the other

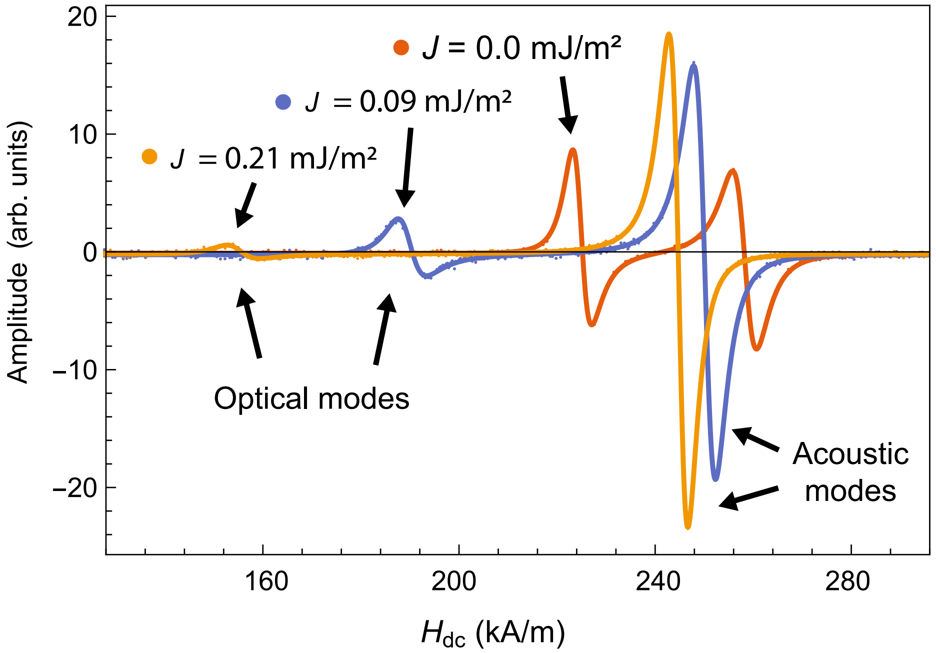

Figure 4.23: The raw FMR absorption data measured at 20 GHz and fit with Eq. 4.51 for samples with the structure MgO(2 nm)/Fe(2.3 nm)/FeCoB(1.2 nm)/Ta(d nm)/FeCoB(1.2 nm)/ /NiFe(4.5 nm)/MgO(2 nm) where $d = 4$ nm, $d = 0.425$ nm, and $d = 0.4$ nm with $J = 0$ mJ/m^2, $J = 0.09$ mJ/m^2, $J = 0.21$ mJ/m^2, respectively. As coupling strength increases, the optical peaks move to a lower field, and the acoustic peaks move toward a fixed point that lies between the two resonance peaks in the uncoupled case.

hand, the optical peak continues to move its resonance field to progressively lower and lower values with increasing J_{total}. This is because for antiphase precession, the magnetization of the two coupled layers, $\boldsymbol{M}_i$, and $\boldsymbol{M}_j$, respectively, never become parallel. So the effective exchange torque in the LLG equation never approaches zero due to $\boldsymbol{M}_i \times \boldsymbol{M}_j$ like it did in the acoustic mode case. This behavior of the acoustic and optical peaks can be seen in Fig. 4.23.

For the antiferromagnetic coupling case, it is the mirrored situation, where the acoustic mode peak decreases in intensity and moves to higher and higher fields, while the optical mode peak increases in intensity and moves to the fixed point.

4.3 Micromagnetic Magnetostatic Theory

Throughout the work in this thesis, we characterize the magnetic properties of our samples through magnetostatic measurements using methods such as SQUID or MOKE. In this section we will explain the physical model used to describe the magnetostatic measurements and allow us to extract physical quantities such as the exchange stiffness, saturation mag-

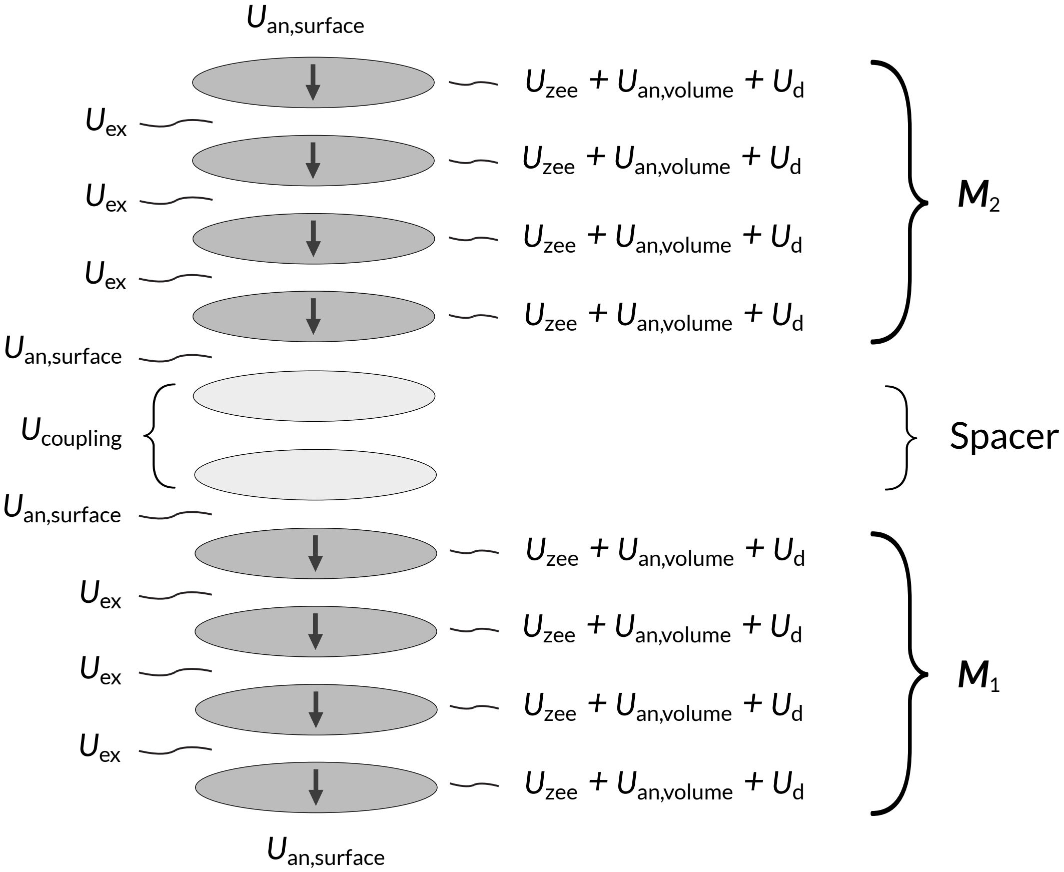

Figure 4.24: A schematic of the individual atomic layers, and their associated energies. The energies on the right side of the stack are for the individual layers. The energies on the left of the stack are the energies in between the atomic layers or on the surface of an atomic layer. The number of layers shown is simplified for illustrative purposes. The samples actually measured can have more or less layers composed of similar or different materials.

netization, and interlayer exchange coupling constants J_1 and J_2. Unlike FMR, this model allows us to extract both J_1 and J_2 individually instead of the mixed $J_{total} = J_1 - 2J_2$.

When the sample contains some AF coupled magnetic layers, we are able to extract all of the physical quantities mentioned. However, when the sample has a single magnetic layer, or multiple magnetic layers that are FC coupled, we are only able to extract the saturation magnetization.

The magnetostatic model is micromagnetic. That means that we use a computer to simulate the magnetic moment at each unpaired spin individually without any approximations, and allow them to interact with one another and the various energies explained earlier.

4.3.1 Magnetic energy

Because our samples have in-plane symmetry, we will calculate energy per unit area for every plane of atoms/magnetic moments in our sample, and then add up the energy of all of the planes to get the total energy per unit area. Like before, to distinguish these energies from the previous ones that were per unit volume, we will use E instead of U. Some of the energies are for the volume of the atomic planes such as U_{zee}, $U_{an,volume}$, and U_d, and must be multiplied by the thickness d of each atomic plane to get energy per area. These energies, per atomic plane, per unit area are given by

$$E_{zee} = -\mu_0 d \boldsymbol{M} \cdot \boldsymbol{H}_{dc}, \tag{4.55}$$

$$E_{an,volume} = -\frac{dK_c}{M_s^2} M_\perp^2, \tag{4.56}$$

$$E_d = \frac{\mu_0}{2} M_\perp^2. \tag{4.57}$$

Other energies are for interactions between planes 1 and 2, or their surfaces, and are given, per unit area by

$$E_{coupling} = -J_1 \frac{\boldsymbol{M}_1 \cdot \boldsymbol{M}_2}{M_{s,1} M_{s,2}} + J_2 \left(\frac{\boldsymbol{M}_1 \cdot \boldsymbol{M}_2}{M_{s,1} M_{s,2}} \right)^2, \tag{4.58}$$

$$E_{ex} = \frac{-2A_{ex}}{d} \cos(\varphi_{M,i} - \varphi_{m,i+1}) \tag{4.59}$$

$$E_{an,surface} = -\frac{K_i}{M_s^2} M_\perp^2. \tag{4.60}$$

These energies are shown schematically in Fig. 4.24 for each atomic plane of two magnetic layers, $\boldsymbol{M}_1$ and $\boldsymbol{M}_2$, separated by a non-magnetic spacer layer.

4.3.2 In-plane Configuration

For the work in this thesis, all micromagnetic measurements were done in-plane. This is because we are studying interlayer exchange coupling, which can be more easily determined from in-plane measurements as opposed to perpendicular measurements. In this configuration $M_\perp = 0$, which allows us to simplify the total energy because $E_{an,volume} = 0$, $E_d = 0$, and $E_{an,surface} = 0$, leaving only E_{zee}, $E_{coupling}$, and E_{ex}.

The coordinate system for this configuration is shown in Fig. 4.12 with $\theta_H = \theta_M = \pi/2$, with H_{dc} pointing along the X axis so that $\varphi_H = 0$ and the angle between $\boldsymbol{H}_{dc}$ and $\boldsymbol{M}$ is equal to φ_M. This simplified coordinate system is shown for convenience in Fig. 4.25.

Depending on the location of the atomic plane of atoms, they can have a different energy. All of the atomic planes i except for those adjacent to the spacer layer will have the following

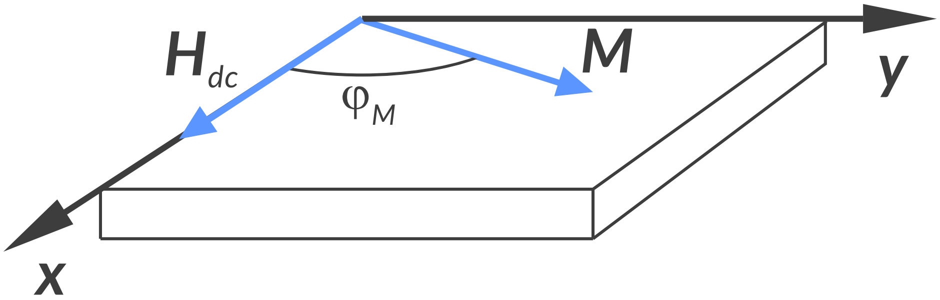

Figure 4.25: The coordinate system used in this section, where $\boldsymbol{M}$ is now the magnetization of an atomic plane.

energy, where it has been rewritten in terms of the in-plane angle of magnetization $\varphi_{M,i}$:

$$E_{plane,i} = -\mu_0 d_i M_{s,i} H_{dc} \cos\varphi_M + \frac{-2A_{ex}}{d}\cos(\varphi_{M,i} - \varphi_{m,i+1}). \tag{4.61}$$

For the atomic planes directly above and below the spacer layer, which we will denote by indices k and $k+1$, they have an additional contribution given by

$$E_{coupling} = -J_1 \cos(\varphi_{M,k} - \varphi_{M,k+1}) + J_2 \cos(\varphi_{M,k} - \varphi_{M,k+1})^2. \tag{4.62}$$

The total energy of the entire structure is found by summing up the energies of all N individual atomic planes of magnetic atoms to give us the total energy per unit area

$$\begin{aligned} E_{total} &= \sum_i^N E_{plane,i} + E_{coupling} \qquad (4.63)\\ &= \sum_i^N \Big[-\mu_0 d_i M_{s,i} H_{dc} \cos\varphi_M \Big] + \\ &\Big[\sum_i^{N/2-1} \frac{-2A_{ex}}{d} \cos(\varphi_{M,i} - \varphi_{M,i+1}) + \sum_{i=N/2}^{N-1} \frac{-2A_{ex}}{d} \cos(\varphi_{M,i} - \varphi_{M,i+1}) \Big] \\ &- J_1 \cos(\varphi_{M,k} - \varphi_{M,k+1}) + J_2 \cos(\varphi_{M,k} - \varphi_{M,k+1})^2, \end{aligned}$$

where the sum of the exchange energy term only includes planes that are exchange coupled to one another. See Fig. 4.24

4.3.3 Numerical Solution

We have used a computer program to numerically solve for $\varphi_{M,i}$ of each individual magnetic atomic plane as a function of the external magnetic field H_{dc} by minimizing the total energy in Eq. 4.63. For ease of reading, we will write down this solution as

$$\varphi_{M,i} = F(H_{dc}, A_{ex}, d_i, M_{s,i}, J_1, J_2) \tag{4.64}$$

In order to compare with magnetostatics measurements from SQUID or VSM, which measure the total magnetic moment of the sample, we need to add up the total magnetic moment of each plane in the X direction. The X direction of the magnetic moment of a single plane i is given by

$$m_{x,i}(\varphi_{M,i}) = M \cos \varphi_{M,i} = M_{s,i} d_i a \cos(\varphi_{M,i}), \tag{4.65}$$

where a is the area of the sample. The total magnetic moment of all the planes is given by the the sum over all N magnetic planes

$$m_{x,total} = \sum_{i}^{N} m_{x,i}(\varphi_{M,i}), \tag{4.66}$$

where we plug in $\varphi_{M,i}$ from Eq. 4.64.

4.3.4 Approximation for MOKE Measurements

MOKE measurements use visible light to probe the magnetization of the surface of the sample. However, the intensity of this light probe decreases as it moves through the material, which is characterized by the penetration depth. If the thickness of the magnetic layers are on the order of the penetration depth of the light, then the measurement will be significantly more sensitive to the layers closer to the surface than further from it.

This can effect the measured signal in several complicated ways. [13] However, we can approximately account for this to first order by utilizing the Beer-Lambert law, which states that the intensity and power of an electromagnetic wave inside a material falls of exponentially relative to the depth from the surface: [102]

$$I(z) = I_0 e^{-z/\delta_p}, \tag{4.67}$$

where I_0 is the intensity at the surface, and δ_p is the penetration depth. The penetration depth depends on many variables such as the wavelength of the MOKE laser, the angle that the laser hits the sample, the sample thin film materials etc... In practice, it is most practical to determine the penetration depth experimentally by measuring one sample using MOKE and another tool such as SQUID, and then fitting for the penetration depth. This penetration depth will only be approximately correct for other samples with the same thickness. So this must be determined for at least one sample for each series of samples that have the same structure.

Since MOKE utilizes an effect between the laser light and the magnetic material, its sensitivity to the magnetic planes in the sample should follow the same exponential trend. We can account for this by modifying Eq. 4.65 as follows

$$m_{x,i}(\varphi_{M,i}) = M \cos\varphi_{M,i} = M_{s,i} d_i a \cos(\varphi_{M,i}) e^{-z_i/\delta_p}, \tag{4.68}$$

where z_i is the depth of layer i from the surface of the sample. Like before, the total magnetic moment of the sample is found by plugging this equation into Eq. 4.66.

Note that other effects can occur that change the MOKE measurement for thicker films. However, we show in a later chapter that accounting for the decrease in light intensity and power as it penetrates into the sample provides a sufficiently accurate description for quick and approximate characterization of our samples. That said, any published results in this work that rely on this micromagnetics model were obtained by fitting to SQUID or VSM measurements.

4.3.5 Example Simulations

Fig. 4.26 shows several simulations of the magnetic moment vectors of each individual atomic plane of two coupled magnetic layers $\boldsymbol{M}_1$ and $\boldsymbol{M}_2$ within an external magnetic field $\boldsymbol{H}_{dc} = 300$ kA/m in the direction shown in the figure, along with the corresponding magnetization plots directly below each stack of vectors. All samples have 10 atomic planes for each magnetic layer, spacing between the planes is $d = 0.2$ nm.

The stack a) is a so-called exchange-spring with $A_{ex} = 0.04\times10^{-11}$ J/m, $J_1 = -2$ mJ/m^2, $J_2 = 0$ mJ/m^2, $M_{s,1} = 1200$ kA/m, $M_{s,2} = 1200$ kA/m. In this simulation, the exchange stiffness was reduced significantly to emphasize the bending of the moments as the distance from the spacer layer is increased. The magnetization plot of a sample with low exchange stiffness is very rounded and doesn't saturate until very high fields.

The stack b) shows the direction of the magnetic moments of each plane when the two magnetic layers are biquadratically coupled with $A_{ex} = 1.5 \times 10^{-11}$ J/m, $J_1 = 0$ mJ/m^2, $J_2 = 1$ mJ/m^2, $M_{s,1} = 1200$ kA/m, $M_{s,2} = 1200$ kA/m. With biquadratic coupling, the magnetic layers are at equilibrium 90° to one another. As the magnitude of $\boldsymbol{H}_{dc}$ is increased from zero, they immediately snap to ±45° away from the direction of $\boldsymbol{H}_{dc}$. As the magnitude of $\boldsymbol{H}_{dc}$ is increased further, they slowly rotate to become aligned with it. The magnetization plot for biquadratically coupled magnetic layers starts from 0 field with a non-zero magnetic moment. Like the magnetization plot for a), it is slightly rounded, but unlike a), it has a sharp peak where magnetization becomes saturated.

The stack c) shows the direction of the magnetic moments of each plane when the two magnetic layers are bilinearly coupled with $A_{ex} = 1.5 \times 10^{-11}$ J/m, $J_1 = -2$ mJ/m^2, $J_2 = 0$ mJ/m^2, $M_{s,1} = 1200$ kA/m, $M_{s,2} = 1200$ kA/m. As the magnitude of $\boldsymbol{H}_{dc}$ is increased from zero, since the two magnetic layers have the same M_s, they immediately

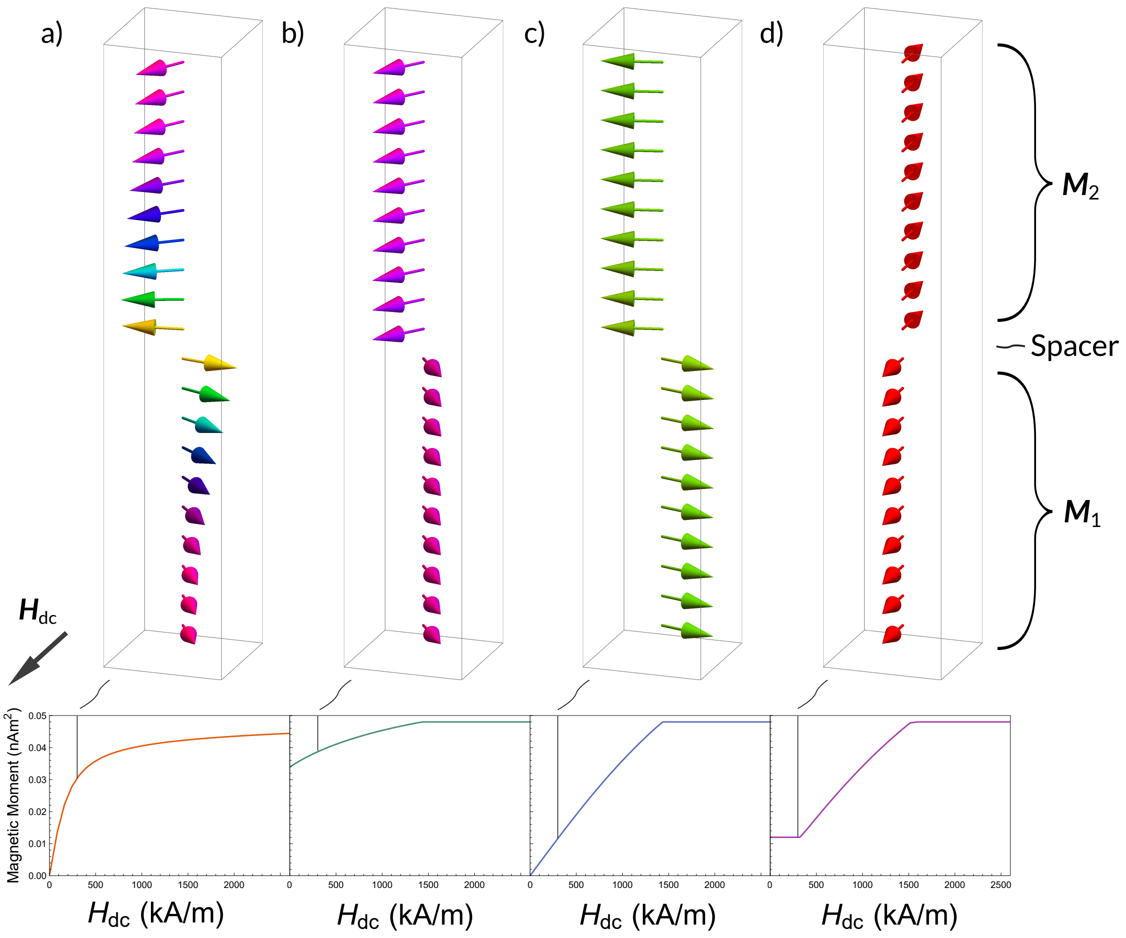

Figure 4.26: Simulations of the magnetic moment vectors of each individual atomic plane of two coupled magnetic layers within an external magnetic field $\boldsymbol{H}_{dc} = 300$ kA/m in the direction shown (top), along with the corresponding magnetization plots directly below each stack of vectors. a) has $A_{ex} = 0.04 \times 10^{-11}$ J/m, $J_1 = -2$ mJ/m^2, $J_2 = 0$ mJ/m^2, $M_{s,1} = 1200$ kA/m, $M_{s,2} = 1200$ kA/m, b) has $A_{ex} = 1.5 \times 10^{-11}$ J/m, $J_1 = 0$ mJ/m^2, $J_2 = 1$ mJ/m^2, $M_{s,1} = 1200$ kA/m, $M_{s,2} = 1200$ kA/m, c) has $A_{ex} = 1.5 \times 10^{-11}$ J/m, $J_1 = -2$ mJ/m^2, $J_2 = 0$ mJ/m^2, $M_{s,1} = 1200$ kA/m, $M_{s,2} = 1200$ kA/m, d) has $A_{ex} = 1.5 \times 10^{-11}$ J/m, $J_1 = -2$ mJ/m^2, $J_2 = 0$ mJ/m^2, $M_{s,1} = 1500$ kA/m, $M_{s,2} = 900$ kA/m. All samples have 10 atomic planes for each magnetic layer, spacing between the planes is $d = 0.2$ nm. The separation between $\boldsymbol{M}_1$ and $\boldsymbol{M}_2$ due to the spacer layer is not shown.

snap to ±90° away from the direction of $\boldsymbol{H}_{dc}$. Then as the magnitude of $\boldsymbol{H}_{dc}$ is increased further, they slowly rotate and become parallel with $\boldsymbol{H}_{dc}$. The magnetization plot for this kind of coupling is almost linear. It is only curved slightly due to the finite A_{ex}.

The stack d) shows the direction of the magnetic moments of each plane when the two magnetic layers are bilinearly coupled with $A_{ex} = 1.5 \times 10^{-11}$ J/m, $J_1 = -2$ mJ/m^2, $J_2 = 0$ mJ/m^2, $M_{s,1} = 1500$ kA/m, $M_{s,2} = 900$ kA/m. The only difference between this configuration and c), is that the M_s of the two layers are different, but the total M_s of the entire sample remains the same. This change gives it significantly different behavior when H_{dc} is ramped up.

As the magnitude of $\boldsymbol{H}_{dc}$ is increased from zero, the magnetic layer with the higher M_s, in this case it is the bottom $\boldsymbol{M}_1$ layer, immediately snaps around to be parallel with $\boldsymbol{H}_{dc}$. At the same time, the lower M_s $\boldsymbol{M}_2$ will snap to pointing antiparallel to $\boldsymbol{H}_{dc}$. Then as the magnitude of $\boldsymbol{H}_{dc}$ is increased further, the directions of $\boldsymbol{M}_1$ and $\boldsymbol{M}_2$ do not change until a critical field. Because of this, the magnetization curve has a flat spot until a critical field at which point the magnetic moment starts to increase in a way similar to c). This flat spot in the magnetization curve is a clear indicator of bilinear coupled magnetic layers with differing M_s, or the same but with differing thickness.

Simulations Including Penetration Depth for MOKE Measurements

If the thickness and M_s of the two coupled layers are the same, then the penetration depth will have no effect on the measurement because the component of magnetization parallel with $\boldsymbol{H}_{dc}$ is the same for both the top and bottom layers. This can be seen in Fig. 4.26 c) where as soon as the magnitude of $\boldsymbol{h}_{dc}$ is increased from zero, the magnetic moments of both layers jump to equal angles from $\boldsymbol{H}_{dc}$.

The penetration depth effects the measurement when the M_s or thickness of the top and bottom layers differ. There are two cases, when the top layer has a larger magnetic moment than the bottom layer, or when the bottom layer has a larger magnetic moment than the top layer.

Fig. 4.27 shows a simulation of the magnetization plot when the layer closer to the surface has a smaller magnetic moment then the one further down. The larger magnetic moment of the bottom layer will cause it to follow $\boldsymbol{H}_{dc}$ for small magnitudes. Since it is AF coupled to the top layer, it causes it to point in the opposite direction. The measurement is more sensitive to the surface layer, which causes the measured magnetic moment to have the opposite sign of $\boldsymbol{H}_{dc}$ for small fields.

Fig. 4.28 shows a simulation of the magnetization plot when the layer closer to the surface has a larger magnetic moment then the one further down. We see the opposite effect from before where the measured magnetic moment for small fields is larger than before.

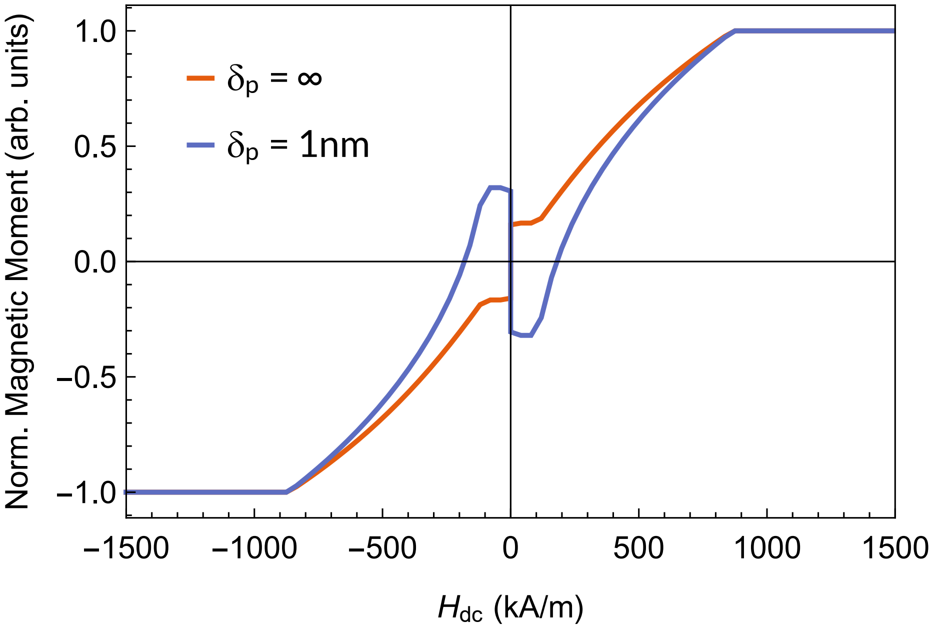

Figure 4.27: Micromagnetics simulations showing the effect of the finite penetration depth in MOKE measurements of two coupled magnetic layers when the bottom layer, further away from the surface, has a larger magnetic moment than the top layer closer to the surface. The orange line is the normal magnetization plot without the effect of the penetration depth, the blue line is the same sample measured with a penetration dept of 1 nm. The two magnetic layers are both 2 nm thick, the M_s of the bottom and top layers are 1400 kA/m and 1100 kA/m, respectively. $J_1 = -2$ mJ/mm, $J_2 = 0$ mJ/mm, and $A_{ex} = 1.5\times10^{-11}$ J/m.

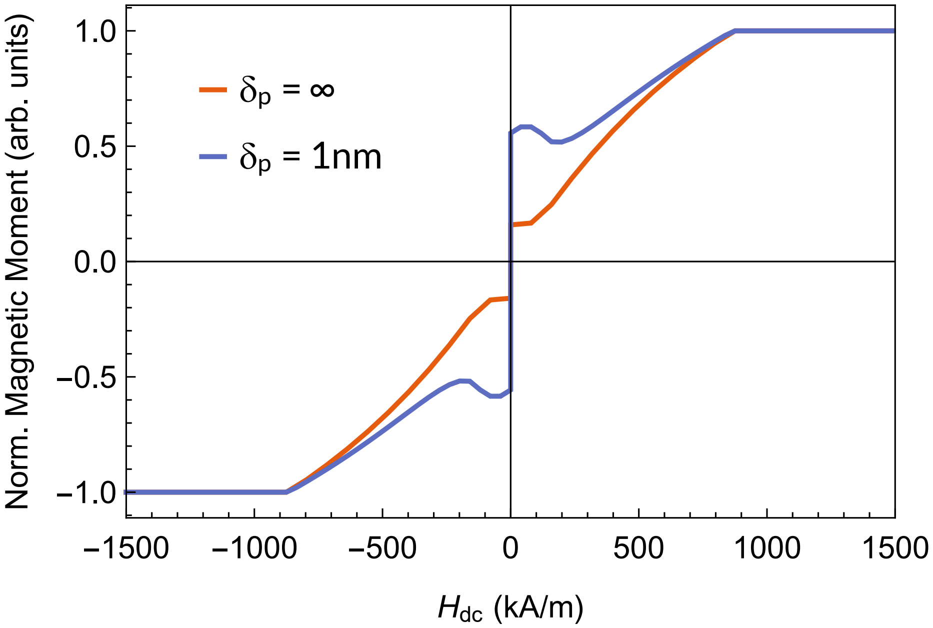

Figure 4.28: Micromagnetics simulations showing the effect of the finite penetration depth in MOKE measurements of two coupled magnetic layers when the bottom layer further away from the surface has a smaller magnetic moment than the top layer closer to the surface. The orange line is the normal magnetization plot without the effect of the penetration depth, the blue line is the same sample measured with a penetration dept of 1 nm. The two magnetic layers are both 2 nm thick, the M_s of the bottom and top layers are 1100 kA/m and 1400 kA/m, respectively.

Chapter 5

Broadband Ferromagnetic Resonance Spectrometer

The first goal of the work in this thesis is to characterize interlayer exchange coupling of two FeCoB layers coupled across various non-magnetic spacer layers both before and after being annealed. It is known that AFC coupled FeCoB layers across a non-magnetic spacer layer become FC coupled after annealing above 200 °C for thinner spacer layers. Thus, we require an experimental technique that is capable of measuring both AFC and FC coupling in order to fully characterize coupling within our samples. The FMR spectrometer that will be developed and tested in this chapter will be capable of this, and is an essential part of this work.

This chapter will explain the details of the FMR spectrometer designed during the work throughout this thesis. The newly designed spectrometer improves on existing narrowband design by using a broadband rf signal generator, a coaxial transmission line to bring the rf signal to the sample, and a coplanar waveguide to transmit the signal to the sample. This allows one to perform FMR measurements for a wide range of frequencies up to approximately 40 GHz with a single setup. The rf signal generator also allows us to improve on the traditional design by having the option to use pulse modulation rather than field modulation, which will be explained in this chapter. We will show that our new design is sensitive enough to detect FMR signals from ultrathin films.

FMR spectroscopy is generally carried out by sweeping the external dc magnetic field, $\boldsymbol{H}_{dc}$ while applying a perpendicular rf magnetic field $\boldsymbol{h}_{rf}$ at a fixed frequency and power. The configuration and geometry of these two magnetic fields are described in Section 4.2.3. In this thesis, all FMR measurements will be done in the parallel configuration as described in Section 4.2.3. When the resonance condition is satisfied, some power from the rf signal will be absorbed by the sample. As the external dc field sweeps through the resonance condition, the transmitted rf power, or its derivative, can be plotted as a function of external magnetic field in order to obtain an absorption line. This measured data will be proportional to the magnetic susceptibility, or its derivative, of the magnetic layers within the sample,

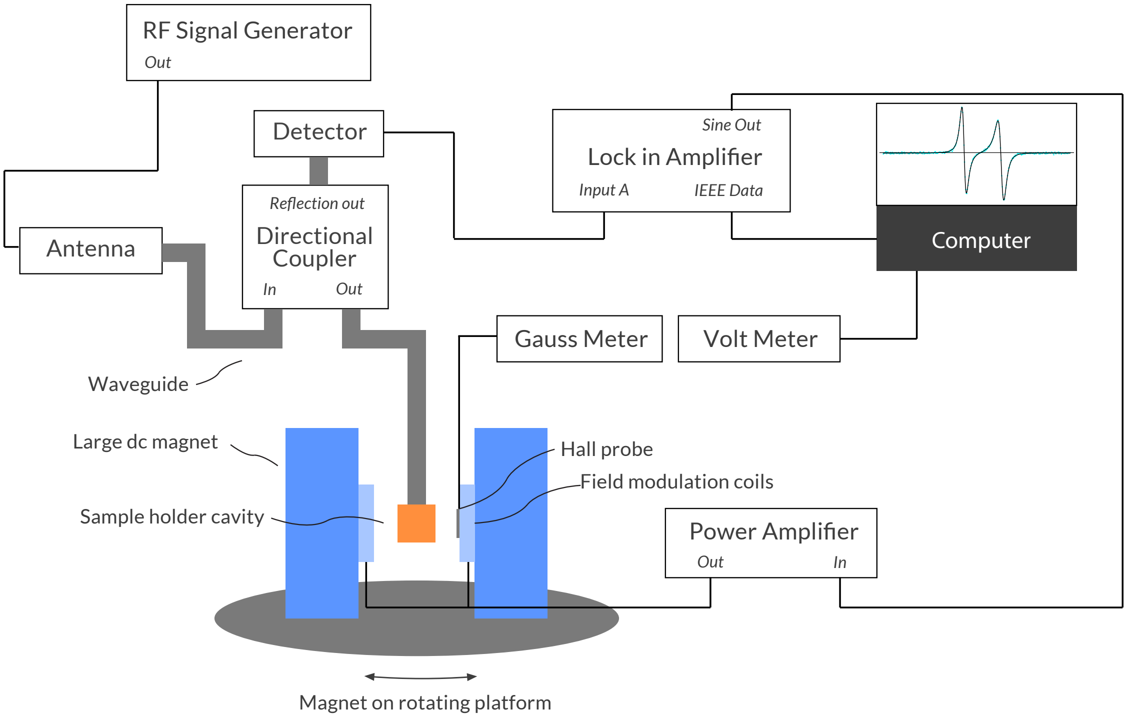

Figure 5.1: Schematic of the initial FMR design using fixed frequency RF generators, EM waveguides, and sample cavity. The thick grey bars are EM waveguides while the thin black lines are electrical cables.

which is described by Eqns. 4.50 and 4.51. The data can be fitted with these equations in order to determine intrinsic properties of the magnetic layers such as the g-factor, magnetic anisotropy, and Gilbert damping, and the interlayer exchange coupling between magnetic layers separated by a spacer layer.

5.1 Traditional FMR Spectrometer Design

A typical traditional FMR spectrometer uses rf signal generators that operate at only fixed frequencies. Usually they will have several different rf generators at different frequencies, along with waveguides capable of propagating only a small window of frequencies. As such, the operator will have to switch out the rf generator and waveguides several times to measure FMR at multiple frequencies for a single sample. This is quite tedious and time consuming when measuring anything more than a couple samples.

The FMR spectrometer that was set up at our lab before the work in this thesis is shown in Fig. 5.1. It had 5 microwave sources that would operate at 9, 14, 24, 36 and 72 GHz. The 9, 14, and 72 GHz sources were reflex klystrons, while the 24 and 36 GHz sources were Gunn diodes. The generated rf signal was carried to a resonating cavity using electromagnetic

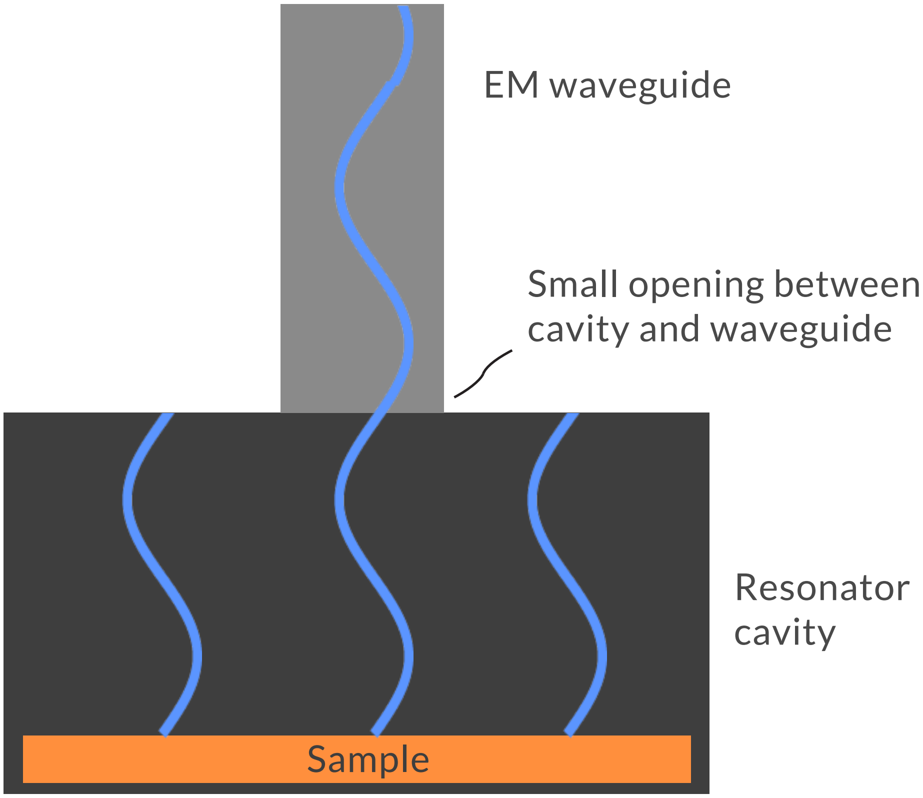

Figure 5.2: Closeup of sample holder and resonator cavity that attaches to the EM waveguide for the initial FMR design. This is located directly between the large dc magnet in Fig. 5.1.

(EM) waveguides. The sample sat inside the resonating cavity where it interacted with the rf magnetic field and absorbed some of the power. A schematic of the sample holder cavity is shown in Fig. 5.2. The mode of the waveguide is chosen such that the oscillating magnetic field component of the wave is perpendicular with the external magnetic field created by the large dc magnet.

A portion of the rf wave is reflected from the sample and cavity and travels back up the waveguide to a directional coupler. The power of this reflected wave will change slightly depending on how much was absorbed by the sample by the precessing magnetization. This reflected rf power is then measured using a detector diode.

A lock in amplifier is used to increase the signal-to-noise ratio (SNR). A lock-in requires a periodic signal, which is created by modulating $\boldsymbol{H}_{dc}$ using the smaller field modulation coils shown in Fig. 5.1. The magnitude of field modulation is orders of magnitude less than the magnitude of $\boldsymbol{H}_{dc}$. The frequency of modulation is also limited by the inductance of the magnet coils, and the maximum output voltage of the power supply. This is because of the current-voltage relation of an inductor: $V = -L\frac{\mathrm{d}I}{\mathrm{d}t}$, where V is the voltage, L is the inductance, and I is the current. With this limitation, the field modulation is set to a prime

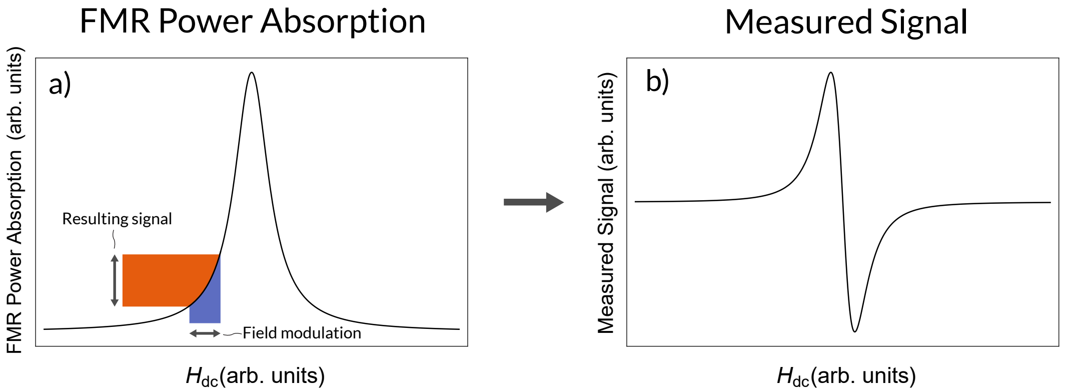

Figure 5.3: This is a plot showing how field modulation results in a measurable signal that is the derivative of the original signal. a) is the simulated FMR power absorption of a precessing magnetic moment, and b) is the measured signal after field modulation is applied. The resulting signal is the derivative of the absorption. The magnitude of modulation has been exaggerated for clarity. In reality, it is much less.

number near 100 Hz so that it is unlikely to interfere with external oscillations. The lock-in detector then locks into the signal created by modulating this field. Instead of measuring absorbed rf power by the sample, modulating $\boldsymbol{H}_{dc}$ results in measuring its derivitive with respect to $\boldsymbol{H}_{dc}$, as shown in Fig. 5.3, and is also described by Eq. 4.51.

The large dc magnet is mounted on top of a rotating platform to allow for measuring FMR with $\boldsymbol{H}_{dc}$ pointing in different in-plane directions. This is not useful for samples used in this thesis, but has been used extensively in the past for characterizing in-plane magnetic anisotropy in single-crystal samples.

The magnetic field strength is measured using a Hall probe positioned in the center of the magnetic field, right next to the sample. Since the magnetic field is being modulated, this signal is averaged over multiple cycles of modulation. The Hall probe reading is calibrated using nuclear magnetic resonance (NMR) of protons in H_2O.

The measurement is made by sweeping $\boldsymbol{H}_{dc}$ through a range of fields while the generated rf frequency is fixed, and measuring the locked in signal from the detector.

The desired magnetic field set during a field sweep measurement is controlled by the computer. This is also calibrated to ensure that the magnet actually goes to the field strength set by the computer.

5.2 Broadband FMR Spectrometer Design

A schematic of the new broadband FMR spectrometer, set up during the work in this thesis, is shown in Fig. 5.4. Much of the setup is the same as the previous design. The differences are in the rf signal generation, rf signal transmission, rf signal-to-sample coupling, rf signal

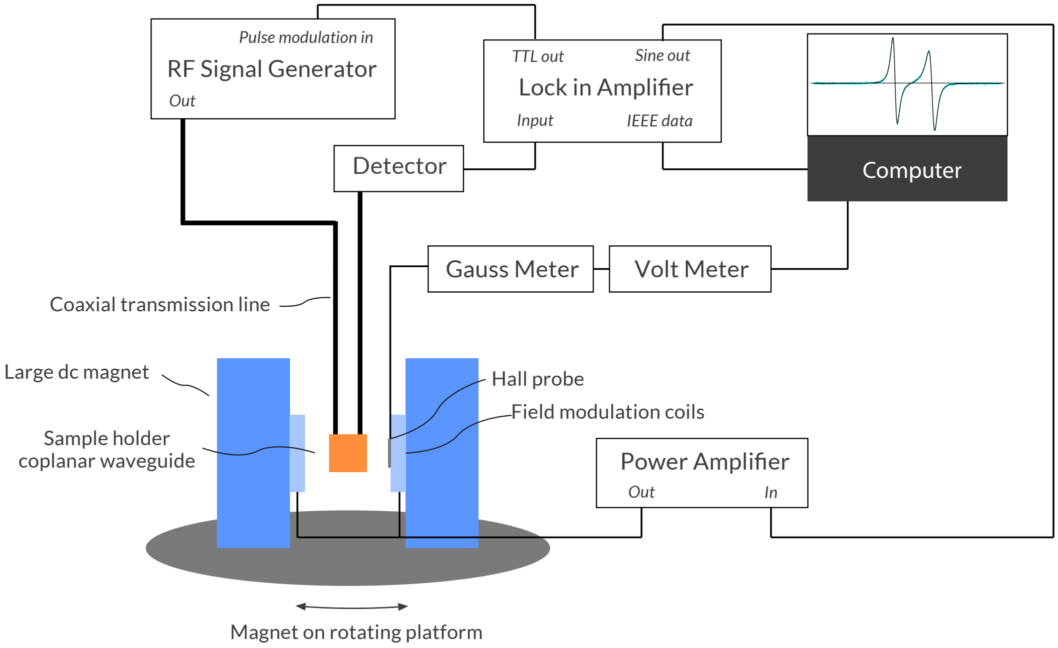

Figure 5.4: Schematic of the the newly designed broadband FMR spectrometer. The thicker black lines are coaxial cables/transmission lines while the thin black lines are signal/data cables.

detection, and measurement modulation. For additional examples of FMR data obtained using this new setup, for single crystal samples, see Ref. [78].

The rf signal is now generated using a broadband signal generator. This signal generator uses internal feedback in order to keep the output power constant for frequencies from 0 to 50 GHz. It also has the ability to modulate the output with frequency modulation, amplitude modulation, and pulse modulation. Next, the signal travels through a coaxial cable down to the sample, as opposed to the EM waveguide used before. Next, the signal passes through a coplanar transmission line on which the sample is held as shown in Fig. 5.5.

The rf electrical signal travels through the center conductor in the coplanar transmission line, while the outer conductors are grounded. The sample sits directly on top of the transmission line with the thin film facing down. This is a so called "flip-chip" configuration. The high conductivity of the transmission line, and thin oxide layer on top stops the electrical signal from travelling through the sample. This creates an rf magnetic field, $\boldsymbol{h}_{rf}$, that is approximately parallel with the surface of the sample. $\boldsymbol{h}_{rf}$ near the edge of the sample will deviate slightly from being in the plane of the sample, but it is still perpendicular to $\boldsymbol{H}_{dc}$, and so it will drive precession just as effectively.

After the rf signal passes through the coplanar transmission line, it transmits through another coaxial transmission line and into a diode detector. Just like before, the diode

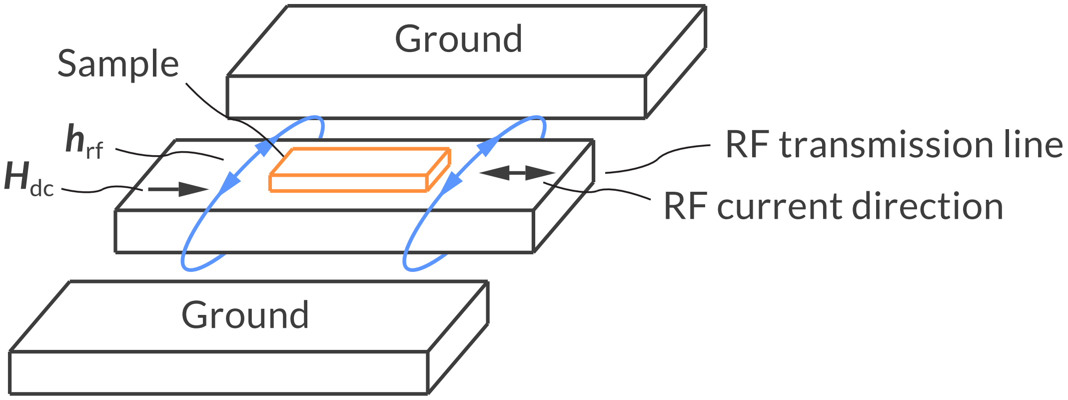

Figure 5.5: Schematic of the coplanar transmission line that couples the magnetic part of the generated rf signal, $\boldsymbol{h}_{rf}$ (blue arrows), with the sample. The sample sits directly on top of the portion of the line carrying the rf electrical signal such that $\boldsymbol{h}_{rf} \perp \boldsymbol{H}_{dc}$ and that they are both in the plane of the sample.

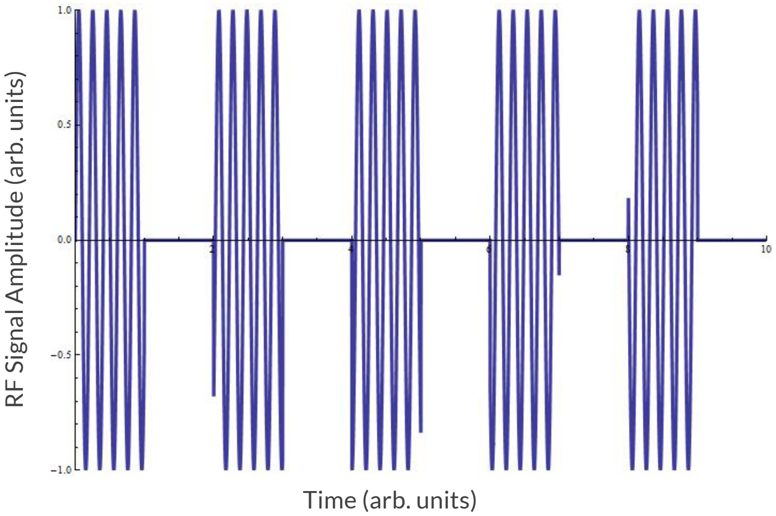

Figure 5.6: A simulation of the pulse-modulated rf signal at the output of the signal generator. The relative signal frequency to pulse frequency ratio is not to scale.

detector is connected to a lock-in amplifier to measure the modulated signal. Instead of measuring the reflected rf signal, we are now measuring the transmitted rf power. This transmitted power will still depend on the amount that is absorbed by the sample which lets us measure absorbed power.

The broadband rf signal generator used, has a pulse modulating feature which allows the rf output to be amplitude modulated by up to 100 MHz. As mentioned earlier, the field modulation normally used in our FMR measurement is limited to around 100 Hz. This presents a potentially huge improvement of signal to noise since the lock-in amplifier will be able to integrate over orders of magnitude more periods of the signal than before. The lock-in amplifier is limited to 100 kHz, which is much less than the rf generator can output, but is still 3 orders of magnitude faster than with the field modulation method. As such, we have used this feature and added the option to use pulse modulation in our spectrometer design. Note, with this spectrometer design, it has both field modulation and pulse modulation, but only one can be used at a time. An example simulation of a pulse modulated signal is shown in Fig. 5.6. Since this method modulates the amplitude of the rf signal, the resulting measurement is no longer the derivative, and is now the true absorbed power. Thus, for measurements using pulse modulation, they are modeled by Eq. 4.50.

5.3 Spectrometer Performance

The broadband spectrometer offers the ability to measure FMR at many different frequencies without making any changes to the setup. However, the use of a single conductor/waveguide for the entire range of frequencies means that it will naturally transmit some frequencies better than others. To investigate how well the system transmits the range of frequencies, we set the rf generator to a fixed output power, and had it scan from 0 to 50 GHz. We measured the transmitted power during this scan, and the result can be seen in Fig. 5.7.

The transmitted power drops dramatically as the rf frequency is increased. This problem is made even worse if the outer conductors of the coplanar transmission line were not soldered to the coaxial cable ground shield as shown in the figure. The effect of this drop in transmitted power means that we are only able to effectively measure up to approximately 40 GHz. However, this range is sufficient to characterize all of the samples created throughout this thesis.

5.4 Linewidth and Damping Measurements

One problem with modulating the field for the lock-in to measure, is that if it is modulated with an amplitude that is too large, it will begin to alter the measured linewidth and half width at half max (HWHM) of the FMR resonance peak as compared to the true value. For small amplitudes of modulation, it has approximately no effect on the linewidth, and can be used to accurately measure the HWHM, and subsequently, the damping of the magnetic layers. However, at high modulating amplitudes, the modulation increases the measured HWHM. This is shown in Fig. 5.8 for a peak that has a true HWHM of approximately 4.4 kA/m.

Because of this, when using the field modulation configuration we must be sure to keep modulation below the threshold where it begins to increase the HWHM of the FMR resonance peak. This limits the amplitude at which we can modulate, which limits the amplitude of the signal that the lock-in detects.

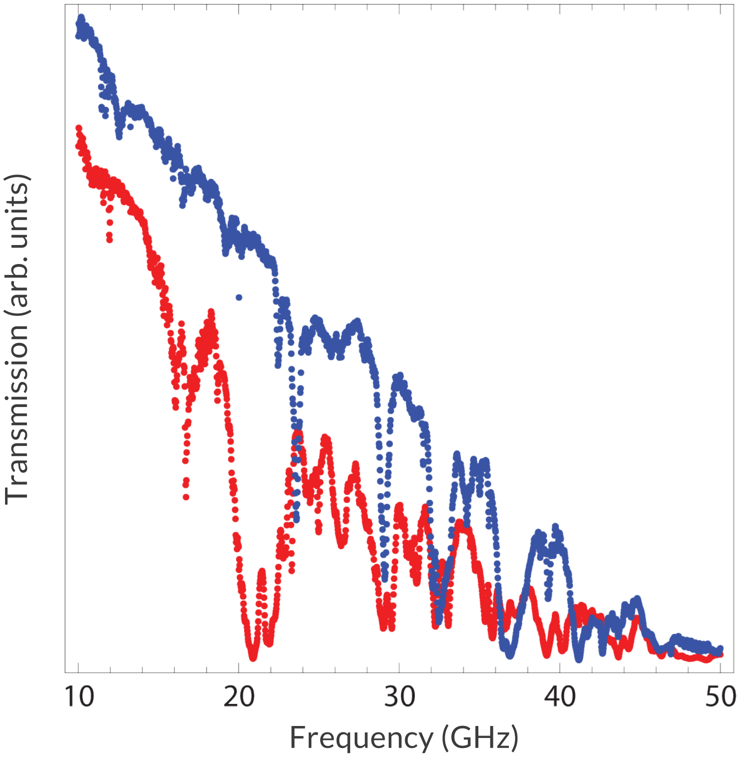

Figure 5.7: Transmitted power of the rf signal, from the rf generator and passing through the system, as a function of frequency both with (blue) and without (red) the side conductors of the co-planar waveguide connected to ground.

One advantage of the pulse modulation configuration is that the modulation has no effect on the measured linewidth. This allows us to increase the amplitude of modulation to the maximum amount the rf signal generator can output, which increases the SNR further.

5.5 Comparison of FMR Measurements

To compare measurements made with the new design versus the original design, we will measure samples grown by Montoya *et.al.* [78] using molecular beam epitaxy (MBE) with the structure GaAs(100)/Fe(4 nm)/Au(4 nm). These samples were created before the new FMR design was implemented.

The FMR measurement of this sample using the original and new design with both field modulation and pulse modulation is shown in Fig. 5.9.

Comparing the measurement from a) the original design to b) the field modulated measurement using the new design we notice several differences. First, there is significantly more noise with the new design, and this is even after collecting data for approximately 3x as long (240 s vs 704 s). The cause of this noise is the significant reduction of transmission of the rf

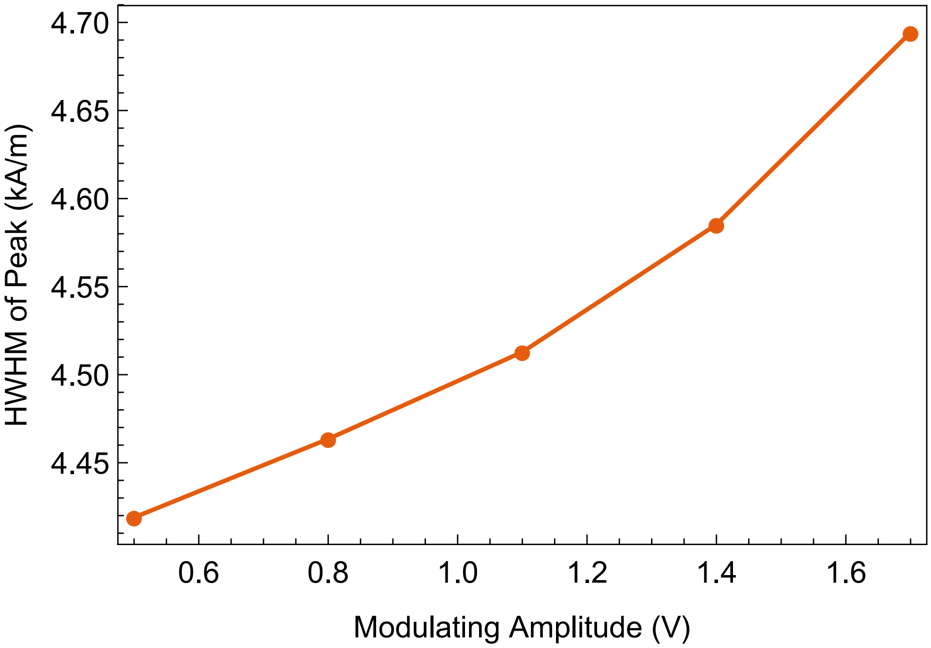

Figure 5.8: Dependency of the HWHM of FMR resonance peaks on the amplitude of modulation when in field modulation configuration. This dependence occurs in both the new spectrometer design and the old design. This particular peak had a true HWHM of approximately 4.4 kA/m. The connecting lines are added as a guide to the eye.

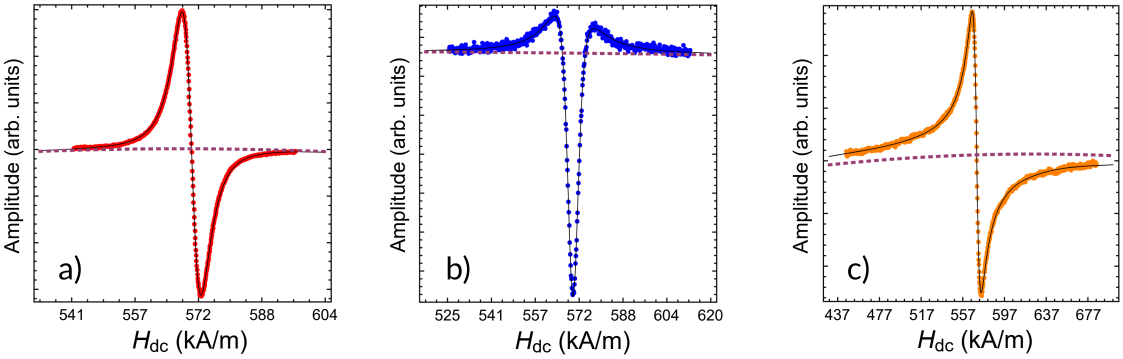

Figure 5.9: In-plane FMR measurements of GaAs(100)/Fe(4 nm)/Au(4 nm) samples at f = 35.6802 GHz using a) the initial FMR design, b) the new broadband design using field modulation, and c) the new broadband design using pulse modulation. The points are measurement data, the dashed line is the background, and the black line is fit using the derivative of Eq. 4.54 with respect to H_{dc} for a) and b), and Eq. 4.54 for c). The parameters obtained from the three fits are a) $H_{FMR} = 571.3 \pm 0.5$ kA/m, $\Delta H_{dc} = 4.11 \pm 0.08$ kA/m, $\phi = 2.8°$, with a collection time t = 240 s, b) H_{FMR} = 570.6 ± 0.5 kA/m, ΔH_{dc} = 4.15 ± 0.08 kA/m, ϕ = 83.7°, t = 704 s, and c) H_{FMR} = 570.2 ± 0.5 kA/m, $\Delta H_{dc} = 4.21 \pm 0.08$ kA/m, $\phi = 88.7°$, $t = 335$ s.

signal through the transmission lines and waveguides at the frequency of 35.6802 GHz, as was shown in Fig. 5.7. The decreased transmission of the signal reduces the SNR, resulting in less signal and more noise as we see in b). Another thing to notice is the absorption line has a significantly different shape. This is due to a phase shift that is occurring between h_{rf} and the magnetic susceptibility of the magnetic layer, as shown in Fig. 4.18. This phase shift is expected between the two designs because h_{rf} is being coupled to the sample in very different ways in each case. In a) the sample is sitting at the bottom of an EM resonating cavity, and in b) the sample is sitting on top of a coplanar waveguide.

The measurement from a) the original design is compared with c) the pulse modulated measurement using the new design. Unlike with b), we now see much less noise, and this measurement only collected data for approximately half of the time that b) did (335 s vs 704 s). This dramatic increase of the SNR is because we are now gaining all the advantages of using pulse modulation. Namely, a much higher modulation rate of 100 kHz vs 104 Hz for field modulation, and modulating the full range of output power from the rf generator as compared to field modulation where we could only modulate using approximately 25% of the output range of the power supply driving the modulating coils, which is limited because of line broadening. Another thing to notice is that the width of the FMR absorption line is much wider in c) with a measurement range from approximately 400 to 700 kA/m as compared to 540 to 600 kA/m for a). This is because now that we are modulating the amplitude of the rf signal instead of the field, we are now measuring the susceptibility directly instead of its derivative with respect to H_{dc}. Taking a derivative of Eq. 4.54 reduces the width of the perceived absorption line. However, the ΔH_{dc} parameter extracted from the fit should be the same in both cases, which is what we see, with $\Delta H_{dc} = 4.11 \pm 0.08$ kA/m for a) and $\Delta H_{dc} = 4.21 \pm 0.08$ kA/m for c), which are within measurement error of one another.

5.5.1 Comparison of Gilbert Damping

For FMR of a single magnetic layer, it can be shown that the damping α is related to the linewidth by the relation [75, 77]

$$\Delta H_{dc}(\omega) = \alpha\frac{\omega}{\gamma} + \Delta H_{dc}(0), \tag{5.1}$$

where $\Delta H_{dc}(0)$ is the zero frequency offset. Thus, by fitting $\Delta H_{dc}(\omega)$ vs ω measurements, we can extract the Gilbert damping parameter α for the GaAs(100)/Fe(4 nm)/Au(4 nm) samples.

Fig. 5.10 shows a plot of linewidths versus frequency determined from FMR measurements. Although there are some small deviations between the three techniques in some of the measurements, they mostly average out over the range of frequencies measured. This results in Gilbert damping parameters, extracted from the linear fit, that all agree with

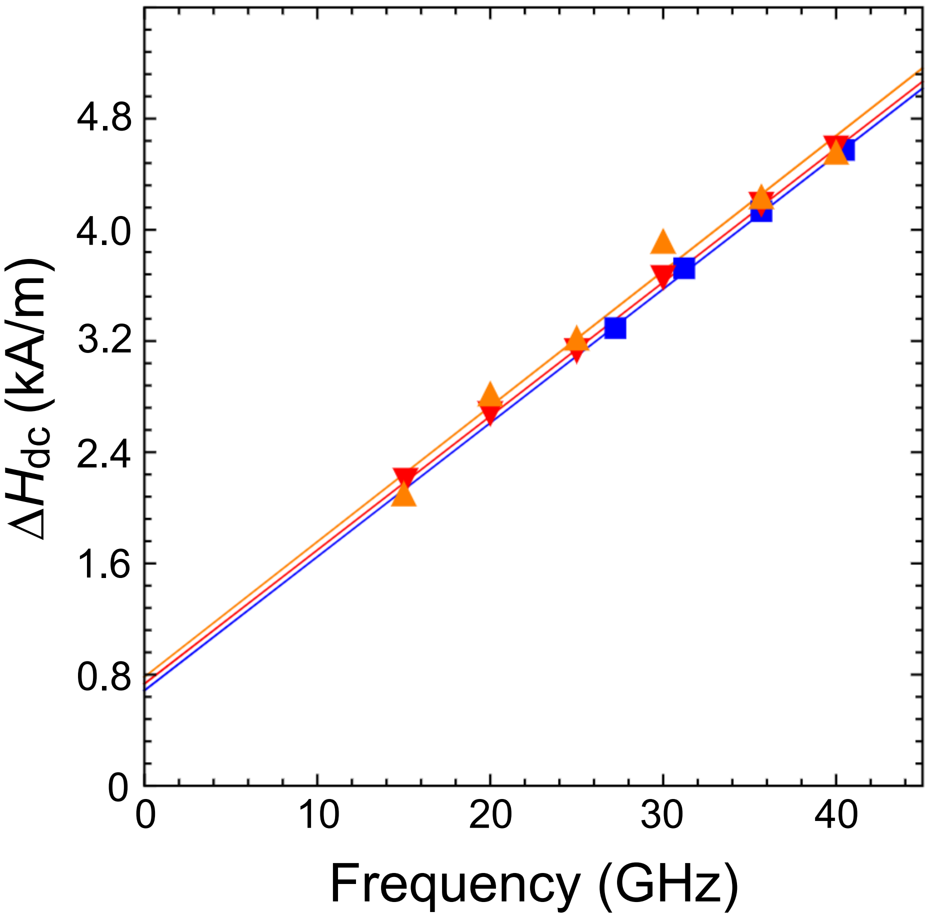

Figure 5.10: FMR linewidth measurements of GaAs(100)/Fe(4 nm)/Au(4 nm) samples using the initial FMR design (blue squares), the new broadband design using field modulation (red inverted triangles), and the new broadband design using pulse modulation (orange triangles). The lines the fit using Eq. 5.5.1 which resulted in Gilbert damping of 0.0035 ± 0.0003 for the first two cases, and 0.0036 ± 0.0003 for the third case using pulse modulation.

one another. This also confirms that the field modulated measurements were modulated at a field strength small enough to not cause significant changes in the FMR absorption linewidth.

5.6 Summary

We have demonstrated a novel broadband FMR spectrometer that is able to operate over a range of frequencies from 0 to 40 GHz with a single setup. This spectrometer design is able to achieve the same level of SNR as the original narrow-band design. The physical quantities extracted from measurements using the new setup and narrow-band setup are also in agreement with one another.

Throughout the rest of the work in this thesis, all FMR measurements will be carried using the novel broadband FMR design.

Chapter 6

Magneto-optic Kerr Effect (MOKE) Magnetometer

In this section, we will demonstrate how to set up a highly sensitive MOKE magnetometer, capable of measuring both in-plane and out-of-plane thin film magnetization, using widely available components, and with relative ease. While this measurement technique is quick and easy, it generally yields only approximately correct results. Thus, its usefulness is in providing a way to quickly characterize the approximate magnetic properties of a sample when rapid turn around is required. For example, when lab equipment is shared between a large number of people and usage time for each researcher is limited. However, for more accurate and reliable results, magnetization measurements of the samples should be done using a tool such as VSM or SQUID.

The MOKE magnetometer, as described in this section, was built during the work in this thesis.

The experimental setup for the MOKE magnetometer is shown in Fig. 6.1. The system can measure thin film magnetization in one of two configurations, the polar and longitudinal configuration. In the polar configuration, the system will measure the out-of-plane magnetization of the thin films, while the external magnetic field is directed perpendicular to the sample surface. In the longitudinal configuration, the system will measure both in-plane and out-of-plane magnetization, while the external magnetic field is directed in the plane of the sample.

Both configurations share the same general setup, except with different geometries as shown in Fig. 6.1. This general setup will be described now before diving into the subtleties of each configuration.

The laser beam is generated by an inexpensive 650 nm diode laser rated from 0-100 kHz time to live (TTL) modulation. The laser is connected directly to the TTL output on the lock-in amplifier. This causes the laser to turn on and off at the frequency that the lock-in is set to detect.

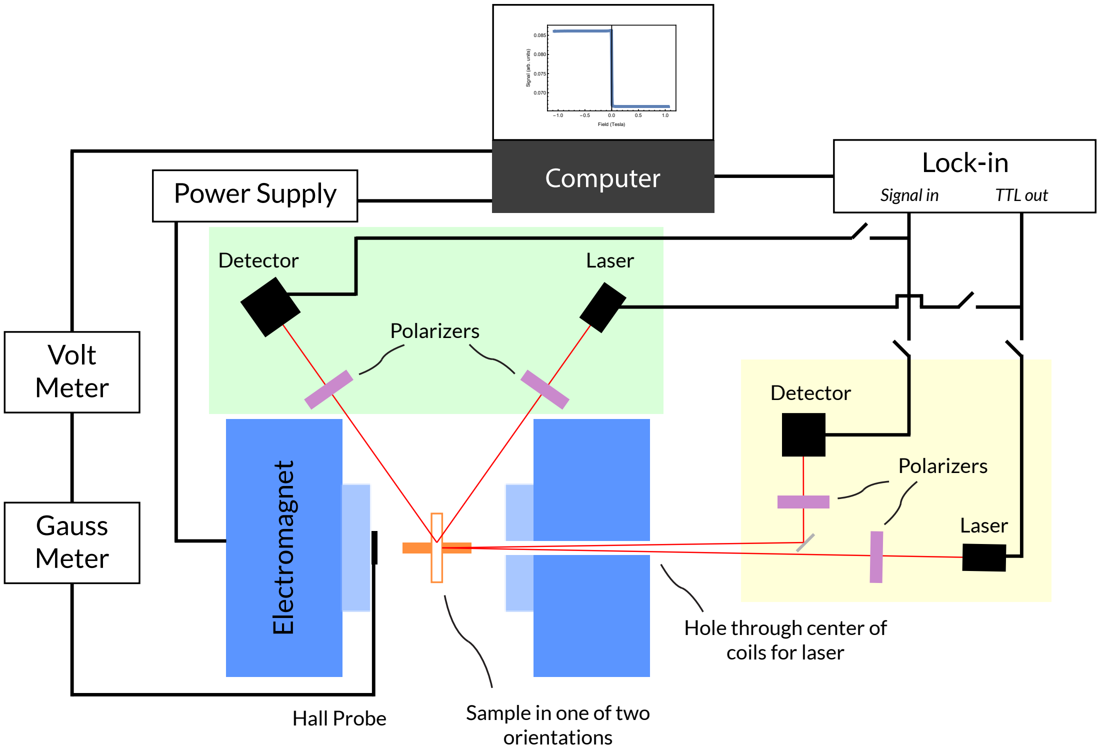

Figure 6.1: Schematic of the MOKE Magnetometer. The bottom right yellow shaded laser, detector, and polarizers are for the polar configuration (out-of-plane measurements), the top left green shaded laser, detector, and polarizers are for the longitudinal configuration (in-plane measurements). The incoming laser light is polarized so that the electric field oscillates perpendicular to the plane of this figure, or perpendicular to the page of this thesis.

The lasers we used generated an approximately polarized beam. We rotated the laser, around the axes of the beam, so that it was S-polarized relative to the sample and mirrors. This means that the electric field oscillates in the plane of the mirror. This is so that there will be minimal mixing of S and P polarizations caused by non-Kerr effects at the reflections of the sample and mirrors. We also placed a polarizer directly in front of the laser so that the light was S-polarized.

Next, the laser beam reflects from the surface of the sample and back into a second polarizer. This second polarizer is rotated so that it is just off of being 90° relative to the first polarizer, or in other words, the two polarizers are almost crossed. In our case, our polarizers were approximately 90.5° relative to each other. It is important that the polarizers are not exactly 90° relative to each other because both clockwise and counterclockwise Kerr rotation will result in an increase in the signal. However, for useful measurements, we want one direction of Kerr rotation to result in a decrease in the signal, and the other direction to result in an increase in the signal. This is achieved by setting the polarizers approximately 90.5° relative to one another.

Finally, the laser beam goes into an Ealing Electro Optics Type S1 detector, and is detected by an SRS model SR810 DSP lock-in amplifier, which is connected to the computer via GPIB. The lock-in amplifier is set to a prime number frequency of 997 Hz to avoid interference from external electromagnetic radiation. Any rotation of the magnetic moment is detected as an increase or decrease in the signal.

We found that using a lock-in amplifier is superior to a DC measurement because it isolates the laser beam signal from any ambient light in the room. Any change in the intensity of ambient light that is not at the same frequency as the lock-in, will not effect the measured signal. This allows the tool to be set up in an existing labratory area where other people may be working and moving around without any optical isolation required.

The magnet used is a Spectromagnetic Industries Model 1003 capable of generating fields of approximately 1.3 Tesla with our cooling solution. The magnet power supply is connected to the computer via GPIB.

The external magnetic field magnitude is measured using a hall probe connected to a F.W Bell Inc. Model 8511 gauss meter, which converts the signal to a voltage. This voltage output is then measured by a Fluke 8842A multimeter, which is connected to the computer via GPIB.

6.0.1 Polar Configuration

The laser, detector, and polarizers for this configuration are shown in the yellow shaded region of Fig. 6.1. The sample is positioned at the location shown as a rectangle with a white interior and orange outline in the schematic, so that the laser beam is close to being perpendicular with the sample surface, and the external magnetic field is in the direction perpendicular to the sample surface.

In this configuration, it is important to make sure the laser beam is as close to being perpendicular to the sample as possible. This is because only the component of magnetization parallel with the beam will cause Kerr rotation. [31] So, when the laser is perpendicular to the sample, only the out-of-plane component of magnetization will be measured, making analysis of the signal much simpler. In practice, it is easier to direct the reflected beam to the detector if there is a very small angle between the incoming and reflected beam, as shown in Fig. 6.1. As long as this angle is very small, the signal from the out-of-plane component of magnetization will be orders of magnitude larger than the in-plane component, allowing one to ignore the latter. To achieve this, we have used the cavity through the center of the electromagnetic coil windings as a path for the laser beam.

6.0.2 Longitudinal Configuration

The laser, detector, and polarizers for this configuration are shown in the green shaded region of Fig. 6.1. The sample is positioned at the location shown as a solid orange rectangle in the schematic, so that the laser beam reflects off of the surface of the sample, and the external magnetic field is directed in the plane of the sample.

In this configuration, the incoming laser beam is approximately 20° from the sample surface normal. A greater angle would result in more sensitive measurements of the in-plane component of magnetization, however for our setup, this angle was limited by the size of the opening between the magnet poles.

With this configuration, the direction of the incoming laser beam causes the measured signal to be sensitive to the in-plane and out-of-plane component of magnetization. This is because any component of magnetization in the same direction of the laser beam will cause Kerr rotation. [31] Thus, in general, there is no way to tell whether the measured signal is caused by a change in the out-of-plane or in-plane component of magnetization. Therefore, to perform useful measurements in this configuration, the magnetization of the sample should always be in-plane, ie. the sample cannot have any anisotropies that cause the magnetization to be out-of-the plane. Additionally, the transmitted and reflected laser beam needs to have a significant component in the plane of the sample. In other words, if the transmitted and reflected laser beam is close to being parallel with the sample normal, then the measured signal will be very small.

6.0.3 Example Data for Ultrathin Films

In order to gauge the accuracy and quality of MOKE measurements using this tool, we have measured the magnetization of a sample with the structure
Ta(3 nm)/Ru(3 nm)/Co(2 nm)/$\mathrm{Ru}_{38}\mathrm{Fe}_{62}$(0.8 nm)/Co(2 nm)/Ta(3 nm) using both MOKE and SQUID, and compared the results. The layers are thin enough that any effect due to the finite penetration depth of laser light can be ignored. Additionally, the equal thickness and saturation magnetization of the two Co magnetic layers means that even if the samples had thickness on the order of the penetration depth, it would not effect the measurement. See Section 4.3 for more details. Fig. 6.2 shows normalized in-plane measurement data using both MOKE (blue points) and SQUID (orange points). It can be seen that the MOKE data lines up very closely with the SQUID data.

Fig. 6.3 shows normalized in-plane measurement data using MOKE (blue points), along with the fit using Eq. 4.66 (orange line). The fit results in $J_1 = -0.82 \pm 0.01$ mJ/m^2, $J_2 = 0.15 \pm 0.01$ mJ/m^2, $A_{ex} = 1.7 \pm 0.1 \times 10^{-11}$ J/m. This can be compared to the results obtained from SQUID data of $J_1 = -0.80 \pm 0.02$ mJ/m^2, $J_2 = 0.15 \pm 0.01$ mJ/m^2, $A_{ex} = 1.7 \pm 0.1 \times 10^{-11}$ J/m. Fits to both data use the same $M_s = 1350$ kA/m, which was determined from the SQUID measurement. Both measurements give results that agree to

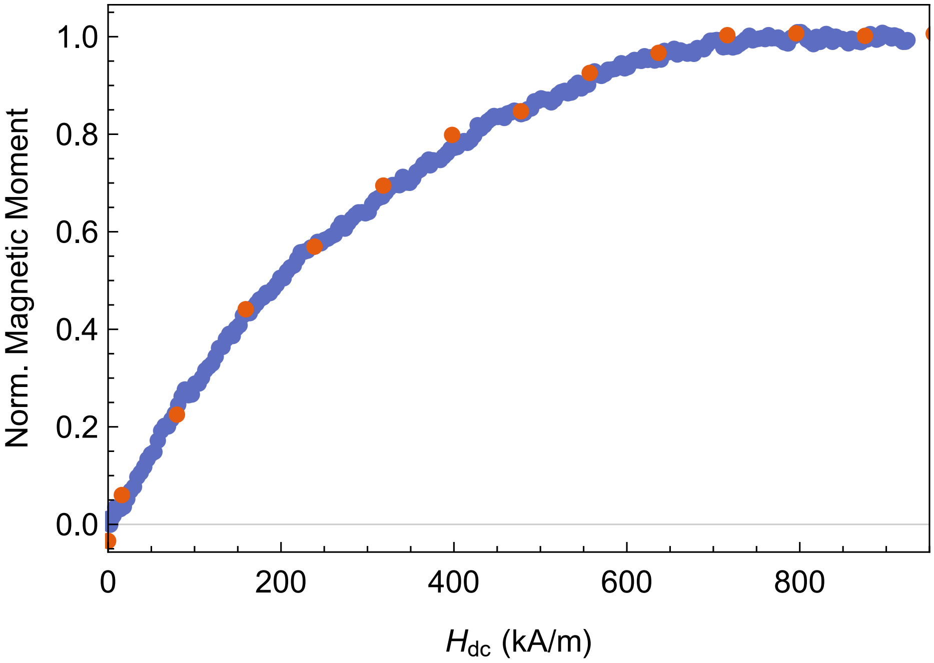

Figure 6.2: In-plane MOKE measurement data (blue) and SQUID (orange) for the Co(2 nm)/$\mathrm{Ru_{38}Fe_{62}}$(0.8 nm)/Co(2 nm) sample.

within the uncertainty of one another, showing that as long as the saturation magnetization of the magnetic layers is known, MOKE can be a reasonably accurate and inexpensive magnetic characterization tool for ultrathin films.

6.0.4 Example Data for Thicker Films

When measuring $M(H_{dc})$ for thicker films, MOKE will be more sensitive to the magnetic material closer to the surface due to the finite penetration depth of the laser light. To approximately account for this to first order, we assume that the tool's measurement sensitivity to the magnetic material drops off exponentially with its depth from the surface of the sample. See Section 4.3 for the full details.

Here, we will show MOKE and VSM measurements of a sample that has thin film thicknesses on the order of the penetration depth. We have previously determined the M_s of each layer using VSM. We will use this known M_s for each layer in our fits to the MOKE data.

We will first show the differences between a magnetization measurement using MOKE and VSM in order to highlight the effect of the penetration depth of the laser light. After this, we will show the fits and parameters when fitting to VSM and MOKE data using our model with and without taking the penetration depth of the laser beam into account.

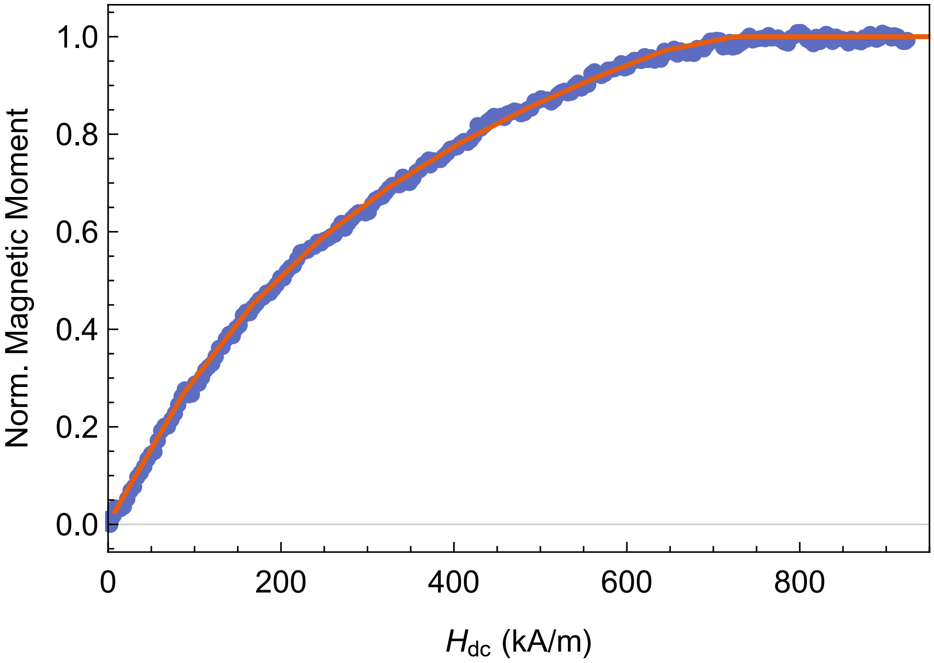

Figure 6.3: In-plane MOKE measurement data (blue points), and fit using Eq. 4.66 (orange line), for the Co(2 nm)/$Ru_{38}Fe_{62}$(0.8 nm)/Co(2 nm) sample. The fit parameters are $J_1 = -0.82{\pm}0.01$ mJ/m^2, $J_2 = 0.15{\pm}0.01$ mJ/m^2, $A_{ex} = 1.7{\pm}0.1{\times}10^{-11}$ J/m, $M_s = 1350$ kA/m.

The structure of the sample is Ta(2.5 nm)/$Ni_{80}Fe_{20}$(6 nm)/$Ru_{85}B_{15}$(7 nm) /$Fe_{75}Co_{25}$(4 nm)/Ta(4 nm). Details of sample preparation of this sample can be found in Chapter 8. We will refer to this sample as the NiFe/$Ru_{85}B_{15}$/FeCo sample.

The normalized in-plane $M(H_{dc})$ plot of the NiFe/$Ru_{85}B_{15}$/FeCo sample is shown in Fig. 6.4 measured both with MOKE (blue points) and VSM (orange points). The difference between the MOKE and VSM measurement is caused by the finite penetration depth of the laser light used in the MOKE measurement. As the layers become thicker, this deviation will become even greater.

Measurements of the in-plane magnetization of the NiFe/$Ru_{85}B_{15}$/FeCo sample using a) VSM, b) and c) MOKE, is shown in Fig. 6.5. b) is fit using a finite penetration depth of 10 nm, while c) is fit with an infinite penetration depth which is equivalent to the model without the penetration depth. It can be seen that if the MOKE measurement data is fit without considering the penetration depth of the laser light, the fitted parameters are quite inaccurate, with $J_1 = -0.010 \pm 0.005$ mJ/m^2 and $J_2 = 0.125 \pm 0.005$ mJ/m^2, which can be compared to the parameters determined from the VSM measurement of $J_1 = -0.055 \pm 0.005$ mJ/m^2 and $J_2 = 0.105 \pm 0.005$ mJ/m^2. On the other hand, when we fit the MOKE data using our model with a penetration depth of 10 nm, the results are in agreement, within the uncertainty, with the results from fitting VSM data. They are $J_1 = -0.050 \pm 0.005$ mJ/m^2 and $J_2 = 0.105 \pm 0.005$ mJ/m^2. The saturation magnetization

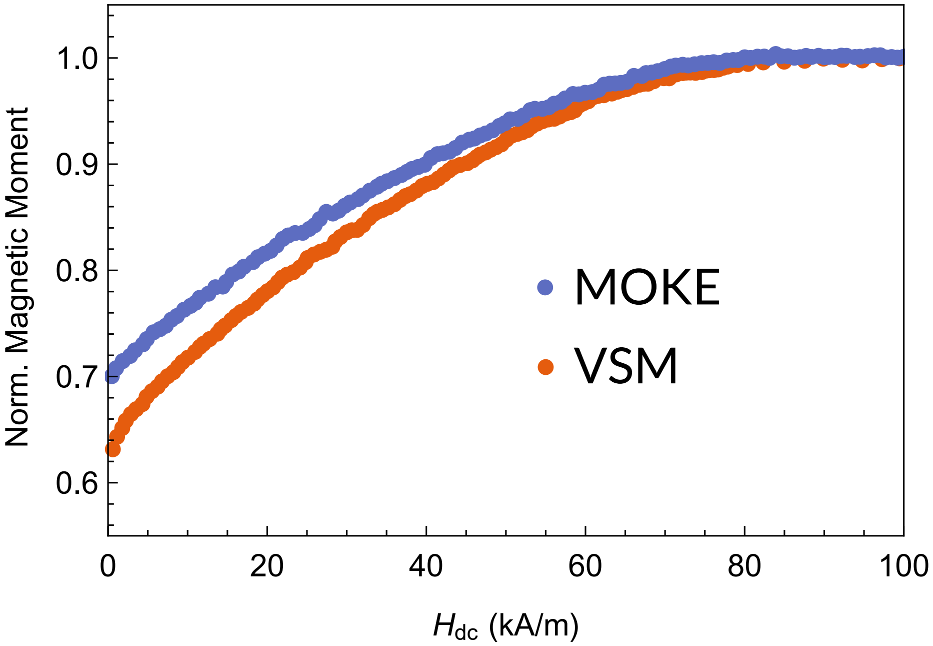

Figure 6.4: Example of in-plane MOKE measurement data (blue) and VSM (orange) for the NiFe/Ru$_{85}$B$_{15}$/FeCo sample showing the effect caused by the finite penetration depth of laser light in the MOKE measurements.

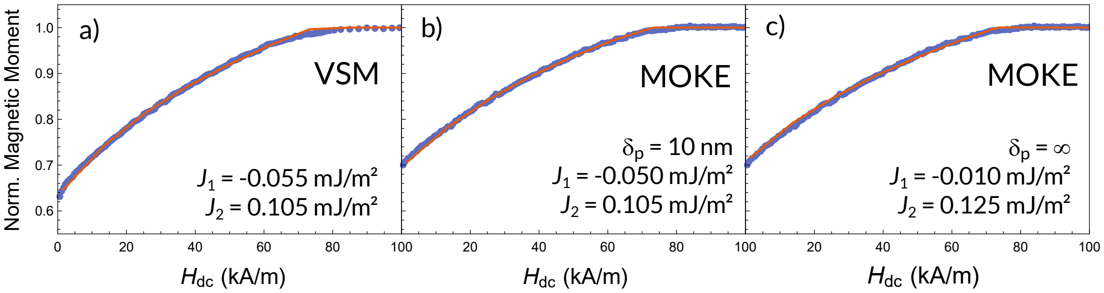

Figure 6.5: Measurements of the in-plane magnetization of the NiFe/Ru$_{85}$B$_{15}$/FeCo sample using a) VSM, b) and c) MOKE. b) is fit using a finite penetration depth of 10 nm, while c) is fit with an infinite penetration depth which is equivalent to the model without the penetration depth. The fitted parameters are shown in the figure overlay. $A_{ex} = 1.7 \pm 0.1 \times 10^{-11}$ J/m for all three fits. The saturation magnetization of each layer is $M_s = 804$ kA/m for the NiFe layer, and $M_s = 1550$ kA/m for the FeCo layer. The uncertainty on J_1 and J_2 is ± 0.005 mJ/m^2.

of each layer is $M_s = 804$ kA/m for the NiFe layer, and $M_s = 1550$ kA/m for the FeCo layer.

These results show that the accuracy of J_1 and J_2 determined from fitting MOKE magnetization measurement data for samples with thicker films, that are on the order of the penetration depth of the tool's laser, can be improved significantly by using a model that takes this penetration depth into account. In our case, by doing this, the J_1 and J_2 parameters determined from MOKE measurements are in agreement with those determined from VSM measurements.

6.1 Summary

We have demonstrated a MOKE experimental apparatus that, along with a micromagnetic model that takes into account the finite penetration depth of the tool's laser probe, can be used to determine J_1 and J_2 that are in agreement with those obtained from VSM magnetization measurement data. This is true for both ultrathin film samples, and samples with films that are on the order of the measurement penetration depth. However, the M_s of each magnetic layer and δ_p for the film structure must be known. Both of these can be determined by measuring a sample using VSM or SQUID. This technique is useful when measuring a large number of very similar samples when the M_s of the layers, and δ_p of the structure is not expected to change significantly from sample to sample.

Throughout the work in this thesis, this technique was used for quick and approximate characterization of our samples immediately after they had been sputtered. This rapid feedback allowed us to validate the plan for which samples to create next. This increased the efficiency of the usage of shared equipment and tools in the lab. However, for the rest of this thesis, all results obtained by fitting to $M(H_{dc})$ measurements were obtained by fitting VSM or SQUID data.

Chapter 7

The Effect of Annealing on Exchange Coupling in FeCoB/Ta,Ru,Mo/FeCoB Trilayer Structures

In this chapter, we will measure the interlayer exchange coupling between two FeCoB layers coupled across a Ta, Ru, and Mo spacer layer with thicknesses ranging from 0.3 to 1.5 nm both as-deposited, and after being annealed at 200 and 300°C. This will allow us to understand exactly how boron within the FeCoB layer effects coupling both before and after annealing. This is an essential step towards our goal of creating a SAF fixed-layer containing FeCoB that can withstand annealing for use in devices containing an FeCoB/MgO/FeCoB tunnel junction.

STT-MRAM devices often contain an FeCoB/MgO/FeCoB tunnel junction because, after annealing, it exhibits a large TMR and PMA at the FeCoB/MgO interfaces. [49, 104] These are both highly desirable properties because they allow for faster operation and higher memory density. For STT-MRAM, the magnetic layers on either side of the tunnel junction are known as the free and fixed layers. The free layer typically has its direction of magnetization be stable in one of two directions, which is used to store a binary 1 or 0. The fixed layer must have its magnetization remain fixed because it is used as a reference for reading and writing.

The ideal fixed layer is composed of two AFC coupled magnetic layers, forming a SAF, where the structure has zero net magnetization. This structure is advantageous as compared to a single magnetic layer because it is more difficult to reverse the direction of magnetization using an external magnetic field, and results in reduced stray fields. [56, 112, 39, 40] This is usually achieved by AFC coupling one FeCoB layer with another ferromagnetic layer, like FeCoB, across an Ru spacer layer. [71]

It is also possible to couple more than two layers together to increase thermal stability. If this is done carefully, one can still achieve 0 net magnetization. In some STT-MRAM designs, this additional coupling is done through a Ta, W, or Mo layer. [1, 96, 26, 116, 68] These materials are chosen because they can allow the structural transition from face-centered cubic (fcc) or hexagonal close-packed (hcp) to body-centered cubic (bcc) and contribute to the absorption of boron from the FeCoB layer upon annealing. [37] Thus, it is of wide interest for device applications to study coupling of two FeCoB layers across Ta, Ru, and Mo spacer layers, and understand how this coupling is effected by annealing.

7.1 Experimental

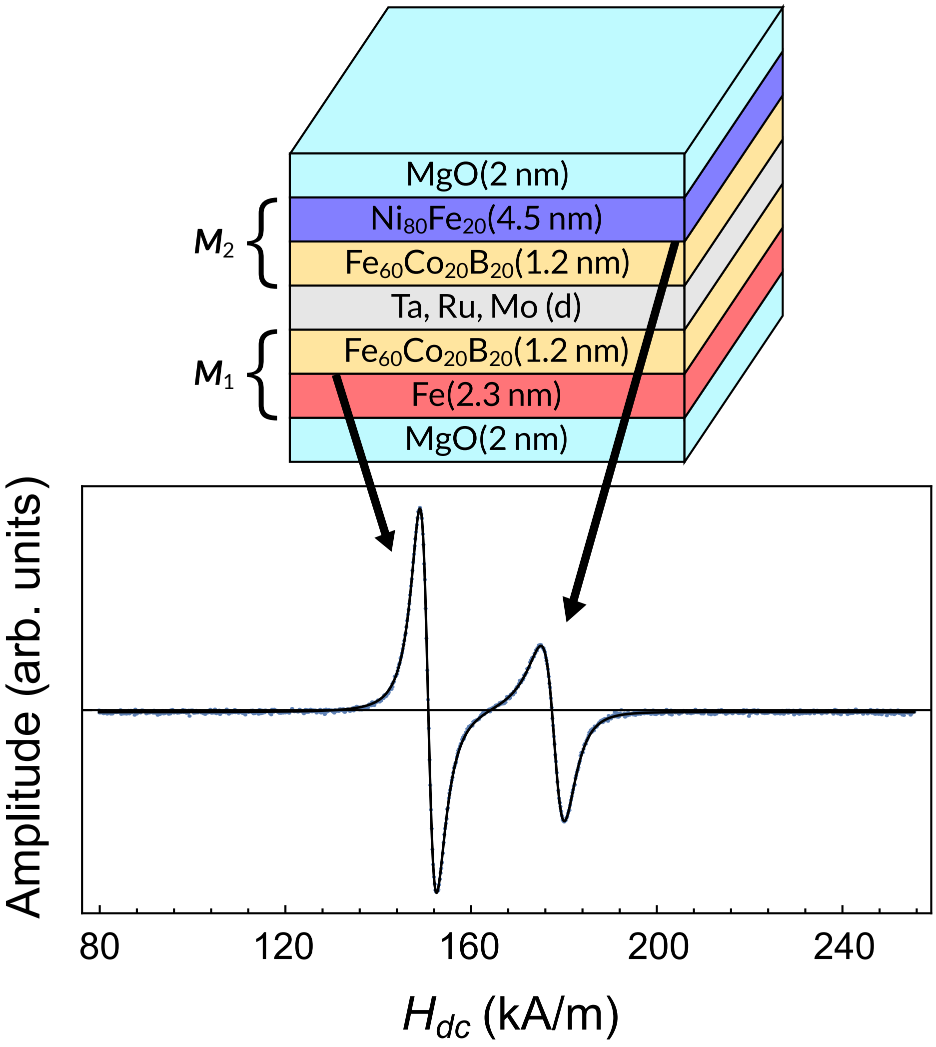

Figure 7.1: Layer structure of the studied samples and the corresponding FMR resonance peaks for $\boldsymbol{M}_1$ and $\boldsymbol{M}_2$ at a frequency of 16 GHz in the case of zero coupling ($d = 4$ nm).

The samples studied in this chapter are shown in Fig. 7.1 and have the following structure: MgO(2 nm)/$\boldsymbol{M}_1$/(Ta, Ru, Mo)(d)/$\boldsymbol{M}_2$/MgO(2 nm), and $\boldsymbol{M}_1$ is Fe(2.3 nm)/$Fe_{60}Co_{20}B_{20}$(1.2 nm), $\boldsymbol{M}_2$ is $Fe_{60}Co_{20}B_{20}$(1.2 nm)/$Ni_{80}Fe_{20}$(4.5 nm), where d is varied from 0.375 nm to 4 nm, 0.3 nm to 1.5 nm, and 0.275 nm to 1 nm for Ta, Ru, and Mo layers, respectively. Throughout the rest of this chapter, we will refer to $Fe_{60}Co_{20}B_{20}$ and $Ni_{80}Fe_{20}$ as FeCoB and NiFe, respectively. Additionally, in later chapters, we will be referring to these series of samples as the FeCoB/Ta/FeCoB, or FeCoB/Ru/FeCoB, or FeCoB/Mo/FeCoB series of samples.

The samples are deposited by means of rf magnetron sputtering on oxidized Si substrates. The deposition conditions, sample preparation and RTA procedure are explained in detail in Chapter 3. All thin films are deposited using 2" targets except for MgO, which is deposited using a 4" target. The samples are also capped with 6 nm of Ta to protect the top MgO layer from further oxidation or water absorption from the atmosphere. After deposition, the samples are cut into 3 pieces. One piece is not annealed, and the other two are RTA in vacuum at 200 and 300 °C, respectively.

These structures are deposited on an underlayer composed of Ta(4 nm)/FeCoB(0.5 nm), in which the FeCoB layer is thin enough to be non-magnetic when MgO is grown on top. [75] This Ta(4 nm)/FeCoB(0.5 nm) underlayer is chosen because MgO grows along the [100] crystallographic orientation when deposited on top of amorphous FeCoB, which is the orientation chosen for typical memory device applications. [83] It is also the orientation that results in well textured [100] Fe when grown on top, which has narrow FMR linewidth, which is a requirement for determining coupling constants from FMR. [70]

7.1.1 MgO Depositon Optimization

In order to optimize the MgO texture, we created several samples. We created two series of samples to test the effect of sputter chamber pressure and rf sputtering power. These series have the structure Ta(3 nm)/MgO(50 nm)/Ta(3 nm), where we varied the chamber pressure and rf power for only the middle MgO layer. We then measured FWHM of the rocking curve for the MgO (002) XRD peak all of the samples using perpendicular XRD. We found that there was no correlation with the FWHM and pressure in the range from 1.3 to 1.7 mTorr. We did find a correlation of the FWHM with the rf power, however, which is shown in Fig. 7.2. It is clear that, in the range of power that tested, we have better [100] textured MgO when we sputter at lower power. We created another sample with the structure Ta(3 nm)/FeCoB(1.2 nm)/MgO(50 nm)/Ta(3 nm), where the rf power and chamber pressure for the MgO layer was 150 W and 1.5 mTorr, respectively. We found that the XRD rocking curve FWHM for the MgO (002) peak decreased from 7.80 to 4.88 degrees by adding the 1.2 nm FeCoB layer below the MgO layer. From these results, MgO grows with the best [100] texture at 100 W rf power on top of a thin FeCoB layer.

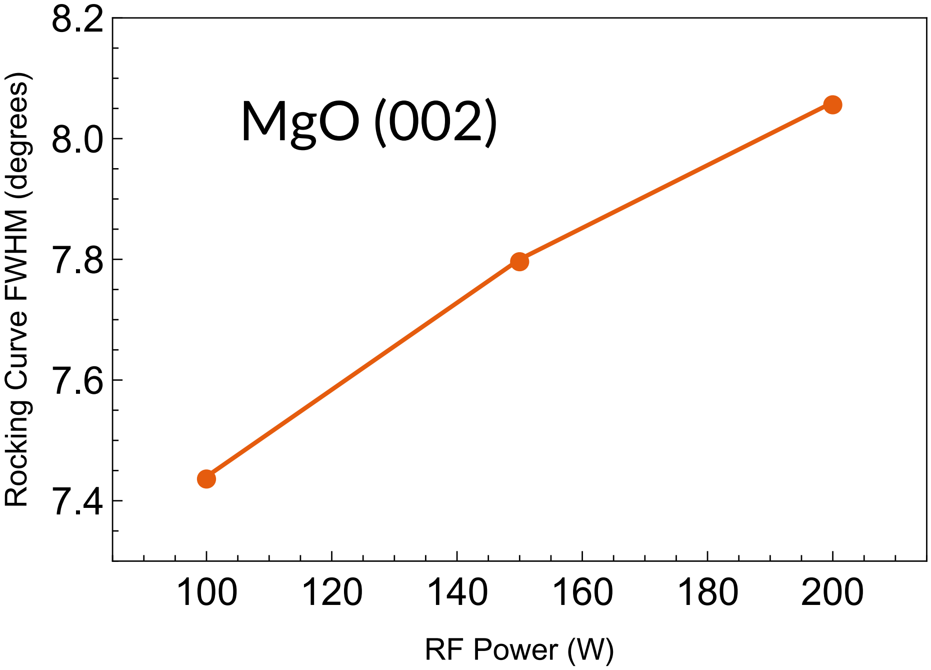

Figure 7.2: The dependence of the XRD rocking curve FWHM of the MgO (002) peak on the rf power used during deposition of the MgO layer in the Ta(3 nm)/MgO(50 nm)/Ta(3 nm) samples. Lines between the points are added as a guide to the eye.

After sputtering many samples containing MgO, we began to notice that approximately 10% of the time, during the deposition of the MgO layer, the sample would be re-sputtered, removing material that was already deposited. This can occur because of several reasons as explained in Chapter 3, but in this case it is mainly because the 4" target is only approximately 5 cm away from the sample. At this distance, the magnetic field intended to confine the electrons just above the target, is also strong at the substrate surface. This results in high electron density even at the sample which has the potential to initiate re-sputtering. See Chapter 3.1.1 for more details. In order to stop this from happening, we deposited a large number of samples with a thin Ru layer, then sputtered MgO on top with various chamber pressures, and then measured the resulting thickness of the Ru layer using XRR. If there was any re-sputtering, it should show up as a reduction of the thickness of the Ru underlayer. We found that by increasing the chamber pressure to 8 mTorr completely eliminated any resputtering. We also noticed, by looking through the sputter chamber window, that the plasma glow discharge became more well confined to the surface of the target as the pressure increased. This indicates that there is no longer a large concentration of Ar ionization taking place near the surface of the substrate. This is likely the reason why re-sputtering stopped after increasing the chamber pressure. The final MgO sputtering conditions we chose after optimization are a power of 100 W, chamber Ar pressure of 8 mTorr, and MgO sputtered on top of 0.5 nm FeCoB layer. These conditions resulted in an XRD rocking curve FWHM of the MgO (002) peak of 3.66 ± 0.01 degrees for a 13.8 nm thick MgO layer. These optimized conditions also show that increasing pressure very far to 8 mTorr has improved the texture as compared to the previous range of pressures that we had tested, which was 1.3 to 1.7 mTorr.

Fe/FeCoB grown on top of well oriented [100] MgO, grown under these optimized conditions, has s sufficiently narrow FMR linewidth that results in well separated absorption peaks, as shown in Fig. 7.1. This is one of the requirements for using our FMR technique to extract coupling constants. See Chapter 4.2.7 for more details.

7.1.2 Additional Samples

We deposit three additional samples with the following structures:
Ta(4 nm)/$Fe_{60}Co_{20}B_{20}$(0.5 nm)/MgO(2 nm)/$\boldsymbol{M}_1$/Ta(6 nm),
Ta(4 nm)/$\boldsymbol{M}_2$/MgO(2 nm)/Ta(6 nm), and Ta(4 nm)/$Fe_{60}Co_{20}B_{20}$(0.5 nm)/MgO(2 nm)/$\boldsymbol{M}_1$. The first two are used to independently measure the M_s of $\boldsymbol{M}_1$ and $\boldsymbol{M}_2$ using SQUID. The measurements show that the saturation magnetization of $\boldsymbol{M}_1$, $M_{s,1}$, is 1470 ± 40 kA/m and $\boldsymbol{M}_2$, $M_{s,2}$ is 817 ± 20 kA/m. The third sample was used to measure the roughness at the interface between $\boldsymbol{M}_1$ and the spacer layer, using AFM, in order to estimate the Néel "orange-peel" coupling strength.

The demagnetizing dipolar fields in the two magnetic layers are much larger than any fields perpendicular to the film that arise from the surface and magnetocrystalline anisotropies, forcing the magnetization to lie in-plane. The samples are polycrystalline, and rotated during deposition, resulting in the in-plane magnetocrystalline anisotropy being averaged out resulting in no in-plane magnetic anisotropy.

The coupling constants were determined using a combination of FMR and $M(H_{dc})$ measurements, along with our models explained in previous chapters. Our FMR model is incapable of differentiating J_1 and J_2. Instead we measure $J_{total} = J_1 - 2J_2$. However, for samples where the magnetic layers are not parallel, ie. they are AFC or non-colinearly coupled, we are able to independently determine J_1 and J_2 by fitting our micromagnetic model to $M(H_{dc})$ measurements.

7.2 Results and Discussion

7.2.1 Ta Spacer Layer

Fig 7.3 shows the results for the exchange coupling strength between $\boldsymbol{M}_1$ and $\boldsymbol{M}_2$ as a function of Ta spacer layer thickness of our samples. Note that for the samples measured in this study, our experimental setup is unable to determine ferromagnetic coupling strengths greater than approximately 1.5 mJ/m^2 due to the optical peak moving to a magnetic field less than 0. This behavior where the optical peak moves to lower fields can be seen in Fig. 4.23, and also beginning to occur in Fig. 7.4 where the lower peak passes 0 field at

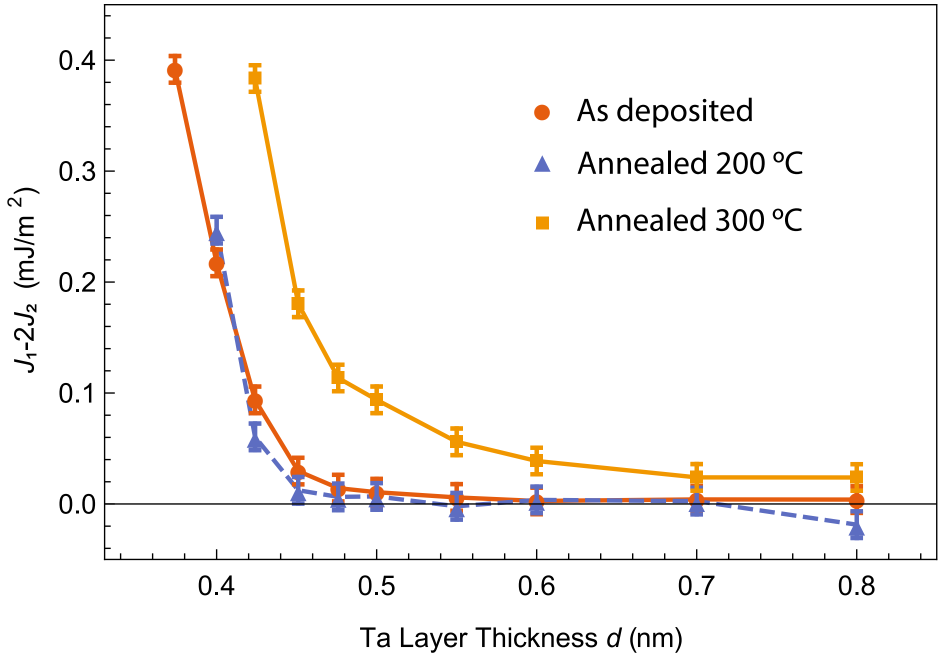

Figure 7.3: The exchange coupling strength between $\boldsymbol{M}_1$ and $\boldsymbol{M}_2$ as a function of Ta spacer layer thickness for non-annealed samples, and those annealed at 200 °C and 300 °C. The samples with a 4 nm Ta spacer layer were not included, and have $J_1 - 2J_2 = 0.019 \pm 0.003$ mJ/m^2. The connecting lines are a guide to the eye.

approximately 10 GHz. The exchange coupling between $\boldsymbol{M}_1$ and $\boldsymbol{M}_2$ in the samples annealed at 200 °C with a Ta spacer layer thickness below 0.4 nm and samples annealed at 300 °C with a Ta spacer layer thickness below 0.45 nm is ferromagnetic and larger than 1.5 mJ/m^2 and thus cannot be measured.

The dependence of the coupling strength on Ta thickness is approximately the same for non-annealed samples and those annealed at 200 °C: the coupling drops to 0 above approximately 0.475 nm and increases rapidly below 0.45 nm. For samples annealed at 300 °C, the coupling begins to increase below a Ta thickness of about 0.7 nm. These Ta spacer layer thicknesses for which coupling increases rapidly are no more than a few atomic layers thick. This leaves the possibility that the coupling may be caused by pinholes in the Ta layer, and not by coupling through the Ta layer itself.

As mentioned in the theory section 4.1.2, surface roughness can lead to ferromagnetic orange-peel coupling. In order to estimate the strength of this contribution, we measured the surface topography of Ta(4)/FeCoB(0.5)/MgO(2)/$\boldsymbol{M}_1$ sample using AFM. We did this for both annealed and non-annealed samples. We used the surface topography measurements to estimate δ as half of the difference between the maximum height and the minimum height, and period L from the Fourier transform. The non-annealed samples, and samples annealed at 200 °C, had roughness amplitude and wavelength of $\delta = 0.2$ nm and $L = 50$ nm. The

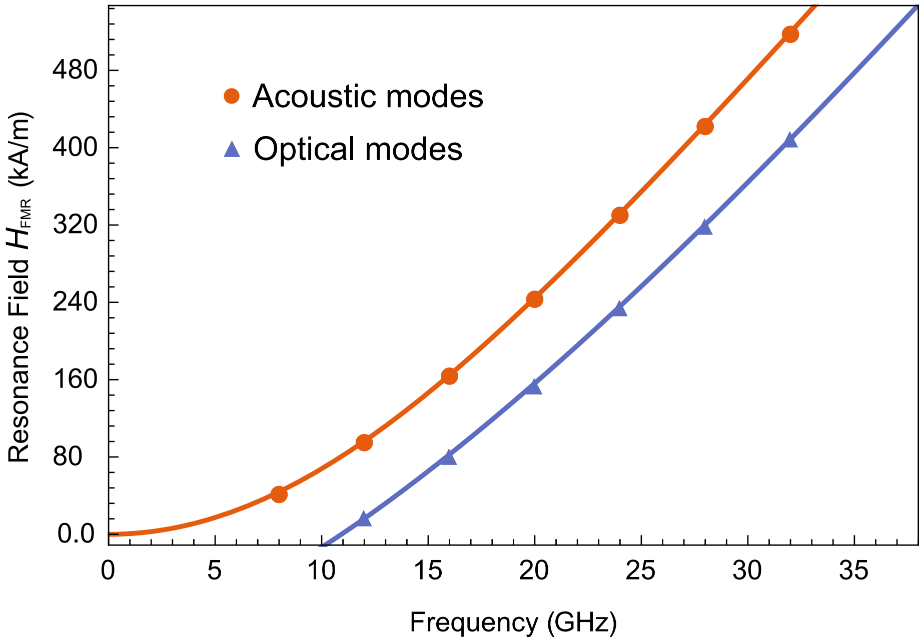

Figure 7.4: The FMR resonance peak positions of the acoustic and optical modes (points) with simultaneous fits using Eqns. 4.52 and 4.53 (lines). The data corresponds to a non-annealed sample with Ta spacer layer thickness $d = 0.4$ nm and coupling strength $J_2 - 2J_2 = 0.21 \pm 0.01$ mJ/m^2. Note that because the optical mode peaks have moved to a significantly lower field due to the ferromagnetic coupling, they pass below 0 field at approximately 10 GHz.

samples annealed at 300 °C had roughness amplitude and wavelength of $\delta = 0.4$ nm and $L = 42$ nm. Using these values in Eq. 4.25, the orange-peel coupling strength is found to be at least an order of magnitude smaller than the coupling strengths studied in this experiment. Specifically, for a Ta spacer layer thickness of 0.4 nm, the orange-peel coupling is approximately 0.001 mJ/m^2 and 0.005 mJ/m^2 for non-annealed samples and samples annealed at 300 °C, respectively. Thus, it is unlikely that orange-peel coupling has any significant contribution to our results.

We can also compare our obtained $J_{total} = J_1 - 2J_2$ values with that found by Pirro *et al.* [90] for perpendicularly magnetized FeCoB layers, which lack any orange-peel coupling. [6] Their value for J_{total} was determined to be $J_{total} = -0.01$ mJ/m^2 for a sample annealed at 250 °C with a Ta spacer layer thickness of $d = 0.75$ nm. If we linearly interpolate J_{total} between $d = 0.7$ and 0.8 nm for our samples annealed at 200 °C and 300 °C, we find that a sample with $d = 0.75$ nm would have $J_{total} = -0.01 \pm 0.01$ mJ/m^2 if annealed at 200 °C and $J_{total} = 0.02 \pm 0.01$ mJ/m^2 if annealed at 300 °C. This indicates that within the uncertainty of our measurements, our result for J agrees with that obtained by Pirro *et al.* and that the contribution from orange-peel coupling in our samples is within the uncertainty of our measurements.

The coupling between $\boldsymbol{M}_1$ and $\boldsymbol{M}_2$ for the non-annealed samples goes to zero for a Ta thickness of approximately 0.5 nm, which is two times less than the spin diffusion length of approximately 1 nm. [79] This indicates that for Ta, interlayer exchange coupling from conduction electrons decays faster than the time retarded response which is responsible for spin pumping. [48]

The range of Ta thickness where strong ferromagnetic coupling occurs, is found to be in agreement with predictions of Sokalski *et al.* [104], which have been extrapolated by measuring coupling from $M(H)$ curves of samples annealed for 30 minutes without RTA. This indicates that the RTA process suggested in this work, with shorter annealing time, is sufficient to achieve the desired coupling requirements for memory and sensor applications.

The Modern FinFet CMOS process can involve a complicated annealing procedure for dopant diffusion comprising many annealing steps at temperatures as low as 500 °C and times as short as a few seconds. [24, 55] While the RTA process suggested in this work has a longer annealing time, the lower temperatures of 200 °C to 300 °C reduce the risk of affecting the underlying integrated circuits, allowing it to be integrated into the backend CMOS process more easily.

7.2.2 Ru Spacer Layer

Measurements of J_{total} and J_2 of as-deposited and annealed $\boldsymbol{M}_1$/Ru(d)/$\boldsymbol{M}_2$ as a function of d are summarized in Fig. 7.5. If $J_1 > 0$ and $J_1 \geq 2J_2$, then the coupling is ferromagnetic, if $|J_1| < 2J_2$, then the coupling is non-collinear, and if $J_1 < 0$ and $|J_1| \geq 2J_2$, then the coupling is antiferromagnetic. In all measured samples, except for as-deposited $\boldsymbol{M}_1$/Mo(0.35 nm)/$\boldsymbol{M}_2$, $|J_1| > 2J_2$, which signifies that the sign of $J_1 - 2J_2$ determines whether the coupling is FC or AFC.

For as-deposited $\boldsymbol{M}_1$/Ru(d)/$\boldsymbol{M}_2$ samples, J_{total} is large and negative for d between 0.3 and 0.4 nm indicating large AFC coupling between FeCoB layers. As d increases above 0.4 nm, the magnitude of J_{total} sharply decreases and for d larger than 0.6 nm, it starts to oscillate around zero as could be seen from the insert in Fig. 7.5 a). Fig. 7.5 b) shows that for as-deposited samples, J_2 sharply decreases with increasing d. Our results for J_{total} and J_2 agree with those found by Hashimoto *et al.* [42] for as-deposited $(\mathrm{Fe}_{50}\mathrm{Co}_{50})_{88}\mathrm{B}_{12}$ layers coupled across an Ru spacer layer.

For samples annealed at 200 °C, the coupling is strongly FC below 0.6 nm, with a weaker AFC region around 0.8 nm, followed by an FC region around 1.3 nm. For samples annealed at 300 °C, coupling is FC over entire studied Ru thickness range. For the samples annealed at 200 °C and 300 °C, and Ru spacer layers thinner than 0.4 nm and 0.7 nm, respectively, the FC is so large that the coupling constants cannot be measured with our experimental setup.

Fig. 7.6 shows typical M(H) data for the $\boldsymbol{M}_1$/Ru(0.4)/$\boldsymbol{M}_2$ and $\boldsymbol{M}_1$/Mo(0.4)/$\boldsymbol{M}_2$ samples, and the fits using Eq. 4.66. The J_1 and J_2 values obtained by fitting SQUID data for

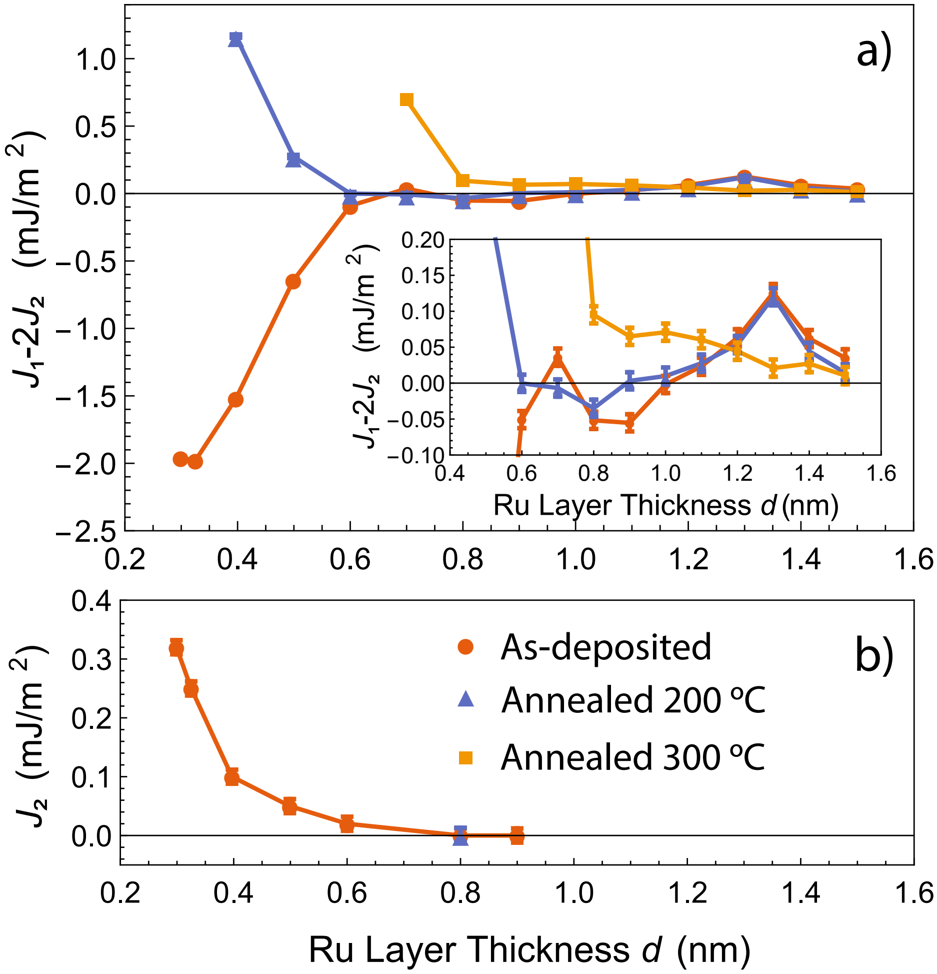

Figure 7.5: a) $J_1 - 2J_2$ and b) biquadratic coupling constants (as determined from SQUID measurements) of as-deposited and annealed $\boldsymbol{M}_1$/Ru(d)/$\boldsymbol{M}_2$ samples versus Ru thickness, d. The connecting lines are a guide to the eye.

all measured samples agree with the results from FMR measurements. From these fits, we also determined that A_{ex}, which is an average of the exchange stiffness of both layers, is $1.7 \pm 0.1 \times 10^{-11}$ J/m. The reported values of A_{ex} for NiFe, FeCoB and Fe are 1.3×10^{-11} J/m, 2.0×10^{-11} J/m, and 2.1×10^{-11} J/m, respectively. [25, 20, 59] Thus, it is expected that the A_{ex} of our ferromagnetic layers NiFe/FeCoB and NiFe/Fe is between that of NiFe and (FeCoB, Fe), as is obtained from our fitting.

7.2.3 Mo Spacer Layer

Fig. 7.7 a) shows the FMR measurements of J_{total} in $\boldsymbol{M}_1$/Mo(d)/$\boldsymbol{M}_2$, where d is varied from 0.3 to 1.0 nm.

In as-deposited samples, coupling between FeCoB layers across Mo is large and ferromagnetic for Mo thicknesses below 0.325 nm, and is weak and antiferromagnetic for Mo

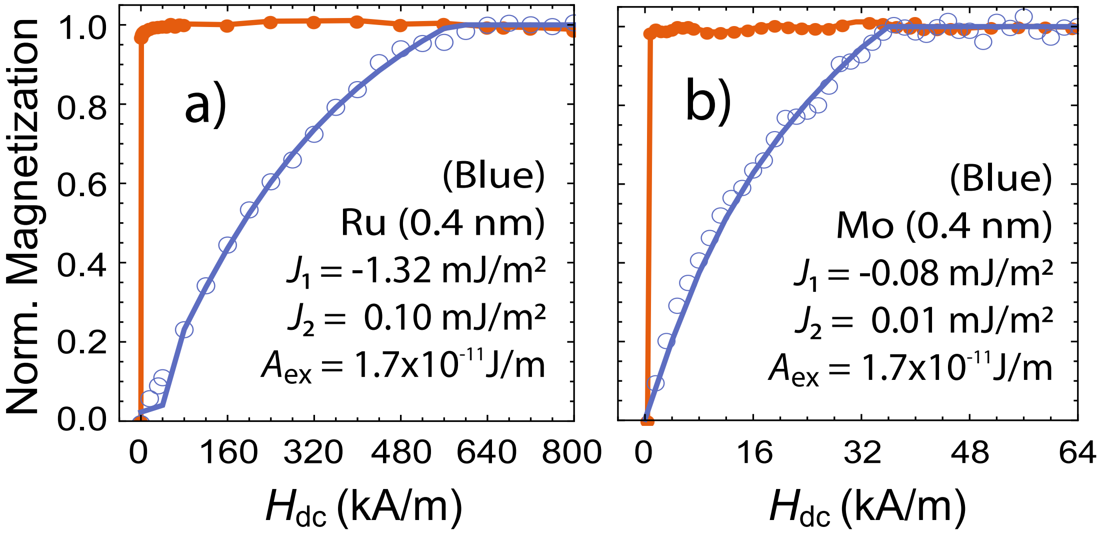

Figure 7.6: Normalized magnetization (blue circles) as a function of field of as-deposited a) $\boldsymbol{M}_1$/Ru(0.4 nm)/$\boldsymbol{M}_2$, and b) $\boldsymbol{M}_1$/Mo(0.4 nm)/$\boldsymbol{M}_2$ samples (points) fit with Eq. 4.66 (solid blue line). Also shown is the normalized magnetization (orange points) for samples with weak FC coupling.

thicknesses between 0.35 and 0.6 nm. The coupling strength is zero for thicknesses greater than 0.65 nm. For samples annealed at 200 °C, the coupling between FeCoB layers is ferromagnetic for Mo spacer layer thicknesses less than 0.4 nm, weakly antiferromagntic for thicknesses between 0.45 and 0.6 nm, and zero for larger thicknesses. For samples annealed at 300 °C, the coupling between FeCoB layers is ferromagnetic for Mo spacer layer thicknesses less than 0.7 nm, and zero for greater thicknesses. As with the samples coupled across Ru, these results show that annealing our samples almost entirely eliminates the negative J_{total} regions and increases FC coupling strength.

J_2 is found to decrease with an increase in the Mo spacer layer thickness, as shown in Fig. 7.7 b). This is the same trend as observed for samples with Ru spacer layers.

7.2.4 Summary

We find that the dependence of the coupling strength on Ta spacer layer thickness is the same for non-annealed samples and those annealed at 200 °C: the coupling drops to 0 above approximately 0.475 nm, and is ferromagnetic and increases rapidly below 0.45 nm. For samples annealed at 300 °C, coupling strength increases rapidly below about 0.7 nm. It was found that the Néel "orange-peel" contribution to coupling is much smaller than measured coupling in any of the studied samples. Thus, it does not play a significant role in coupling in our samples.

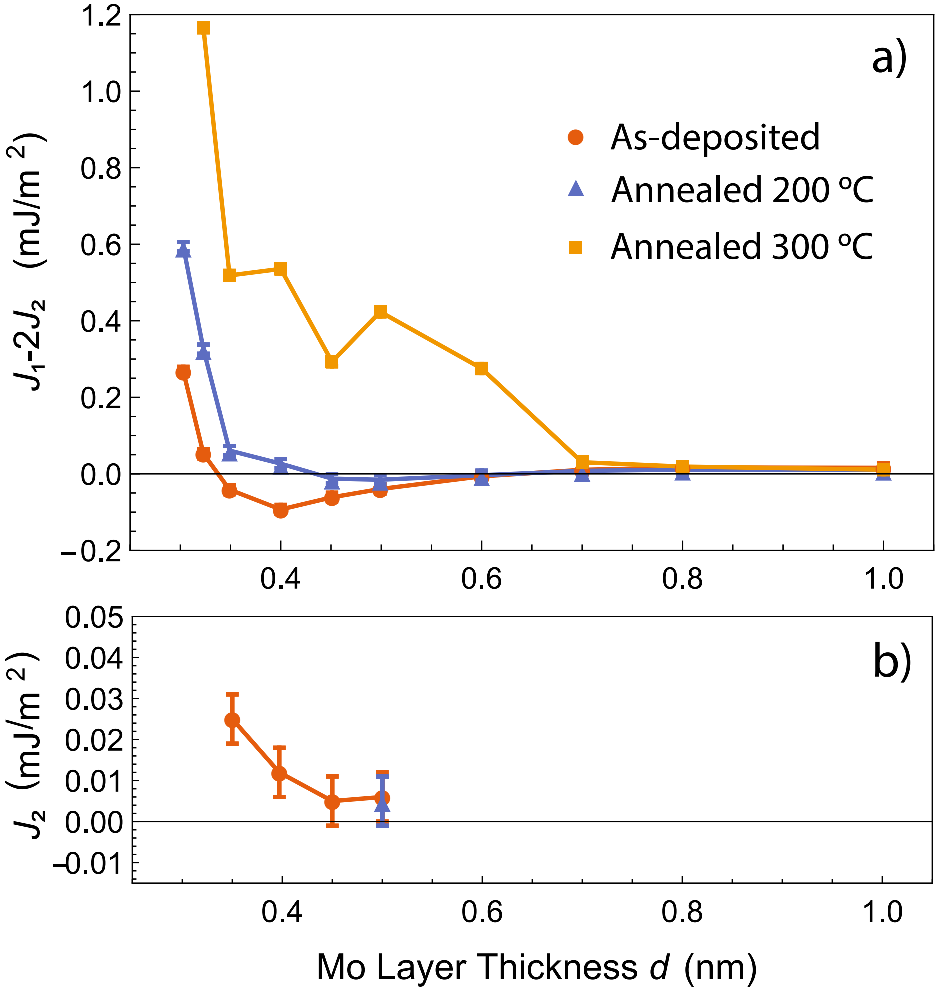

Figure 7.7: a) $J_1 - 2J_2$, and b) biquadratic coupling constants (as determined from SQUID measurements), as a function of Mo spacer layer thickness for as-deposited samples, and those annealed at 200 and 300 °C. The sample structures are $\boldsymbol{M}_1$/Mo(d)/$\boldsymbol{M}_2$. The connecting lines are a guide to the eye.

We find that annealing the samples with Ru and Mo spacer layers increases the FC coupling strength. In these samples annealed at 300 °C, the coupling between FeCoB layers is ferromagnetic if the spacer layer thickness is below 0.7 nm and is zero above 0.8 nm.

Most importantly, these results indicate that, in the structures studied, it is impossible to maintain strong AFC coupling for FeCoB/MgO based MRAM devices when annealed at temperatures of 200 °C or greater. This is unexpected considering that other AFC coupled thin film structures such as Co/Ru/Co and Co/Ru/FeCo show little change in coupling when annealed up to temperatures of approximately 350 °C. We have confirmed this by creating 2 series of samples with the structures Ta(2.5 nm)/Ru(3 nm)/Co(5 nm)/Ru(d)/Co(5 nm)/Ta(4 nm), and

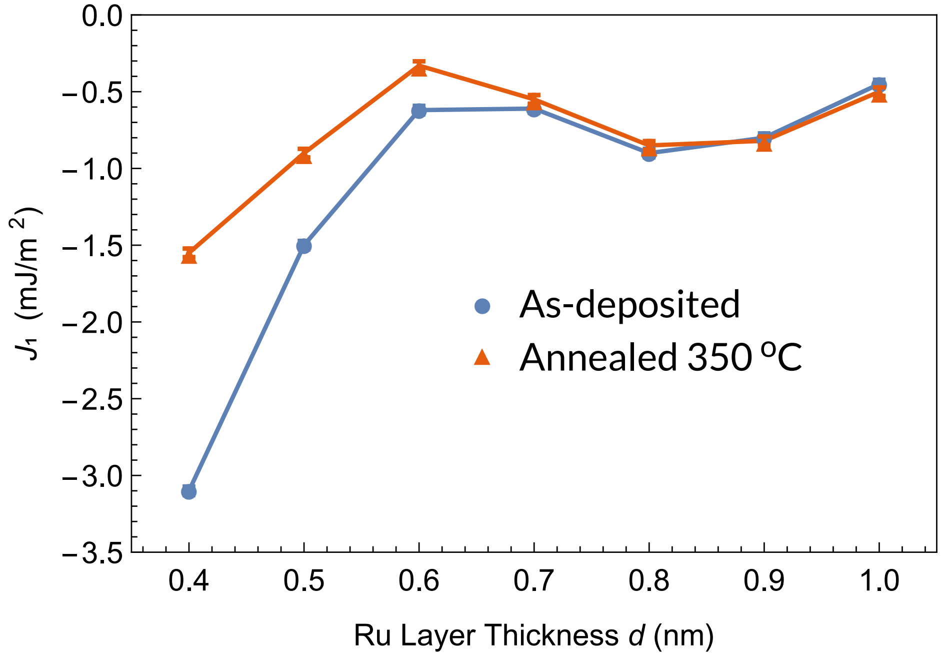

Figure 7.8: J_1 for the Co/Ru(d)/Co series of samples as deposited and annealed at 350 °C, with blue circles and orange triangles, respectively. The connecting lines are a guide to the eye.

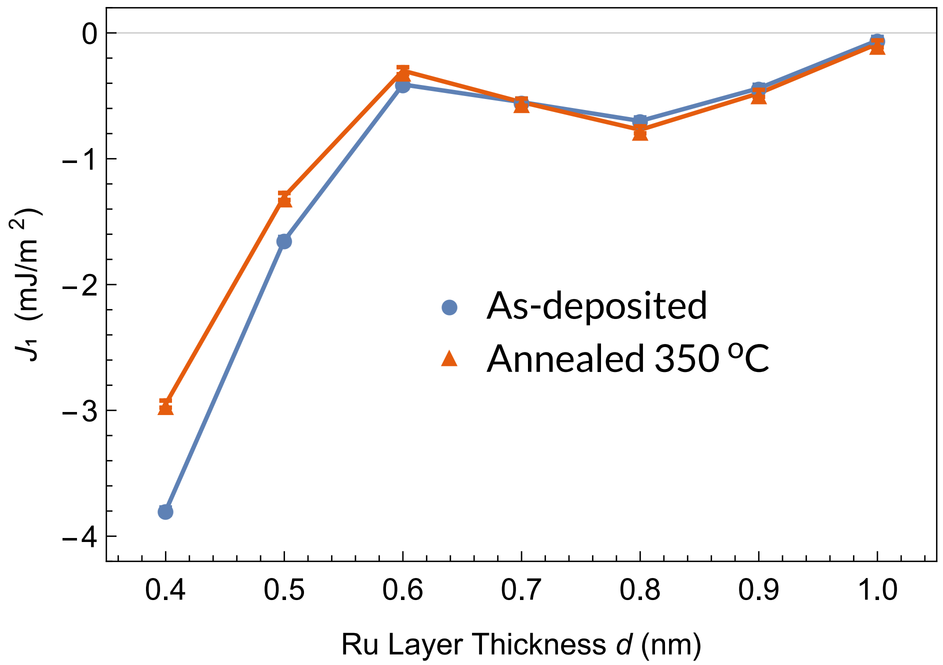

Figure 7.9: J_1 for the Co/Ru(d)/FeCo series of samples as deposited and annealed at 350 °C, with blue circles and orange triangles, respectively. The connecting lines are a guide to the eye.

Ta(2.5 nm)/Ru(3 nm)/Co(5 nm)/Ru(d)/$Fe_{75}Co_{25}$(34 nm)/Ta(4 nm), where d is the Ru spacer layer thickness and is varied from 0.4 to 1 nm. We then annealed the samples at 200, 250, 300, and 350 °C and measured J_1 and J_2. Figs. 7.8 and 7.9 show J_1 for these two series as deposited and annealed at 350 °C. These results show that even after annealing at 350 °C, coupling is only reduced slightly and still has regions of strong AFC coupling.

Since annealing at temperatures of greater than 200 °C is a required step for achieving the desired PMA and TMR in FeCoB/MgO tunnel junctions, further investigation needs to take place to determine the cause of the significant change in coupling we have seen. The obvious difference between the structures that are strongly effected by annealing and those that are not is the presence of boron within FeCoB. In the next chapter, we will investigate the role that boron has on interlayer exchange coupling and learn why it has such a strong effect on coupling.

Chapter 8

The Role of Boron on Interlayer Exchange Coupling in NiFe/Ru$_{1-x}$B$_x$/FeCo Trilayer Structures

In the previous chapter, we saw that the AFC coupling within FeCoB/Ru(d)/FeCoB trilayer structures was dramatically reduced and, in most cases, changed to strong FC coupling after the samples were annealed above 200 °C. We also demonstrated that AFC coupled trilayer structures of the form Co/Ru(d)/Co and Co/Ru(d)/FeCo did not show the same annealing dependence, and could be annealed to at least 350 °C and still have spacer layer thickness regions with strong AFC coupling. One obvious difference between these samples is the presence of boron in the magnetic layers.

In this chapter, we will investigate the role that boron has on interlayer exchange coupling and learn why it has such a strong effect on coupling after the samples are annealed. The first possibility, is that annealing the sample causes boron to diffuse from the magnetic layer into the Ru spacer layer, which creates a Ru-B alloy, and that this alloy exhibits FC coupling. In order to test whether this is the case, we have created samples where boron is only contained within the spacer layer. This allows us to isolate and study the scenario where boron has diffused into the spacer layer after annealing.

Another possible cause of the change of coupling from AFC to FC after annealing above 200 °C is that the presence of boron enhances diffusion of magnetic materials into the Ru spacer during the annealing step. It has been shown previously that a high enough concentration of ferromagnetic atoms within the Ru spacer layer can result in FC coupling. [82]

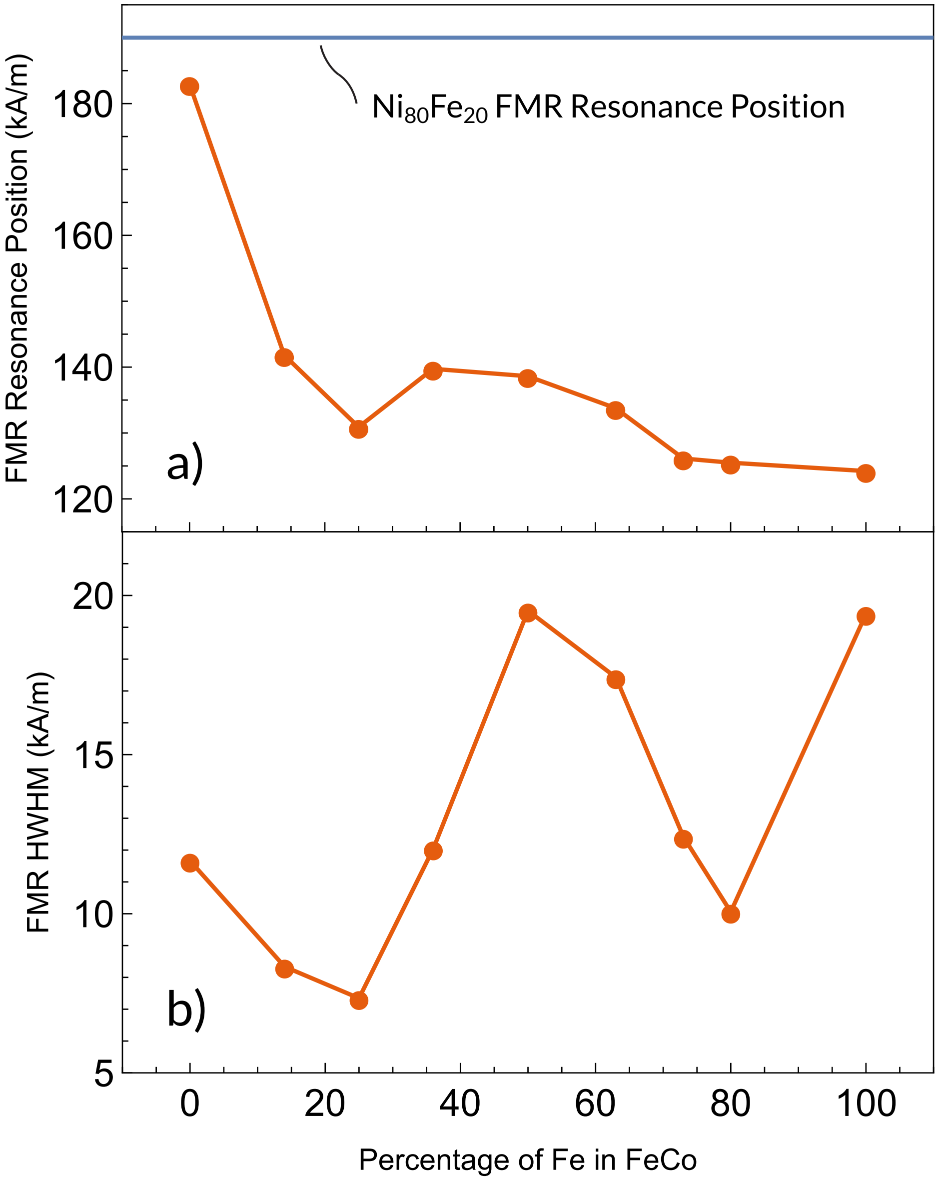

Figure 8.1: The FMR resonance position, a), and HWHM linewidth, b), of the Fe_xCo_{1-x} peak for the series of samples with the structure Ta(2.5 nm)/$Ni_{80}Fe_{20}$(6 nm)/Ru(100 nm)/Fe_xCo_{1-x}(33 nm)/Ta(4 nm) as the ratio of Fe to Co in the FeCo alloy is varied. The resonance position of $Ni_{80}Fe_{20}$ is also shown as the blue line for comparison. The connecting lines are a guide to the eye.

8.1 Experimental

8.1.1 Optimization of Magnetic Layer Composition

Our FMR experimental technique for determining coupling constants of two coupled magnetic layers separated by a non-magnetic spacer layer requires that we can determine the FMR resonance positions of both magnetic layers. This means that their resonance positions must be sufficiently well separated and have sufficiently narrow linewidths, as explained in chapter 4.2.

To determine the composition of the two coupled magnetic layers that meets these needs, we created a series of samples with the structure Ta(2.5 nm)/$Ni_{80}Fe_{20}$(6 nm)/Ru(100 nm) /Fe_xCo_{1-x}(3.3 nm)/Ta(4 nm), where we have co-sputtered Fe and Co at range of ratios from $x = 0$ to $x = 1$. We then measured the samples using FMR in order to determine the resonance positions and HWHM of the lines. We have chosen to fix the composition of $Ni_{80}Fe_{20}$ because it has relatively narrow linewidth, relatively low saturation magnetization, and also results in well textured Ru (0001) grown on top, all of which are desired.

Fig. 8.1 shows the FMR resonance position and HWHM of the FeCo peak for this series of samples. The results show that there are two ideal FeCo compositions that give well separated resonance positions with sufficiently narrow line widths. These compositions are approximately $Fe_{25}Co_{75}$ and $Fe_{80}Co_{20}$. We chose to use the latter composition and varied it slightly to $Fe_{75}Co_{25}$ so that the ratio of Fe to Co would match that of $Fe_{60}Co_{20}B_{20}$ used in other chapters of this thesis so that we could make better comparisons between samples containing the two.

8.1.2 Sample Preparation

In order to test whether boron diffusion into the Ru spacer layer is causing the change in coupling that we discussed in the previous chapter, we created a series of samples with different concentrations of boron within the Ru spacer layer. The exact structure that was sputtered is Ta(2.5 nm)/$Ni_{80}Fe_{20}$(6 nm)/$Ru_{1-x}B_x$(d)/$Fe_{75}Co_{25}$(4 nm)/Ta(4 nm), where the spacer layer thickness d is varied from 0.4 to 0.9 nm, and the boron concentration within the spacer layer x is varied from 0 to 0.15 in increments of 0.05, as is shown in Fig. 8.2. For brevity, we will sometimes refer to $Ni_{80}Fe_{20}$ and $Fe_{75}Co_{25}$ as NiFe and FeCo, respectively, throughout this chapter. These samples will be refereed to as the NiFe/RuB/FeCo series.

The samples are deposited by means of RF magnetron sputtering on oxidized Si substrates. The deposition conditions, sample preparation and RTA procedure are explained in detail in Chapter 3. All materials are deposited from 2" targets. After deposition, the samples are cut into 2 pieces. One piece is left as is, and the other is RTA in vacuum at 250 °C.

The coupling constants were determined using a combination of FMR and $M(H_{dc})$ measurements, along with our models explained in previous chapters. Our FMR model is

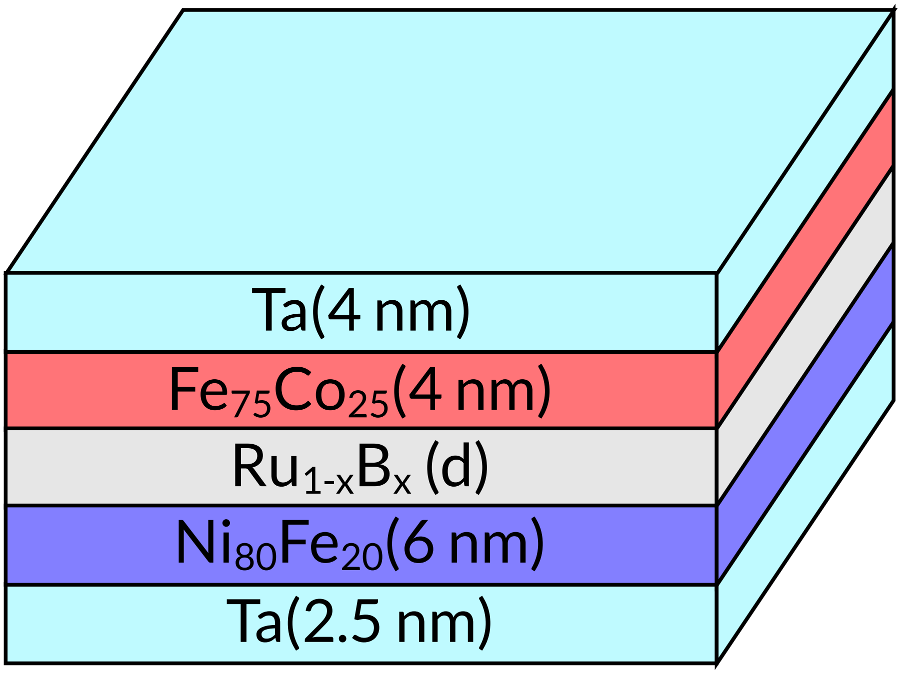

Figure 8.2: The thin film structure of the samples studied in this chapter. The numbers in parentheses indicate the layer thicknesses in nm, where d is varied from 0.4 nm to 0.9 nm, and x represents the fraction of boron in the ruthenium alloy, which is varied from 0 to 0.15.

incapable of differentiating J_1 and J_2. Instead we measure $J_{total} = J_1 - 2J_2$. However, for AFC or non-colinear (the angle between the magnetic moments of $\boldsymbol{M}_1$ and $\boldsymbol{M}_2$ is between 0 and 180) coupled samples, we are able to independently determine J_1 and J_2 from fitting $M(H_{dc})$ measurements with our micromagnetic model.

In order to investigate whether having boron within the Ru spacer layer causes increased diffusion of atoms from the adjacent magnetic layers into the Ru layer, we sputtered a second series of samples to be measured with EDXS. The structures of these samples are Ta(2.5 nm)/$Ni_{80}Fe_{20}$(0.8 nm)/$Ru_{1-x}B_x$(23 nm), where x is varied from 0 to 0.2 in increments of 0.05. These samples will be refereed to as the NiFe/RuB series. These samples were then cut into three different pieces. One of them was annealed at 250 °C, the second was annealed at 450 °C, and the third one was left as is. These samples are sputtered using the same deposition conditions as the first series of samples.

Spectrum imaging analysis based on EDXS was performed on the second series of samples in STEM mode. Prior to EDXS analysis, TEM lamellae were prepared using a Ga-focused-ion beam (FIB). To minimize sidewall damage, Ga ions with only 5 keV energy were used for final thinning of the TEM lamella to electron transparency. For more details, see Chapter 2.7.

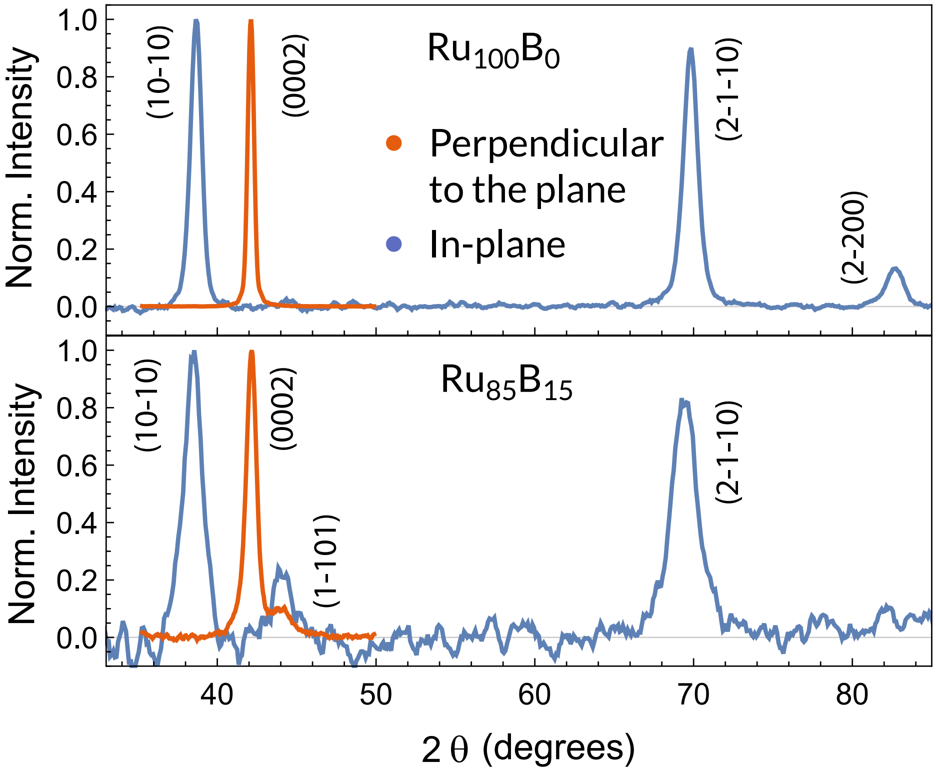

Figure 8.3: Example of typical XRD data for two NiFe/RuB series samples annealed at 250 °C with 0 and 15% boron. Blue lines are in-plane reflections, orange lines are reflections perpendicular to the plane. The patterns are consistent with an HCP structure.

This second series of samples were also characterized using XRD in order to determine the effect that adding B has on the Ru crystal lattice.

We also sputtered two additional samples in order to measure the saturation magnetization of the two magnetic layers. These samples have the structure $\mathrm{Ta(2.5\,nm)/Ni_{80}Fe_{20}(6\,nm)/Ru(3\,nm)}$ and $\mathrm{Ta(2.5\,nm)/Ru(3\,nm)/Fe_{75}Co_{25}(4\,nm)/Ta(4\,nm)}$. We then measured the magnetization of each of these samples using VSM up to fields of 7 T, and determined the two magnetic layers have saturation magnetizations of 804 ± 20 kA/m and 1556 ± 20 kA/m for the $Ni_{80}Fe_{20}$ and $Fe_{75}Co_{25}$ layers, respectively.

8.2 Results and Discussion

XRD patterns for two NiFe/RuB series samples, one with 0% B, and one with 15% B, both annealed at 250 °C are shown in Fig. 8.3. The XRD measurements are much more sensitive to the Ru and RuB layers rather than the Ta and NiFe layers due to the order of magnitude difference in their thickness. Thus, the dominant peaks in the XRD patterns are that of the Ru and RuB.

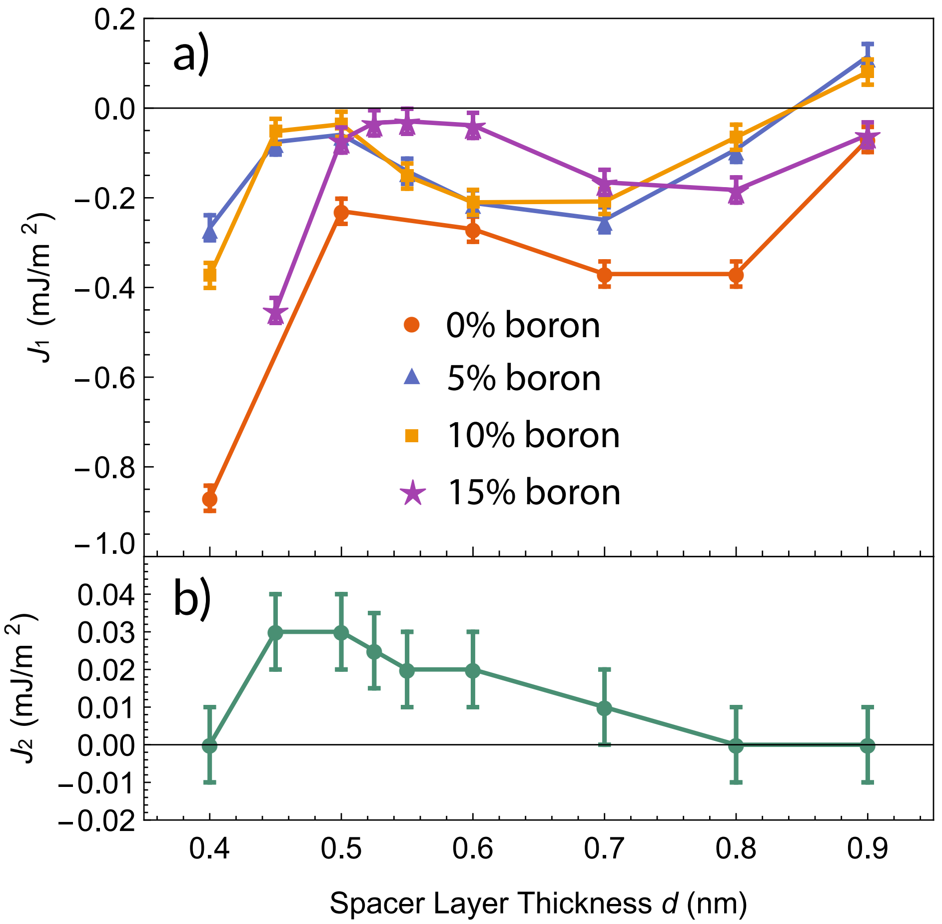

Figure 8.4: a) J_1, and b) J_2 coupling constants (as determined from VSM measurements), as a function of spacer layer thickness for as-deposited NiFe/Ru$_{1-x}$B$_x$/FeCo series samples. The concentrations of boron within the spacer layer was varied from 0 to 15%, as shown in the legend. The green data in b) is for all boron concentrations, as J_2 did not depend on the boron concentration. The connecting lines are a guide to the eye.

With 0% B, the Ru layer is very well textured along the [0002] direction. As we add more B to the Ru layer, it becomes less and less textured. In samples with 15% B, a small in-plane (1-101) peak is visible in the in-plane XRD pattern, as shown in Fig. 8.3. The small size of this peak indicates that the RuB layer is still mostly textured along the [0002] direction, but not as well textured as the Ru layer in the 0% B sample was. Maintaining a similar texture for the RuB layer for the whole range of compositions is ideal because it means that the FeCo layer on top will have the same texture throughout all of the samples, maintaining the FMR resonance position and narrow linewidth.

Measurements of J_1, a), and J_2, b), of the as-deposited NiFe/Ru$_{1-x}$B$_x$/FeCo series samples, with B concentrations within the RuB alloy of 0, 5, 10, and 15%, are shown in

Fig. 8.4. We were able to determine both J_1 and J_2 for all samples using a combination of our FMR technique and fitting $M(H_{dc})$ with our micromagnetic model. It can be seen that as the percentage of boron is increased, there is a slight decrease in coupling strength, and a shift of the coupling strength oscillations. These coupling strength oscillations are a characteristic indicator of RKKY-like coupling, which has been shown to be dependent on the properties of the spacer layer Fermi surface. [11] Thus, these changes in oscillatory behavior are likely the result of changes to the Fermi surface of the spacer layer caused by the increased B concentration. Similar effects have been seen when adding different concentrations of Ni into a Cu spacer layer. [85] These coupling oscillations will be studied in detail in Chapter 10.4.

Although the addition of boron into the spacer layer has changed the amplitude and period of RKKY-like coupling oscillations, it did not result in coupling changing from AFC to FC for spacer layer thicknesses between 0.4 and 0.9 nm. This indicates that for FeCoB/Ru/FeCoB SAF structures annealed above 200 °C [74], the change of coupling from AFC to FC for spacer layer thicknesses less than 0.6 nm is not the result of B diffusing into the Ru spacer layer alone. Instead, the annealing step must have some effect other than B diffusion into the Ru spacer layer that causes the FC region for spacer layer thicknesses less than 0.6 nm.

Fig. 8.4 shows that the dependence of J_2 on spacer layer thickness is very similar to what was seen in the previous chapter with FeCoB/Ru/FeCoB and FeCoB/Mo/FeCoB samples. J_2 increases with decreasing thickness, and goes to zero for thicknesses greater than 0.7 nm. J_2 was found to not depend on the concentration of boron within the spacer layer, as such, we have shown a single color for all data in Fig. 8.4 b).

Measurements of $J_1 - 2J_2$ and J_2 of the NiFe/Ru$_{1-x}$B$_x$/FeCo series samples annealed at 250 °C are shown in Fig. 8.5. Some samples had coupling strengths that were too strong to be measured using our FMR technique. For such samples, we determined if they were AFC or FC coupled using VSM. The connecting lines with arrows indicate that the coupling is FC and that the coupling strength is to large to be measured using our FMR technique. Our micromagnetic model only allows us to determine J_2 for samples that are not FC coupled where the magnetization of both magnetic layers isn't parallel. Additionally, when the two magnetic layers are very close to being parallel, ie. J_1 is positive, and J_2 is just slightly greater than $J_1/2$, we are unable to determine J_2 to a reasonable degree of accuracy. Because of this, we were only able to determine J_2 for some samples, which is why some points are missing from the figure. Since we couldn't determine all J_2 values, were were unable to determine J_1 from our FMR measurements. As such, we have shown $J_1 - 2J_2$ data as determined from our FMR measurements.

J_1 for the samples with boron in the spacer layer showed a much greater increase in FC coupling for thinner spacer layer thicknesses than the samples without boron in the spacer layer. The two magnetic layers are never fully FC coupled, where the magnetization

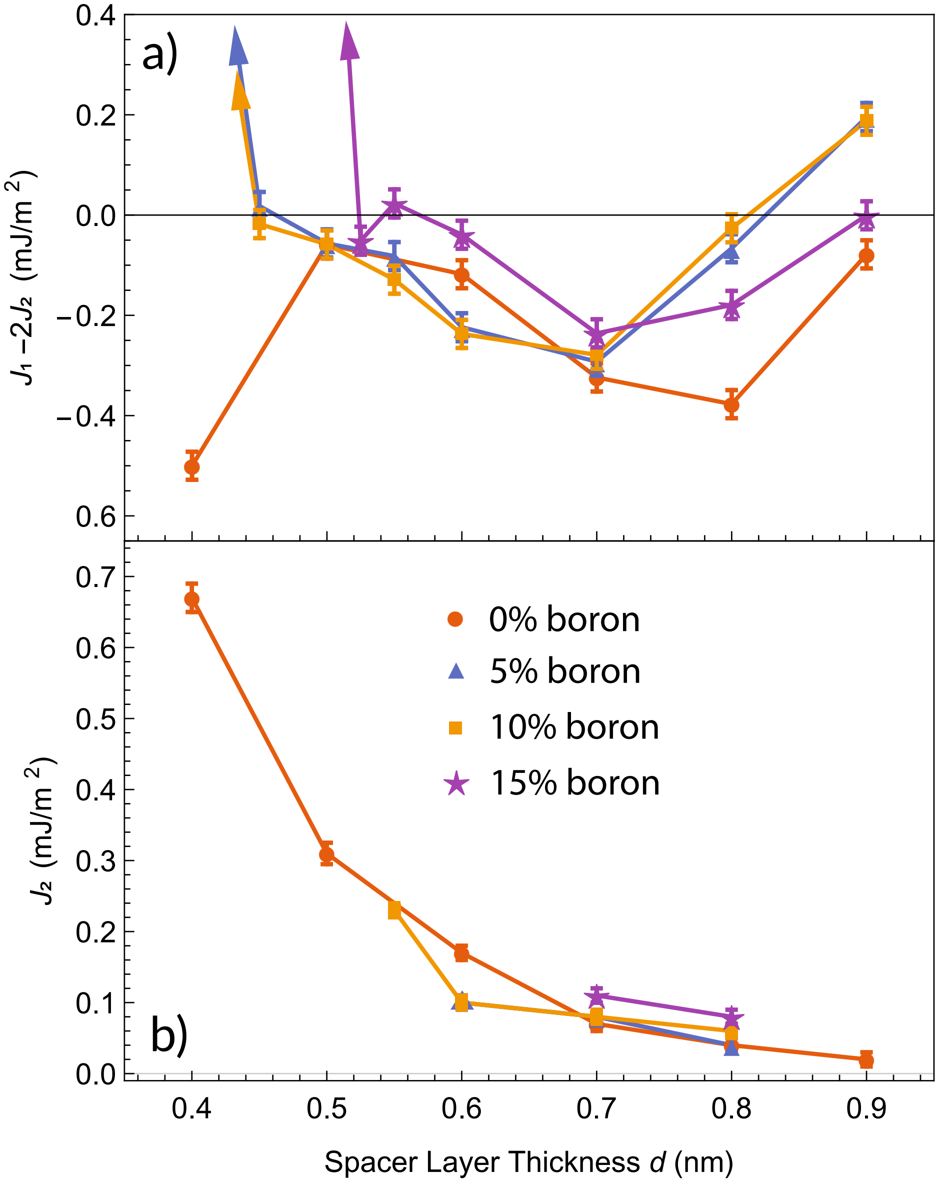

Figure 8.5: a) $J_1 - 2J_2$, and b) J_2 coupling constants (as determined from VSM measurements), as a function of spacer layer thickness for NiFe/Ru$_{1-x}$B$_x$/FeCo series samples after being annealed at 250 °C. The concentrations of boron within the spacer layer was varied from 0 to 15%, as shown in the legend. We were unable to measure J_2 for all samples. All J_2 values that we were able to determine are shown in b). The connecting lines with arrows indicate that the coupling is FC and that the coupling strength is to great to be measured using our FMR technique. The connecting lines are a guide to the eye.

of the two magnetic layers is parallel, for any samples without boron in the spacer layer with thicknesses from 0.4 to 0.9 nm. The samples with 5 and 10% boron have a strong FC region for spacer layers thinner than 0.45 nm, while the samples with 15% boron have a strong FC region for spacer layers thinner than 0.525 nm. These strong FC regions have replaced what was previously an AFC region before annealing. This is the same behavior as seen in FeCoB/Ru/FeCoB samples annealed above 200 °C with spacer layers less than 0.6 nm in the previous chapter. 7

J_2 for samples with 0% boron within the spacer layer increased after annealing for the entire range of spacer layer thickness tested. For the samples where we were able to measure J_2, it appears that adding boron into the spacer layer had a minimal effect. This can be seen for the datapoints for a spacer layer thickness of 0.7 and 0.8 nm where all samples could be measured. That said, it is likely that J_2 for these samples after annealing would differ from one another for thinner spacer layers where we were unable to determine the values for all samples.

These changes that we see to J_1 after annealing, in samples containing boron within the spacer layer, are the same as we saw previously in samples containing the FeCoB/Ru/FeCoB trilayer structure. Specifically, samples containing boron within the spacer layer have a strong AFC region for thin Ru spacer layers around 0.4 nm in thickness. But after annealing, this AFC thickness region of thickness becomes FC.

These results indicate that having boron in the sample causes the same effect after annealing regardless of whether the boron is in the magnetic FeCo layer or in the Ru spacer layer. This is likely due to a phenomenon known as transient enhanced diffusion (TED), which is well known in the semiconductor industry to cause boron to diffuse faster than is expected from normal thermal diffusion. [52] This would cause the boron atoms to diffuse rapidly into virtually all layers upon annealing, making them relatively uniformly distributed regardless of which layer they started in.

EDXS measurements of the elemental composition of the NiFe/$Ru_{1-x}B_x$ series samples with 15% boron within the Ru layer, as deposited, annealed at 250 °C, and annealed at 450 °C, are shown in Fig. 8.6. These results show the effect that annealing has on diffusion of the key elements, except boron, which was not accessible in the present analyses due to a strong overlap of the boron-K line with the Ru-M line.

Before annealing, there is a slight magenta background signal within the top Ru region. This may be partially due to a small amount of Fe diffusion resulting from the energy involved during the sputtering process, and the negative enthalpy of formation of RuFe. [97] Ni, on the other hand, has a positive enthalpy of formation with Ru, so it has not diffused into the RuB layer. Additionally, Fe fluorescence radiation caused by high-energy Ru X-rays is likely partially responsible for the magenta Fe signal within the top Ru region.

After annealing at 250 °C, we now see that the magenta Fe signal of the NiFe film is no longer superimposing with the cyan Ni signal, but has moved upwards towards the surface

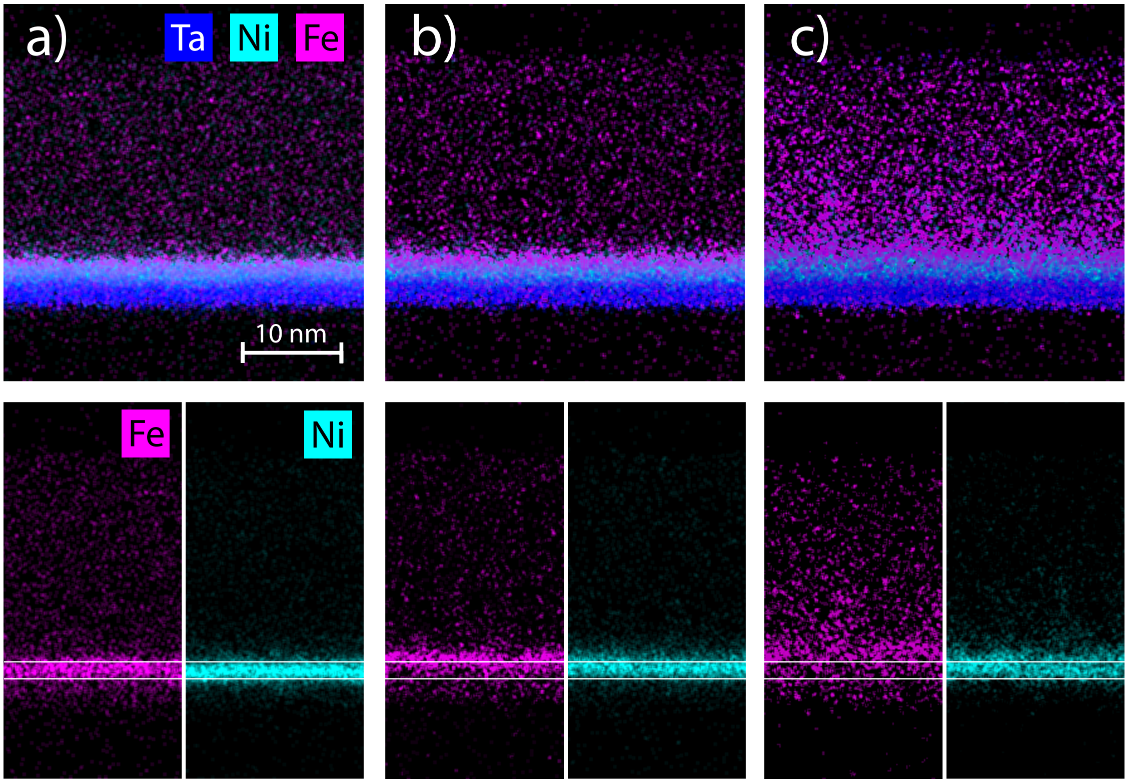

Figure 8.6: EDXS spectroscopy images of NiFe/Ru$_{1-x}$B$_x$ series samples with 15% boron within the Ru layer, a) as deposited, b) annealed at 250 °C, and c) annealed at 450 °C. Blue is Ta, cyan is Ni, and magenta is Fe. The second row of images is the same results from the adjacent image above, except looking at only the Fe signal on the left side, and only the Ni signal on the right side. The white horizontal lines in the second row are a guide to the eye to indicate where the NiFe layer was before annealing.

of the sample. This indicates that the bulk of the Ni and Fe atoms are beginning to separate within the NiFe layer. The Fe atoms have begun to diffuse into the RuB layer, while the Ni atom positions have been relatively unaffected. This differs from the as-deposited sample, in which Ni and Fe atoms are relatively uniformly mixed within the NiFe layer. For this sample annealed at 250 °C, we can see that the center of the Fe signal has moved slightly into the RuB layer (Fig. 8.6).

After annealing at 450 °C, we see that a large fraction of the Fe atoms have diffused into the RuB layer. Again, this is caused by the negative enthalpy of formation of Fe with Ru, and is in agreement with the results from Schmalhorst *et al.* [97], who found that in FeCo/Ru structures, Fe and Co, which also has a negative enthalpy of formation with Ru, diffused into the Ru spacer when annealed above 325 °C.

Fig. 8.7 shows the elemental composition line profiles, which have been extracted from EDXS measurements, for two NiFe/Ru$_{1-x}$B$_x$ series samples, one with 15% boron, and one with 0% boron in the Ru layer. Both samples were annealed at 250 °C, just like the

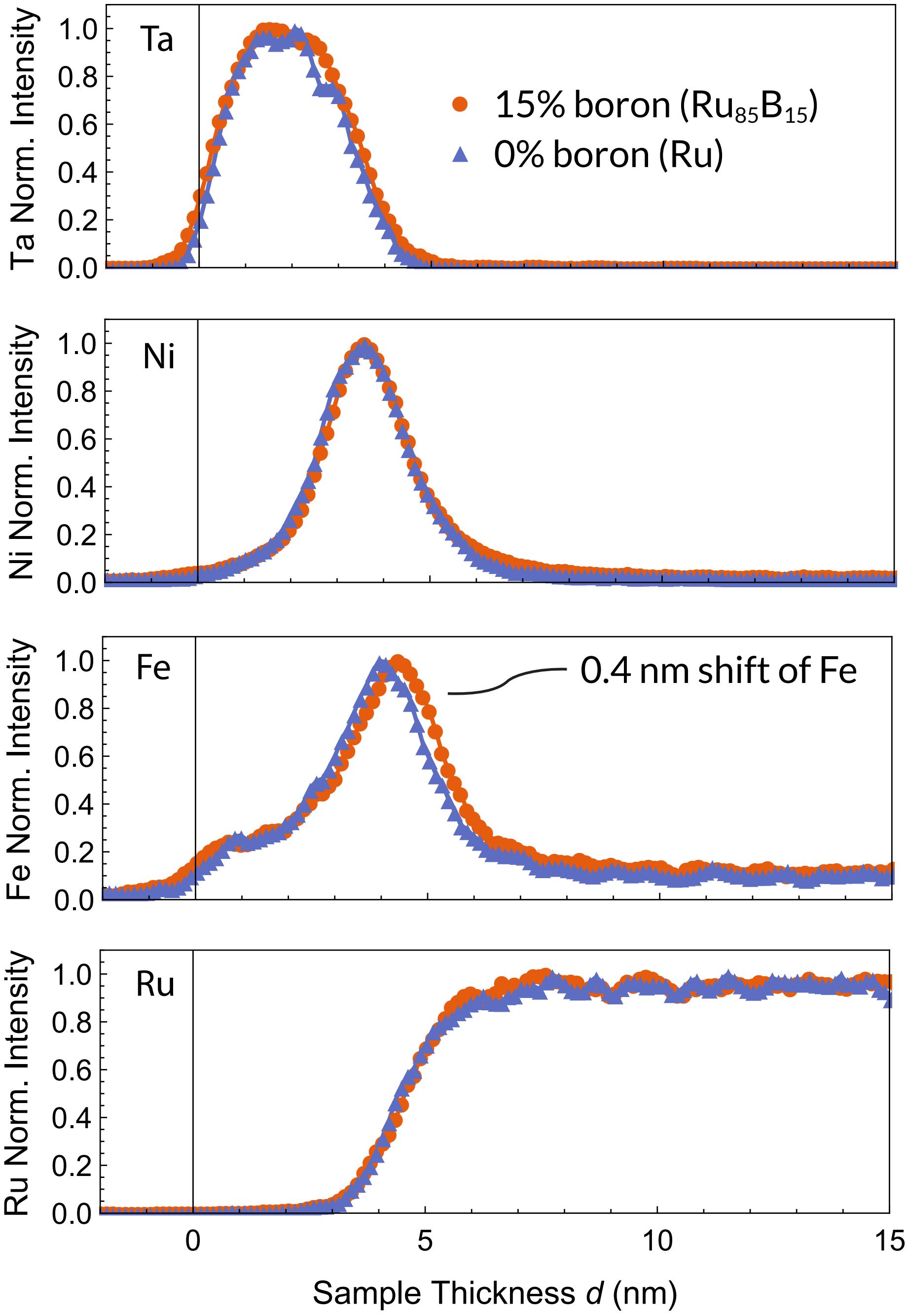

Figure 8.7: Line profiles showing the distribution of Ta, Ni, Fe, and Ru (from top to bottom) in NiFe/$Ru_{1-x}B_x$ series samples with 15% (orange) and 0% boron (blue) within the Ru layer, after being annealed at 250 °C.

NiFe/Ru$_{1-x}$B$_x$/FeCo series samples shown in Fig. 8.5. These results show the effect that adding boron to the Ru layer has on diffusion of the Ta, Ni, Fe, Ru atoms, after being annealed at 250 °C. It can be seen that the addition of boron has caused the Fe signal to shift 0.4 nm further into the top Ru layer than it did in the sample without boron. The Ta, Ni, and Ru signals were relatively unaffected by the addition of boron into the Ru layer. These results indicate that the presence of boron enhances the diffusion of Fe into the adjacent spacer layer.

The observed diffusion of Fe into Ru is likely responsible for the change in the sign of coupling in the 250 °C annealed NiFe/Ru$_{1-x}$B$_x$/FeCo series samples with 15% boron and for spacer layer thicknesses less than 0.525 nm as shown in Fig. 8.5. This diffusion increases the concentration of Fe atoms in the region of the Ru spacer layer close to the interface, to the point where thin Ru spacer layers become ferromagnetic. Nunn *et al.* have demonstrated the same effect by showing that in Co/Ru/Co films, a large concentration of Co or Fe in the Ru spacer layer causes a change in the sign of coupling from AFC to FC. [82] Furthermore, it is likely that the presence of boron would have a similar effect on the diffusion of Co into the spacer layer because it also has a negative enthalpy of formation with Ru. Therefore, NiFe/Ru$_{1-x}$B$_x$/FeCo series samples containing boron within the spacer layer, likely have increased Fe and Co diffusion from both the adjacent NiFe and FeCo ferromagnetic layers after annealing, causing the observed change in the interlayer coupling.

8.3 Summary

In summary, we studied the exchange coupling between NiFe and FeCo in NiFe/Ru$_{1-x}$B$_x$/FeCo SAF layer structures before and after annealing, with boron concentrations ranging from 0 to 15 at.%. The emphasis was on the spacer layer thickness between 0.4 nm and 0.9 nm for which the coupling is predominantly AFC in as-deposited samples.

In as-deposited samples, the presence of boron in the spacer layer was found to cause a small change in the amplitude and period of RKKY-like coupling oscillations, but did not cause the sign of coupling to change from AFC to FC. However, after annealing, the addition of boron in the spacer layer causes increased diffusion of Fe, and most likely Co, into the Ru spacer layer. This enhanced diffusion results in a change in sign of coupling from AFC to FC in samples with Ru spacer layers thinner than 0.45 nm, for 5 and 10% boron, and thinner than 0.525 nm for 15% boron.

The results in this chapter indicate that change in coupling from AFC to FC seen in our FeCoB/Ru/FeCoB samples from the previous chapter, for thinner spacer layer thicknesses after being annealed above 200°, may be caused by a 2 step process: 1) as the samples are annealed, boron begins to diffuse throughout the sample, including into the spacer layer, then 2) the presence of boron within the thin films cause an increase in diffusion of ferromagnetic atoms into the spacer layer. Finally, the diffusion of ferromagnetic atoms into the spacer layer results in FC coupling between the two magnetic layers for thinner spacer layer thicknesses.

One possible solution to eliminate this effect would be to place diffusion barriers between the FeCoB layers and the spacer layer so that boron and magnetic atoms would be unable to diffuse into the spacer layer. This is exactly what we will do in the next chapter.

Chapter 9

Diffusion Barrier to Achieve Annealing Resistant Strong AFC Coupling in FeCoB/Ru/FeCoB Trilayer Structures

In the previous chapter, we learned that the boron contained within the FeCoB layers in AFC coupled FeCoB/Ru/FeCoB trilayer structures was likely causing increased diffusion of ferromagnetic atoms into the Ru spacer layer during annealing, as compared to a structure without boron such as FeCo/Ru/FeCo. This increased diffusion of ferromagnetic atoms into the Ru layer results in a transition from AFC to FC coupling for thinner Ru layers, and makes it virtually impossible to achieve strong AFC coupling after annealing of films at temperatures of 200 °C or greater. If this is the case, then the insertion of a new boron-free layer between the Ru and FeCoB layers should act as a diffusion barrier to reduce diffusion of both boron and magnetic atoms during annealing, and maintain strong AFC coupling for thinner Ru layers. This technique is commonly employed effectively in the semiconductor industry, with diffusion barrier elements such as Ta and Ti, as they require an annealing step to activate the silicon dopants. [47, 72]

In this chapter, we will begin by determining the difference, in terms of coupling before and after annealing, between having the FeCoB layer above or below the Ru spacer layer. Next, we will study the effect of inserting a diffusion barrier next to the FeCoB layer in an attempt to stop diffusion of boron, and magnetic atoms, and maintain strong AFC coupling after annealing. Finally, we will demonstrate several different FeCoB-containing trilayer structures that are able to maintain strong AFC coupling even after being annealed at 350 °C for 30 minutes. These structures will be ideal for use in a fixed magnetic layer within a nanomagnetic device that requires an FeCoB/MgO/FeCoB tunnel junction.

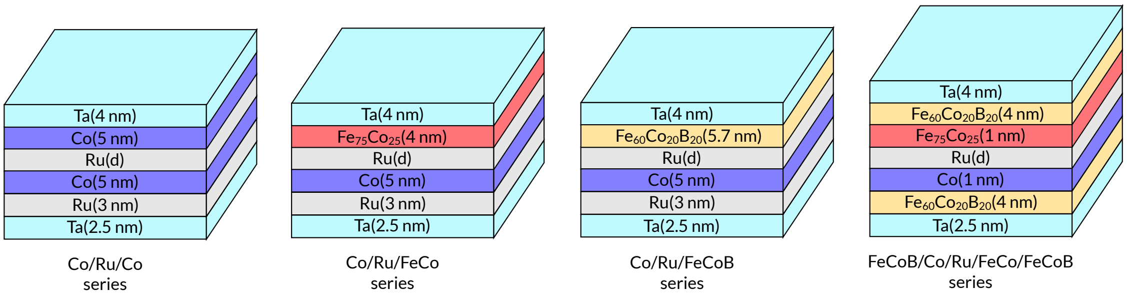

Figure 9.1: The thin film structures and names of the four series of samples studied in this chapter. The thickness of the Ru spacer layer, d is varied from 0.4 to 1 nm.

9.1 Experimental

The thin film structures and names of the series of samples studied in this chapter are shown in Fig. 9.1. The first series has the structure
Ta(2.5 nm)/Ru(3 nm)/Co(5 nm)/Ru(d)/Co(5 nm)/Ta(4 nm), where d is varied from 0.4 to 1 nm. This series will serve as a baseline for what to expect, in terms of coupling before and after annealing, when the structure doesn't contain any boron within any of the layers. The bottom Ru layer has been added to improve the (0001) texture of the Co layer above it, which also improves the (0001) texture of the Ru layer above that.

The second series has the structure
Ta(2.5 nm)/Ru(3 nm)/Co(5 nm)/Ru(d)/$Fe_{75}Co_{25}$(4 nm)/Ta(4 nm), where d is varied from 0.4 to 1 nm. This series will demonstrate increased AFC coupling strength for thinner Ru spacer layers and improved thermal robustness, as compared to the Co/Ru/Co series. This series will be referred to as the Co/Ru/FeCo series.

The third series has the structure
Ta(2.5 nm)/ Ru(3 nm)/Co(5 nm)/Ru(d)/$Fe_{60}Co_{20}B_{20}$(4 nm)/Ta(4 nm), where d is varied from 0.4 to 1 nm. This series will be used to determine whether the FeCoB layer on top of the spacer layer has the same effect, on coupling after the sample is annealed, as when there is an FeCoB layer both above and below the spacer layer. If this structure can maintain AFC coupling for thin Ru spacer layers after annealing, then it would be clear that it is the bottom FeCoB layer that is playing a larger role in the change in coupling seen after annealing. This series will be referred to as the Co/Ru/FeCoB series.

The fourth series has the structure
Ta(2.5 nm)/$Fe_{60}Co_{20}B_{20}$(4 nm)/Co(1 nm)/Ru(d)/$Fe_{75}Co_{25}$(1 nm)/
$Fe_{60}Co_{20}B_{20}$(4 nm)/Ta(4 nm) where d is varied from 0.4 to 1 nm. This series will be used to study the effect that placing a thin Co and FeCo diffusion barrier into the top and bottom FeCoB/Ru interfaces in the FeCoB/Ru/FeCoB structure has on coupling. The bottom Ru layer that was present in the other structures is missing, but the Co and Ru spacer layers

are still well textured in the (0001) direction, as confirmed using XRD. This series will be referred to as the FeCoB/Co/Ru/FeCo/FeCoB series.

We will also be comparing these four series to the samples studied in Chapter 7 containing a FeCoB/Ru/FeCoB trilayer structure.

We also grew some additional samples to investigate the texture of Ru when grown on top of different underlayers. These additional samples have the structures Ta(2.5 nm)/Ru(1 nm)/Co(1.2 nm)/Ru(11 nm) and Ta(2.5 nm)/$Fe_{60}Co_{20}B_{20}$(4 nm)/ Co(1 nm)/Ru(11 nm). The Ru (0002) peak rocking curve for these samples were measured using perpendicular XRD measurements. These samples will be referred to as Ru/Co/Ru and FeCoB/Co/Ru for brevity. In the Ru/Co/Ru series, the bottom Ru layer is an order of magnitude thinner than the top Ru layer, and is not expected to cause X-Ray reflections of significant intensity. Therefore, the Ru (0002) rocking curve measurement of this sample is a good indication of the texture of the top Ru layer.

Although the top Ru layers in the Ru/Co/Ru and FeCoB/Co/Ru samples are much thicker than the spacer layers of the other series of samples being studied, the texture of the first few atomic layers will, to an extent, continue as more layers are deposited on top. Thus, the width of the rocking curve for a 11 nm Ru layer will give us a good indication of the texture of Ru spacer layers.

We cut all of the samples grown from the four series (not including the additional samples) into two pieces, and annealed one of them at 350 °C for 30 minutes. We chose to anneal at this temperature because it was the temperature where J_1 and J_2 began to change in Co/Ru/Co samples. Thus, this is close to the highest temperature any devices containing boron-free layers can be annealed before having their functionality destroyed by diffusion. Any increased diffusion caused by boron will also be amplified at this temperature, allowing us to be very confident in any conclusions we draw from these results. We then measure $M(H_{dc})$ (magnetization as a function of external magnetic field) of all as-deposited and annealed samples using VSM up to a field of 7 T. Finally, we determine J_1 and J_2 for all samples in the three series using the VSM measurements and our micromagnetic model.

The samples are deposited by means of RF magnetron sputtering on oxidized Si substrates. The deposition conditions and sample preparation are explained in the previous chapter. In this chapter we are using a different annealing procedure as compared to the previous chapter. We now use a heating rate of 20 °C/min instead of the 60 °C/min that was used previously. We have also left the samples at the set temperature for 30 minutes now. See Chapter 3.1.4 for details.

According to the results from Chapter 7, we expect that at our new annealing temperature of 350 °C, an FeCoB/Ru/FeCoB trilayer structure would be strongly FC coupled for a wide range of spacer layer thickness of at least 0.7 nm. In order to confirm that the new annealing procedure results in the same expected behavior, we sputtered several new samples with the structure

Ta(2.5 nm)/$Fe_{60}Co_{20}B_{20}$(5 nm)/Ru(d)/$Fe_{60}Co_{20}B_{20}$(5 nm)/Ta(4 nm), where d ranges from 0.4 to 0.8 nm. We then measured the coupling strength by fitting VSM measurements, both before and after annealing at 350 °. We found that after annealing all of the samples were FC coupled, as expected. Thus, we are confident that both annealing procedures are comparable.

The saturation magnetization of the various magnetic layers studied in this section were determined from VSM measurements. We first determined the M_s of the Co layers using measurements of the Co/Ru/Co series of samples. After that, we were able to determine the M_s of the FeCo and FeCoB layers from measurements of the Co/Ru/FeCo and Co/Ru/FeCoB series of samples. We went through this process for all thicknesses of magnetic layers used, as shown in Fig. 9.1, to determine any thickness dependence that M_s might have, and to ensure we have the correct value for each layer tested. The determined values for FeCo are 1250 ± 20 kA/m and 1550 ± 20 kA/m for 1 nm and 4 nm thick layers, respectively. We found that, for thicknesses of 1 and 5 nm, the M_s for Co is independent of layer thickness, with a value of 1350 ± 20 kA/m. We also found that, for thicknesses of 4 and 5.7 nm, the M_s for FeCoB is independent of layer thickness, with a value of 1270 ± 20 kA/m.

For the FeCoB/Co/Ru/FeCo/FeCoB series of samples, since our micromagnetics model handles each atomic plane independently, we gave each plane the correct M_s corresponding to its composition. In other words, we modeled all 4 magnetic layers separately so we didn't have to take the average M_s for the bottom and top magnetic layers.

9.2 Results and Discussion

Fig. 9.2 shows J_1 and J_2 results for the Co/Ru/Co series of samples as deposited and annealed at 350 °C, with blue circles and orange triangles, respectively. It can be seen that all samples are AFC coupled both before and after annealing for the entire range of spacer layers tested. There is a first and second AFC peak around 0.4 nm, and 0.8 nm, respectively. After annealing, J_1 for the first peak decreases in magnitude from -3.10 ± 0.03 mJ/m^2 to -1.55 ± 0.03 mJ/m^2 at an Ru spacer layer thickness of 0.4 nm, while the second peak remained relatively the same, changing from -0.90 ± 0.03 mJ/m^2 to -0.85 ± 0.03 mJ/m^2.

J_2 for the Co/Ru/Co samples increases with decreasing Ru spacer layer thickness, and is approximately zero for spacer layers with thickness greater than 0.7 nm. After annealing, the magnitude of J_2 increases slightly for all Ru spacer layers less than 0.8 nm in thickness, while increasing dramatically for spacer layer thickness of 0.4 nm. At 0.4 nm spacer layer thickness, J_2 increased from 0.20 ± 0.03 mJ/m^2 to 0.70 ± 0.03 mJ/m^2.

Even though J_2 increases after annealing, J_1 is still large enough to hold the coupling angle at 180 °. Thus, even after annealing at a temperature of 350 °C, the trilayer structures maintained strong AFC coupling. This is unlike the FeCoB/Ru/FeCoB trilayer structures

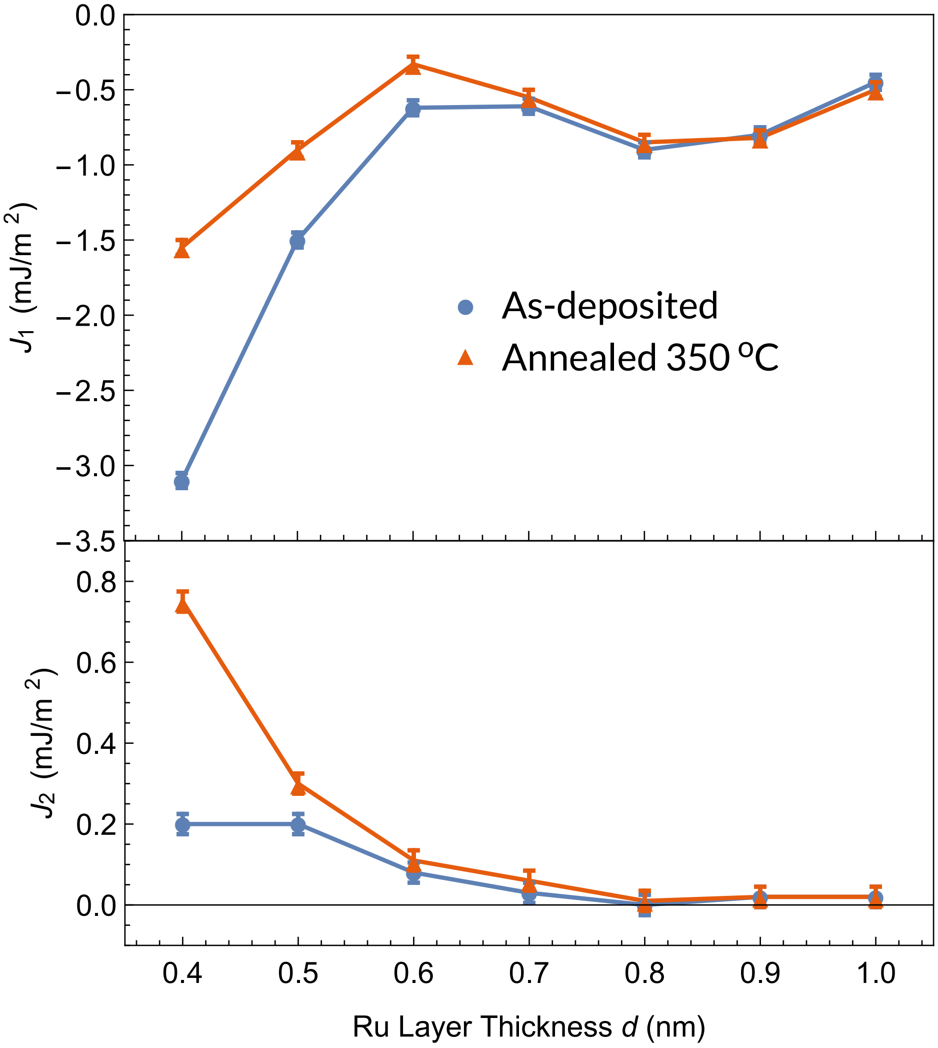

Figure 9.2: J_1 and J_2 for the Co/Ru(d)/Co series of samples as deposited and annealed at 350 °C, with blue circles and orange triangles, respectively. d is the thickness of the Ru spacer layer. The connecting lines are a guide to the eye.

studied previously that lost their AFC coupling, for Ru spacer layers in this range of thicknesses, after annealing beyond only 200 °C.

Fig. 9.3 shows J_1 and J_2 results for the Co/Ru/FeCo series of samples as deposited and annealed at 350 °C, with blue circles and orange triangles, respectively. Just like for the Co/Ru/Co series, all samples are AFC coupled both before and after annealing for the entire range of spacer layers tested. Unlike the Co/Ru/Co series, however, the Co/Ru/FeCo series maintains a more negative J_1, and similar J_2 for thin Ru spacer layers of around 0.4 nm, meaning that it maintains stronger AFC coupling at the first AFC peak. This series was

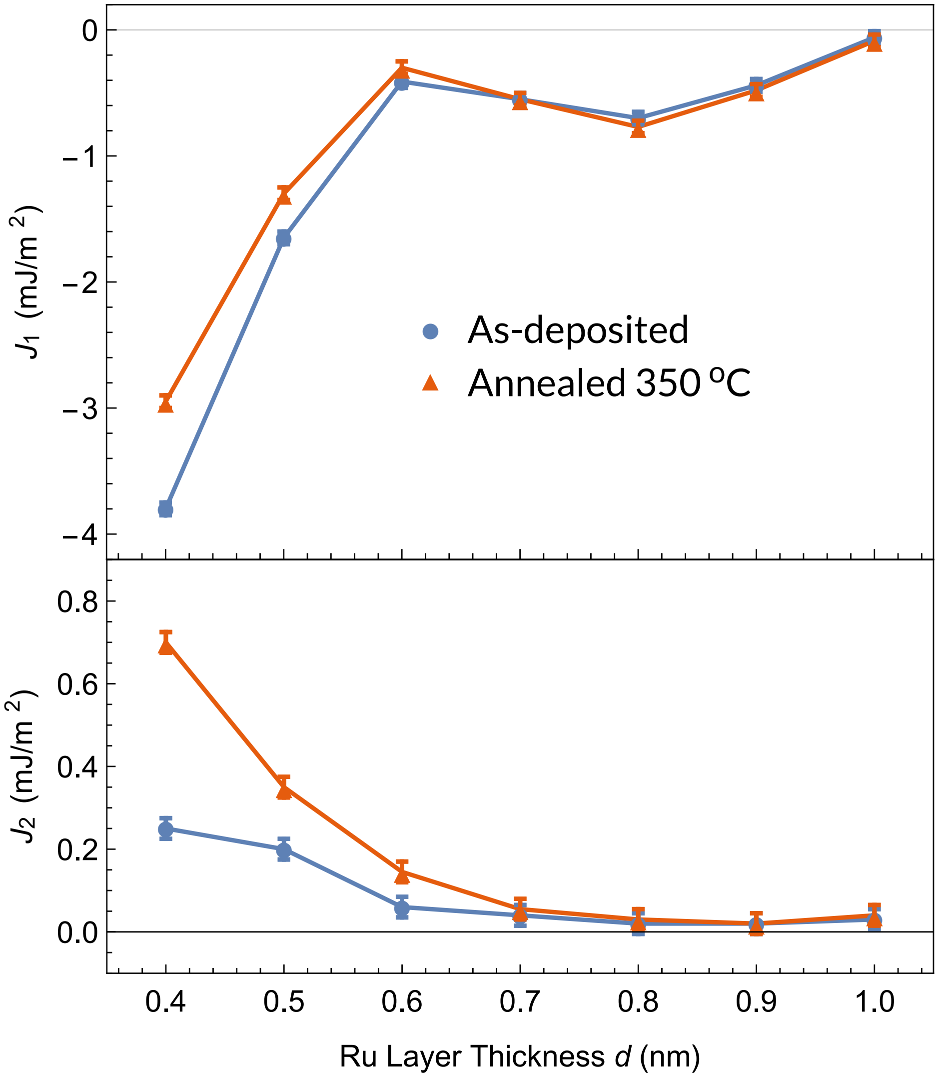

Figure 9.3: J_1 and J_2 for the Co/Ru(d)/FeCo series of samples as deposited and annealed at 350 °C, with blue circles and orange triangles, respectively. d is the thickness of the Ru spacer layer between the two Co layers. The connecting lines are a guide to the eye.

also less affected by annealing, changing from -3.8 ± 0.03 mJ/m^2 to -2.95 ± 0.03 mJ/m^2 for as-deposited and annealed samples, respectively.

J_2 for the Co/Ru/FeCo series of samples, as shown in Fig. 9.3, is approximately the same as that of the Co/Ru/Co series.

Just like the Co/Ru/Co series of samples, all of the Co/Ru/FeCo series samples maintain a 180°C coupling between the two magnetic layers.

Since both RuFe and RuCo have negative enthalpy of formation, they likely both diffuse into the Ru spacer layer during annealing. We have confirmed this for the case of Fe atoms diffusing into the Ru spacer layer in the previous chapter. That would mean that after annealing of the Co/Ru/Co samples, the Ru spacer layer will be alloyed with a small amount of Co. On the other hand, after annealing the Co/Ru/FeCo samples, the Ru spacer layer will be alloyed with a small amount of Co and Fe. Since the top layer is 75% Fe, mostly Fe atoms will diffuse from the top while only Co atoms can diffuse in from the bottom, which should result in an approximate 50/50 ratio of Co and Fe alloyed into the Ru spacer layer.

Nunn *et al.* deposited related samples with the structure Co(2 nm)/$\mathrm{Ru}_{1-x}\mathrm{Co}_x$(d)/Co(2 nm) and Co(2 nm)/$\mathrm{Ru}_{1-x}\mathrm{Fe}_x$/Co(2 nm), where d is varied from 0.4 to 1.4 nm, and x is varied from 0 to 1. [82] They alloyed a known concentration of Co and Fe into the Ru spacer layer by cosputtering Ru with Fe or Co. They found that adding Co to the Ru layer decreased J_1 and increased J_2. This is exactly what we see after annealing our Co/Ru/Co series of samples, indicating that Co has likely diffused into the Ru layer.

Conversely, Nunn *et al.* found that adding Fe into the Ru layer causes J_1 to increase until more than 50% of Fe has been added, at which point J_1 begins to decrease. They also found that adding Fe into the Ru layer increases J_2 similarly to adding Co to Ru. The J_1 measurements of our Co/Ru/FeCo series of samples after annealing decreased in magnitude less than for the Co/Ru/Co series, which is indicative of Fe diffusing into the Ru layer from the top FeCo layer, which would increase J_1 and help offset the decrease caused by Co.

Comparing our results with that of Nunn *et al.*, it is clear that the effects we see in terms of J_1 and J_2 after annealing our samples are consistent with Co and Fe atoms diffusing into the Ru layer from the adjacent magnetic layers.

These results show that stronger AFC coupling that is more resistant to changes caused by annealing is achieved by using a Co/Ru/FeCo structure rather than Co/Ru/Co, making the former case more ideal for fixed layers within nanomagnetic devices.

Fig. 9.4 shows J_1 and J_2 results for the Co/Ru/FeCoB series of samples as-deposited and annealed at 350 °C, with blue circles and orange triangles, respectively. Here we see quite a different situation after annealing than we had when FeCoB was below the Ru layer as well, which can be seen in Fig. 7.5. In that case, after annealing at 200 °C, there were no longer any regions of spacer layer thicknesses with strong AFC coupling, and when annealed at 300 °C, all of the samples within this entire range of spacer layer thicknesses exhibited FC coupling. Conversely, for the new Co/Ru/FeCoB series, where we only have an FeCoB layer on top of the Ru spacer layer, the two magnetic layers remain AFC coupled even after being annealed at 350 °C. Furthermore, we now see that J_1 remains approximately unchanged after annealing, having two regions of strong AFC coupling at Ru spacer layer thicknesses of approximately 0.4 and 0.8 nm.

J_2 for the Co/Ru/FeCoB series of samples is approximately the same as that of the Co/Ru/FeCo series before being annealed. However, after annealing, we see that J_2 doesn't increase quite as much for the Co/Ru/FeCoB series as it did for the Co/Ru/FeCo series.

Like the previous two series of samples, all of the samples measured in the Co/Ru/FeCoB series, except for the one with an Ru spacer layer of 1.0 nm after being annealed at 350 °C,

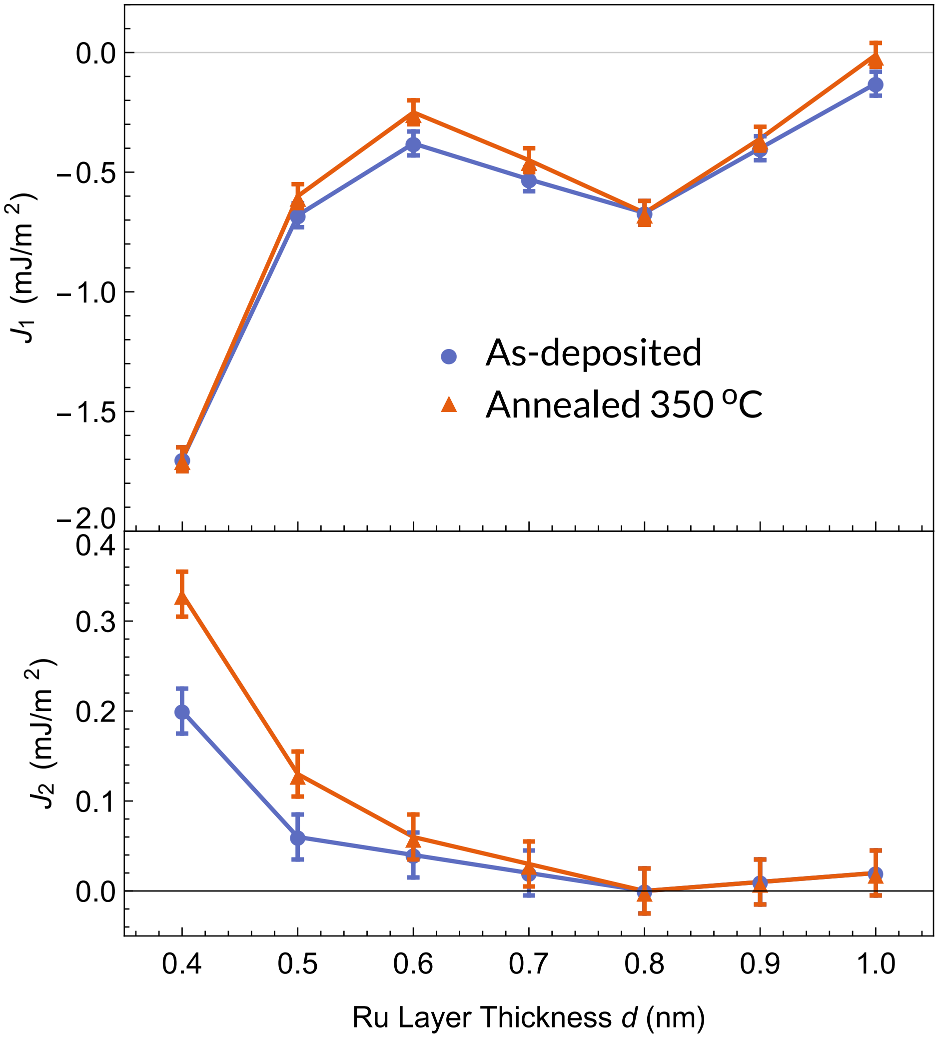

Figure 9.4: J_1 and J_2 for the Co/Ru(d)/FeCoB series of samples as deposited and annealed at 350 °C, with blue circles and orange triangles, respectively. d is the thickness of the Ru spacer layer between the two Co layers. The connecting lines are a guide to the eye.

are fully AFC coupled with the two magnetic layers having their magnetization oriented 180° relative to one another.

This series of samples is also interesting because after annealing, the top FeCoB layer crystallizes to become the same composition as the FeCo layer in the Co/Ru/FeCo sample, both with the same ratio of Fe to Co in the top layer. That would effectively give the two series the same structure and composition. Thus, we can attribute any differences between the two series as being caused by the boron that was initially in the top FeCoB layer. For Ru spacer layers of 0.4 and 0.5 nm, the Co/Ru/FeCoB series exhibits J_1 values that are approximately half as much as the Co/Ru/FeCo series after both series have been annealed. For Ru spacer layers thicker than 0.5 nm, coupling is approximately the same between the

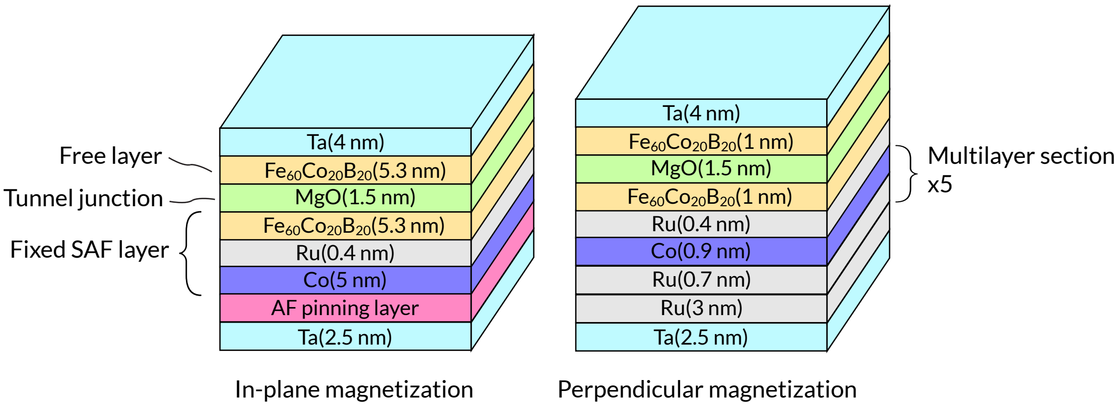

Figure 9.5: Proposed approximate structures for in-plane and perpendicularly magnetized FeCoB/MgO/FeCoB tunnel junctions for use in STT-MRAM devices.

two series both before and after being annealed. This difference in coupling between the two series for 0.4 and 0.5 nm Ru spacer layer thickness, shows that having FeCoB on top appears to increase diffusion of magnetic atoms into the Ru spacer layer, which is causing the AFC coupling to become weaker.

Although we do see a reduction in AFC coupling strength for 0.4 and 0.5 nm Ru spacer layer thickness in the Co/Ru/FeCoB series as compared to the Co/Ru/FeCo series, it is a much smaller effect than when we had FeCoB on both sides of the Ru layer. This indicates that boron within the magnetic layer below the spacer layer has a larger role in causing increased diffusion of magnetic atoms into the spacer layer during the annealing process. One possible explanation is that this is due to a phenomenon that sometimes occurs during the sputter deposition process in which a very small fraction of the atoms in a layer can effectively float on the surface of the sample as more layers are being deposited on top. [2] This only occurs for some elements and not others. For our EDXS measurements that were made in the previous chapter, shown in Figs. 8.6 and 8.7, we were unable to determine if boron was floating to the surface of the sample because there is a strong overlap of the boron-K line with the Ru-M line which causes the Ru and boron signal to be indistinguishable from one another. However, in the work done by Arora *et al.*, they saw, in their EDXS images, evidence of several different elements floating on the surface during the deposition process. [2] Thus, it is possible that something similar is occurring here, where a small amount of the boron within the FeCoB layer is floating upwards towards the Ru layer during the deposition process. This could increase the concentration of boron at the FeCoB/Ru interface, or even increase the concentration of boron within the Ru layer. If the latter is occuring, it would lead to increased diffusion of magnetic atoms into the Ru layer during the annealing process, just as we found in the previous chapter.

These results for the Co/Ru/FeCoB series of samples have revealed one possible solution to create a SAF fixed layer for a nanomagnetic device, such as STT-MRAM, that utilizes an

FeCoB/MgO/FeCoB tunnel junction. Fig. 9.5 shows this solution for both the in-plane and perpendicularly magnetized configuration. This is made possible by having the SAF fixed layer on the bottom, so that the FeCoB layer that needs to be AFC coupled to another layer is above the Ru spacer layer. These proposed structures have only approximate thicknesses of the layers, which would need to be optimized. The 1.5 nm MgO tunnel junction layer was chosen because that thickness has been shown to result in the largest TMR of 604% for the in-plane magnetization configuration. [49] The relative thickness of the Co and FeCoB layers within the SAF fixed layer were chosen so that they would have zero net magnetic moment, assuming an M_s of 1350 and 1275 kA/m for the Co and FeCoB layers, respectively. The FeCoB layer thickness in the perpendicularly magnetized configuration was chosen because this thickness was shown to result in the largest PMA, which would pull the FeCoB layer magnetization out of the plane. [103] The fixed layer in the perpendicularly magnetization configuration includes 5 multilayers of Co/Ru. These are added because they contain significant PMA that helps ensure the layer is perpendicularly magnetized. Another option for that layer would be Co/Ni multilayers which also have PMA. [2] The in-plane magnetized configuration includes an antiferromagnetic (AF) pinning layer below the fixed layer. This is required because it stops the fixed layer from rotating in the plane, which would be possible otherwise because of the lack of in-plane magnetic anisotropy.

Fig. 9.6 shows J_1 and J_2 results for the FeCoB/Co/Ru/FeCo/FeCoB series of samples as deposited and annealed at 350 °C, with blue circles and orange triangles, respectively. Some datapoints for Ru spacer layer thicknesses of 0.9 and 1.0 nm are missing because the magnetic layers were FC coupled, which means we were unable to determine the coupling constants using magnetostatics measurements. We were also unable to determine coupling strengths using our FMR measurement technique because the FMR absorption lines for the two magnetic layers were not separated enough. That said, we have a large enough range of data in order to draw some useful conclusions.

We can see that the addition of the Co and FeCo diffusion barriers into the FeCoB/Ru interfaces has resulted in coupling that remains AFC for Ru spacer layer thicknesses of 0.8 nm and less, and strongly AFC coupled for Ru thicknesses of 0.5 nm and less, after annealing at 350 °C. We can compare this to results from FeCoB/Ru/FeCoB trilayer structures, where coupling became strongly FC when annealed above 200 °C, for spacer layer thickness of 0.7 nm and less. By comparing these two results, it appears as though the Co and FeCo layers are acting as effective diffusion barriers and reducing the diffusion of boron towards the Ru layer. The results in boron no longer being able to increase the diffusion of magnetic atoms into the spacer layer during the annealing process.

Another thing to notice is that J_1 for as-deposited samples of the FeCoB/Co/Ru/FeCo/FeCoB series, for spacer layer thickness of 0.4 and 0.5 nm, are about 2/3 of the magnitude of J_1 of the Co/Ru/FeCo series even though the spacer layer and two adjacent interfaces have the same composition. One possible cause of this difference could

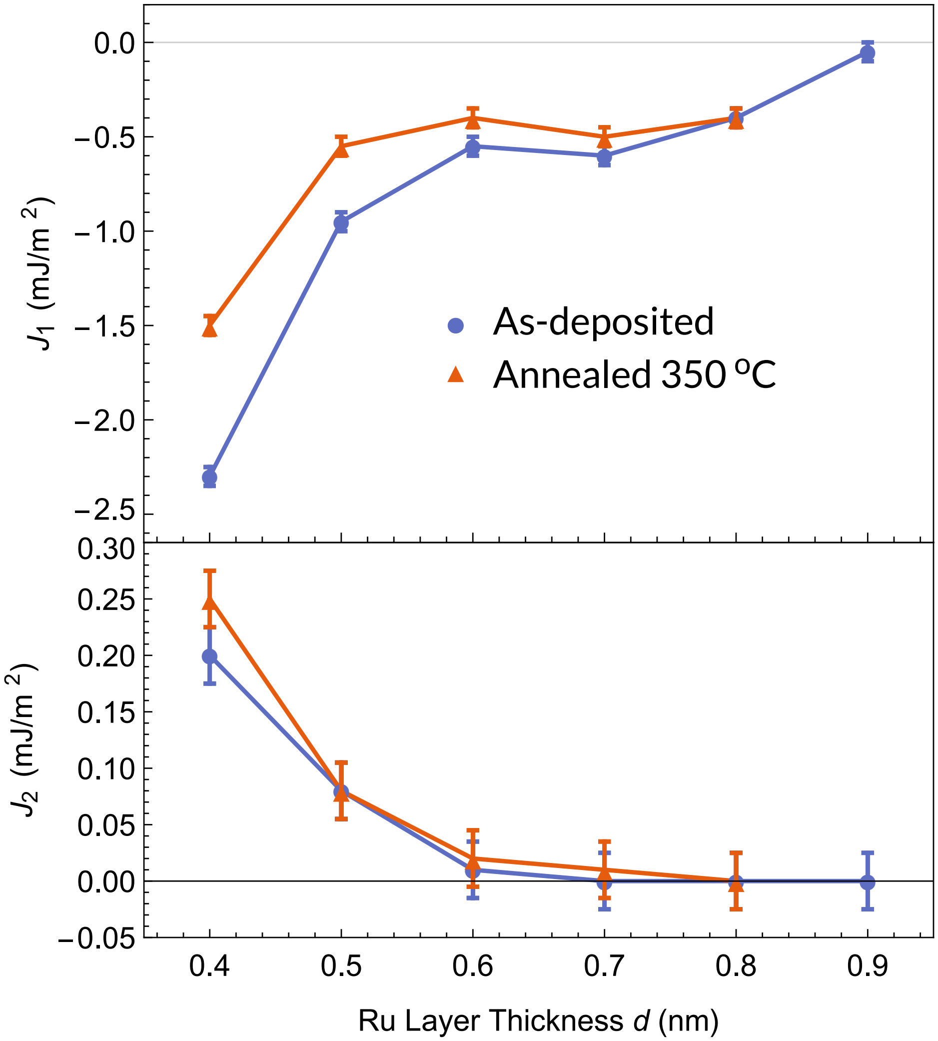

Figure 9.6: J_1 and J_2 for the FeCoB/Co/Ru(d)/FeCo/FeCoB series of samples as-deposited and annealed at 350 °C, with blue circles and orange triangles, respectively. d is the thickness of the Ru spacer layer between the two Co layers. The connecting lines are a guide to the eye.

be that the spacer layers are slightly different in each case. In order to find a difference between the two spacer layers, we measured the Ru (0002) rocking curve of the Ru/Co/Ru and FeCoB/Co/Ru samples. The resulting rocking curves have a FWHM of 3.95 and 6.58° for the Ru/Co/Ru and FeCoB/Co/Ru samples, respectively. One thing that a wider rocking curve can indicate, is that the layer may have increased dislocations and lattice defects. [64, 76, 45, 108, 8] If this is occurring, the defects will increase the scattering of the electrons responsible for interlayer exchange coupling, reducing, in turn, the size of the oscillatory coupling. [106] The wider rocking curve also indicates that the spacer layer crystalites are not all oriented so that coupling across the spacer layer is exactly in the [0001] direction. Instead,

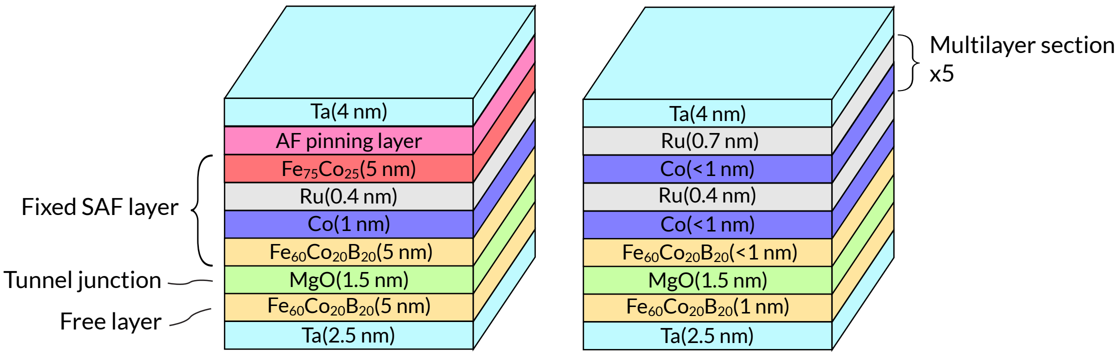

In-plane magnetization

Perpendicular magnetization

Figure 9.7: Proposed approximate structures for in-plane and perpendicularly magnetized FeCoB/MgO/FeCoB tunnel junctions for use in STT-MRAM devices.

the direction of coupling, which is normal to the magnetic layer/spacer layer interface, is slightly different for each crystallite and the sum is a superposition of coupling in a distribution of directions centered around the [0001] direction. This results in a distribution of critical spanning vectors, and a distribution in the periods of oscillation of interlayer exchange coupling. The end result will be the smearing out of shorter period oscillations, which can manifest itself as a reduction in the magnitude of J_1. These two effects are likely to be a significant cause of the decrease in magnitude of J_1 measurements for the FeCoB/Co/Ru/FeCo/FeCoB series as compared to the Co/Ru/FeCo series.

J_2 for the FeCoB/Co/Ru/FeCo/FeCoB series is approximately the same as for the Co/Ru/FeCoB series, except being even less affected by the annealing process. In the latter case we see approximately 60% increase in J_2 at a Ru spacer layer thickness of 0.4 nm, while in the former case we see only a 25% increase for the same thickness, and remaining approximately the same for the rest of the thicknesses.

These results for the FeCoB/Co/Ru/FeCo/FeCoB series of samples have revealed additional solutions that can be potentially used to create a SAF fixed layer for a nanomagnetic device, such as STT-MRAM, that utilizes an FeCoB/MgO/FeCoB tunnel junction. Since the structure in this series of samples sits on top of an FeCoB layer, it is suitable for devices that need to have the fixed layer at the top of the layer stack. Fig. 9.7 shows two approximate layer structures for both the in-plane and perpendicularly magnetized configuration that contain strongly AFC coupled fixed layers sitting on top of an FeCoB/MgO/FeCoB tunnel junction. The thickness of the layers were chosen for the same reasons as described above. For the perpendicularly magnetized case, we have proposed a layer structure that is a combination of the structure of the FeCoB/Co/Ru/FeCo/FeCoB and Co/Ru/FeCoB series of samples. The AF pinning layer, and the Co/Ru multilayers have been added for the same reasons discussed earlier. Like our previous examples, the thicknesses of the layers in these proposed structures are only approximate and would need to be optimized through experiment. One may also need to insert a thin Ta layer above the top FeCoB layer so that, during annealing, the FeCoB layer crystalization nucleates at the MgO interface. If this is done, our results from Chapter 7 can be used to determine which Ta layer thicknesses result in strong coupling.

9.3 Summary

We have shown that J_1 of a Co/Ru/FeCo trilayer structure is increased in magnitude for spacer layers thinner than 0.6 nm as compared to J_1 of a Co/Ru/Co trilayer structure. We have also shown that J_1 of a Co/Ru/FeCo trilayer structure is approximately twice as strong as compared to J_1 of a Co/Ru/Co trilayer structure, for spacer layers thinner than 0.6 nm, after annealing at 350 °C. This is thought to be caused by Fe diffusing into the Ru spacer layer when there is an adjacent FeCo layer, which has been shown to increase J_1 for Fe concentrations up to 50%. [82]

We have shown that having an FeCoB layer on both sides of the Ru spacer layer, in a structure such as FeCoB/Ru/FeCoB, leads to a much larger change in coupling after annealing as compared to a structure where FeCoB is only above the Ru layer, in a structure such as Co/Ru/FeCoB. J_1 in samples containing the Co/Ru/FeCoB trilayer structure was found to remain AFC even after the sample was annealed at 350 °C, up to a spacer layer thickness of at least 1 nm.

We have shown that inserting thin 1 nm Co and FeCo diffusion barriers into the FeCoB/Ru interfaces of an FeCoB/Ru/FeCoB SAF appears to stop the diffusion of boron into the Ru spacer layer. This, in turn, allows the magnetic layers to remain AFC coupled even after being annealed at temperatures of up to 350 °C, for spacer layers up to 0.8 nm.

We have demonstrated the ability to create samples that contain FeCoB layers that are strongly AFC coupled to another magnetic layer to form a SAF fixed layer structure. These SAF fixed layers remain strongly AFC coupled even after being annealed at 350 °C, making them ideal structures for use in devices with FeCoB/MgO/FeCoB tunnel junctions, where they require an annealing step at a temperature of between 200 °C and 350 °C in order to achieve large PMA and TMR. This is in contrast to the behavior of two AFC coupled FeCoB layers across an Ru spacer layer which we have shown previously to become FC coupled after annealing above 200 °C, for spacer layers as thick as 0.7 nm.

Using our results in this work, we have proposed 4 possible layer structures that can potentially be used as part of a nanomagnetic device, such as a STT-MRAM device containing FeCoB/MgO/FeCoB tunnel junction. These proposed layer structures contain a SAF fixed layer with zero net magnetization and have significantly reduced stray fields. In addition, we have proposed example structures where the fixed layer is below the FeCoB/MgO/FeCoB tunnel junction, and above it. Allowing the use of these results in a larger range of devices that may require the fixed layer to be on one side or the other due to external factors.

Chapter 10

Analysis of Oscillatory Interlayer Exchange Coupling Between Various Magnetic Layers Across Ruthenium Based Spacer Layers.

Throughout the previous chapters in this thesis, we studied interlayer exchange coupling and its dependence on annealing for several different trilayer structures. Those chapters were focused on the particular problem of trying to create a SAF fixed layer structure that includes FeCoB that can withstand annealing while maintaining AFC coupling of the magnetic layers. However, it was seen that the dependence of J_1 on the spacer layer thickness, particularly Ru based spacer layers, in coupled trilayer structures exhibited oscillations that varied in both magnitude and period from series to series.

In this chapter we will dive deeper into the physics of these J_1, or bilinear, interlayer exchange coupling oscillations. Specifically, we will study the interlayer exchange coupling oscillations in all of the trilayer series of samples containing Ru-based spacer layers. We will use the RKKY-like model known as the interface-reflection model, as explained in a previous chapter 4.1.2, to understand the oscillations, and why they differ from series to series.

This chapter will be broken up into different sections that focus on specific series of samples, or comparisons between different series of samples.

10.1 Theory

In order to use the interface-reflection interlayer exchange coupling model, as described by Eq. 4.17, we first need to determine the critical spanning vectors $q_{\perp}^{\alpha}$ for the spacer layer, which is Ru textured in the [0001] direction in our case. In order to have the most accurate values, we have determined the critical spanning vectors from experimental measurements of the Ru Fermi surface from Refs. [21] and [54].

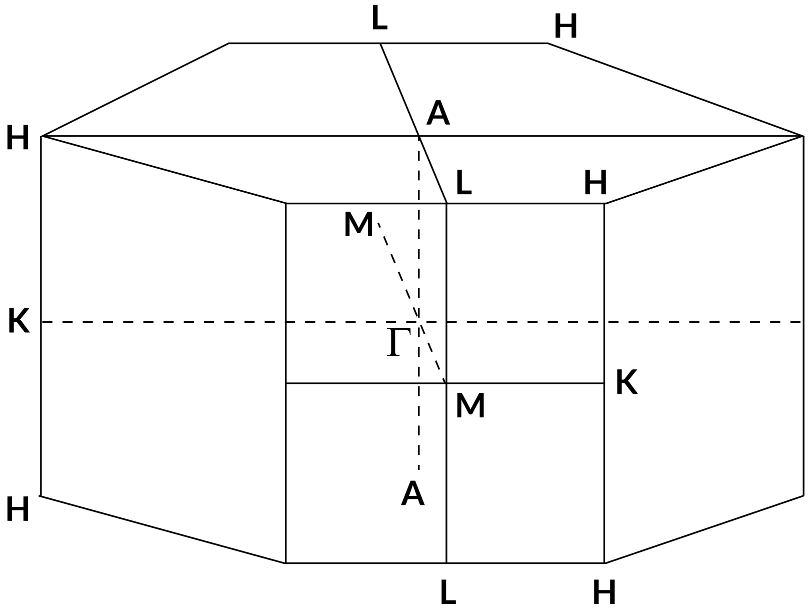

Figure 10.1: The Brillouin zone for hexagonal close packed (HCP) Ru with relevant high symmetry points labeled.

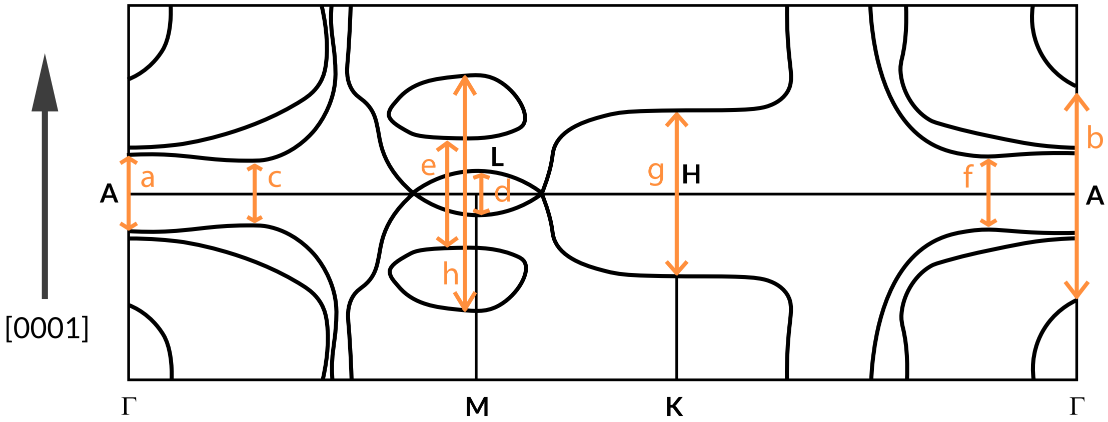

Figure 10.2: A selection of single-sheet critical spanning vectors for a Ru spacer layer in the [0001] direction. The orange arrows labeled a to h are the critical spanning vectors. The vectors are superimposed on top of two mirrored Ru Fermi surface diagrams based on the one from Ref. [54], which have been created using the LMTO method and fit to experimentally determined sheet radii obtained through Haas-van Alphen measurements in Ref. [21]. The values for these vectors can be found in Table 10.1.

Table 10.1: A selection of single-sheet real critical spanning vectors and phase shifts for a Ru spacer layer in the [0001] direction corresponding to the labeled vectors in Fig. 10.2. All of the $q_\perp^\alpha$ values were obtained from Refs. [21, 54] where they measured the values experimentally as determined by the de Haas-van Alphen effect. Labels denoted with * are approximated from the (LMTO) Fermi surface fit to Haas-van Alphen measurements, while the others are obtained directly from Haas-van Alphen measurements. Note, these critical spanning vectors are for bulk Ru. All of these critical spanning vectors start and stop on the same Fermi surface sheet. The phase shifts are determined by the Fermi surface topology.

Label	$q_\perp^\alpha$ (nm^{-1})	ϕ^α (radians)
a_1^*	3.01	π
a_2^*	2.54	$\pi/2$
b	9.21	π
c*	1.61	π
d*	1.86	0
e	3.77	π
f*	2.08	$\pi/2$
g*	6.89	π
h*	9.43	0

A selection of the real critical spanning vectors for bulk Ru in the [0001] direction are shown in Fig. 10.2 superimposed on top of two mirrored slices of the Fermi surface diagram, labeled from a to h. The Fermi surface diagram is from Ref. [54], and was calculated using the linear-muffin-tin-orbital method (LMTO) and fit to experimentally determined sheet radii obtained through Haas-van Alphen measurements in Ref. [21]. The labeled high symmetry points in the Fermi surface diagram correspond to locations in the Brillouin zone for Ru as shown in Fig. 10.1. The critical spanning vector lengths, along with their phase shifts ϕ^α are also shown in Table 10.1. Labels denoted with * are approximated from the LMTO Fermi surface fit to Haas-van Alphen measurements, while the others are obtained directly from Haas-van Alphen measurements. The phase ϕ^α of each state α is defined by the topology of the Fermi surface of the spacer layer at the endpoints of its critical spanning vector $q_\perp^\alpha$. For thick spacer layers, ϕ^α is equal to 0, $\pi/2$, and π when the Fermi surface at this location is a minimum, a saddle point, and a maximum, respectively. [12]

Critical spanning vectors that correspond to evanescent states cannot be measured experimentally in bulk material. They have been measured in finite systems such as photonic crystals [94], however, those are for different materials than we are studying here. As such, the only way to determine the evanescent state critical spanning vectors is to simulate the complex Fermi surface with methods such as the LMTO method, which is known to be only approximately correct without fitting to experimental results. The complex Fermi surface sheets are also very intricate and numerous, leading to a large number of imaginary critical spanning vectors. [10] Thus, instead of calculating the expected decay lengths of any imaginary critical spanning vectors, we will leave the decay lengths as fitting parameters and allow the fit to J_1 measurements to determine the appropriate decay lengths.

If there are any imaginary critical spanning vectors in Ru(0001), the exponentially decreasing contribution to J_1 means that one with the largest decay length will dominate. Thus, we have chosen to approximate the sum of any possible imaginary critical spanning vectors with a single exponentially decaying term. For other metallic spacer layers with simpler Fermi surfaces, like Cu, Ag, Au, most of the imaginary critical spanning vectors, if any, have decay lengths of between 0.2 and 0.5 nm. [10] Therefore, we have chosen to limit the range of the decay length fitting parameter to between 0.1 and 1 nm, and allow the fit to determine exactly which decay length fits the data best. This term has the form

$$J_1(d) = \frac{-J^\alpha}{d^2} e^{-d/\delta_\perp^\alpha}, \tag{10.1}$$

where we constrain $0.1 \text{ nm} < \delta_\perp^\alpha < 1 \text{ nm}$ and we have also assumed $e^{i\phi^\alpha} = -1$ because the purpose of this non-oscillatory term is to account for antiferromagnetic coupling in our case.

The interface-reflection interlayer exchange coupling model [10, 105] only takes into account critical spanning vectors within the same sheet. So, we will not include any critical spanning vectors between two different sheets.

Using these critical spanning vectors, we can now fit our experimental J_1 data with Eq. 4.17 in order to determine the coupling constants corresponding to each critical spanning vector, J^α.

It should be noted that in this section we will use the non SI electron volt (eV) unit for J^α so that it can be directly compared to the predicted values in Ref. [105].

10.2 Lack of a Non-Oscillatory Contribution to Bilinear Interlayer Exchange Coupling in Co/Ru(d)/Co Structures

Interlayer exchange coupling in Co/Ru multilayers has been studied previously by Parkin *et al.* [88] by measuring the saturation field and magnetoresistance of the samples. Their measurements showed the expected RKKY-like J_1 oscillations, except with the addition of an antiferromagnetic bias. In some cases this would cause the oscillations to be entirely within the antiferromagnetic region and not cross into the ferromagnetic region.

Lacroix *et al.* explained that this behavior could be attributed to a type of superexchange-like coupling that can occur across metallic spacer layers containing discrete density of states at energy levels that are split for spin up and spin down electrons. [66] This superexchange-like contribution would result in a logarithmically increasing antiferromagnetic component to J_1.

Later, Bruno *et al.* [10, 9] proposed an interlayer exchange coupling theory, which is the one we are using here, that unifies coupling across insulators and metals. This theory

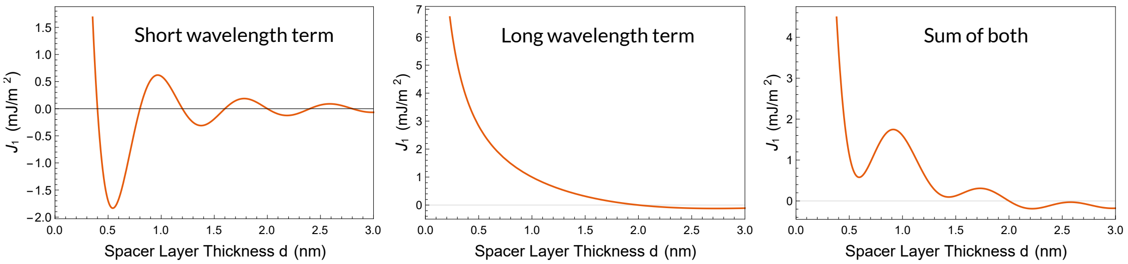

Figure 10.3: Demonstration of apparent non-oscillatory behavior created from the addition of short and long period oscillating terms in the sum in Eq. 4.17, which is purely RKKY-like coupling without any superexchange-like contributions. Each plot is of Eq. 4.17 with parameters $q_\perp^\alpha = 7.8$ nm^{-1}, $\phi^\alpha = 0$ for the short period oscillations, and $q_\perp^\alpha = 1.57$ nm^{-1}, $\phi^\alpha = 0$ for the long period oscillations.

predicts that, just like coupling across insulators, coupling across metals can also have an exponentially decreasing non oscillating contribution caused by evanescent waves.

It is possible that the antiferromagnetic bias seen in coupling across thin Ru spacer layers could be explained by either of these two theories. However, a close look at just the oscillatory terms in Eq. 4.17, which we have shown explicitly in Eq. 4.22, will show that, for thinner spacer layers, they can account for what appears to be non-oscillatory coupling. Eq. 4.22 is composed of a sum where each term has a sinusoidal oscillating part multiplied by a $1/d^2$ dependence, where d is the thickness of the spacer layer. The period of oscillations of the sinusoidal part is determined by the critical spanning vectors of the spacer layer material. For short period oscillations, they oscillate faster than the $1/d^2$ decay, which makes them look clearly oscillatory. But for the longer period oscillations, it is possible that they can oscillate more slowly than the $1/d^2$ decay, which makes those terms look like a non-oscillatory contribution. This is demonstrated in Fig. 10.3, where we have shown a plot of a short period oscillation term, a long period oscillation term, and the sum of the two. Each plot is obtained from Eq. 4.17 where the first two plots are individual terms of the sum, with parameters $q_\perp^\alpha = 7.8$ nm^{-1}, $\phi^\alpha = 0$ for the short period oscillations, and $q_\perp^\alpha = 1.57$ nm^{-1}, $\phi^\alpha = 0$ for the long period oscillations, and the final plot is the sum of the two other plots. It can be seen that the plot of the sum of the two terms appears to have oscillations with a non-oscillatory background, but the background is really just another term in the sum with longer period oscillations.

To our knowledge, there is no consensus on whether the apparent antiferromagnetic bias in exchange coupling across thin Ru layers is caused by the logarithmic non-oscillatory coupling as described by Lacroix *et al.*, or the exponential non-oscillatory coupling due to evanescent electron states, or the standard oscillatory RKKY-like coupling.

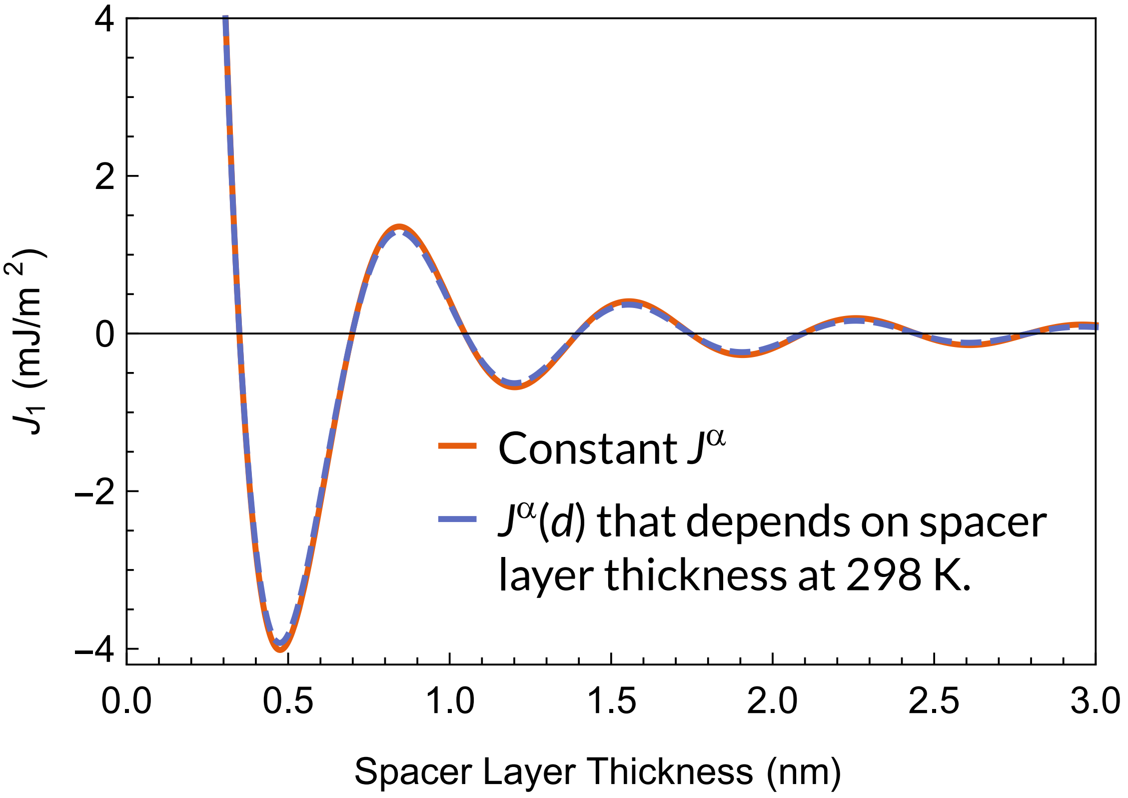

Figure 10.4: J_1 for a single critical spanning vector as determined by Eq. 4.17 with $q_\perp^\alpha = 9$ nm^{-1}, $J^\alpha = 1$ mJ/m^2, $v_\perp^\alpha = 8 \times 10^5$ m/s, $D_\phi^\alpha = 2 \times 10^{19}$ J^{-1}. The orange line is assuming a constant J^α, and the dashed blue line uses a $J^\alpha(d)$ that depends on the spacer layer thickness due to $F^\alpha(d, T)$ at 298 K.

Thus, before we can proceed to analyze the bilinear interlayer exchange coupling of our Ru based trilayer structures, we need to determine if the physics is accurately described using only real critical spanning vectors, or if a non-oscillatory contribution is required.

In this section, we will determine this by fitting Eq. 4.17 to J_1 measurements for samples containing Co/Ru(d)/Co trilayer structures over a wide range of spacer layer thicknesses from 0.4 to 3.4 nm. We have chosen this particular trilayer structure because it contains the same single layer structure as the multilayers created by Parkin *et al.*, which is what sparked this non-oscillatory discussion. To gain additional insight, we will also fit the temperature dependence of J_1 for several different spacer layer thicknesses.

It should be noted that when fitting J_1 oscillations measured at room temperature, using Eq. 4.17, we have assumed that J^α doesn't depend on spacer layer thickness. This is only approximately correct since the temperature dependence term, $F^\alpha(d, T)$, within J^α has a weak thickness dependence. However, it is a much smaller contribution than the $1/d^2$ dependence that J_1 already has, and can be safely ignored. Fig. 10.4 shows the accuracy of this approximation for J_1 for a single critical spanning vector with $q_\perp^\alpha = 9$ nm^{-1},

$J^\alpha = 1$ mJ/m^2, $v_\perp^\alpha = 8 \times 10^5$ m/s, $D_\phi^\alpha = 2 \times 10^{19}$ J^{-1}. These are all typical values for critical spanning vectors for Ru spacer layers. [32, 67, 27] It can be seen that this approximation is fairly accurate.

Temperature Dependence Theory

The interface-reflection model predicts that any superexchange-like contribution to J_1 caused by evanescent states will have the opposite temperature dependence to RKKY-like oscillating contributions. This has also been verified by experiment. [10] We will investigate the J_1 temperature dependence in our thinner spacer layer samples to determine which kind of coupling we have, and whether there is a superexchange-like contribution.

At zero temperature, $F^\alpha(d, T = 0) = 1$, then as temperature increases, $F^\alpha(d, T)$ becomes larger or smaller. The effect of this is to simply scale J^α from its zero temperature value, and subsequently, it scales the critical spanning vector's contribution to J_1. Because of this, the temperature dependence of each term in Eq. 4.17 can be re-written as the temperature dependence multiplied by the zero temperature coupling strength:

$$J_1(d, T) = \sum_\alpha J_1^\alpha(d, T = 0) F^\alpha(d, T), \tag{10.2}$$

where

$$J_1^\alpha(d, T) = \mathrm{Im} \frac{J^\alpha(d, T)}{d^2} e^{i(q_\perp^\alpha d + \phi^\alpha)}, \tag{10.3}$$

which is just an individual term from within the sum in Eq. 4.17, and we have explicitly showed that $J^\alpha(d, T)$ is a function of the spacer layer thickness and temperature, and $F^\alpha(d, T)$ is given by 4.19. Because of the oscillatory or exponential contribution to $J_1^\alpha(d, T)$, the weighting of the temperature dependence of each term will change in magnitude relative to one another depending on the spacer layer thickness.

The contributions from any evanescent states are exponentially decreasing functions and they will dominate for thinner spacer layers. Therefore, if they exist, we would expect J_1 to increase with temperature for thinner spacer layers, similarly to the blue line in Fig. 4.11.

In order to determine $J_1^\alpha(d, T = 0)$ for use in Eq. 10.2, we will use the bulk Ru $q_\perp^\alpha$ values from Table. 10.1, and the J^α values obtained from the fit of room temperature J_1 data. With these, we can calculate the room temperature $J_1^\alpha(d, T = 298\text{ K})$ for each critical spanning vector.

This is related to the zero temperature $J_1^\alpha(d, T = 0)$ by the relation $J_1^\alpha(d, T = 298\text{K}) = J_1^\alpha(d, T = 0) \times F^\alpha(d, T = 298\text{ K})$. Thus, we can determine $J_1^\alpha(d, T = 0)$ by

$$J_1^\alpha(d, T = 0) = \frac{J_1^\alpha(d, T = 298\text{K})}{F^\alpha(d, T = 298\text{K})} \tag{10.4}$$

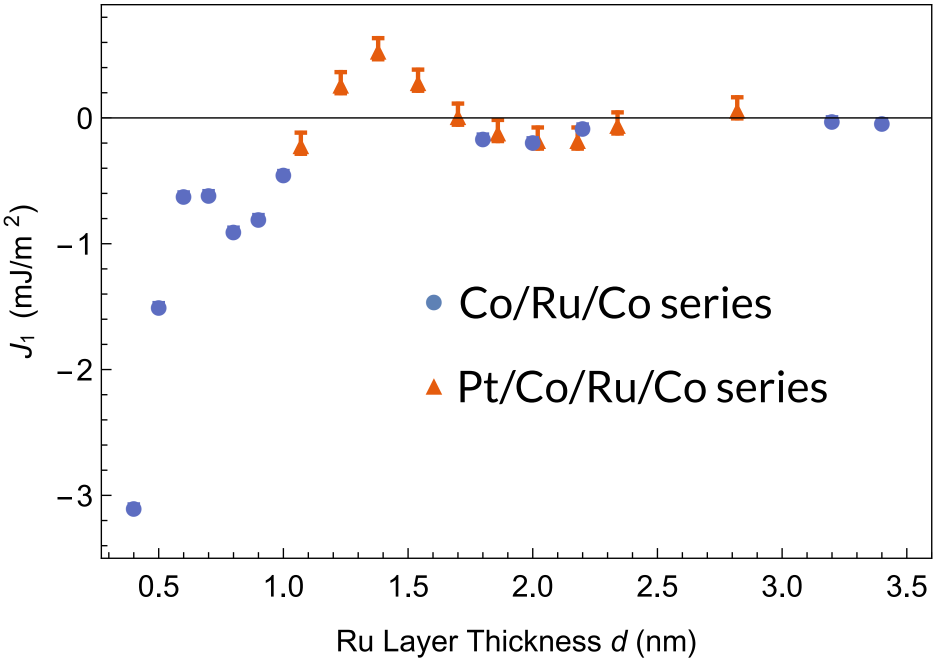

Figure 10.5: Coupling strength, J_1, as a function of the thickness of the Ru spacer layer for our Co/Ru/Co series of samples, blue circles, and the Pt/Co/Ru/Co/Pt samples from Girt *et al.* [35], orange triangles.

Additionally, instead of fitting the absolute temperature dependence, we will be fitting the ratio $J_1(d,T)/J_1(d,T=0)$. Considering all of this, our temperature dependence fitting function will be

$$\frac{J_1(d,T)}{J_1(d,T=0)} = \frac{\sum_\alpha \frac{J_1^\alpha(d,T=298\mathrm{K})}{F^\alpha(d,T=298\mathrm{K})} F^\alpha(d,T)}{J_1(d,T=0)}. \tag{10.5}$$

Our fitting procedure is as follows: we will first fit the room temperature J_1 data as explained above, and then use the results to determine $J_1^\alpha(d,T=298\mathrm{K})$ for each critical spanning vector. Next, we will plug those into Eq. 10.5, and then use this equation to simultaneously fit the temperature dependence of J_1 for several samples with different Ru spacer layer thicknesses. In these temperature dependence fits, the only fitting parameters will be $v_\perp^\alpha$ and D_ϕ^α, as shown in Eq. 4.20.

10.2.1 Experimental

We have sputtered a series of samples with the structure
Ta(2.5 nm)/Ru(3 nm)/Co(5 nm)/Ru(d)/Co(5 nm)/Ta(4 nm), where d is the Ru spacer layer thickness and is varied from 0.4 to 3.4 nm. This is the same series of samples studied in the previous chapter, except in this case we have added more samples with greater spacer layer thicknesses. Like before, this series of samples will be referred to as the Co/Ru/Co

series. The Co and Ru thin films are textured in the [0001] direction, as confirmed by XRD measurements.

Since both magnetic layers are identical, we could only use our micromagnetic model to determine J_1 in non FC coupled samples, and couldn't use our FMR technique to determine $J_1 - 2J_2$ for the FC coupled samples. As such, we have decided to also include previously obtained data from Girt *et al.* Ref. [35] for J_1 measurements for samples with the structure [Pt(0.9 nm)/Co(0.25 nm)]/Ru(4 nm)/[Co(0.25 nm)/Pt(0.9 nm)]/Co(0.25 nm)/ Ru(d)/[Co(0.25 nm)/Pt(0.9 nm)] where the parts in square brackets are multilayers. This series of samples will be referred to as the Pt/Co/Ru/Co series. In this case, J_1 is the coupling strength of the two Co layers across the second Ru layer, which has a thickness, d, which is varied from 1.07 to 2.82 nm. Since the Co layer is only 0.25 nm, and is grown on top of Pt instead of Ru, it is possible that it has a strained lattice that is slightly different from our samples. In order to determine if this has a significant effect on coupling oscillations, we have plotted our data along with data from Girt *et al.* in Fig. 10.5, where we can compare measurements. The blue circles are the Co/Ru/Co series data, while the orange triangles are the Pt/Co/Ru/Co series data. It can be seen that the data from the two different series of samples seems to differ only slightly in the range from 1.7 to 2.3 nm. We have also confirmed that Co/Ru/Co series samples with Ru layer thicknesses of 1.6, 2.4, 2.8, and 3.0 nm are all FC coupled, which is in agreement with data for the Pt/Co/Ru/Co series. Thus, by increasing the size of the error bars of the Pt/Co/Ru/Co data, both series are in agreement within the uncertainty. Additionally, we will only be using the Pt/Co/Ru/Co data within the range of the first FC peak, for spacer layer thicknesses from 1.1 to 1.7 nm.

With this combination of data from the Co/Ru/Co series and Pt/Co/Ru/Co series, we are able to fit our coupling model over a wider range of spacer layer thicknesses to better evaluate its accuracy. It is important to have a wide range of spacer layers for fitting our model because of the number of critical spanning vectors we have. Just like a Fourier series, the more oscillatory terms there are in Eq. 4.17, the easier it will be to approximate any shape of coupling oscillations. By fitting a wide range of spacer layer thicknesses, we are increasing the number of periods of oscillations being fitted which will allow us to extract more accurate J^{α} values and be more confident in the accuracy of the model.

The magnetization plots of the Co/Ru/Co series were measured using VSM and fit with our micromagnetics model to extract J_1. The low temperature measurements were done with the same VSM tool which has a liquid helium cryostat. For the purpose of normalizing our J_1 measurements to zero temperature, we have assumed that J_1 from 5 K data is equal to that of 0 K data. This is an accurate assumption since the slope of $F(d, T)$ near 0 degrees is 0.

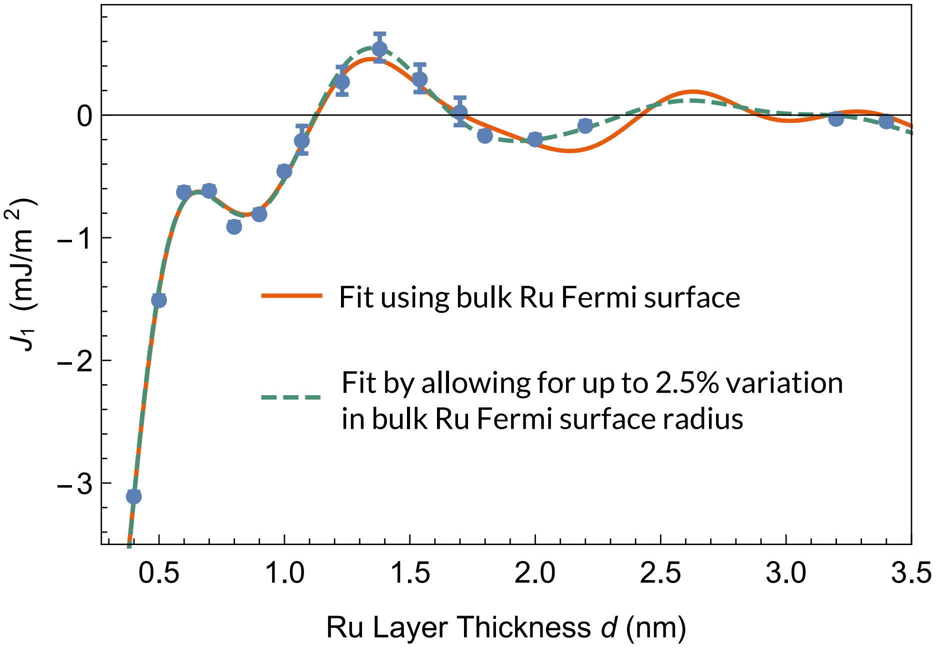

Figure 10.6: Coupling strength, J_1, as a function of the thickness of the Ru spacer layer for the Co/Ru/Co series of samples. The blue points are data. Larger thickness data within the range of 1.1 to 1.7 nm is taken from Ref. [35]. The orange line is the fit with Eq. 4.17 using critical spanning vectors from Table. 10.1. The dashed green line is the fit using the same equation and critical spanning vectors, except now the length of the critical spanning vectors are allowed to vary in length corresponding to up to 2.5% in the Fermi surface sheet radius.

10.2.2 Results and Discussion

The J_1 coupling strength measurements for the Co/Ru/Co series are shown in Fig. 10.6. The orange line fit was obtained using Eq. 4.17 with the critical spanning vectors listed in Table. 10.1, along with an additional imaginary critical spanning vector corresponding to an exponentially decaying non-oscillating contribution to J_1.

The coupling strengths of each critical spanning vector, J^α, obtained from the orange line fit are shown in Fig 10.7.

The fit shown in Fig. 10.6 has resulted in fitting parameters for the exponentially decaying contribution, as shown in Eq. 10.1, of a decay length of 0.35 nm, with a weight of $J^\alpha = 1 \times 10^{-5}$ eV. This is 5 orders of magnitude smaller than the contributions from real critical spanning vectors as shown in Fig 10.7. This indicates that there is likely no exponentially decaying superexchange-like contribution to J_1 from evanescent electron states, in the samples measured.

The coupling strengths in Fig. 10.7 show that all but two of the critical spanning vectors have a significant contribution to the overall interlayer exchange coupling. Qualitatively, this

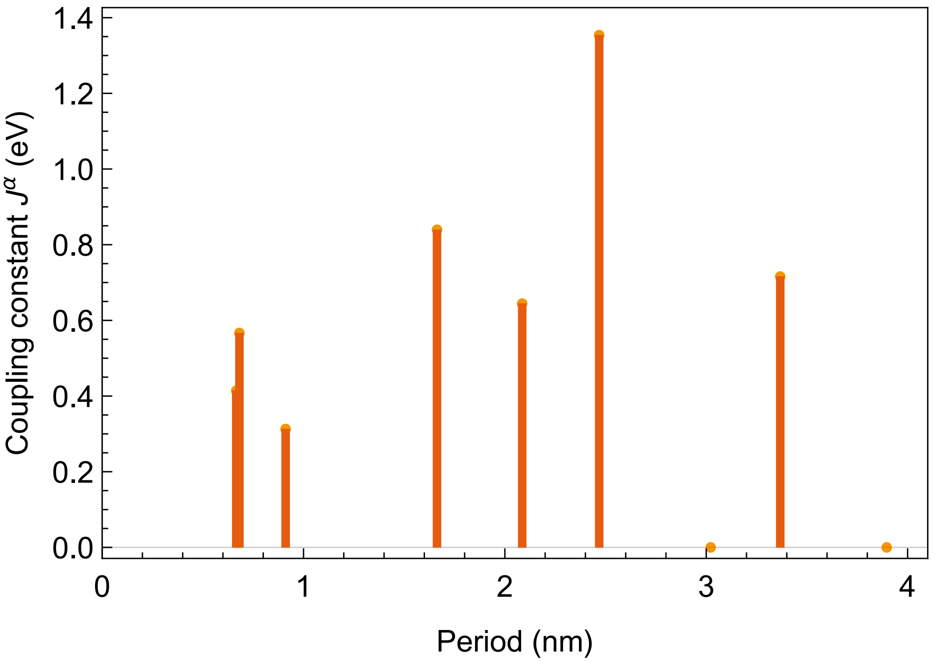

Figure 10.7: J^{α} values for the critical spanning vectors from Table 10.1 with corresponding periods of oscillation $(2\pi/q_{\perp}^{\alpha})$ as obtained by fitting J_1 for the Co/Ru/Co series of samples, as shown as the orange line in Fig. 10.6, using Eq. 4.17.

is in agreement with the approximate weights predicted by Stiles *et al.* [105], which also showed significant contributions from wide distribution of critical spanning vectors. The exact periods for each critical spanning vector differ from their work slightly because they approximated them using the local density approximation (LDA) theoretical method, while we used values from experiment. However, the qualitative distribution of weights appears to be in agreement. This indicates that the interface-reflection model appears to accurately predict the approximate magnitude of each J^{α} in our samples.

It is remarkable how accurate this fit is considering that the model is only exact with very thick spacer layers as shown in Fig. 4.7. Additionally, we have used the critical spanning vectors obtained from the Fermi surface of bulk Ru. On the thin end of the series, the Ru spacer layer is only a few atomic layers thick. The 8% lattice between Co and Ru in the (0001) plane is very likely to compress the Ru crystallographic unit cell in the plane, and expand it along the c-axis. This will result in a modification of the Fermi surface, causing it to deviate significantly from that of bulk Ru. It will also result in a change in height of the Brillouin zone. Both of these factors could result in critical spanning vectors that deviate from those obtained from bulk Ru.

To account for these two factors, we have added an additional fit to the data, shown as a dashed green line in Fig. 10.6. This fit is the same as that of the orange line, except that now an additional fitting parameter has been added for each critical spanning vector, allowing

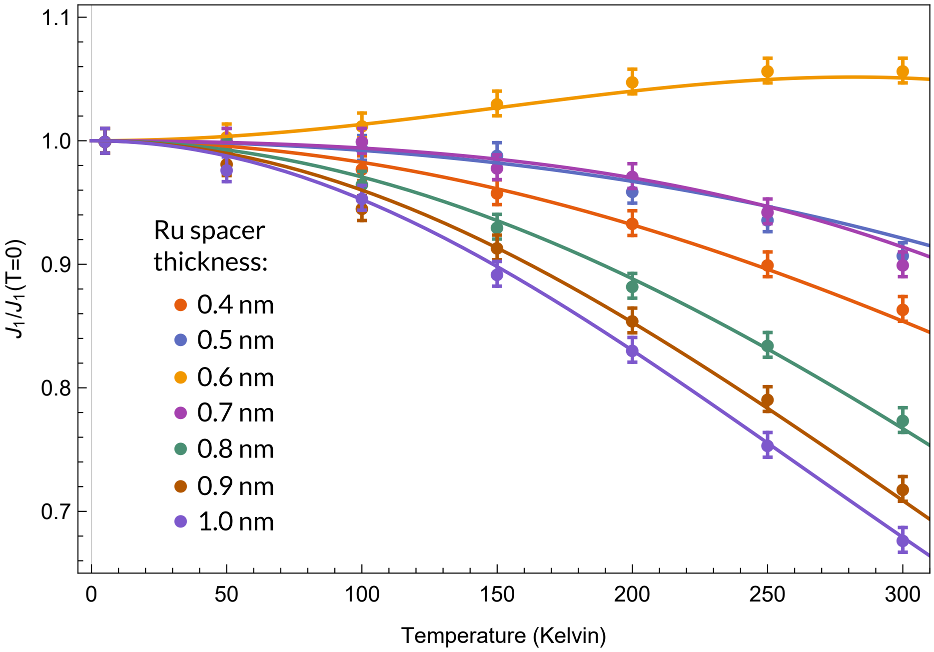

Figure 10.8: J_1 temperature dependence for the Co/Ru/Co series with spacer layer thickness ranging from 0.4 to 1 nm and temperatures from 5 to 300 K, normalized to the zero temperature J_1. The circles are data, and the lines are fits using Eq. 10.5. The fits were performed on all measurements simultaneously so that each fit has the same parameters. The colors corresponding to spacer layer thicknesses are shown in the figure. See Fig. 10.9 for a 3D image of the fit.

the length to be scaled in the form $q_{\perp}^{\alpha'} = Cq_{\perp}^{\alpha}$, where $q_{\perp}^{\alpha'}$ is the new critical spanning vector, C ranges from 0.95 to 1.05, which corresponds to a maximum of a 2.5% change in the perpendicular component of the radius of the Fermi surface sheet. This additional fitting parameter can take into account small changes to the Fermi surface that is expected for the samples studied. It can be seen that by making this change, the fit is improved significantly, going through almost all datapoints. This indicates that the Fermi surface of thin Ru spacer layer is likely slightly different from that of bulk Ru, and once this is accounted for, the model fits the data quite well.

Judging by the quality of the fits in Fig. 10.6, it is clear that the bilinear coupling in Co/Ru/Co trilayer structures is accurately described by the interface-reflection model without the need for an additional logarithmic non-oscillatory contribution.

Fig. 10.8 shows the J_1 temperature dependence for the Co/Ru/Co series with spacer layer thickness ranging from 0.4 to 1 nm and temperatures from 5 to 300 K, normalized to the zero temperature J_1. The circles are data, and the lines are a single simultaneous fit using Eq. 10.5. The same fit is also shown in a 3D plot in Fig. 10.9. This 3D plot gives a better visualization of how the temperature dependence changes with spacer layer thickness. The $v_{\perp}^{\alpha}$ and D_{ϕ}^{α} parameters obtained from the fit are shown in Table. 10.2.

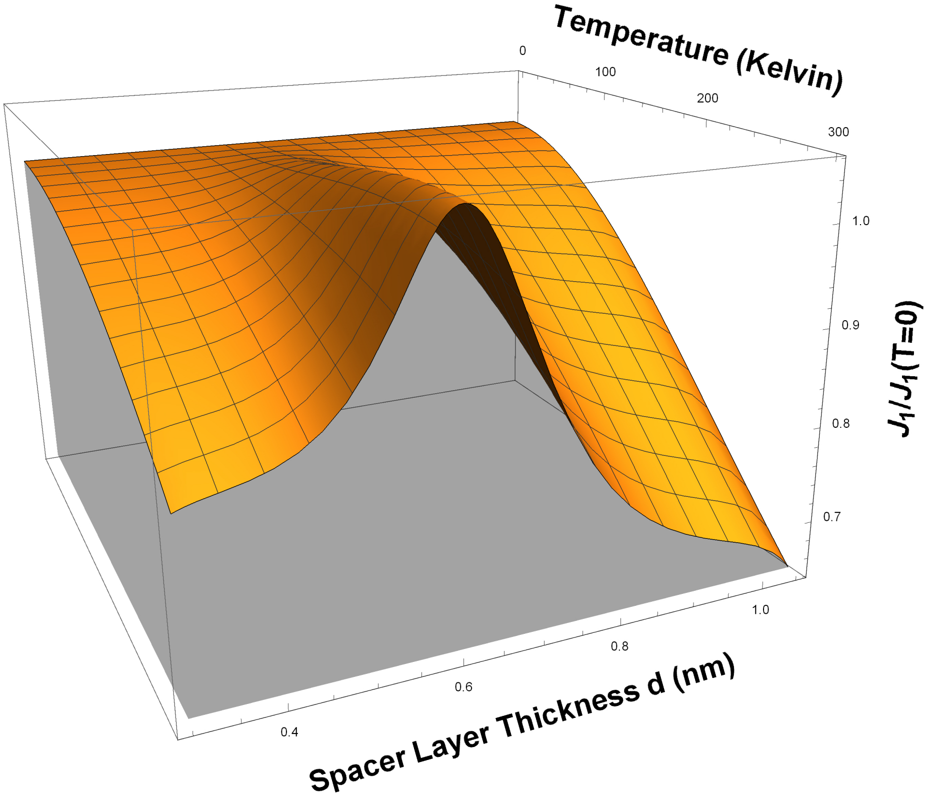

Figure 10.9: A 3D plot of J_1 normalized to the zero temperature value, as described in Eq. 10.5, using parameters determined from fitting J_1 temperature dependence data for the Co/Ru/Co series with spacer layer thickness ranging from 0.4 to 1 nm and temperatures ranging from 5 to 300 K. This fit is the same fit shown in Fig. 10.8, except in 3D.

Table 10.2: $v_\perp^\alpha$ and D_ϕ^α from Eq. 4.20 for each critical spanning vector as determined from fitting the temperature dependence data in Fig. 10.8 using J^α values from Fig. 10.7 and bulk Ru critical spanning vectors.

CSV Label	$v_\perp^\alpha \pm 0.6$ (10^5m/s)	$D_\phi^\alpha \pm 0.5$ (eV^{-1})
a_1	4.8	3.1
a_2	1.7	0.0
b	2.9	4.1
c	3.5	3.2
d	8.0	6.4
e	6.0	5.4
f	3.5	3.2
g	9.8	0.0
h	15.9	6.6

The $v_{\perp}^{\alpha}$ values shown in Table. 10.2 obtained from fitting the J_1 temperature dependence agree within the approximate ranges calculated by Gall *et al.* [32] using density functional calculations and the projector-augmented wave method. Specifically, the critical spanning vectors a, c, b, and f, which are located on the "inner electron star" in the 3d Fermi surface (which can be seen in the reference of Gall *et al.* [32]), all have relatively low $v_{\perp}^{\alpha}$ values within the range of 1.5 to 5×10^5 m/s. The critical spanning vectors d, e, and h, which are located in the outer "hole ring" in the 3d Fermi surface, have relatively large $v_{\perp}^{\alpha}$ values within the range of 6 to 16×10^5 m/s. The h critical spanning vector from our fit has the largest $v_{\perp}^{\alpha}$, which is also in agreement with the calculations by Gall *et al.* [32]. The relative differences of $v_{\perp}^{\alpha}$ between the critical spanning vectors are also in agreement with those calculated by Philip *et al* [89] using the Perdew-Burke-Enzerhof (PBE) generalized gradient approximation (GGA) method.

The D_{ϕ}^{α} values shown in Table. 10.2 obtained from fitting the J_1 temperature dependence have a wide range of values from 0 to 6.6 eV^{-1} depending on the critical spanning vector. These values are the same order of magnitude as the 2.4 eV^{-1} that Lee *et al.* [67] found for Co/Cu/Co trilayer structures with (111) oriented Cu, which only has 1 critical spanning vector, making it value a good indication of what to expect for each individual critical spanning vector. Additionally, Castro *et al.* [27] calculated, using fully realistic tight-binding bands, a theoretical value of $D_{\phi}^{\alpha} = 4.53\ \text{eV}^{-1}$ for one of the critical spanning vectors in the Cu [001] direction for the Co/Cu/Co trilayer structure. This is also the same order of magnitude as the values obtained from our fit.

One large difference between our samples and that of Lee *et al.* is that instead of only having 1 critical spanning vector, we have 9. This means that for our samples, our fitting model has 9 times more parameters than that of a Cu spacer layer. This would allow our model to easily overfit any J_1 temperature dependence for a single spacer layer thickness, or even a small number of spacer layer thicknesses. In order to mitigate this problem, we have measured the J_1 temperature dependence of 7 different samples, all with different spacer layer thicknesses, and then simultaneously fit them all together. This provides more data so that there is less probability of an overfit, and because the data is for different spacer layer thicknesses, allows us to determine both temperature dependence parameters. The fact that our fitted D_{ϕ}^{α} values for out individual critical spanning vectors are on the same order as those obtained from a single critical spanning vector show that our fit are yielding reasonable results.

An important thing to notice in Fig. 10.8 is that, for the thinnest spacer layer of 0.4 nm, J_1 decreases with temperature. This is made visually obvious in the 3D plot in Fig. 10.9. If there was an exponential contribution to J_1 caused by evanescent electron states, it would dominate at the smallest spacer layer thickness, and cause J_1 to increase with temperature. [10] The fact that we don't see this is another strong indication that the non-oscillatory coupling seen in thinner Ru spacer layers is not an exponential contribution caused by evanescent electron states, and is instead caused by a linear combination of contributions from oscillatory electron states.

The opposite temperature dependence seen in the sample with a 0.6 nm thick spacer layer may look like an indication of contributions from evanescent states, but as you can see by the fit, it is well described without any evanescent states. This is because we have a linear combination of the temperature dependence of each of the critical spanning vectors weighted by their zero temperature coupling strength, which is oscillating with spacer layer thickness. Depending on the thickness, some of these weighting factors will be positive and some will be negative. This can lead to the temperature dependence being in the opposite direction for some critical spanning vectors relative to the others which can cause the opposite temperature dependence seen in our data. For illustrative purposes, we have shown a simulation of this taking place for a system with only 2 critical spanning vectors, which is shown in Fig. 10.10. In this figure, critical spanning vector 1 has parameters $q_\perp^\alpha = 9$ nm^{-1}, $J^\alpha = 1$ mJ/m^2, $v_\perp^\alpha = 1 \times 10^5$ m/s, $D_\phi^\alpha = 0$ J^{-1}, $\phi^\alpha = 0$, and critical spanning vector 2 has parameters $q_\perp^\alpha = 3$ nm^{-1}, $J^\alpha = 1$ mJ/m^2, $v_\perp^\alpha = 2 \times 10^5$ m/s, $D_\phi^\alpha = 0$ J^{-1}, $\phi^\alpha = 0$. The temperature dependence was taken at $d = 1.6$ nm. a) shows J_1 for the two critical spanning vectors, and the sum of them together. b) and c) shows the temperature dependence of each of the individual critical spanning vectors, described by Eq. 4.19 weighted by the value of J_1 at 1.6 nm for each critical spanning vector. d) shows what would be the actual measured temperature dependence (normalized to 0 temperature) which is the sum of both contributions. The main requirement for an inverted temperature dependence is that there are two or more critical spanning vectors with comparable J^α magnitudes, but with opposite signs, which will occur periodically with spacer layer thickness for most spacer layers that have more than 1 dominant critical spanning vector.

The quality of the fit in Fig. 10.8, and the reasonable values of $v_\perp^\alpha$ and D_ϕ^α obtained from it, indicate that the model accurately represents the temperature dependence of J_1 that is occurring in our samples.

There may be an additional contribution to the temperature dependence caused by thermal fluctuations of the magnetic moments of the magnetic layers. The magnitude of this contribution is not well understood. One prediction is that, within the temperature range that we have studied, this contribution can be approximately proportional to the saturation magnetization of the magnetic layers according to [27, 69, 98]

$$J(T) \propto (M_s/M_{s,0})^n, \tag{10.6}$$

where $M_{s,0}$ is the zero temperature saturation magnetization of the magnetic layers, and the exponent n is approximately equal to 2. This temperature dependence contribution is not actually part of J_1. It originates from the dot product in Eq 4.16, which is $\frac{\boldsymbol{M}_1 \cdot \boldsymbol{M}_2}{M_{s,1} M_{s,2}} = \cos\theta$, where θ is the angle between $\boldsymbol{M}_1$ and $\boldsymbol{M}_2$. The thermal fluctuations of the magnetic moments

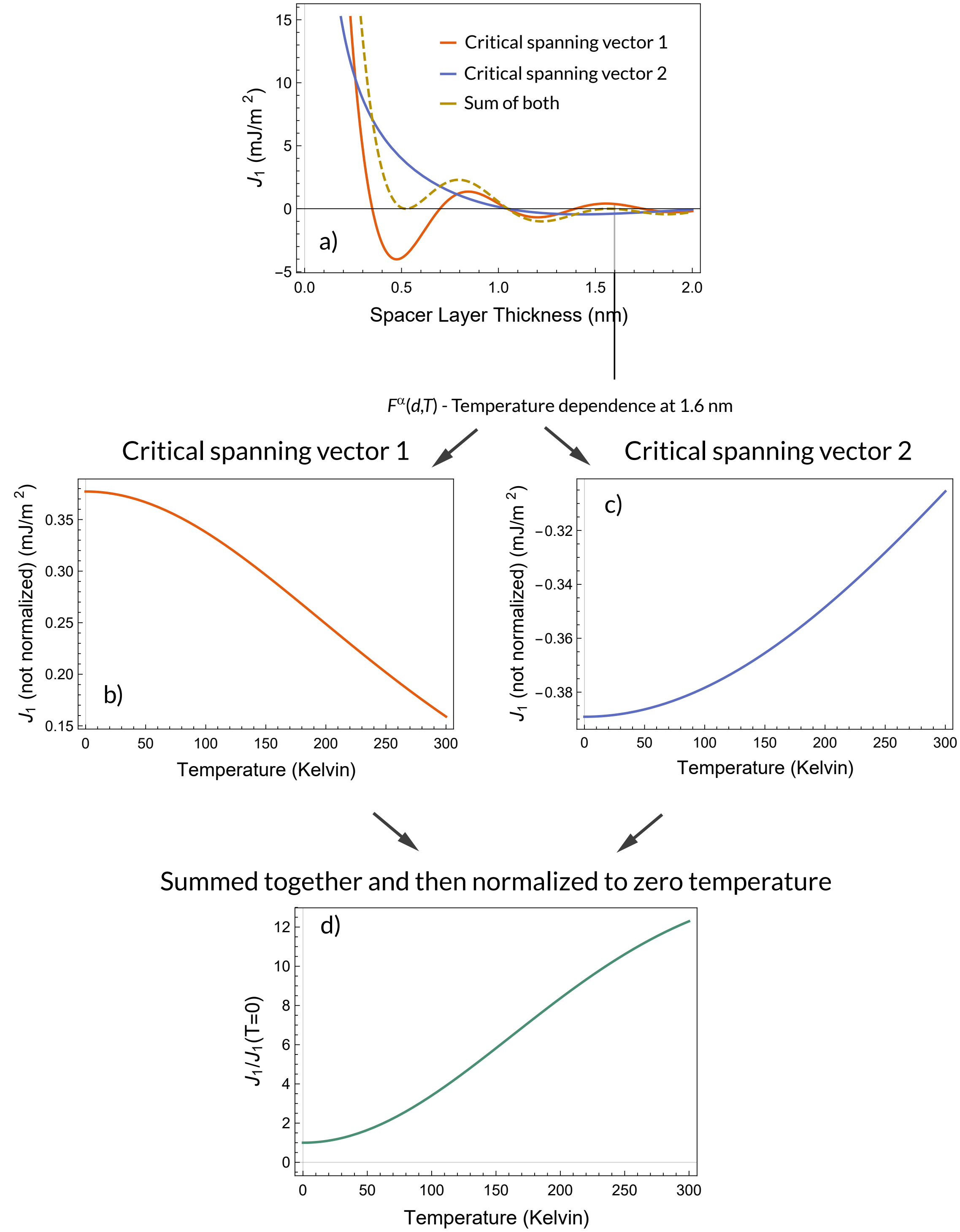

Figure 10.10: a) is J_1 for two different critical spanning vectors, and the sum of them together, described by Eq. 4.17. b) and c) shows the temperature dependence of each of the individual critical spanning vectors, described by Eq. 4.19 weighted by the value of J_1 at 1.6 nm for each critical spanning vector. d) shows what would be the actual measured temperature dependence which is the sum of both contributions (normalized to 0 temperature after being added.)

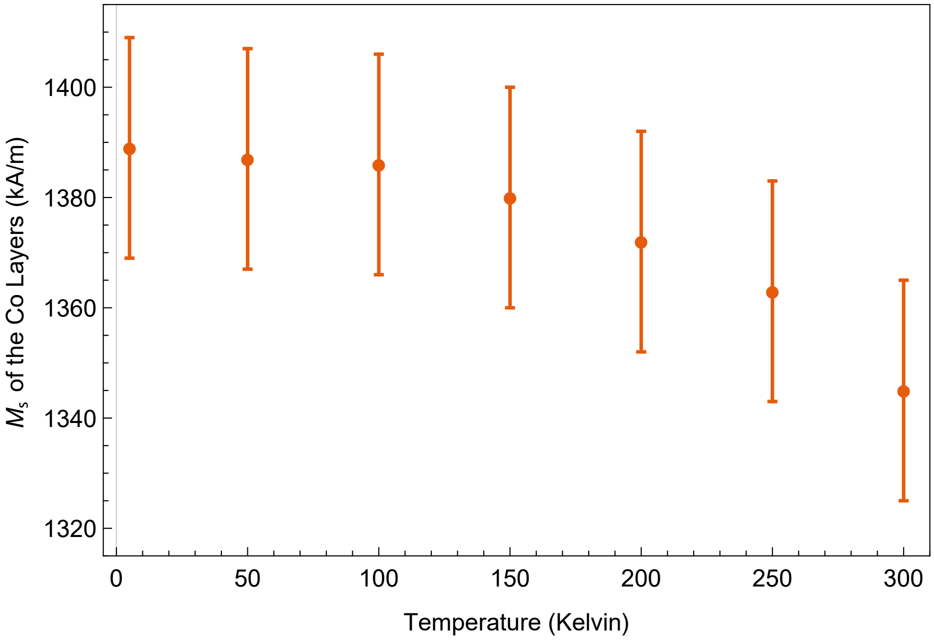

Figure 10.11: The temperature dependence of the saturation magnetization of the Co layers in the Co/Ru/Co series of samples. This is the average saturation magnetization of all samples within the spacer layer thicknesses range from 0.4 to 1 nm.

result in fluctuations of θ. The total measured temperature dependence is the product of the Eq. 10.5 with Eq. 10.6.

In order to estimate the magnitude of this contribution, we measured the temperature dependence of the saturation magnetization of the Co layers within the Co/Ru/Co series of samples, with spacer layer thicknesses from 0.4 to 1 nm. We found that the M_s of Co changed slightly within the range of temperatures studied. This dependence is shown in Fig. 10.11. The change is small, with an approximate 3.1% change in M_s between 5 and 300 K, which is expected considering its high Curie temperature of 1400K. [86] Thus, any additional contribution to the temperature dependence from Eq. 10.6 is expected to be small compared to the large dependence that we measured. However, for completeness, we have fit the J_1 temperature dependence, of the Co/Ru/Co series, with a fitting function that includes this contribution where we have assumed $n = 2$ in Eq. 10.6. The results of this fit can be seen in the appendix. The $v_\perp^\alpha$ and D_ϕ^α values obtained with this new fit only differ from the values in Table 10.2 by a small amount. This confirms that the temperature dependence contribution, in the form of Eq. 10.6 with $n = 2$, is small compared to the other temperature dependence contributions, and doesn't significantly effect our results.

10.2.3 Summary

These results show that the bilinear interlayer exchange coupling in our Co/Ru/Co series of samples, with additional data from the Pt/Co/Ru/Co series of samples, is well described by the interface-reflection model including only contributions from real critical spanning vectors obtained from bulk Ru.

By fitting spacer layer thickness and temperature dependent J_1 measurements using the interface-reflection model, we have determined that there is likely no superexchange-like contribution to coupling. The non-oscillatory AFC bias of J_1 seen in thinner Ru spacer layers appears to be caused by a linear combination of oscillatory RKKY-like coupling from several different critical spanning vectors.

The J^α values for each of the critical spanning vectors, as determined from fitting thickness dependent J_1 measurements, show that there are significant contributions to coupling from several different critical spanning vectors with different periods of oscillations. This indicates that bilinear interlayer exchange coupling cannot be characterized by only a single period of oscillations. This is in agreement with predictions made by Stiles *et al.* in ref. [105].

The fit to temperature dependent J_1 measurements has resulted in $v_\perp^\alpha$ for each of the critical spanning vectors that are in approximate agreement with the Fermi surface calculated in Ref. [32]. The fit also resulted in D_ϕ^α values that are within the expected range as reported for similar experimental measurements and theoretical calculations. These results indicate that the temperature dependence theory we have used appears to be capable of describing our J_1 measurements.

These results also show that, at least for cobalt layers coupled across a Ru spacer layer, this model is able describe bilinear interlayer exchange coupling with spacer layers as thin as 0.4 nm to a reasonable level of accuracy. This is in spite of the theory only exact for infinitely thick spacer layers.

For the remainder of this chapter, we will be using the interface-reflection model including only the real critical spanning vectors as shown in Table 10.1, which is described by Eq. 4.22.

10.3 The Effect of Changing the Magnetic Layer Composition in M/Ru/M Trilayers

The first three series of samples studied in this section explore the effect of changing only the top magnetic layer in the trilayer structure so that the growth and crystal structure of the Ru spacer layer is left unchanged. This allows us to investigate the effect that the composition of the magnetic layer has on interlayer exchange coupling in the absence of changes in the Fermi surface of the Ru spacer layer. This is expected to only alter the second term in Eq. 4.18, which would result in a change in oscillatory coupling amplitude, and only a relatively small change in its period.

We also studied bilinear interlayer exchange coupling for several series of samples where the composition of only the bottom magnetic layer is changed. When the bottom layer is altered, it is possible to see much larger changes in coupling oscillations because the growth of the spacer layer can differ.

If the spacer layer is strained, having an expansion or contraction in lattice spacing caused by a lattice mismatch between the layer below it, then this can lead to changes in the Fermi surface and Brillouin zone of the spacer layer. This would result in different critical spanning vectors with different coupling strengths which could lead to a significant change in the period and amplitude of coupling oscillations.

As explained in the previous chapter, during the sputter deposition process, it is possible for a small amount of the material from the layer below to float up and become trapped in the layer above while its being deposited. [2] This can lead to a small amount of impurities within a layer that will depend on what layer it is grown on top of. These impurities may have a different valence from the atoms within the spacer layer, causing a shift in the Fermi level in the same way as doping a semiconductor. Like the previous effect, this can result in different critical spanning vectors with different coupling strengths which could lead to a significant change in the period and amplitude of coupling oscillations.

The texture of the spacer layer can be effected by the material that it grows on top of. If the texture is poor, with a large FWHM in the XRD rocking curve, then there can be an increased number of lattice dislocations and imperfections that electrons can scatter from. If this occurs, then the amplitude of the coupling oscillations will decrease.

Finally, similar to the result when altering the top magnetic layer, altering the bottom magnetic layer can change the reflection amplitudes of the critical connecting vectors (the second term in Eq. 4.18). This will lead to a change in the amplitude and period of coupling oscillations.

Considering all of these effects, it is expected that if we change the material of the bottom magnetic layer, the coupling oscillations have the potential to change much more significantly than was seen in the samples where only the top magnetic material is changed.

10.3.1 Experimental

The series of samples used to investigate the effect of changing the top magnetic layer are the Co/Ru/Co series from above, and the Co/Ru/FeCo and Co/Ru/FeCoB series from the previous chapter. The only difference between these three series is the top magnetic layer, which is Co, $Fe_{75}Co_{25}$, and $Fe_{60}Co_{20}B_{20}$ in the first, second, and third series, respectively. We only have data for the Co/Ru/FeCo and Co/Ru/FeCoB series for Ru spacer layer thickness within the range of 0.4 to 1 nm. As discussed earlier, the spacer layer may have its lattice strained when it is thinner, in addition, our interlayer exchange model is only approximate for thinner spacer layer. Therefore, fitting to data within a smaller range of thinner spacer layers will give different results. So, in order to be able to compare relative differences between these three series, we are going to limit ourselves to the same range of thickness for the Co/Ru/Co series.

We study a total of 4 different series of samples to investigate the effect of changing the composition of the bottom magnetic layer. The first two of these series of samples are the NiFe/Ru/FeCo series from Chapter 8, where the Ru spacer layer contains no boron, and the Co/Ru/FeCo series described above. The only difference between these two series of samples is that in one case the bottom magnetic material is $\mathrm{Ni}_{80}\mathrm{Fe}_{20}$, and in the other case it is Co.

The next two series of samples that we will compare in order to investigate the effect of changing the composition of the bottom magnetic layer are the FeCoB/Ru/FeCoB series as described in Chapter 7, and the Co/Ru/FeCoB series from the previous chapter. The only difference between these two series of samples is the composition of the bottom magnetic layer, which is Co in one case, and $\mathrm{Fe}_{60}\mathrm{Co}_{20}\mathrm{B}_{20}$ in the other case. Like before, we will be limiting ourselves to data within the spacer layer thickness range of 0.4 to 1 nm for all of these comparisons.

We also grew some additional samples to investigate the texture of Ru when grown on top of different underlayers. These additional samples have the structures Ta(2.5 nm)/Ru(1 nm)/Co(1.2 nm)/Ru(11 nm) and Ta(2.5 nm)/$\mathrm{Fe}_{60}\mathrm{Co}_{20}\mathrm{B}_{20}$(14 nm)/Ru(11 nm). The Ru (0002) peak rocking curve, Ru lattice constants, and Ru unit cell volume, for these samples were determined from XRD measurements. These samples were sputtered on the same substrates and with the same conditions as the samples in the previous chapter. These samples will be referred to as Ru/Co/Ru and FeCoB/Ru for brevity. In the Ru/Co/Ru series, the bottom Ru layer is an order of magnitude thinner than the top Ru layer, and is not expected to cause X-Ray reflections of significant intensity to effect the measured peak. Therefore, the Ru (0002) rocking curve measurement of that sample is a good indication of the texture of the top Ru layer. Although these top Ru layers are much thicker than the spacer layers of the other samples being studied, the texture of the first few atomic layers will, to an extent, continue as more layers are deposited on top. Thus, the width of the rocking curve for a 11 nm Ru layer will give us a good indication of the texture of thinner Ru layers.

10.3.2 Results and Discussion

The J_1 coupling strength measurements for the Co/Ru/Co, Co/Ru/FeCo, and Co/Ru/FeCoB series of samples are shown in Fig. 10.12 as orange circles, and blue triangles, and purple squares, respectively. The lines are fits using Eq. 4.17 with critical spanning vectors from the Ru Fermi surface as shown in Table.10.1. Changing the top magnetic layer from Co to FeCo results in an increase in coupling strength for the first AFC peak around 0.4 nm, with a slight decrease in coupling strength for the second AFC peak around 8 nm. There is also a very slight shift in the position of the second AFC peak from approximately 0.84 to

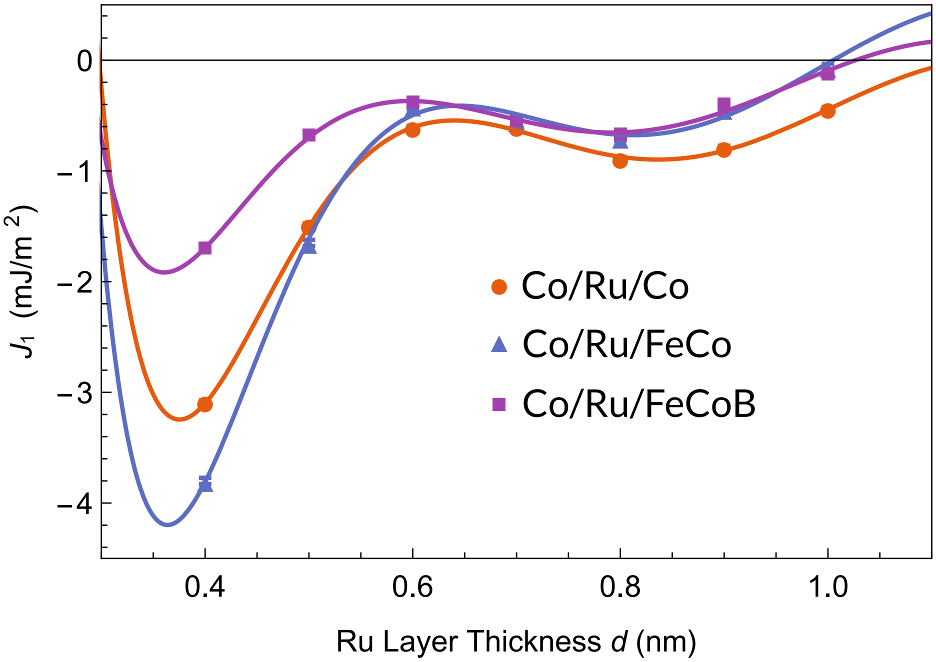

Figure 10.12: J_1 measurements for the Co/Ru/Co series, orange circles, the Co/Ru/FeCo series, blue triangles, and the Co/Ru/FeCoB series, purple squares. The lines are fits using Eq. 4.17 with critical spanning vectors from the bulk Ru Fermi surface as shown in Table.10.1. The fitted values of J^α for each critical spanning vector are shown in Fig. 10.13

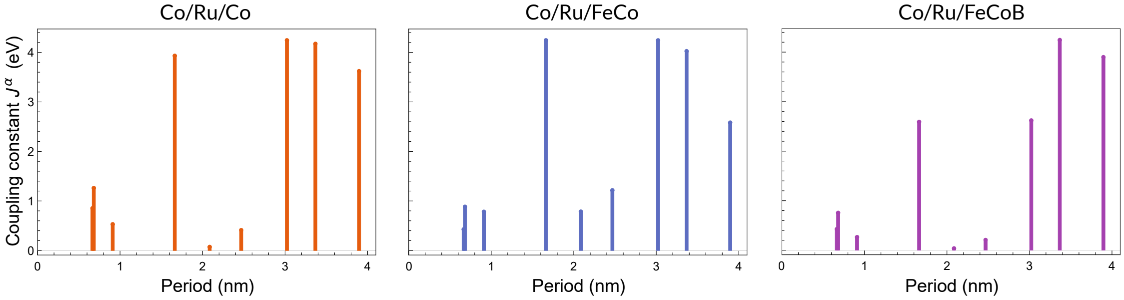

Figure 10.13: J^α values for the critical spanning vectors with corresponding periods of oscillation ($2\pi/q_\perp^\alpha$) as obtained by fitting coupling oscillation data in Fig. 10.12 for the Co/Ru/Co, Co/Ru/FeCo, and Co/Ru/FeCoB series using Eq. 4.17 with the bulk Ru critical spanning vectors listed in Table.10.1. From left to right, the three plots are for the Co/Ru/Co series, the Co/Ru/FeCo series, and the Co/Ru/FeCoB series. The x and y axis of all three plots have the same ranges.

0.82 nm. Changing the top magnetic layer from Co to FeCoB results in a relatively larger decrease in coupling strength over the entire range from 0.4 to 1 nm. It also results in a slightly larger shift of the position of the second AFC peak from approximately 0.84 to 0.80 nm.

The slight change in the apparent period of oscillations in Fig. 10.12 can be attributed to the fact that the measured coupling is the sum of many non-linear terms from each critical spanning vector. When the amplitude of these terms change, it will shift some of the peaks and valleys of the oscillations which makes it appear as though the period is changing when it really isn't. This effect is shown in Fig. 4.9.

The fitted values of J^{α} for each critical spanning vector for the Co/Ru/Co, Co/Ru/FeCo, and Co/Ru/FeCoB series of samples are shown Fig. 10.13. The first thing to notice is that the J^{α} values obtained for the Co/Ru/Co series by fitting the range of spacer layer thicknesses from 0.4 to 1 nm are quite different from those obtained from fitting the range from 0.4 to 3.4 nm. However, the relative magnitude of the three shortest period J^{α}'s for the Co/Ru/Co series are almost identical in both cases. There are two main factors causing this difference. The first one is that the interlayer exchange coupling model that we are using is only approximately correct for thinner spacer layers, as described in the theory chapter, and shown in Fig. 4.7. Secondly, determining the contribution from critical spanning vectors with periods much larger than the range of that we are fitting becomes increasingly inaccurate because we only see a small fraction of a period. This second factor is the reason why the relative magnitude of the three shortest period J^{α}'s for the Co/Ru/Co series are almost identical. It is because the period of oscillation of these three shortest J^{α}'s are on the same order as the range of thicknesses of the data that we are fitting to, and are accurately determined from the fit in both cases.

All that said, while the J^{α} values determined from fitting from 0.4 to 1 nm are not representative of coupling across thicker spacer layers, we can still make useful relative comparisons between results obtained from these three series because the range of thicknesses measured is identical in all three cases.

Fig. 10.14 shows the J_1 measurements for the Co/Ru/FeCo series, blue triangles, and the NiFe/Ru/FeCo series, orange circles. The lines are fits using Eq. 4.17 which allow us to obtain the J^{α} values shown in Fig. 10.15. The oscillatory coupling behavior of these two series varies significantly from one another. The magnitude of the first AFC peak has dropped by almost a factor of 5 for the NiFe/Ru/FeCo series as compared to the Co/Ru/FeCo series. Switching the bottom magnetic layer from Co to NiFe has also resulted in the position of the second AFC peak moving from 0.82 to 0.73 nm. This is more than twice as much movement than we saw between any of the previous samples where only the top magnetic layer was changed.

The FWHM of the rocking curve of the top Ru layer (0002) peak for the Ru/Co/Ru sample was found to be 3.92°. We can compare this to the FWHM of the rocking curve

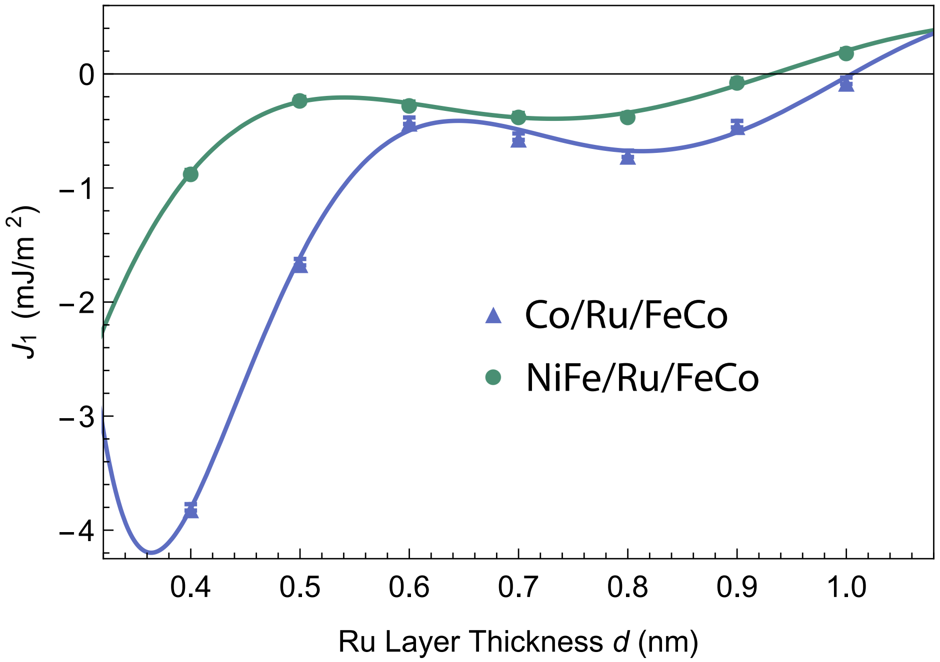

Figure 10.14: J_1 measurements for the Co/Ru/FeCo series, blue triangles, and the NiFe/Ru/FeCo series, orange circles. The lines are fits using Eq. 4.17 with critical spanning vectors from the bulk Ru Fermi surface as shown in Table.10.1. The Co/Ru/FeCo data is the same as in Fig. 10.12, and is only shown for comparison purposes.

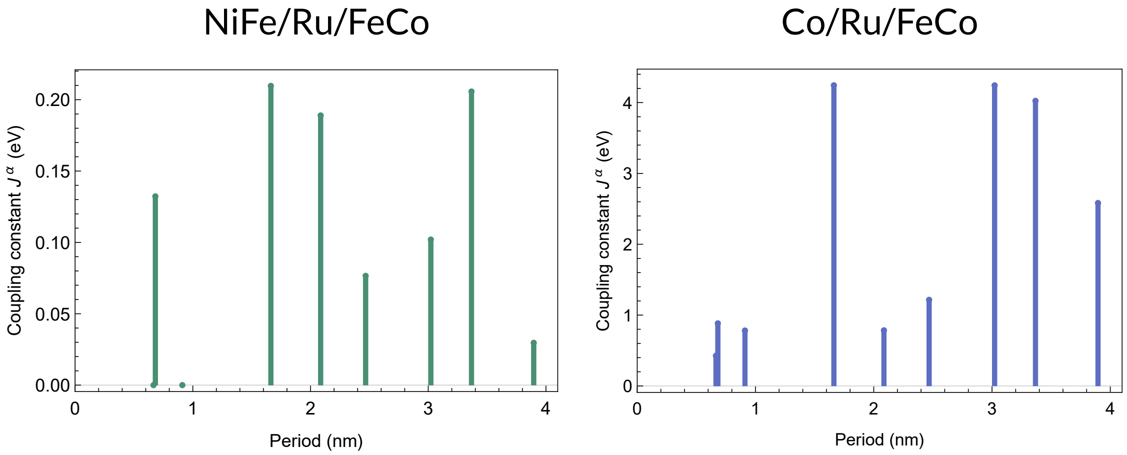

Figure 10.15: J^α values for the critical spanning vectors with corresponding periods of oscillation ($2\pi/q_\perp^\alpha$) as obtained by fitting coupling oscillation data for the NiFe/Ru/FeCo and Co/Ru/FeCo series as shown in Fig. 10.14 using Eq. 4.17 with the bulk Ru critical spanning vectors listed in Table.10.1. The Co/Ru/FeCo data is the same as in Fig. 10.13, and is only shown for comparison purposes.

of the top Ru layer (0002) peak for the Ta(2.5 nm)/$Ni_{80}Fe_{20}$(0.8 nm)/ Ru(23 nm) sample from Chapter 8, which is 4.04°. In this second case, the top Ru layer is more than twice as thick as in the Ru/Co/Ru sample. It is known that as the Ru layer grows thicker, its texture is improved, and the FWHM of the rocking curve will reduce. We have confirmed this many times ourselves as well. Considering this, the fact that the Ru (0002) peak in the Ta(2.5 nm)/$Ni_{80}Fe_{20}$(0.8 nm)/Ru(23 nm) sample has a rocking curve that is larger than that of the Ru/Co/Ru sample, even though it is more than twice as thick, means that the lower atomic layers have much worse texture in the former case as compared to the latter. From this, we can conclude that the Ru spacer layer in the NiFe/Ru/FeCo series has worse texture. This wider rocking curve may also indicate that the NiFe/Ru/FeCo series spacer layer will have more dislocations and lattice defects, [64, 76, 45, 108, 8] as compared to the Ru layer in the Co/Ru/FeCo series. Defects will increase the scattering of the electrons responsible for interlayer exchange coupling, reducing, in turn, the size of the oscillatory coupling. [106] The wider rocking curve also indicates that the polycrystalline crystalites are not all oriented so that coupling across the spacer layer is exactly in the [0001] direction. Instead, the direction of coupling, which is normal to the magnetic layer/spacer layer interface, is slightly different for each crystallite and the sum is a superposition of coupling in a distribution of directions centered around the [0001] direction. This results in a distribution of critical spanning vector lengths and a distribution in the periods of oscillation of interlayer exchange coupling. The end result will be the smearing out of shorter period oscillations, which can manifest itself as a reduction in the magnitude of J_1. These two effects are likely to be a large cause of the decreased in magnitude of J_1 measurements for the NiFe/Ru/FeCo series as compared to the Co/Ru/FeCo series.

The lattice parameters and unit cell volume for the Ru layer, as calculated from the Ru peaks in the XRD measurements of the Ru/Co/Ru and Ta(2.5 nm)/$Ni_{80}Fe_{20}$(0.8 nm)/ Ru(23 nm) samples were found to be the same within measurement uncertainty. However, Monika *et al.* have shown that large amounts of strain can relax on the order of nanometers. Therefore, it is likely that the first few atomic layers of the Ru layers in these samples are strained differently and have different lattice parameters from one another.

Fig. 10.16 shows the J_1 measurements for the Co/Ru/FeCoB series, blue triangles, and the FeCoB/Ru/FeCoB series, orange circles. The lines are fits using Eq. 4.17 which allow us to obtain the J^{α} values shown in Fig. 10.17. Like in the previous case where the bottom magnetic layer was changed, we can see that the oscillatory coupling behavior of these two series varies significantly from one another. Changing the bottom magnetic layer from Co to FeCoB has caused the magnitude of the first AFC peak around 0.4 nm to decrease slightly, and the second peak around 0.8 nm has decreased so dramatically that it is practically gone. It has also caused the second AFC peak to move from approximately 0.8 to 0.9 nm. Like the previous series where the bottom magnetic layer was changed, we see that the position

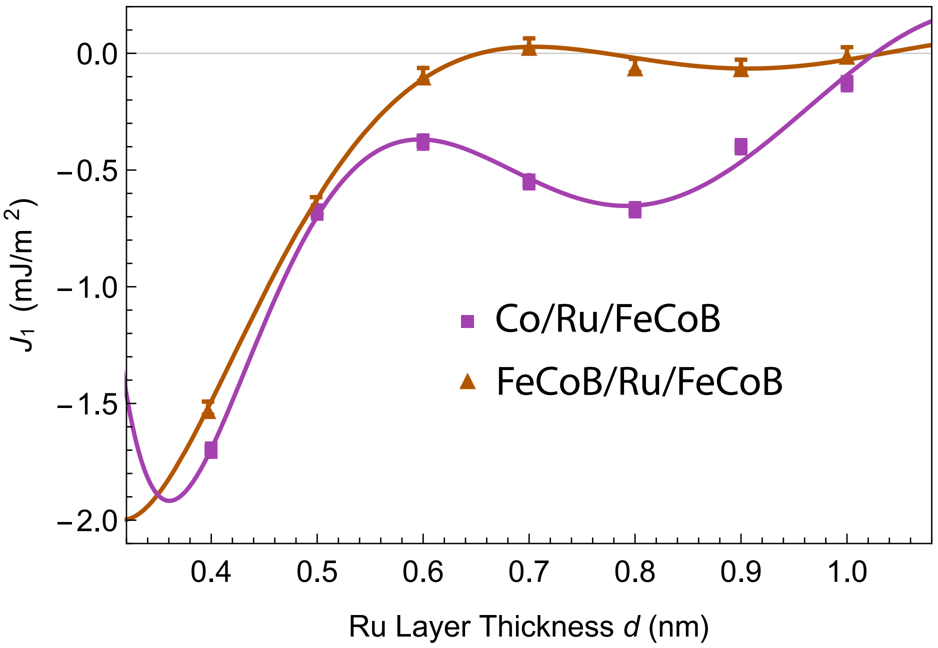

Figure 10.16: J_1 measurements for the Co/Ru/FeCoB series, purple circles, and the FeCoB/Ru/FeCoB series, green triangles. The lines are fits using Eq. 4.17 with critical spanning vectors from the bulk Ru Fermi surface as shown in Table.10.1. The Co/Ru/FeCoB data is the same as in Fig. 10.12, and is only shown for comparison purposes.

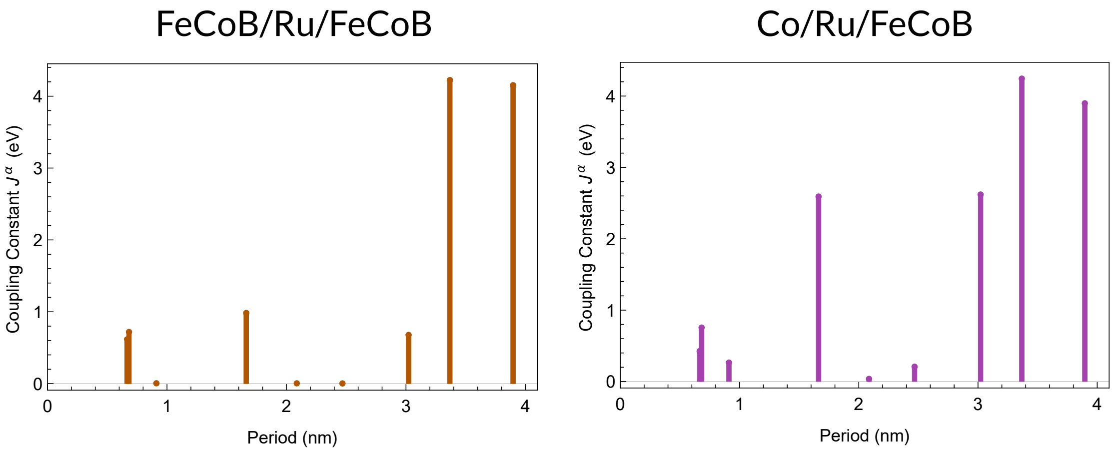

Figure 10.17: J^α values for the critical spanning vectors with corresponding periods of oscillation $(2\pi/q_\perp^\alpha)$ as obtained by fitting coupling oscillation data for the FeCoB/Ru/FeCoB and Co/Ru/FeCoB series as shown in Fig. 10.16 using Eq. 4.17 with the bulk Ru critical spanning vectors listed in Table.10.1. The Co/Ru/FeCoB data is the same as in Fig. 10.13, and is only shown for comparison purposes.

movement of the second AFC peak is more than twice as much as between any two of the samples where only the top magnetic layer was changed.

The FWHM of the rocking curve of the top Ru layer (0002) peak was found to be 3.92° and 6.58° for the Ru/Co/Ru and FeCoB/Ru samples, respectively. Like the previous case, this shows that Ru grown on top of FeCoB likely has worse texture than when it is grown on top of Ru/Co. For the same reasons discussed earlier, this is likely partly responsible for the decrease in magnitude of J_1 measurements for the FeCoB/Ru/FeCoB series as compared to the Co/Ru/FeCoB series.

With all of the data presented, we can now compare the effect of changing the bottom magnetic layer with changing the top magnetic layer. It is clear from the changes in amplitude and period of oscillations in Figs. 10.12, 10.14, and 10.16, that there is a much larger effect when changing the bottom magnetic layer than the top.

These differences are also made clear when looking at the values of J^{α} from each of the series as shown in Figs. 10.13, 10.15, and 10.17. When only the top magnetic layer was changed, the distribution of J^{α}'s remains similar, and they are all approximately the same order of magnitude. The three shortest period J^{α}'s, which are most accurate with the data we have fit, have not changed in magnitude by more than 50 % relative to one another for the three series.

This is quite a different story when we look at the effect of changing the bottom magnetic layer in Fig. 10.15. Here we see that the distribution of J^{α}'s is quite different in each case. The NiFe/Ru/FeCo series has J^{α} values that are more than an order of magnitude smaller than those of the Co/Ru/FeCo series. Further, the NiFe/Ru/FeCo series is missing two of the three shortest period J^{α}'s entirely. Comparing J^{α} values between the FeCoB/Ru/FeCoB and Co/Ru/FeCoB series, where the bottom magnetic layer is changed, is a similar situation. The distribution of values is quite different in each case, and in many cases they have vanished entirely for the FeCoB/Ru/FeCoB series.

10.3.3 Summary

These results make it clear that changing the bottom magnetic layer has a much larger effect on the magnitude and period of oscillations of the bilinear interlayer exchange coupling as compared to just changing the top magnetic layer. This agrees with predictions from the interface-reflection model that we are using. Specifically, when only the top magnetic layer is changed, the growth of the Ru spacer layer, and all layers below it, are identical in each case. This results in the Ru spacer layer Fermi surface to be the same in each case. The only effect that changing the composition of the top magnetic layer can have on the coupling oscillations, is to modify the electron reflection amplitude in the potential barrier shown in Fig. 4.6, which is the second term in Eq. 4.18. This could potentially result in a change in the magnitude of J^{α} for some critical spanning vectors, leading to a change in coupling oscillation amplitude, and small change in peak position, which is what we see. On the other hand, when the composition of the bottom magnetic layer is changed, it will most likely cause significant changes in the Ru spacer layer grown on top, which results in changes to the Fermi surface. Since this has the largest part in determining the nature of bilinear interlayer exchange coupling, it will cause larger changes in coupling.

10.4 Changes in Oscillatory Interlayer Exchange Coupling After Doping the Ru Spacer Layer with Interstitial Donors in NiFe/$\mathrm{Ru}_{1-x}\mathrm{B}_x$(d)/FeCo Structures

In this section we will study bilinear interlayer exchange coupling between a NiFe and FeCo magnetic layer coupled across a Ru spacer layer that has been doped with up to 15% of boron. We will be using the same samples that were described in Chapter 8. Like before, we will refer to these samples as the NiFe/$\mathrm{Ru}_{1-x}\mathrm{B}_x$/FeCo series, or the NiFe/Ru/FeCo series for the ones without boron.

When we studied the effect that annealing has on J_1 of these NiFe/Ru/FeCo samples in Chapter 8, we noticed that the addition of boron into the Ru spacer layer caused a significant change in the magnitude and period of J_1 oscillations. In this section we will investigate why the addition of boron has such an effect on J_1, and how it causes it.

The approach we have taken, is to first determine how we expect coupling to change after the addition of boron into the spacer layer. This includes effects from changing the Fermi level, crystal lattice expansion, and change in spacer layer texture. We will modify our interlayer exchange coupling parameters, from that of bulk Ru, in order to accommodate these effects. After this, we will use our modified parameters and model to fit the J_1 data for samples containing boron within the Ru spacer layer, which will allow us to determine if our assumptions are correct, or if something unexpected is occurring.

10.4.1 Theory and Experiment

Because of the large size difference between boron and Ru, it is expected that, instead of substituting the Ru atoms, boron will occupy interstitial locations. If this is occurring, we would expect the lattice volume to increase with the addition of boron into the Ru layer. Otherwise, since boron is a much smaller atom than Ru, if boron atoms were being substituted in for the Ru atoms, we would expect the lattice volume to decrease.

In order to determine which of the two is occurring, we have measured the unit cell volume of the NiFe/RuB series from Chapter 8 using XRD. These results are shown in Fig. 10.18, where it can be seen that the volume increases until 10% boron has been added into the spacer layer, and adding additional boron causes the volume to decrease. This indicates that the boron is occupying interstitial locations until up to 10% boron has been added, after which it begins to alter the crystal structure in additional ways.

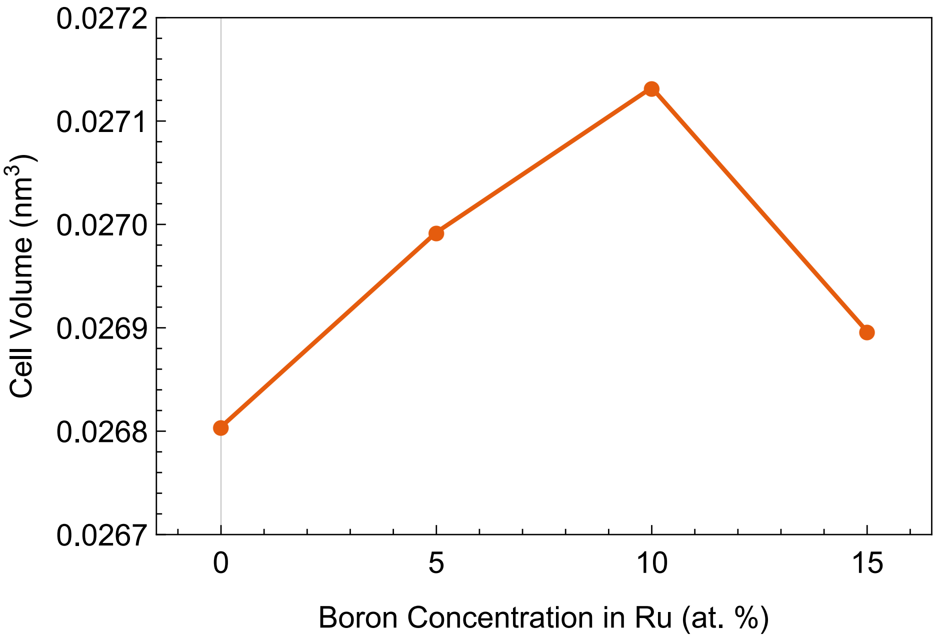

Figure 10.18: The crystallographic unit cell volume of the $\mathrm{Ru}_{1-x}\mathrm{B}_x$ alloy as the concentration of boron is increased.

Expansion of the lattice causes change in both the Brillouin zone dimensions, and the shape of the Fermi surface, both of which determine the length of the critical spanning vectors used in our interlayer exchange coupling model. In order to quantify the effect of these two changes, we will make use of the rigid-band model. This model assumes that the band structure remains fixed to that of a pure Ru spacer layer, and the addition or subtraction of conduction electrons from dopants simply shifts the Fermi level up or down, which causes a corresponding change in the Fermi surface. This rigid-band model was shown experimentally to be accurate for predicting the Fermi surface due to a change in Fermi level, and consequently, bilinear interlayer exchange coupling, for at least 10% Ni in NiCu alloy spacer layers. [87]

Since our magnetic layers are coupled through [0001] oriented RuB, our critical spanning vectors are also in this direction. This causes any change in the c-axis lattice spacing to change the length of our critical spanning vectors, and consequently, the period of oscillations of the interlayer exchange coupling. Specifically, the expansion of the c-axis lattice spacing with the addition of boron will cause a proportional decrease in the width of the Brillouin zone in the [0001] direction ($\Gamma \rightarrow \mathrm{A}$), which can be seen in Fig. 10.1. Using the rigid band model, as the Brillouin zone [0001] direction width decreases, the Fermi surface in that direction will simply be scaled proportionally, leading to a proportional change in length of our critical spanning vectors that go into Eq. 4.17.

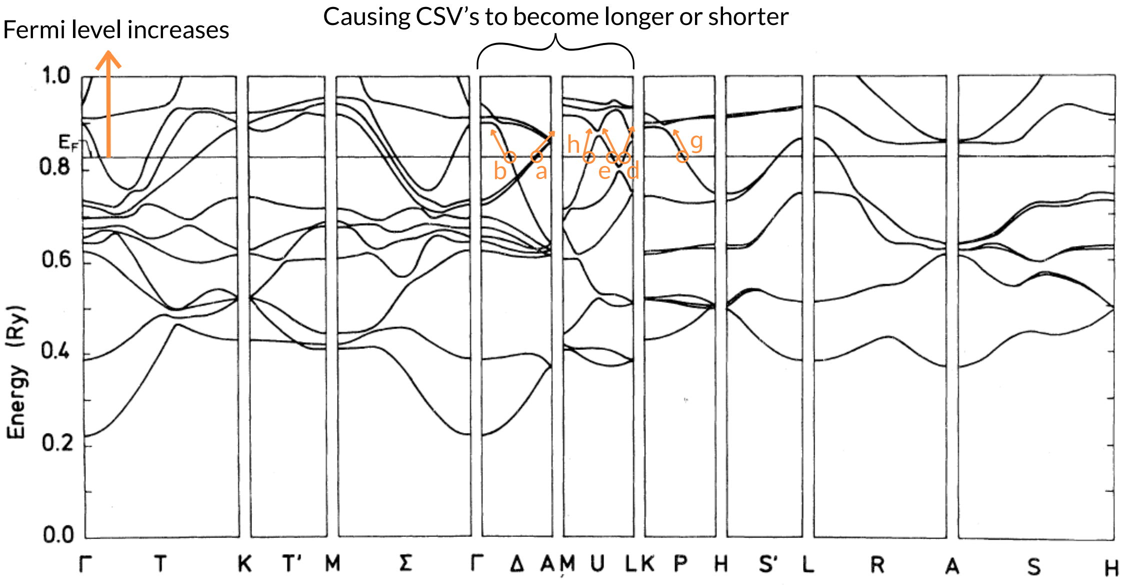

Figure 10.19: The relativistic band structure diagram of Ru with annotations showing directions in which some select Fermi surface sheets move as the Fermi level increases according to the rigid-band model. Some arrows are shown for sheet locations corresponding to the critical spanning vectors (CSV) labeled by a, b, d, e, g, and h from Fig. 10.6 and Table 10.1. Band structure reproduced from Ref. [54] with kind permission from APS (https://aps.org/).

Ru has 8 valence electrons, while boron has only 3. Just like in semiconductors, if boron was substituting for Ru atoms, we would expect fewer valence electrons to lower the Fermi level. However, in our samples, boron is undergoing interstitial addition for up to 10% boron. In this case boron is only very weakly bonded to the surrounding atoms, which results in there being approximately 0 of its 3 valence electrons used in the bonds. This allows approximately all of the 3 valence electrons on boron atoms to be used as donors in the conduction band, which instead of lowering the Fermi level, actually raises it. [14, 114, 80] Therefore, for up to 10 % boron addition into the Ru spacer layer, we would expect the Fermi level to be increased slightly.

As the Fermi level is increased, it causes the length of the critical spanning vectors, $q_{\perp}^{\alpha}$ in Eq. 4.17, to change, leading to longer or shorter periods of oscillation in coupling strength J_1. The rate of change of the Fermi surface radius as the Fermi level is changed, $dq_{\perp}^{\alpha}/dEf$ was estimated from the band structure diagram in Fig. 10.19, where we have circled the relevant locations of some critical spanning vectors.

One additional consequence of adding interstitial boron atoms into the Ru spacer layer is that the boron atoms are expected to increase the disorder and create lattice defects. One source of disorder is the random locations of the boron atoms. Another source of disorder is that interstitial boron tends to alter the crystal lattice of the host material that can lead to variations in atomic displacements from the bulk equilibrium positions. [117] These defects

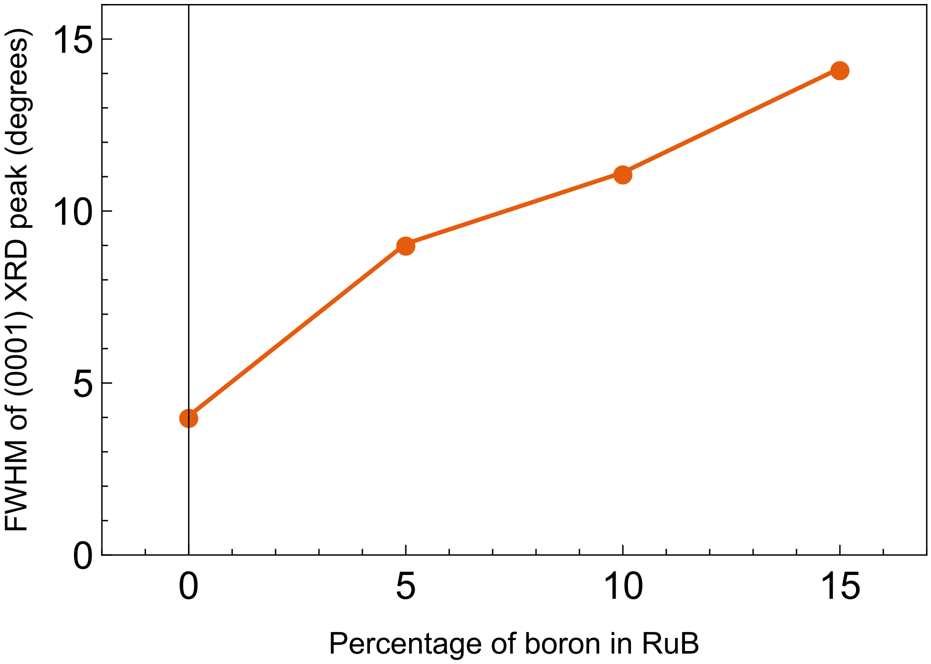

Figure 10.20: The FWHM of the Ru (0001) XRD peak rocking curve as boron is added into the Ru spacer layer. XRD measurements were done using the perpendicular configuration.

and disorder will increase the scattering of the electrons responsible for interlayer exchange coupling, reducing, in turn, the size of the oscillatory coupling. [106] In order to quantify the relative amount of dislocations, lattice defects, and disorder, caused by the addition of boron into the Ru spacer layer, we have used perpendicular XRD to measure the rocking curve of the Ru (0001) peak for samples with 0, 5, 10, and 15 % boron. The FWHM of each of these rocking curve measurements is shown in Fig. 10.20. There is an almost linear relationship between the FWHM and the concentration of boron within the layer. This indicates that the amount of dislocations and lattice defects within the spacer layer is likely increasing as boron is added. [64, 76, 45, 108, 8] This is in agreement with the findings when adding boron into FeCo thin films. [117] Thus, in addition to changing the length of the critical spanning vectors, we expect that adding boron into the Ru spacer layer will also attenuate the J_1 coupling strength. The widening of the rocking curve also indicates that crystallites within the polycrystal have a distribution of slight lattice rotations from one another so that the [0001] lattice direction points slightly off from the direction normal to the plane. This means that instead of the direction of coupling being exactly in the [0001] lattice direction, it is in a distribution of directions with slight offsets from the [0001] lattice direction. This will cause a slight broadening of the critical spanning vectors where instead of having a single length for the entire film, there is a distribution of lengths. The result of this will be a slight averaging out of short period oscillations, which can add an additional attenuation to J_1.

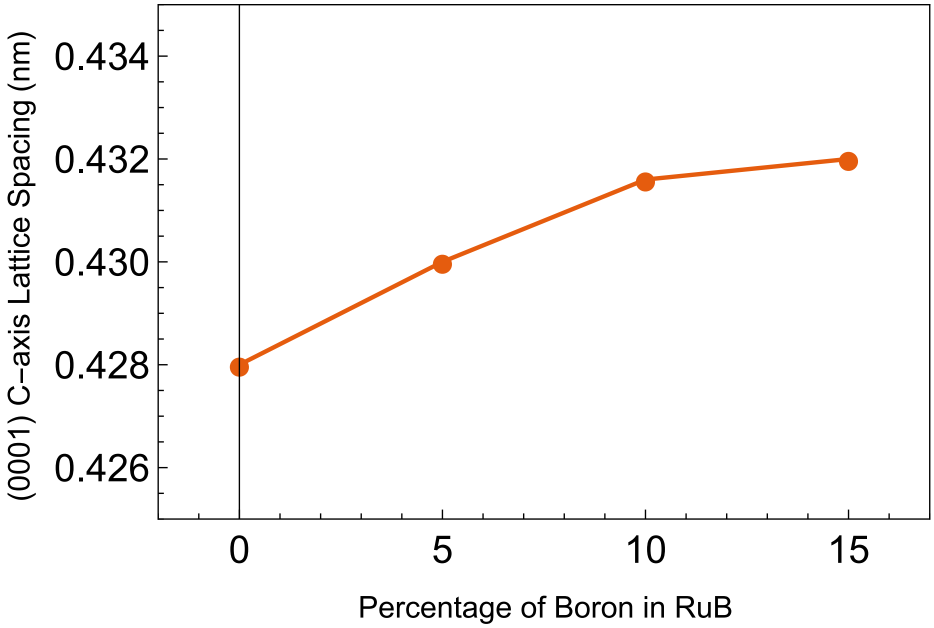

Figure 10.21: The change in (0001) c-axis lattice spacing of a sputtered RuB alloy as the percentage of boron within the alloy is increased from 0 % to 15 %. Lines between the data points are added as a guide to the eye.

Now that we know what changes to expect, in terms of coupling, from the addition of boron into the Ru spacer layer, we can modify the J^α parameters obtained from pure Ru spacer layers, and $q_\perp^\alpha$ values from bulk Ru, to accommodate these changes. We have started with the parameters obtained from the fit to the NiFe/Ru/FeCo data, as shown in Figs. 10.14 and 10.15, and modified them.

We have made 3 modifications: 1) decrease the length of the bulk Ru [0001] direction critical spanning vectors proportionally to the increase in the c-axis lattice spacing of the Ru spacer layer, 2) modify these critical spanning vectors to allow for a slight increase in the Fermi level from the addition of 3 boron valence electrons per atom, and 3) allow for an attenuation of the magnitude of all of the J^α coupling strengths equally.

All three of these modifications result in the following fitting equation, which has been modified from Eq. 4.17,

$$J_1(d) = \sum_\alpha \frac{J_{\mathrm{Ru}}^\alpha C_1}{d^2} \sin((q_\perp^\alpha C_2 + f(F))d + \phi^\alpha), \tag{10.7}$$

where J_{Ru}^α are the J^α values determined from fitting the NiFe/Ru/FeCo data, $q_\perp^\alpha$ are critical spanning vectors of bulk Ru, C_1 is a fitting parameter allowing for the attenuation caused by crystal disorder, C_2 is a factor to scale the length of the critical spanning vectors corresponding with a change in the c-axis lattice spacing, as calculated from XRD measurements,

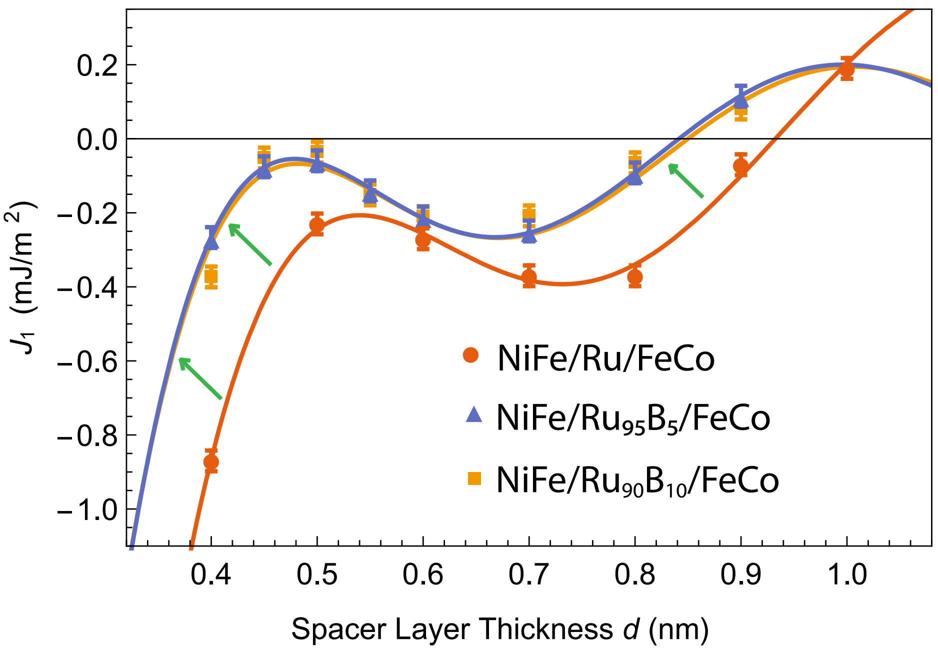

Figure 10.22: Coupling strength, J_1, as a function of thickness of the spacer layer. The orange points are data for a NiFe/Ru/FeCo series, the blue triangles are data for a NiFe/Ru$_{95}$B$_5$/FeCo series, and the yellow squares are data for the NiFe/Ru$_{90}$B$_{10}$/FeCo series. The orange line is the same fit from Fig. 10.14 using J^α values from Fig. 10.15. The blue and yellow lines are fit using Eq. 10.7. The fit to NiFe/Ru$_{95}$B$_5$/FeCo data corresponds to an increase in the Fermi level by 0.7 %, and an attenuation of $C_1 = 0.68$. The fit to NiFe/Ru$_{90}$B$_{10}$/FeCo data corresponds to an increase in the Fermi level by 0.7 %, and an attenuation of $C_1 = 0.66$.

and $f(F)$ is a function that depends on the Fermi level that will increase or decrease the length of each critical spanning vector as determined by Fig. 10.19.

Finally, we will take Eq. 10.7 and fit it to data from the series with 5 and 10% boron within the spacer layer in order to determine if our predictions are correct.

10.4.2 Results and Discussion

Fig. 10.22 shows the J_1 measurements, along with fits for the NiFe/Ru/FeCo (orange), NiFe/Ru$_{95}$B$_5$/FeCo (blue), and NiFe/Ru$_{90}$B$_{10}$/FeCo (yellow) series of samples.
The NiFe/Ru/FeCo data has the same fit as used in Fig. 10.14 with J^α values from Fig. 10.15. The NiFe/Ru$_{95}$B$_5$/FeCo and NiFe/Ru$_{90}$B$_{10}$/FeCo data are fit using Eq. 10.7. The fit to NiFe/Ru$_{95}$B$_5$/FeCo data corresponds to an increase in the Fermi level by 0.7 %, and an attenuation of $C_1 = 0.68$. The fit to NiFe/Ru$_{90}$B$_{10}$/FeCo data corresponds to an increase in the Fermi level by 0.7 %, and an attenuation of $C_1 = 0.66$.

It can be seen that by accounting for the lattice expansion, and increasing the bulk Ru Fermi level by only 0.7 %, and attenuating the J^α values by 32 %, we have obtained a very good fit to the NiFe/$Ru_{95}B_5$/FeCo data. This indicates that going from 0 to 5 % boron within the Ru spacer layer, the Fermi level moved as predicted by interstitial boron donor atoms, and the J^α values have been attenuated as predicted by the increased crystal disorder. The increase in the Fermi level confirms that the interstitial boron atoms are acting as electron donors and are not using their valence electrons for bonds with the atoms around them. The shift in J_1 oscillations with the increase of the Fermi level is also in agreement with the results found by Parkin *et al.* [87] and Okuno *et al.* [85] where they saw a shift in oscillations after the Fermi level was altered by the addition of Ni into a Cu spacer layer.

As we move from 5 to 10 % boron, our fits indicate that the Fermi level didn't move any further, and the J^α values were attenuated by an additional 2 %. According to the rigid band model, and boron atoms acting as electron donors, we would expect the Fermi level to continue to increase like it did moving from 0 to 5 % boron. If the Fermi level had increased further, our model predicts that the dominant short period oscillations caused by the critical spanning vector labeled as b should become even shorter. The obvious reason for this divergence from predictions is that the large addition of boron has changed the shape of the Fermi surface, drastically changing lengths of existing critical spanning vectors, and giving rise to new ones. Thus, the rigid band model has broken down for samples with 10 % boron or higher.

The divergence from the rigid band model in these results occurs at a much lower concentration of dopants than the results of Parkin *et al.* [87]. In our case, we see the model break down after adding boron to Ru at concentrations greater than 5 %, while in the latter case, it was accurate adding Ni to Cu at up to 10 %, and was only slightly less accurate at 15 %. The likely reason for this difference is the fact that in our case, boron atoms are much smaller than Ru atoms and have a vastly different electronic configuration, and are taking interstitial locations in the Ru lattice, while Ni and Cu atoms are much more similar to one another and Ni atoms take the place of Cu atoms in the Cu lattice. The addition of interstitial boron atoms changes the lattice of Ru much more quickly than that of the substitutional Ni atoms into Cu. This is made clear by the widening rocking curve as boron is added to Ru, as shown in Fig. 10.20, that indicates the lattice is likely becoming more disordered with increased lattice dislocations and defects. [64, 76, 45, 108, 8] This is also a well known effect of the addition of boron to transition metals, and it is the reason why boron is added to FeCo which destabilizes the lattice to the point where $Fe_{60}Co_{20}B_{20}$ is amorphous. [117] On the other hand, Ni and Cu atoms are both FCC, have similar lattice parameters, and are completely soluble with one another over the complete composition range from pure Cu to pure Ni. [87] As such, adding Ni to Cu is expected to have a much smaller effect on the lattice.

The attenuation of coupling strength by 32 % after adding 5 % boron into the Ru layer seems reasonable considering the increase in the FWHM of the Ru (0001) XRD rocking

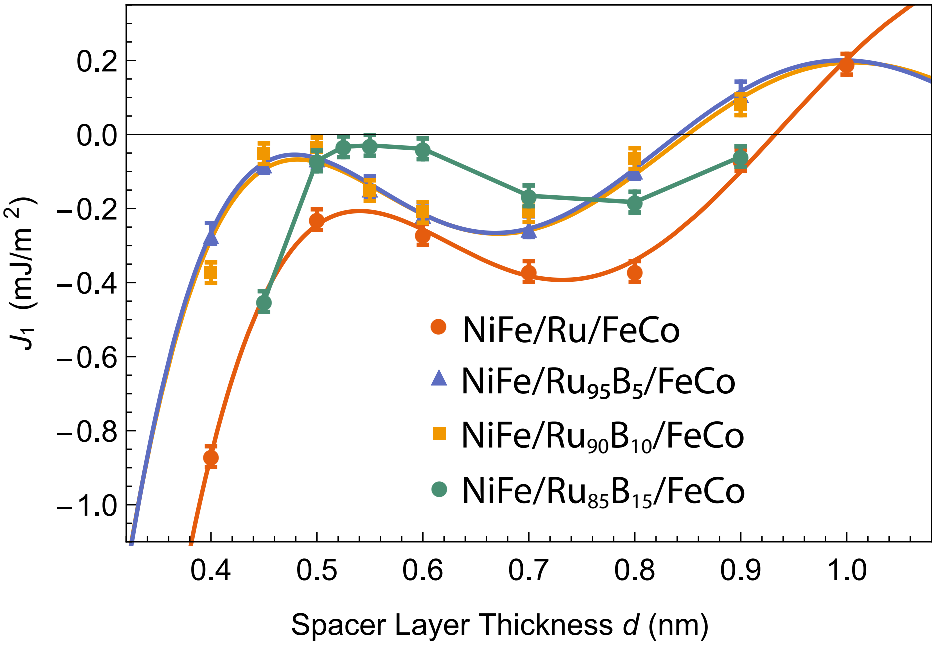

Figure 10.23: Coupling strength, J_1, as a function of thickness of the spacer layer. This plot contains the same as Fig. 10.22, with the addition of data for the series of samples with 15 % boron within the Ru spacer layer, shown as green circles. The 15 % boron data has not been fit, instead, connecting lines between the points have been added as a guide to the eye.

curve. As discussed earlier, this is expected to reduce coupling strength by scattering the electrons responsible for coupling. This scattering effect is amplified by the fact that interlayer magnetic coupling requires electron wavefunctions to reflect from the walls of the potential well formed by the M/NM/M trilayer structure. That means that the electrons take a large number of round trips through the spacer layer and have many more chances to scatter from any defects. Considering that the FWHM increases by about the same amount going from 5 to 10 % boron within the Ru spacer layer, we would expect J_1 to be significantly more attenuated in the samples with 10 % boron as compared to the samples with 5 % boron. From the fit, we see that J_1 is attenuated by an additional 2 %, but that is much smaller than the 32 % attenuation we saw going from 0 to 5 % boron. One possible explanation for this is that the attenuation of J_1 is being counteracted by the addition of new critical spanning vectors due to large changes in the Fermi surface.

Fig. 10.23 shows additional J_1 measurements for the NiFe/Ru$_{85}$B$_{15}$/FeCo series of samples. The 15 % boron series has to high of a boron concentration for the rigid band model, as such we have not fit it like the others. It can be seen that for the samples with 15 % boron, the J_1 oscillations have shifted to longer periods, which is the opposite to that predicted by the rigid-band model. We also see that going from 10 to 15 % boron within the spacer layer has caused a significant amount of attenuation to J_1. Like before, this is expected since the addition of boron is known to cause increased lattice disorder. [117] This is also confirmed by the FWHM of the Ru (0001) XRD rocking curve continuing to increase, which can indicate increased lattice defects and dislocations. This effect is expected to continue as more boron is added until Ru becomes amorphous just like $Fe_{60}Co_{20}B_{20}$.

10.4.3 Summary

We have shown that the change in interlayer exchange coupling seen, by adding 5 % boron to the Ru spacer layer in the NiFe/Ru/FeCo trilayer structure, can be explained by a slight increase in the Fermi level, expansion of the c-axis, and increased the lattice disorder, all due to the interstitial boron donor atoms. We have included all three of these changes into the interface-reflection model and shown that it accounts for changes in J_1 seen in our measurements of samples with 0 and 5 % boron in the spacer layer.

We have used the rigid band model to predict how these changes have effected the Fermi surface of the Ru spacer layer. We modified the interface-reflection RKKY-like model to account for the changes in the Fermi surface, which allowed it to fit very well to the J_1 measurements for the series with 5 % boron within the spacer layer. This indicates that the dependence of bilinear interlayer exchange coupling on the topology of the Fermi surface is correctly predicted by the interface-reflection model that we have used.

We have also shown that the addition of 10 % or more boron into the Ru spacer layer in the NiFe/Ru/FeCo trilayer structure has caused the Fermi surface to change dramatically, likely giving rise to new critical spanning vectors, to the point where the rigid band approximation is no longer accurate.

Chapter 11

Conclusions

The work of this thesis was brought about due to the inability to create a synthetic antiferromagnetic (SAF) fixed layer containing FeCoB that could withstand being annealed above 200 °C. We had created a layer structure such as FeCoB/Ru(4 nm)/FeCoB, and it was strongly AFC coupled as deposited, but after annealing above 200 °C, the two FeCoB layers were now FC coupled. It is important to note that if boron-free magnetic layers are used, such as FeCo or Co, the SAF structure remains AFC after annealing at up to 350 °C, which we have also confirmed. We required a SAF layer that contains FeCoB, and has coupling that is resistant to change during the annealing step, for use as a fixed layer in FeCoB/MgO/FeCoB tunnel junction based STT-MRAM devices. Thus, throughout this thesis, the work has focused on understanding why coupling in such SAF structures changes after annealing, and after that, how to prevent such changes.

Firstly, a novel broadband FMR spectrometer was developed that is capable of determining the coupling strength of magnetic layers coupled across a non-magnetic spacer layer when they are both FC or AFC coupled. We have demonstrated that this broadband FMR spectrometer is able to measure over a range of frequencies from 0 to 40 GHz with a single setup. This new spectrometer design is able to achieve the same level of SNR as the original narrow-band design.

We sputtered several series of samples containing trilayer structures of the form FeCoB/Ta,Ru,Mo(d)/FeCoB where d is the thickness of the spacer layer that was varied over a range of thicknesses of at least 0.4 to 1 nm. These samples were then measured using the FMR spectrometer, and from these we were able to characterize the interlayer exchange coupling between the two FeCoB layers both as deposited and after being annealed at 200 °C and 300 °C.

We found that the dependence of the coupling strength on Ta spacer layer thickness is the same for non-annealed samples and those annealed at 200 °C: the coupling drops to 0 above approximately 0.475 nm and increases rapidly below 0.45 nm. For samples annealed at 300 °C coupling increases rapidly below about 0.7 nm. The coupling interface topography of the $\boldsymbol{M}_1$ layer was estimated in order to rule out a significant Néel "orange-peel" contribution to the coupling, which is true for all three spacer layers.

We found that annealing the samples with Ru and Mo spacer layers increases the FC coupling strength. In these samples annealed at 300 °C, the coupling between FeCoB layers is ferromagnetic if the spacer layer thickness is below 0.7 nm and is zero for spacer layer thicknesses greater than 0.8 nm.

Most importantly, these results showed that it is almost impossible to maintain AFC coupling within an FeCoB based SAF fixed layers composed of the structures studied when annealed above 200 °C.

Next, we investigated the role that boron within the FeCoB magnetic layers has on interlayer exchange coupling after annealing. It was thought that during the annealing process, boron may be diffusing into the spacer layer which causes the coupling to change. In order to explore this possibility, we sputtered samples containing the trilayer structure NiFe/$\mathrm{Ru}_{1-x}\mathrm{B}_x$(d)/FeCo, where x is varied from 0 to 15% boron, and the spacer layer thickness, d is varied from 0.4 to 0.9 nm. We then characterized the interlayer exchange coupling within all of the samples both before and after annealing at 250 °C. We also characterized the elemental diffusion using TEM-EDXS. We found that samples containing boron within the Ru spacer layer had increased diffusion of magnetic atoms into the spacer layer after annealing, causing the coupling to become FC.

Next, we sputtered samples containing the trilayer structure Co/Ru/FeCoB, and found that, unlike the FeCoB/Ru/FeCoB structure, these samples remained AFC coupled over the range of spacer layer thicknesses from 0.4 to 1 nm after annealing at 350 °C. These results, along with previous results allowed us to hypothesize about what might be occuring in the FeCoB/Ru/FeCoB samples that leads to FC coupling: During the sputter deposition process, boron from the lower FeCoB layer floats upwards into the Ru spacer layer. Then during the annealing process, the presence of boron within the Ru spacer layer causes increased diffusion of the magnetic atoms into the spacer layer, leading to FC coupling.

Finally, we created a series of samples where we placed 1 nm FeCo and Co diffusion barriers at the FeCoB/Ru interfaces within the FeCoB/Ru(d)/FeCoB layer structure, where d is varied from 0.4 to 1 nm. We found that these diffusion barriers were effective at blocking the boron diffusion and allowed us to achieve AFC coupling that remained AFC even after annealing at a higher temperature of 350 °C.

As an additional study, we showed that the physics of interlayer exchange coupling within the Co/Ru/Co layer structure is well described by the RKKY-like interface-reflection model over a wide range of Ru layer thicknesses from 0.4 to 3.4 nm without the need for an exponentially decaying contribution fron evanescent electron states, or an additional superexchange-like contribution. We showed this by fitting the dependence of J_1 on spacer layer thickness, and temperature. We also showed that, in trilayer structures with the form X/Ru/Y, where X and Y are the bottom and top magnetic layers coupled across the Ru spacer layer, the composition of the bottom magnetic layer has a much larger effect on interlayer exchange coupling than the top. This is because the composition of the bottom magnetic layer effects the growth of the Ru layer above, which changes its Fermi surface, and consequently, causes a large change in coupling. Lastly, we found that adding 5 % boron into the Ru spacer layer in samples with the structure NiFe/Ru/FeCo caused the lattice to expand, the Fermi level to increase, and lattice disorder to increase. We found that by accounting for these changes, the interface-reflection RKKY-like model accurately predicted the interlayer exchange coupling after the addition of 5 % boron.

Bibliography

[1] M. Arora, C. Fowley, T. McKinnon, E. Kowalska, V. Sluka, A. M. Deac, B. Heinrich, and E. Girt. Spin torque switching in nanopillars with antiferromagnetic reference layer. *IEEE Magnetics Letters*, 8:1–5, 2017.

[2] Monika Arora. *Origin of perpendicular magnetic anisotropy in Co/Ni multilayers and their use in STT-RAM.* PhD thesis, Science: Department of Physics, 2017.

[3] Neil W Ashcroft, N David Mermin, et al. Solid state physics, 1976.

[4] Mark Bachman. RCA-1 silicon wafer cleaning. *INRF application note Engineering of Microworld at the University of California. Irvine*, 1999.

[5] Mark Bachman. Cleaning procedures for silicon wafers. *INRF Application Note, Spring*, 2002.

[6] J.A.C Bland and B. Heinrich. *Ultrathin Magnetic Structures III.* Findamentals of Nanomagnetism. Springer, 2005.

[7] J. F. Bobo, H. Kikuchi, O. Redon, E. Snoeck, M. Piecuch, and R. L. White. Pinholes in antiferromagnetically coupled multilayers: Effects on hysteresis loops and relation to biquadratic exchange. *Physical Review B*, 60:4131–4141, Aug 1999.

[8] I Booker, L Rahimzadeh Khoshroo, JF Woitok, V Kaganer, C Mauder, H Behmenburg, J Gruis, M Heuken, H Kalisch, and RH Jansen. Dislocation density assessment via X-ray GaN rocking curve scans. *Physica Status Solidi C*, 7(7-8):1787–1789, 2010.

[9] P Bruno. Theory of intrinsic and thermally induced interlayer magnetic coupling between ferromagnetic films separated by an insulating layer. *Physical Review B*, 49(18):13231, 1994.

[10] P Bruno. Theory of interlayer magnetic coupling. *Physical Review B*, 52(1):411, 1995.

[11] P. Bruno and C. Chappert. Oscillatory coupling between ferromagnetic layers separated by a nonmagnetic metal spacer. *Physical Review Letters*, 67:1602–1605, Sep 1991.

[12] P. Bruno and C. Chappert. Ruderman-kittel theory of oscillatory interlayer exchange coupling. *Physical Review B*, 46:261–270, Jul 1992.

[13] M Buchmeier, R Schreiber, DE Bürgler, and CM Schneider. Thickness dependence of linear and quadratic magneto-optical kerr effects in ultrathin fe (001) films. *Physical Review B*, 79(6):064402, 2009.

[14] Manuel Cardona and Y Yu Peter. *Fundamentals of semiconductors*. Springer, 2005.

[15] C. Chappert, A. Fert, and F. Van Dau. The emergence of spin electronics in data storage. *Nature Materials*, 6:813, 2007.

[16] Boris Chesca, Reinhold Kleiner, and Dieter Koelle. *SQUID Theory*, chapter 2, pages 29–92. John Wiley & Sons, Ltd, 2005.

[17] S. Chikazumi. *Physics of Ferromagnetism*. International Series of Monographs on Physics. OUP Oxford, 2009.

[18] Soshin Chikazumi. *Physics of Ferromagnetism (The International Series of Monographs on Physics)*. The International Series of Monographs on Physics. Oxford University Press, USA, 2 edition, 2009.

[19] S. . Chung, T. Kishi, J. W. Park, M. Yoshikawa, K. S. Park, T. Nagase, K. Sunouchi, H. Kanaya, G. C. Kim, K. Noma, M. S. Lee, A. Yamamoto, K. M. Rho, K. Tsuchida, S. J. Chung, J. Y. Yi, H. S. Kim, Y. S. Chun, H. Oyamatsu, and S. J. Hong. 4gbit density stt-mram using perpendicular mtj realized with compact cell structure. In *2016 IEEE International Electron Devices Meeting (IEDM)*, pages 27.1.1–27.1.4, Dec 2016.

[20] J. M. D. Coey. *Magnetism and Magnetic Materials*. Cambridge University Press, 2010.

[21] PT Coleridge. The fermi surface of ruthenium as determined by the de haas-van alphen effect. *Journal of Low Temperature Physics*, 1(6):577–594, 1969.

[22] M. Cubukcu, O. Boulle, N. Mikuszeit, C. Hamelin, T. Brächer, N. Lamard, M. Cyrille, L. Buda-Prejbeanu, K. Garello, I. M. Miron, O. Klein, G. de Loubens, V. V. Naletov, J. Langer, B. Ocker, P. Gambardella, and G. Gaudin. Ultra-fast perpendicular spin?orbit torque mram. *IEEE Transactions on Magnetics*, 54(4):1–4, April 2018.

[23] JR Cullen and KB Hathaway. A phenomenological theory for the temperature dependence of the antiferromagnetic coupling in thin-film sandwiches and multilayers. *Journal of Applied Physics*, 70(10):5879–5879, 1991.

[24] M. I. Current, Y. J. Lee, Y. L. Lu, T. C. Cho, T. S. Chao, H. Onoda, K. Sekar, and N. Tokoro. Microwave and rta annealing of phos-doped, strained si(100) and (110) implanted with molecular carbon ions. In *2013 13th International Workshop on Junction Technology (IWJT)*, pages 84–87, June 2013.

[25] T. Devolder, J.-V. Kim, L. Nistor, R. Sousa, B. Rodmacq, and B. Diény. Exchange stiffness in ultrathin perpendicularly magnetized cofeb layers determined using the spectroscopy of electrically excited spin waves. *Journal of Applied Physics*, 120(18):183902, 2016.

[26] T. Devolder, E. Liu, J. Swerts, S. Couet, T. Lin, S. Mertens, A. Furnemont, G. Kar, and J. De Boeck. Ferromagnetic resonance study of composite co/ni - fecob free layers with perpendicular anisotropy. *Applied Physics Letters*, 109(14):142408, 2016.

[27] J d'Albuquerque e Castro, J Mathon, Murielle Villeret, and A Umerski. Confinement mechanism for strong temperature dependence of the interlayer exchange coupling in co/cu (001). *Physical Review B*, 53(20):R13306, 1996.

[28] DM Edwards, J Mathon, RB Muniz, and MS Phan. Oscillations of the exchange in magnetic multilayers as an analog of de haas–van alphen effect. *Physical review letters*, 67(4):493, 1991.

[29] RP Erickson, Kristl B Hathaway, and James R Cullen. Mechanism for non-heisenberg-exchange coupling between ferromagnetic layers. *Physical Review B*, 47(5):2626, 1993.

[30] Robin FC Farrow, Bernard Dieny, Markus Donath, Albert Fert, and BD Hermsmeier. *Magnetism and Structure in Systems of Reduced Dimension*, volume 309. Springer Science & Business Media, 2013.

[31] Gayanath W. Fernando. Chapter 5 - probing layered systems: A brief guide to experimental techniques. In Gayanath W. Fernando, editor, *Metallic Multilayers and their Applications*, volume 4 of *Handbook of Metal Physics*, pages 111 – 130. Elsevier, 2008.

[32] Daniel Gall. Electron mean free path in elemental metals. *Journal of Applied Physics*, 119(8):085101, 2016.

[33] Thomas L. Gilbert. A phenomenological theory of damping in ferromagnetic materials. *IEEE Transactions on Magnetics*, 40, 2004.

[34] E. Girt and H. J. Richter. Antiferromagnetically coupled perpendicular recording media. *IEEE Transactions on Magnetics*, 39(5):2306–2310, Sept 2003.

[35] Erol Girt and Hans Jürgen Richter. Antiferromagnetically coupled perpendicular recording media. *IEEE Transactions on Magnetics*, 39(5):2306–2310, 2003.

[36] Joseph I. Goldstein, Dale E. Newbury, Joseph R. Michael, Nicholas W. M. Ritchie, John Henry J. Scott, and David C. Joy. *X-Rays*, pages 39–63. Springer New York, New York, NY, 2018.

[37] A. A. Greer, A. X. Gray, S. Kanai, A. M. Kaiser, S. Ueda, Y. Yamashita, C. Bordel, G. Palsson, N. Maejima, S.-H. Yang, G. Conti, K. Kobayashi, S. Ikeda, F. Matsukura, H. Ohno, C. M. Schneider, J. B. Kortright, F. Hellman, and C. S. Fadley. Observation of boron diffusion in an annealed Ta/CoFeB/MgO magnetic tunnel junction with standing-wave hard x-ray photoemission. *Applied Physics Letters*, 101(20):202402, 2012.

[38] David J Griffiths and Darrell F Schroeter. *Introduction to quantum mechanics.* Cambridge University Press, 2018.

[39] YK Ha, JE Lee, H-J Kim, JS Bae, SC Oh, KT Nam, SO Park, NI Lee, HK Kang, U-I Chung, et al. Mram with novel shaped cell using synthetic anti-ferromagnetic free layer. In *Digest of Technical Papers. 2004 Symposium on VLSI Technology, 2004.*, pages 24–25. IEEE, 2004.

[40] Guchang Han, Michael Tran, Cheow Hin Sim, Jacob Chenchen Wang, Kwaku Eason, Sze Ter Lim, and Aihong Huang. Control of offset field and pinning stability in perpendicular magnetic tunnelling junctions with synthetic antiferromagnetic coupling multilayer. *Journal of Applied Physics*, 117(17):17B515, 2015.

[41] J. J. Hanak and J. P. Pellicane. Effect of secondary electrons and negative ions on sputtering of films. *Journal of Vacuum Science and Technology*, 13(1):406–409, 1976.

[42] A. Hashimoto, S. Saito, D. Y. Kim, H. Takashima, T. Ueno, and M. Takahashi. Fe content dependence of synthetic-antiferromagnetic coupling in subnano-crystalline FeCoB/Ru/FeCoB films. *IEEE Transactions on Magnetics*, 42(10):2342–2344, Oct 2006.

[43] Kristl B Hathaway and James R Cullen. A free-electron model for the exchange coupling of ferromagnets through paramagnetic metals. *Journal of Magnetism and Magnetic Materials*, 104:1840–1842, 1992.

[44] Eugene Hecht. *Optics, 5e.* Pearson Education, 2002.

[45] H. Heinke, V. Kirchner, S. Einfeldt, and D. Hommel. X-ray diffraction analysis of the defect structure in epitaxial GaN. *Applied Physics Letters*, 77(14):2145–2147, 2000.

[46] B. Heinrich and J.F. Cochran. Ultrathin metallic magnetic films: magnetic anisotropies and exchange interactions. *Advances in Physics*, 42(5):523–639, 1993.

[47] Karen Holloway and Peter M. Fryer. Tantalum as a diffusion barrier between copper and silicon. *Applied Physics Letters*, 57(17):1736–1738, 1990.

[48] E. Šimánek and B. Heinrich. Gilbert damping in magnetic multilayers. *Physical Review B*, 67:144418, Apr 2003.

[49] S. Ikeda, J. Hayakawa, Y. Ashizawa, Y. M. Lee, K. Miura, H. Hasegawa, M. Tsunoda, F. Matsukura, and H. Ohno. Tunnel magnetoresistance of 604% at 300k by suppression of ta diffusion in CoFeB/MgO/CoFeB pseudo-spin-valves annealed at high temperature. *Applied Physics Letters*, 93(8):082508, 2008.

[50] S. Ikeda, K. Miura, H. Yamamoto, K. Mizunuma, H. D. Gan, M. Endo, S. Kanai, J. Hayakawa, F. Matsukura, and H. Ohno. A perpendicular-anisotropy CoFeB/MgO magnetic tunnel junction. *Nature Materials*, 9(9):721–724, 2010.

[51] Kyohei Ishikawa, Mikihiko Oogane, Kousuke Fujiwara, Junichi Jono, Masaaki Tsuchida, and Yasuo Ando. Investigation of magnetic sensor properties of magnetic tunnel junctions with superparamagnetic free layer at low frequencies for biomedical imaging applications Investigation of magnetic sensor properties of magnetic tunnel junctions with superparamagnet. *Japanese Journal of Applied Physics*, 55:123001, 2016.

[52] S. C. Jain, W. Schoenmaker, R. Lindsay, P. A. Stolk, S. Decoutere, M. Willander, and H. E. Maes. Transient enhanced diffusion of boron in si. *Journal of Applied Physics*, 91(11):8919–8941, 2002.

[53] Youngman Jang, Chunghee Nam, J. Y. Kim, B. K. Cho, Y. J. Cho, and T. W. Kim. Magnetic field sensing scheme using CoFeB/MgO/CoFeB tunneling junction with superparamagnetic cofeb layer. *Applied Physics Letters*, 89(16):163119, 2006.

[54] Ove Jepsen, O Krogh Andersen, and Allan Roy Mackintosh. Electronic structure of hcp transition metals. *Physical Review B*, 12(8):3084, 1975.

[55] K.-F. Yu, C. H. Tsai, Patent No. US 9337316. Method for finfet device, 2016.

[56] Jimmy J Kan. *Engineering of metallic multilayers and spin transfer torque devices*. PhD thesis, UC San Diego, 2014.

[57] Bartlomiej Kardasz. *Anisotropies and Spin Dynamics in Ultrathin Magnetic Multilayer Structures*. PhD thesis, Simon Fraser University, 2009.

[58] S. V. Karthik, Y. K. Takahashi, T. Ohkubo, K. Hono, S. Ikeda, and H. Ohno. Transmission electron microscopy investigation of CoFeB/MgO/CoFeB pseudospin valves annealed at different temperatures. *Journal of Applied Physics*, 106(2):023920, 2009.

[59] Safa Kasap and Peter Capper. *Springer Handbook of Electronic and Photonic Materials*. Springer Handbooks. Springer, 2006.

[60] Andrew D. Kent and Daniel C. Worledge. A new spin on magnetic memories. *Nature Nanotechnology*, 10:187, 2015.

[61] Werner Kern. The evolution of silicon wafer cleaning technology. *Journal of the Electrochemical Society*, 137(6):1887, 1990.

[62] Daniel J. Kester and Russell Messier. Macro-effects of resputtering due to negative ion bombardment of growing thin films. *Journal of Materials Research*, 8(8):1928?1937, 1993.

[63] Behrouz Khodadadi, Jamileh Beik Mohammadi, Joshua Michael Jones, Abhishek Srivastava, Claudia Mewes, Tim Mewes, and Christian Kaiser. Interlayer exchange coupling in asymmetric Co−Fe/Ru/Co−Fe trilayers investigated with broadband temperature-dependent ferromagnetic resonance. *Physical Review Applied*, 8:014024, Jul 2017.

[64] Mikhail A Krivoglaz. *X-ray and neutron diffraction in nonideal crystals*. Springer Science & Business Media, 2012.

[65] Lifshits L. Landau, E. On the theory of the dispersion of magnetic permeability in ferromagnetic bodies. *Phys. Zeitsch. der Sow.*, 8, 1935.

[66] C Lacroix and JP Gavigan. Interlayer coupling in magnetic multilayers: analogy to superexchange processes in insulators. *Journal of magnetism and magnetic materials*, 93:413–417, 1991.

[67] BC Lee and Y-C Chang. Interlayer exchange coupling in (111) Co/Cu/Co trilayers: Full-band versus reflection-amplitude calculations. *Physical Review B*, 62(6):3888, 2000.

[68] Du-Yeong Lee, Seung-Eun Lee, Tae-Hun Shim, and Jea-Gun Park. Tunneling-magnetoresistance ratio comparison of MgO-based perpendicular-magnetic-tunneling-junction spin valve between top and bottom co2fe6b2 free layer structure. *Nanoscale Research Letters*, 11(1):433, Sep 2016.

[69] J Lindner, C Rüdt, E Kosubek, P Poulopoulos, K Baberschke, P Blomquist, R Wäppling, and DL Mills. T 3/2 dependence of the interlayer exchange coupling in ferromagnetic multilayers. *Physical review letters*, 88(16):167206, 2002.

[70] Xiaoxi Liu, Hidetoshi Matsuoka, Hong Zhang, and Akimitsu Morisako. Manipulating the crystallographic properties of Fe/MgO/Fe trilayers. *Journal of Applied Physics*, 105(7):07C909, 2009.

[71] Cuchet Léa, Rodmacq Bernard, Auffret Stéphane, Sousa Ricardo C, Prejbeanu Ioan L, and Dieny Bernard. Perpendicular magnetic tunnel junctions with a synthetic storage or reference layer: A new route towards Pt- and Pd-free junctions. *Scientific Reports*, 6:2045–2322, 2016.

[72] M Mändl, H Hoffmann, and P Kücher. Diffusion barrier properties of Ti/TiN investigated by transmission electron microscopy. *Journal of applied Physics*, 68(5):2127–2132, 1990.

[73] J. Mathon, Murielle Villeret, R. B. Muniz, J. d'Albuquerque e Castro, and D. M. Edwards. Quantum well theory of the exchange coupling in Co/Cu/Co(001). *Phys. Rev. Lett.*, 74:3696–3699, May 1995.

[74] Tommy McKinnon and Erol Girt. Exchange coupling in FeCoB/Ru, Mo/FeCoB trilayer structures. *Applied Physics Letters*, 113(19):192407, 2018.

[75] Tommy McKinnon, Pavlo Omelchenko, Bret Heinrich, and Erol Girt. Fmr study of interlayer exchange coupling in FeCoB|Ta|FeCoB trilayers with in-plane anisotropy. *Journal of Applied Physics*, 123(22):223903, 2018.

[76] T Metzger, R Höpler, E Born, O Ambacher, M Stutzmann, R Stömmer, M Schuster, H Göbel, S Christiansen, M Albrecht, et al. Defect structure of epitaxial GaN films determined by transmission electron microscopy and triple-axis X-ray diffractometry. *Philosophical magazine A*, 77(4):1013–1025, 1998.

[77] Eric Montoya. *Spin pumping and spin transport in magnetic heterostructures.* PhD thesis, Science: Department of Physics, 2016.

[78] Eric Montoya, Tommy McKinnon, Atieh Zamani, Erol Girt, and Bret Heinrich. Broadband ferromagnetic resonance system and methods for ultrathin magnetic films. *Journal of Magnetism and Magnetic Materials*, 356:12–20, 2014.

[79] Eric Montoya, Pavlo Omelchenko, Chris Coutts, Nicholas R. Lee-Hone, René Hübner, David Broun, Bret Heinrich, and Erol Girt. Spin transport in tantalum studied using magnetic single and double layers. *Physical Review B*, 94:054416, Aug 2016.

[80] Jonathan E. Moussa and Marvin L. Cohen. Constraints on T_c for superconductivity in heavily boron-doped diamond. *Physical Review B*, 77:064518, Feb 2008.

[81] Jari Mäkinen. Chapter seven - thick-film soi wafers: Preparation and properties. In Veikko Lindroos, Markku Tilli, Ari Lehto, and Teruaki Motooka, editors, *Handbook of Silicon Based MEMS Materials and Technologies*, Micro and Nano Technologies, pages 107 – 136. William Andrew Publishing, Boston, 2010.

[82] Zachary Raymond Nunn and Erol Girt. Non-collinear coupling across RuCo and RuFe alloys. *arXiv preprint arXiv:1901.07055*, 2019.

[83] Se Young O, Chan-Gyu Lee, Alexander J. Shapiro, William F. Egelhoff Jr., Mark D. Vaudin, Jennifer L. Ruglovsky, Jonathan Mallett, and Philip W. T. Pong. X-ray diffraction study of the optimization of MgO growth conditions for magnetic tunnel junctions. *Journal of Applied Physics*, 103(7):07A920, 2008.

[84] Milton Ohring. Chapter 5 - plasma and ion beam processing of thin films. In Milton Ohring, editor, *Materials Science of Thin Films (Second Edition)*, pages 203 – 275. Academic Press, San Diego, second edition edition, 2002.

[85] S. N. Okuno and K. Inomata. Dependence on fermi surface dimensions of oscillatory exchange coupling in Co/Cu$_{1-x}$Ni$_x$(110) multilayers. *Physical Review Letters*, 70:1711–1714, Mar 1993.

[86] Greg Parker. Encyclopedia of materials: science and technology. 2001.

[87] SSP Parkin, C Chappert, and F Herman. Oscillatory exchange coupling and giant magnetoresistance via Cu-X alloys (X= Au, Fe, Ni). *EPL (Europhysics Letters)*, 24(1):71, 1993.

[88] SSP Parkin, N More, and KP Roche. Oscillations in exchange coupling and magnetoresistance in metallic superlattice structures: Co/ru, co/cr, and fe/cr. *Physical review letters*, 64(19):2304, 1990.

[89] Timothy M Philip, Nicholas A Lanzillo, Tue Gunst, Troels Markussen, Jonathan Cobb, Shela Aboud, and Robert R Robison. First-principles evaluation of fcc ruthenium for its use in advanced interconnects. *Physical Review Applied*, 13(4):044045, 2020.

[90] P. Pirro, A. Hamadeh, M. Lavanant-Jambert, T. Meyer, B. Tao, E. Rosario, Y. Lu, M. Hehn, S. Mangin, and S. Petit Watelot. Perpendicularly magnetized CoFeB multilayers with tunable interlayer exchange for synthetic ferrimagnets. *Journal of Magnetism and Magnetic Materials*, 432:260 – 265, 2017.

[91] Z. Q. Qiu and S. D. Bader. Surface magneto-optic kerr effect. *Review of Scientific Instruments*, 71(3):1243–1255, 2000.

[92] Farnaz Rashidi. *A study of thickness distribution and crystal structure of sputter-deposited silicon thin films.* PhD thesis, Science:, 2015.

[93] W. Reohr, H. Honigschmid, R. Robertazzi, D. Gogl, F. Pesavento, S. Lammers, K. Lewis, C. Arndt, Yu Lu, H. Viehmann, R. Scheuerlein, Li-Kong Wang, P. Trouilloud, S. Parkin, W. Gallagher, and G. Muller. Memories of tomorrow. *IEEE Circuits and Devices Magazine*, 18(5):17–27, Sep. 2002.

[94] Vicente Romero-García, Juan Vicente Sánchez-Pérez, Sergio Castiñeira-Ibáñez, and LM Garcia-Raffi. Evidences of evanescent Bloch waves in phononic crystals. *Applied Physics Letters*, 96(12):124102, 2010.

[95] Samsung Electronics. *Flash Memory*, 3 2007. Rev. 1.

[96] H. Sato, E. C. I. Enobio, M. Yamanouchi, S. Ikeda, S. Fukami, S. Kanai, F. Matsukura, and H. Ohno. Properties of magnetic tunnel junctions with a MgO/CoFeB/Ta/CoFeB/MgO recording structure down to junction diameter of 11 nm. *Applied Physics Letters*, 105(6):062403, 2014.

[97] J. Schmalhorst, H. Brückl, G. Reiss, G. Gieres, and J. Wecker. Thermally induced changes of magnetic coupling in a pinned artificial antiferromagnet used in magnetic tunnel junctions. *Journal of Applied Physics*, 94(5):3268–3270, 2003.

[98] S Schwieger and W Nolting. Origin of the temperature dependence of interlayer exchange coupling in metallic trilayers. *Physical Review B*, 69(22):224413, 2004.

[99] R. Singh. Rapid isothermal processing. *Journal of Applied Physics*, 63(8):R59–R114, 1988.

[100] J. C. Slonczewski. Fluctuation mechanism for biquadratic exchange coupling in magnetic multilayers. *Physical Review Letters*, 67:3172–3175, Nov 1991.

[101] J. C. Slonczewski. Origin of biquadratic exchange in magnetic multilayers (invited). *Journal of Applied Physics*, 73(10):5957–5962, 1993.

[102] Daniel G Smith. *Field guide to physical optics.* SPIE Press, 2013.

[103] V. Sokalski, D. M. Bromberg, M. T. Moneck, E. Yang, and J. Zhu. Increased perpendicular tmr in fecob/mgo/fecob magnetic tunnel junctions by seedlayer modifications. *IEEE Transactions on Magnetics*, 49(7):4383–4385, 2013.

[104] Vincent Sokalski, Matthew T. Moneck, En Yang, and Jian-Gang Zhu. Optimization of ta thickness for perpendicular magnetic tunnel junction applications in the MgO-FeCoB-Ta system. *Applied Physics Letters*, 101(7):072411, 2012.

[105] Mark D Stiles. Exchange coupling in magnetic heterostructures. *Physical Review B*, 48(10):7238, 1993.

[106] Mark D Stiles. Interlayer exchange coupling. *Journal of Magnetism and Magnetic Materials*, 200(1-3):322–337, 1999.

[107] D. Suess, T. Schrefl, S. Fähler, M. Kirschner, G. Hrkac, F. Dorfbauer, and J. Fidler. Exchange spring media for perpendicular recording. *Applied Physics Letters*, 87(1):012504, 2005.

[108] Yue Jun Sun, Oliver Brandt, Tian Yu Liu, Achim Trampert, Klaus H. Ploog, Jürgen Bläsing, and Alois Krost. Determination of the azimuthal orientational spread of GaN films by x-ray diffraction. *Applied Physics Letters*, 81(26):4928–4930, 2002.

[109] Jacob Torrejon, Mathieu Riou, Flavio Abreu Araujo, Sumito Tsunegi, Guru Khalsa, Damien Querlioz, Paolo Bortolotti, Vincent Cros, Kay Yakushiji, Akio Fukushima, et al. Neuromorphic computing with nanoscale spintronic oscillators. *Nature*, 547(7664):428–431, 2017.

[110] R. H. Victora and X. Shen. Composite media for perpendicular magnetic recording. *IEEE Transactions on Magnetics*, 41(10):537–542, 2005.

[111] Bert Voigtländer. *Atomic Force Microscopy*. Springer, 2019.

[112] Yung-Hung Wang, Sheng-Huang Huang, Ding-Yeong Wang, Kuei-Hung Shen, Cheng-Wei Chien, Keng-Ming Kuo, Shan-Yi Yang, and Duan-Li Deng. Impact of stray field on the switching properties of perpendicular mtj for scaled mram. In *2012 International Electron Devices Meeting*, pages 29–2. IEEE, 2012.

[113] Y. Waseda, E. Matsubara, and K. Shinoda. *X-Ray Diffraction Crystallography: Introduction, Examples and Solved Problems*. Springer Berlin Heidelberg, 2011.

[114] Mirko Weidner. *Fermi level determination in tin oxide by photoelectron spectroscopy: relation to optoelectronic properties; band bending at surfaces and interfaces; modulation doping*. PhD thesis, Technische Universität, 2016.

[115] Kay Yakushiji, Akio Fukushima, Hitoshi Kubota, Makoto Konoto, and Shinji Yuasa. Ultralow-voltage spin-transfer switching in perpendicularly magnetized magnetic tunnel junctions with synthetic antiferromagnetic reference layer. *Applied Physics Express*, 6(11):113006, 2013.

[116] Kay Yakushiji, Akio Fukushima, Hitoshi Kubota, Makoto Konoto, and Shinji Yuasa. Ultralow-voltage spin-transfer switching in perpendicularly magnetized magnetic tunnel junctions with synthetic antiferromagnetic reference layer. *Applied Physics Express*, 6(11):113006, 2013.

[117] Aria Yang, Hassan Imrane, Jing Lou, Johnny Kirkland, Carmine Vittoria, Nian Sun, and Vincent G. Harris. Effects of boron addition to the atomic structure and soft magnetic properties of FeCoB films. *Journal of Applied Physics*, 103(7):07E736, 2008.

Appendix A

Additional Material for Chapter 10

A.1 Fit Including Additional Temperature Dependence

This section shows the J_1 temperature dependence of the Co/Ru/Co series from Chapter 10 that has been fit with a function that includes the temperature dependence shown in Eq. 10.6. See the relevant chapter for details. This section will also show the parameters obtained from this fit.

It can be seen in Fig. A.1 that the model fits the data quite well even when we account for the temperature dependence from Eq. 10.6. It can also be seen that the parameters obtained from this fit, as shown in Table A.1, are approximately the same as those obtained when this additional temperature dependence was ignored, as shown in Table 10.2.

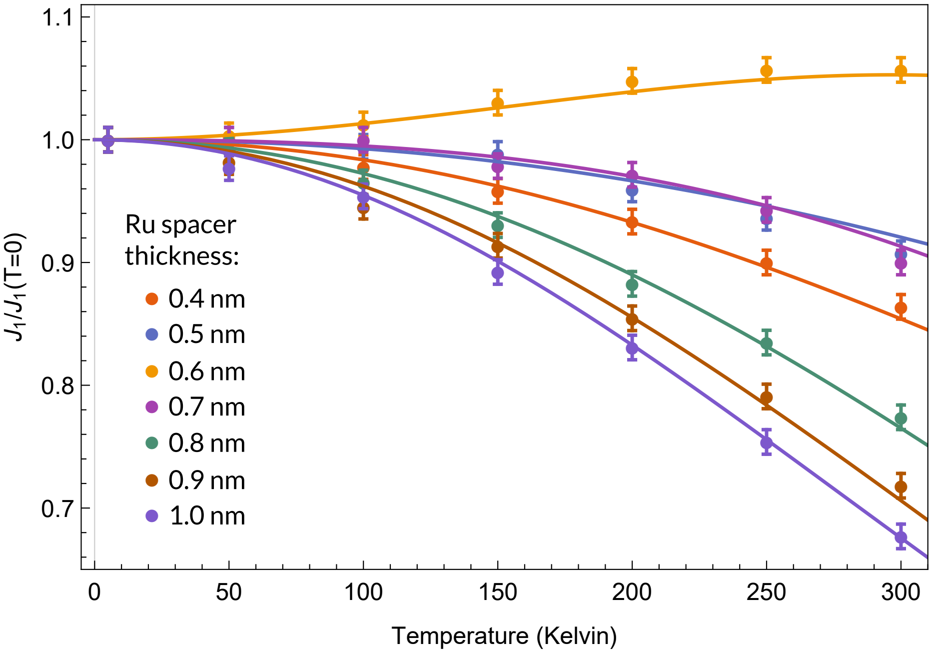

Figure A.1: J_1 temperature dependence for the Co/Ru/Co series with spacer layer thickness ranging from 0.4 to 1 nm and temperatures from 5 to 300 K, normalized to the zero temperature J_1. The circles are data, and the lines are fits using Eq. 10.5 multiplied by $(M_s/M_{s,0})^2$ (See Eq. 10.6 for details). The fits were performed on all measurements simultaneously so that each fit has the same parameters. The colors corresponding to spacer layer thicknesses are shown in the figure.

Table A.1: $v_\perp^\alpha$ and D_ϕ^α from Eq. 4.20 for each critical spanning vector as determined from fitting the temperature dependence data in Fig. A.1 using J^α values from Fig. 10.7 and bulk Ru critical spanning vectors. The fitting function includes the temperature dependence contribution shown in Eq. 10.6

CSV Label	$v_\perp^\alpha \pm 0.6$ (10^5m/s)	$D_\phi^\alpha \pm 0.5$ (eV^{-1})
a_1	4.8	1.3
a_2	1.9	1.3
b	3.1	4.0
c	3.5	3.0
d	8.0	6.2
e	6.3	5.8
f	3.5	3.1
g	9.9	0.0
h	15.9	6.4